



The
University
Of
Sheffield.

**Synthesis, structure and
characterisation of advanced
ceramics for actinide immobilisation**

Laura Danielle Casey

A thesis submitted in partial fulfilment for the degree of Doctor of Philosophy

**Immobilisation Science Laboratory
Department of Materials Science and Engineering
The University of Sheffield**

January 2017

Summary

Ceramic materials are proposed for the immobilisation of actinide bearing materials, including separated uranium and plutonium oxides. While stocks of uranium and plutonium oxide are not currently considered as a waste within the UK nuclear materials inventory, the possibility of this changing in the future cannot be eliminated.

Uranium and plutonium oxides from reprocessing spent nuclear fuel (SNF) have trace quantities of fission products still associated with them, these are a by-product of the irradiation of the fuel within the reactors. Fission products vary depending on the reactor design and irradiation conditions.

The aim of this project was to assess the chemical flexibility of the ceramic materials, which adopted either the pyrochlore or brannerite phase. Both phases have been identified within natural minerals to retain radioactive species on time scales, and in conditions, indicative of those required for long term disposal within a geological disposal facility (GDF). Studies include:

- The incorporation of uranium within lanthanum zirconate pyrochlore $\text{La}_2\text{Zr}_2\text{O}_7$ to form materials of the series $\text{La}_2\text{Zr}_{2-x}\text{U}_x\text{O}_7$. Synthesis occurred within both air and hydrogen / nitrogen atmospheres in order to understand the variation in the average uranium oxidation state by XANES analysis.
- Analysis of the structural flexibility of the pyrochlore phase through minor variations in composition, characterised by the r_A/r_B , ionic radius ratio, of the general composition $\text{CaLn}^{3+}\text{M}^{3+}_{0.5}\text{Nb}_{1.5}\text{O}_7$, where Ln = La, Nd, Sm, Gd, Ho or Yb and M = Al, Fe, Cr, Sc or Y.
- Analysis of the chemical composition dependence to radiation induced damage via in-situ irradiation studies, at the IVEM-Tandem facility, of materials with target composition $\text{CaLn}^{3+}\text{Fe}_{0.5}\text{Nb}_{1.5}\text{O}_7$, where Ln = La, Nd, Sm, Gd, Ho or Yb.
- Analysis of the structural flexibility of uranium brannerite with target composition $\text{U}_{1-x}\text{M}_x\text{Ti}_2\text{O}_6$ with M= Cr, Fe, Pr, Y or Yb.

Acknowledgements

First of all I would like to express my gratitude to my supervisors; Prof. Neil Hyatt, Prof. Karl Whittle and Dr Martin Stennett, for their continued support and patience throughout this research work, both at the University of Sheffield and away.

There are too many people I have met during my studies who, without their support and guidance, my work would not have been possible. However, there are two people who have always been there for me, my parents, and I will never be able to thank them enough for all that they do.

At The University of Sheffield a special thanks has to go to Dr Nik Reeves-McLaren and Andrew Mould for their help, support and training.

At the Institute for Transuranium Elements (ITU) I would like to thank; Dr Thierry Wiss, Dr Jean-Christophe Griveau, Dr Eric Colineau and Dr Oliver Dieste, for their guidance and support during my experiments. An opportunity that would not have been possible without funding from the European Commission through the Actinide User Facility (AUL-162) and Talisman studentship (JRP n° TALI_C04-03) nor without support and company from Dr Martin Stennett.

To Argonne National Laboratory (ANL) I would like to send a special thanks across the Atlantic to Dr Peter Baldo and Dr Edward P Ryan for their support and training at the IVEM-TANDEM Facility. Work funded as a User Facility by the U.S. DOE, Basic Energy Sciences, under contract W-31-10-ENG-38.

For experiments at ISIS, Rutherford Appleton Laboratory I would like to send my gratitude to Dr Kevin Knight for support on the HRPD instrument (proposals RB1320471 and RB1320442) and Prof. Karl Whittle for doing his fair share of 4am sample changes.

And finally to my now husband, Dr James Dixon, from undergraduate to postgraduate we have always been better together, without your support and friendship I don't know where I would be. Love you, always.

Contents

<i>Chapter 1 Introduction</i>	<i>1</i>
1.1 <i>Introduction</i>	<i>1</i>
1.2 <i>Fission</i>	<i>1</i>
1.3 <i>Radioactive Waste Generation</i>	<i>2</i>
1.4 <i>Current Issues and Objectives</i>	<i>7</i>
1.5 <i>References</i>	<i>7</i>
<i>Chapter 2 Literature Review</i>	<i>9</i>
2.1 <i>Ceramic materials for actinide immobilisation</i>	<i>9</i>
2.1.1 <i>Historical ceramic trends</i>	<i>10</i>
2.1.2 <i>Radiation Induced Damage</i>	<i>12</i>
2.2 <i>The Characteristics of the Pyrochlore Structure</i>	<i>14</i>
2.2.1 <i>Natural Analogues</i>	<i>17</i>
2.2.2 <i>Promising attributes of the pyrochlore structure</i>	<i>17</i>
2.3 <i>Titanate Ceramic Materials</i>	<i>19</i>
2.3.1 <i>Multiphase ceramics systems: Synroc</i>	<i>20</i>
2.3.2 <i>Brannerite Structure</i>	<i>21</i>
2.3.3 <i>Natural Analogues</i>	<i>22</i>
2.4 <i>Project Aims</i>	<i>23</i>
2.5 <i>References</i>	<i>24</i>
<i>Chapter 3 Analytical Techniques</i>	<i>31</i>
3.1 <i>X-ray diffraction</i>	<i>31</i>
3.1.1 <i>Basic principles of X-ray diffraction for crystalline materials</i>	<i>31</i>
3.1.2 <i>X-ray Diffraction Instruments Used</i>	<i>33</i>
3.1.2.1 <i>STOE- Image Plate and Stadi P Diffractometer</i>	<i>33</i>
3.2 <i>Scanning electron microscopy and energy dispersive spectroscopy</i>	<i>34</i>

3.2.1	SEM and EDS Theory.....	35
3.3	<i>Neutron Diffraction</i>	37
3.3.1	Neutron diffraction theory: ISIS spallation source	37
3.3.2	High resolution powder diffractometer (HRPD), ISIS, Oxford.	38
3.3.3	The Rietveld Method	39
3.4	<i>Transmission Electron Microscopy</i>	40
3.4.1	Technai G2 F20 XT, Institute of Transuranium Elements	41
3.4.2	Hitachi H-9000NAR TEM (IVEM-Tandem), Argonne National Laboratory	42
3.5	<i>X-ray Absorption Spectroscopy</i>	44
3.5.1	XANES Experimental set up	45
3.6	<i>References</i>	46
 <i>Chapter 4 Systematic substitutions of the calcium niobate pyrochlore system</i>		49
4.1	<i>Introduction</i>	49
4.2	<i>Experimental Methods</i>	52
4.3	<i>Results</i>	53
4.3.1	Scanning electron microscopy and energy dispersive spectroscopy	53
4.3.2	X-ray Diffraction	58
4.3.3	Neutron Diffraction	61
4.3.3.1	<i>Lattice parameter analysis</i>	61
4.3.3.2	<i>Tuning the structure through the r_A/r_B ratio</i>	63
4.4	<i>In-situ irradiation of materials with composition $\text{CaLnFe}_{0.5}\text{Nb}_{1.5}\text{O}_7$</i>	68
4.4.1	Experimental Set Up.....	69
4.4.2	Material Analysis	70
4.5	<i>Discussion</i>	74
4.5.1	Discussions on the in-situ irradiations of $\text{CaLnFe}_{0.5}\text{Nb}_{1.5}\text{O}_7$ materials	76
4.6	<i>Conclusions</i>	78
4.7	<i>Future Work</i>	78
4.8	<i>References</i>	79

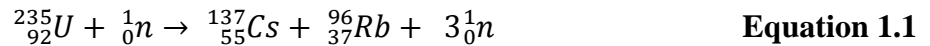
Chapter 5 Uranium Substituted Lanthanum Zirconate Pyrochlores.....	85
5.1 Introduction.....	85
5.2 Experimental Method.....	88
5.2.1 Material Synthesis.....	88
5.3 Results.....	89
5.3.1 Scanning Electron Microscopy and Energy Dispersive X-ray Spectroscopy	89
5.3.1.1 Materials formed in an air atmosphere	90
5.3.1.2 Materials formed in a hydrogen / nitrogen atmosphere	91
5.3.2 X-ray diffraction.....	93
5.3.2.1 Materials formed in an air atmosphere	93
5.3.2.2 Materials formed in a hydrogen / nitrogen atmosphere	98
5.3.3 X-ray Absorption Near Edge Structure Spectroscopy	101
5.3.3.1 Materials formed in an Air Atmosphere	102
5.3.3.2 Material formed in a Hydrogen / Nitrogen atmosphere	104
5.3.4 Transmission Electron Microscopy	107
5.3.3.1 Materials formed in an air atmosphere	107
5.3.3.2 Materials formed in a reducing hydrogen/nitrogen atmosphere	109
5.4 Discussion.....	109
5.4.1 Discussions on Air formed Materials	109
5.4.2 Discussions on Hydrogen / Nitrogen formed Materials.....	112
5.5 Conclusions	115
5.6 Future Work.....	116
5.7 References.....	116
Chapter 6 Formation of Uranium Titanate Materials	121
6.1 Introduction.....	121
6.2 Experimental Method.....	123
6.3 Brannerite Materials Results and Discussions	125
6.3.1.1 Rare Earth Element (REE) Substitution.....	125
6.3.1.2 Iron (Fe) Substitution.....	125
6.3.5 REE Brannerite Bond Valence Summations	132

6.3.6 Brannerite Conclusions	136
6.3.6.1 Rare Earth Element (REE) Substitution Conclusions	138
6.3.6.2 Iron Brannerite Conclusions	139
6.4 Chromium Substituted Material Results and Discussions	139
6.5 Future Work.....	158
6.6 References	159
Chapter 7 Conclusions	163
Appendix A	167
A.1 Introduction.....	167
A.2 Iron Materials.....	167
A.3 Scandium Materials Experimental Data and Discussion.....	169
A.4 Yttrium Materials	173
A.5 Aluminium Materials	178
A.6 Chromium Materials.....	183
Appendix B	187
B.1 Introduction.....	187
B.2 Additional Experimental Data and Discussion.....	187
B.2.1 Additional X-ray Diffraction Refinement Data	187
B.2.1.1 Air Formed Materials.....	187
B.2.1.2 Hydrogen / Nitrogen formed materials	190
B.3 Appendix B Reference.....	194
Appendix C	195
C.1 Introduction.....	195
C.2 Additional Experimental Data and Discussion.....	195

Chapter 1 Introduction

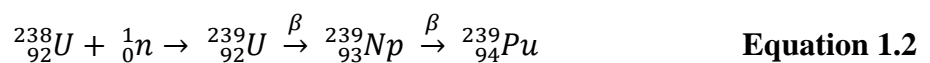
1.1 Introduction

In the United Kingdom nuclear power generation accounts for approximately 18% of the electricity supplied to the National Grid (end of 2014) [1]. Nuclear power is generated from the absorption of a neutron within a fissionable element, primarily uranium-235 (U-235). This causes the U-235 to split into two lighter elements, an excess of neutrons and energy released as heat. This process is known as fission, an example of the reaction is shown in Equation 1.1. The heat, as with conventional gas and coal power stations, is transferred to a steam generator, which itself powers a turbine, generating electricity [2].



1.2 Fission

In order to generate a fission event, very distinct conditions are required, these are dependent on the target fissionable atom. Within the civil nuclear industry a slightly enriched U-235, a fissionable isotope of uranium, is used. U-235 natural abundance in mined ore is found at ~0.7% [2]. The dominate uranium isotope within natural ore is U-238. Civil nuclear reactors in the UK use uranium enriched to between 2-5% U-235 [3]. This increases the likelihood of fission occurring within the fuel as there is an increased chance of the neutron interacting with the U-235 over the U-238. The energy of the neutron determines whether the neutron scatters off of, or is absorbed by, the nucleus. U-235 fission required a neutron with energy described as a thermal neutron. If a neutron was absorbed by U-238, U-239 would form. This is an unstable isotope of uranium and undergoes 2 successive beta minus decays, forming Np-239 and then finally fissionable Pu-239 (Equation 1.2). Pu-239 is fissionable with higher energy (fast) neutrons.



The fission of Pu-239 with fast neutrons is utilised within Fast Reactors. There have been several small test fast reactors across the UK looking at the next generation (Gen-IV) reactors utilising this reaction.

In order to optimise the fission reaction, moderators are used. Moderators within a reactor are designed to control the speed of the neutrons, so that they have optimal energy to interact with U-235 [2]. This will also limit the number of fissile events with Pu-239. Some neutrons will have sufficient energy to be considered as fast neutrons, and therefore able to fission fissile Pu-239. This interaction cannot be eliminated within a fission reactor. Moderators are often a fluid medium consisting of elements with a small absorption cross section, such as gas or heavy water. They are designed to slow the neutrons via scattering, not absorb them. Moderators also serve the purpose of a transfer medium for heat. This acts as a coolant to the reactor core, as well as transferring heat to a secondary loop, which is used to ultimately generate electricity via a steam turbine. A secondary loop ensures no release of radioactive substances can occur [2].

An additional safety feature of the reactor includes the use of control rods [2]. These are typically vertically inserted so that, in the event of a loss of power, these can be lowered through the use of gravity. However, there are a vast array of reactor designs and some do not have vertically inserted control rods. Control rods can be physically inserted or removed from the reactor core even whilst energy is being generated. The proportion of the control rods within the reactor core will be dependent on the optimising the fission chain reaction. The chain reaction is caused by the excess of neutrons released from the initial fission event. A fission event can release up to 3 neutrons, the rate of this chain reaction needs to be controlled to ensure the reaction rate is optimised [2].

Fission does not have to be induced, spontaneous fission within an unstable atom is possible, and it is spontaneous fission which can potentially cause a problem for the long term storage of large quantities of highly enriched uranium and plutonium material. For this reason it is advantageous to have a medium which is passively safe and does not enable the fission reaction to occur [2].

1.3 Radioactive Waste Generation

As with all methods of generating power, waste is produced. Waste produced as a by-product of nuclear power generation have a radioactive substances associated with them. If not contained and disposed of correctly, radioactive materials could have a detrimental effect of the environment and living organisms. In order to ensure the long term safety,

to both the environment and public, the wastes are processed into a suitable package whose integrity will be maintained for the radioactive elements lifetime. The lifetime is a description of how long the radioactive material takes to fully decay.

The probability of a decay occurring is described by the activity of the isotope, Equation 1.3. Where N is the number of radioactive nuclei, N_0 is the number of nuclei at time (t) zero ($t=0$), and λ is the decay constant. The decay constant is unique for each isotope of each element, and is a measure of the number of decays in 1 second. The half-life ($t_{1/2}$) (Equation 1.4) is defined the time in which it takes for the radioactivity of a particular isotope to half. This shows the expression to calculate the time for the unique situation where there are half the original radioactive atoms.

$$N = N_0 e^{-\lambda t} \quad \text{Equation 1.3}$$

$$t_{1/2} = \frac{\ln(2)}{\lambda} \quad \text{Equation 1.4}$$

Ideally, radioactive material will be stored underground in a long term geological disposal facility (GDF), however the current location of this within the UK is yet to be decided. Assuming the ultimate disposal within a GDF, the radioactive wastes within the UK are categorised and packaged for disposal. Waste package requirements are dependent on the category, the categories are summarised in Table 1.1. The Radioactive Waste Management (RWM), a government body, is in place to offer guidance on the compatibility of any proposed waste forms with the GDF concept.

The route for lower activity wastes (VLLW and LLW) is defined depending on the material type. Where an item can be decontaminated, reducing the volume of radioactive waste, then measures are taken to ensure this is completed. Examples of decontamination methods include steam cleaning individual items in-situ, or sandblasting at Studsvik, Workington, a nuclear licensed facility which uses sand blasting in order to remove the contaminated surface layer of metallic object. Any material which cannot be decontaminated is sentenced to the Low Level Waste Repository (LLWR) near Drigg. This is a near surface repository which places either material directly, or within iso-frait containers, into shallow engineered trenches. The trenches are concrete lined and capped off to minimise surface exposure. Recently the site has moved to using super-compacting in order to reduce the volume of material and increase the capacity of the limited space within the facility. This approach to waste volume reduction is being adopted by nuclear licensed facilities across the UK for LLW, with the move to super-compacting ILW material expected.

Table 1.1: Categories for radioactive waste utilised within the United Kingdom as defined by Radioactive Waste Management (RWM) [4].

Higher Activity Wastes	High Level Waste (HLW)	Heat generating materials due to the energy from the radioactive decay. Dissipation of this heat needs to be taken into consideration during long term disposal.
(HAW)- Require GDF	Intermediate Level Waste (ILW)	Wastes which have activity levels higher than those categorised as LLW however do not have an element of heat to take into consideration for long term disposal.
Low Activity Wastes	Low Level Waste (LLW)	Waste with radioactive levels which do not exceed 4GBq/tonne of alpha (α) decay or 12GBq/tonne of Beta (β) or Gamma (γ) decay.
	Very Low Level Waste (VLLW)	Wastes with radioactive levels which do not exceed 4MBq/tonne. Specific activity for tritium is not to exceed 40MBq/tonne.

The long term strategy of highly active waste (HAW) within the UK is yet to be implemented, however it is recommended for the UK to adopt a long term geological disposal facility with a co-storage of HLW and ILW [5, 6]. The GDF concept will be a purposefully designed underground facility with vaults, designed to accommodate specific HAW packages. The GDF will also offer the solution for the long term disposal of spent nuclear fuel, if the decision to reprocess within the UK is continued. Currently the Nuclear Decommissioning Authority (NDA) strategy is designed to reduce the hazards on individual nuclear licensed facilities through the consolidation of spent nuclear fuels on the Sellafield or the Capenhurst sites [7]. Where possible the spent fuel is sent for reprocessing in order to recover the uranium and plutonium asset. Material, which is not suitable for reprocessing, is stored on the Sellafield site while a decision is made about alternative reprocessing / disposal strategy for spent fuels inventory.

Nuclear fission can generate large numbers of fission products, and the chemical composition of these are dependent on the original fuel, as well as irradiation qualities, such as fuel burn up. Fuel burn up describes the characteristics of fuel (temperature, reactivity and physical composition) base on how long it has resided within the reactor core. Each isotope of an element should be considered, but generally a focus is made on the identification of those which have the potential to be reactive within future processes. The nuclides of interest, excluding the isotopes of U, Pu, Th, Am and Np, are; Mo-95,

Tc-99, Ru-101, Rh-103, Ag-109, Cs-133, Nd-143, Nd-145, Sm-147, Sm-149, S-150m, Sm-151, Sm-152, Eu-153 and Gd-155. Within uranium oxide fuel these make up between 25-30% of the waste product inventory of spent nuclear fuel [8].

There are currently two reprocessing facilities in operation on the Sellafield site, the Thermal Oxide Reprocessing Plant (THORP) and Magnox Reprocessing Plant.

THORP is situated on the Sellafield Site, Cumbria, and is designed to recover uranium and plutonium from spent nuclear fuel via a nitric acid dissolver. The fuel is primarily from the Advances Gas-cooled Reactor (AGR) fleet within the UK. However, it serves the needs of other metallic fuel reactors where the recovery of the uranium / plutonium is viable, both within the UK and abroad. Spent Nuclear Fuel consists of 96% uranium, 1% plutonium and 3% a waste by-product from the fission reaction [9]. The waste by product consists of a variety of fission products, including long lived fission and / or high activity products, transition elements and heavy rare earth elements and is produced as a liquor in THORP. Currently the THORP facility is due to close in 2018 but the NDA, the site licence holder of Sellafield, has agreed to take liability of all future arising from the UK's Magnox and AGR fleets, which extends beyond the closing date of the facility. Currently there are >3000 tonnes of unprocessed material which could potentially remain in its current form and either; require packaging in a suitable containment for disposal within the GDF, or, a new reprocessing facility is to be made available.

Currently the highly active liquor waste from the THORP process is immobilised through vitrification within a borosilicate glass matrix. This is achieved by mixing the liquor within a pre-produced glass frit within a calciner to produce the glassy product. The glassy matrix is then poured into a stainless steel canister and placed into interim storage in air-cooled vaults within the Sellafield reprocessing plant (Figure 1.1). A glass material is an amorphous matrix with a disordered structure. When subject to radiation induced damage, caused through the decay of radionuclides, a minimal effect on a glassy matrix is observed, although swelling and cracking is possible.

High enriched plutonium and uranium materials which are unsuitable within a borosilicate system in high concentrations due to their low solubility and the increased risk of a critical event [10]. A critical event is where fissile material is unintentionally collected into a mass such that a nuclear chain reaction can occur. Glasses also have a slow rate of heat dissipation. The incorporation of heat generating products can also cause the glassy matrix to devitrify and become unstable. Within a glassy waste form no control mechanisms, such as neutron absorbing elements or physical separation in a crystalline unit cell, are in place. For highly enriched actinides, the long range crystalline

ordering of an inorganic ceramic material are now being considered for future HLW disposal conditioning. This is not only in the UK, but also worldwide, due to their ability to position cations on distinct cation locations.



Figure 1.1: Images of (left) the canisters in which the glass HLW matrix is poured and (right) the HLW glass canister stored within the Sellafield reprocessing plant, Cumbria.

The Magnox Reprocess Plant (Sellafield, U.K.) was built to recover the uranium and plutonium oxides from the Magnox fleet of reactors within the U.K. This is achieved through the shearing of the fuel in order to remove the magnesium alloy cladding. The cladding is managed as ILW material, and grout encapsulated within 500 litre drums. The remaining fuel rod is dissolved in a nitric acid solution in order to extract the uranium / plutonium asset as a nitrate solution. As with the waste products from THORP the waste material is transferred for vitrification on the Sellafield site.

Capenhurst offers the facilities to store uranium trioxide (UO_3) material as an asset for the NDA estate, as well as facilities for re-enrich of reprocessed uranium material [11]. This ensures the re-use of the reprocessed stocks through the formation of new fuel. The enrichment of uranium produces a by-product referred to as tails. Tails consist of uranium with an enrichment lower than natural abundance with the fission products / actinides removed with the original spent material [12].

Ceramic materials can withstand notably higher temperatures than glasses before melting. The properties of ceramic materials are composition and environment (pH and pressure) dependant, but have the potential to incorporate greater quantities of actinides including uranium and plutonium when compared to a glass matrix [10, 13].

1.4 Current Issues and Objectives

The nuclear waste inventory for the UK does not include spent nuclear fuel (SNF) or reprocessed and separated plutonium / uranium oxides, these are considered an asset and are therefore not included within the waste inventory within Table 1.2 [14]. Additional sources of radioactive material beyond the civil nuclear industry include: defence, medical and research / educational facilities.

In addition, there are stocks of exotic fuel from the UK alternative nuclear fuel cycle. This exotic fuel is predominantly plutonium oxide from both experimental test reactors and from the production of plutonium for the nuclear weapons programme. The total expected arising of plutonium within the UK at the end of reprocessing is ~140 tonnes [15].

Table 1.2: Summary table of 2013 UK Radioactive waste inventory from all sources as extracted from the 2013 UK radioactive waste inventory white paper [14].

	HLW	ILW	LLW	VLLW	Total
Volume (m³)	1080	286000	1370000	2840000	4490000
Mass (tonnes)	2900	310000	1700000	2900000	4900000

The inventory is accounted for within the NDA ‘Higher Activity Waste Strategy’ which defines the use of a GDF [10]. Should the stock of uranium and plutonium oxides, from across the industries, in the future be re-classified as waste, each source will require a tailored disposal strategy, along with substantiation of the long term safety and stability of the material.

Due to the promising properties of ceramic materials for the immobilisation of large quantities of heat generating actinide materials the objectives of this project include analysis of; the chemical flexibility of ceramic materials, the accommodation of multiple cations with the pyrochlore and brannerite structures, and the implications of the natural decay of the radioactive materials within the crystalline structures is required.

1.5 References

- [1] Association WN. Nuclear Power in the United Kingdom. In: 2014.
- [2] Wilson PD. The Nuclear Fuel Cycle: From Ore to Waste. Oxford Science Publications; 1997.

- [3] Department for Business EIS, Authority ND. Radioactive Wastes in the UK: A summary of the 2016 Inventory. In: 2017.
- [4] Implementing Geological Disposal. In: Edited by: Change DoEC. Crown; 2014.
- [5] CoRWM. Managing our radioactive waste safely: CORWM's recommendations to Government. In: 2006.
- [6] Authority ND. Integrated Waste Management: NDA Higher Activity Waste Strategy. In: May 2016.
- [7] Strategy- Effective from April 2016. In: Edited by: Authority ND. March 2016.
- [8] Committee NS, Safety WPoNC, Fuel EGoADoSN. Spent Nuclear Fuel Assay Data for Isotopic Validation; State of the art Report. In: Organisation for Economic Co-operation and Development; 2011.
- [9] Ltd S. Spent Fuel Management: Thorp Reprocessing. In.
- [10] Lumpkin GR. Ceramic waste forms for actinides. Elements 2006; 2:365-372.
- [11] Urenco takes on Capenhurst site. In: World Nuclear News; 2012.
- [12] Ltd T. Capenhurst Nuclear Services | What We Do. In: 2017.
- [13] Roy R. Rational Molecular Engineering of Ceramic Materials. Journal of the American Ceramic Society 1977; 60:350-363.
- [14] Authority ND. 2013 UK Radioactive Waste Inventory: Waste quantities from all sources. In: Edited by: (DECC) DoEaCC. 2013.
- [15] Authority ND. Progress on approaches to the management of separated plutonium-Position Paper. In: Edited by: (DECC) DoEaCC. 2014.

Chapter 2 Literature Review

2.1 Ceramic materials for actinide immobilisation

Ceramic materials are an oxide based solid, formed through high temperature synthesis. In nature, minerals and rock formations are found to retain naturally occurring radioactive species, for timescales indicative of those required for a final geological disposal facility (GDF). Ceramic materials for actinide immobilisation was first suggested Hatch et al., who proposed the retention of radioactive actinides in clay materials [1]. Actinide immobilisation within ceramic materials is explored due to the crystallinity, which ceramic materials can exhibit. Crystallinity is defined as a material with a regular array of atoms, giving rise to long range ordered structure. The regular arrangement of the atoms within a crystalline structure is described by the lattice parameters. A unit cell of the structure is the smallest repeatable arrangement, in 3-dimensional space, of the atoms within the structure. The symmetry of the unit cell defines its space group. Lattice parameters are described by vectors relative to the x , y , z planes, and are denoted as a , b and c . The angle between the vectors are denoted as α , β and γ . The vectors and planes of crystal lattice are described by Miller indices (h , k , l) which are the reciprocals of the intercepts on the a , b and c axis, respectively [2]. The spacing between the planes described by the Miller indices is defined by the d-spacing (Å). The relationship between the Miller indices and the d-spacing is dependent on the crystal structure, examples of which can be found in Table 2.1.

Table 2.1: Relationship between the Miller indices (h , k , l) and the d-spacing between lattice planes for structures with a cubic, tetragonal or hexagonal structure, as taken from reference [2].

Cubic	Tetragonal	Hexagonal
$\frac{1}{d^2} = \frac{h^2 + k^2 + l^2}{a^2}$	$\frac{1}{d^2} = \frac{h^2 + k^2}{a^2} + \frac{l^2}{c^2}$	$\frac{1}{d^2} = \frac{4}{3} \left(\frac{h^2 + hk + k^2}{a^2} \right) + \frac{l^2}{c^2}$

This regular arrangement can be utilised with highly active species whose critical mass is low. The critical mass is defined as the minimum mass of fissile material required to create a sustainable fission chain reaction. Controlling the cation locations within a crystalline material, and potentially co-locating fissionable cations with neutron absorbing cations, mitigates of the risk of a critical event occurring. Ceramics are also

notable difficult to reverse engineer, offering a security advantage as a deterrent for proliferation. The ceramic composition can be selected based on the source of the material that requires immobilisation.

2.1.1 Historical ceramic trends

Naturally occurring ceramic materials containing radioactive species have been proposed since the early 50's for the immobilisation of radioactive species (actinides) not only physically but chemically [1].

The use of ceramics as an alternative for calcined HLW waste was suggested by G.J. McCarthy [3] and R. Roy [4] in the 1970s as an advantageous wastefrom over a glassy matrix, through minor oxide additives, to form a material with a 50-75% waste loading. This is developed further to enable the inclusion of uranium and plutonium species without the need for separation, ideal within countries who have chosen not to reuse uranium / plutonium so have no driver for reprocessing spent nuclear fuel. This required the development of ceramic materials which are compatible with a varied waste stream but still able to maintain the physical and chemical properties that are desirable for the wastefrom.

Specific waste streams have tailored chemical compositions for the long term passively safe immobilisation of plutonium and uranium stocks. An example is the titanate pyrochlore rich ceramic wastefrom for the disposal of impure plutonium stocks in the U.S.A., tailored primarily by Lawrence Livermore National Laboratory (LLNL). A chemical composition of $\text{Ca}_{0.89}\text{Gd}_{0.22}\text{Hf}_{0.23}\text{Pu}_{0.22}\text{U}_{0.44}\text{Ti}_2\text{O}_7$ was defined to ensure the long term criticality risks with the storage of Pu-239 were minimised [5, 6]. This includes the use of neutron absorbing gadolinium and hafnium as well as uranium-238 to ensure that the natural decay of Pu-239 to U-235 does not increase the likelihood of a critical event [5].

In additional to the exploration of single phase ceramic materials for the immobilisation of separated actinide materials, A.E. Ringwood et al., at the Australian National Science and Technology Organisation (ANSTO), pioneered the production of a synthetic rock (SYNROC) in the 1970s [7]. SYNROC is a multi-component matrix utilised to simultaneously host several radioactive materials in a single body. The ceramic phases are chosen depending on the waste stream, thereby selecting the physical and chemical properties. The radioactive precursor components are additives to a mix of inert

matrices, which are designed to be thermodynamically stable with each other [7]. Further discussion of the concept can be found in Section 2.3.1.

Information on the phase and composition of naturally occurring minerals are used to provide information for synthesised ceramic materials. As well as minerals being older than defined as required for the GDF, the minerals are often found in environments far more aggressive than those in a desirable of a GDF [8]. The use of naturally occurring minerals provides information of a materials long term ability to retain radioactive species, stability and behaviours[9]. Minerals are found in a metamict state, an amorphous state of a previously crystalline material, where the long range ordering within the structure has been lost. Direct analysis of the metamict materials ability to retain the radioactive species can be made to understand the long term behaviours [10].

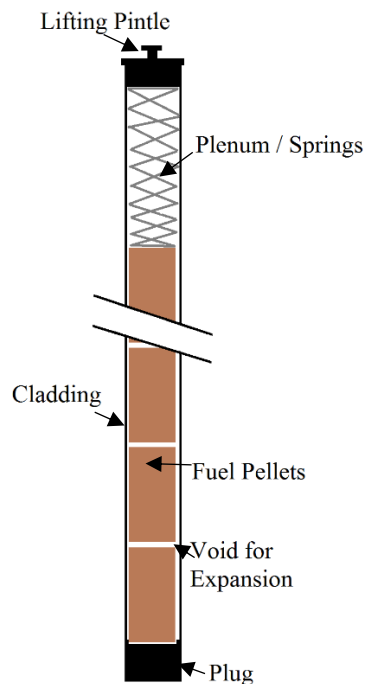


Figure 2.1: A schematic (not to scale) of a typical fuel pin designed to accommodate both physical expansion of the fuel within the cladding and includes a plenum within the design designed to accommodate any gases released.

Analysis of radiation damage of ceramic fuels can provide information for the disposability of actinide materials [11-21]. For ceramic fuels a metal alloy cladding is used. This is designed to contain any fragments of ceramic fuel which arise due to the physical radiation induced changes of the material. This also physically separates individual fuel pellets in an ordered, and maintained, structure. A schematic of a fuel pin

is shown in Figure 2.1. Large numbers of fuel pins are arranged within a fuel sub-assembly, the number and design is dependent on the reactor and fuel type.

2.1.2 Radiation Induced Damage

In order to understand the long term integrity of a ceramic waste form two aspects must be analysed. Firstly, the long term behaviour of the ceramic within the environment, focusing on those expected within a geological disposal facility, including the interaction with the direct facility components. Secondly, the internal effect on the ceramic due to the inclusion of radioactive isotopes, whose decay leads to radiation induced damage. There are four sources of radiation damage which can impact upon the ceramic structure arise due to:

- i. Spontaneous fission of unstable (fissionable) isotopes within the wastefrom. This changes the local environment around the cation within the ceramic lattice, due to a single cation splitting into; 2 lighter elements, excess neutrons and excess energy. Excess energy is initially in the form of momentum associated with the new particles. This is converted to heat as the momentum dissipates through interactions with further atoms. If the energy provided by the decay is sufficient, an atom can be displaced from the crystalline lattice. The displaced atom rests within the crystalline lattice, interrupting the regular array of the structure.
- ii. Gamma (γ) decay. This is a form of electromagnetic energy released from the stabilisation of a nucleus from a higher energy state to a lower energy state. Gamma particles are a high energy radiation and are difficult to shield against.
- iii. Beta (β) decay. The conversion of a neutron to a proton resulting in the release of an electron from a nucleus, this electron could be captured within a nucleus resulting in a beta plus (β^+) emission. This is the inverse of a β emission, where a proton converts to a neutron, with the release of a positron (anti-proton).
- iv. Alpha (α) decay. The ejection of a positively charged helium nucleus, ${}^4\text{He}^{2+}$, which will readily accumulate electrons from its surrounding environment to form a helium ion, ${}^4\text{He}$.

Physically, radiation damage can cause cracks and swelling of the material. Damage is caused by the decay particle released, or by the recoil energy in the parent atom. The parent atom is the decaying nuclide. The recoil energy within the parent atom arises from the conservation of momentum where, with no external force, an equal force is exerted on the parent atom, but in an opposite direction to that of the decay particle. In order to

be able to determine the effect of the damage on a specific composition the synthesised crystalline material are experimentally irradiated using ion beams. While all decay mechanisms will cause damage to materials, the following is to establish, within a crystalline structure, which causes the greatest damage, and therefore the highest risk to the integrity of the structure.

Gamma radiation will be able to penetrate the furthest within the crystal lattice. Energy is transferred to atoms within the lattice as they interact with the electromagnetic radiation, causing localised damage. Gamma radiation is non-directional, as an electromagnetic wave the energy is dispersed in equal magnitudes in all directions, transferring a fraction of the energy to its local environment. This energy dissipates through the material via vibration of the atoms within the lattice. As there is no mass associated with a gamma particle, there is minimal recoil energy in the parent atom when a gamma decay occurs. This also means, as a result of this gamma decay, no decay particle is implanted within the structure.

Beta and alpha decay have a different dominating effect within a ceramic material than gamma due to the fact that the greatest impact of the decay is not from the particle which is released, but the momentum which is felt within the parent atom.

A beta particle is the release of an electron with a single charge, a low mass ($\sim 9.109 \times 10^{-31}$ kg) and low energy. The small mass and energy results very little recoil energy within the parent atom. The chemical changes, as a result of the beta decay, need to be accommodated within the lattice.

An alpha particle when released has a greater mass than an electron during beta decay ($\sim 6.644 \times 10^{-27}$ kg). An alpha particle is a positive charge helium cation with; 2 neutrons, 2 protons and is missing 2 electrons. In order to stabilise an alpha particle readily captures electrons from its local environment to become a helium atom. The increased mass of an alpha particle means that a greater magnitude of energy is released during the decay to occur. The alpha particle is also larger for the lattice to accommodate. The greater mass and energy of the alpha particle, relative to the beta and gamma energies, results in a greater recoil energy exerted on the parent atom. Alpha decay predominantly occurs in atoms where the ratio of protons to neutrons is most imbalanced, this requires atoms with large masses including actinides. The recoil energy due to the alpha decaying event within the parent atom is large, however as the parent atoms are heavy actinides the momentum is insufficient to displace it from the lattice. The energy in the recoil is sufficient damage to the localised structure. This includes localised stresses / strains with the material, or the formation of a vacancy within the lattice due to subsequent displaced atoms. The stress

/ strain defects and / or vacancies can result in a localised loss of the crystalline ordering of the atoms, creating an amorphous fraction of material. The accumulation of the damage can result in a complete loss of the crystalline order throughout the material. An alpha decay of Pu-239 to U-235 typically equated to 4.5-5.8MeV of energy associated with the decay particle, and a recoil energy in the parent atom of 70-100keV. The alpha particle has sufficient energy to penetrate the material, transferring energy and causing damage. When sufficient energy is lost, so that the alpha particle is unable to penetrate further, a larger area of damage is formed. The recoil energy, while insufficient to displace the parent atom from the lattice, has a significant quantity of energy to damage to localised lattice environment. This typically causes >1000 atomic displacements [22, 23].

The recoil energy in the parent atom due to an alpha decay is identified as the decay mode which produces the greatest damage. However, by providing energy to the lattice radiation damage can be reduced, or even eliminated, if the material has sufficient energy to recover from the damage as it occurs. Additional energy can be provided by heat. The effects of the induced damage may cause cracking within the surface as a result of swelling. This increases the reactive surface area of the material, reducing the stability of the ceramic wastefrom. This can accelerate the release of radioactive nuclides when placed within a potentially aqueous environment, as with a geological disposal facility. Therefore a materials ability to remain crystalline of the lifetime of the radioactive isotopes is advantageous. Natural analogues have been identified to contain higher concentrations of naturally occurring uranium and thorium actinides [15, 24-36]. When considering the potential long term immobilisation of highly active species, natural analogues can provide information on the radioactive decay of isotopes, and the damage to the crystalline structure. This can be used when studying synthesised materials, of interest to this work ceramic materials with the pyrochlore and brannerite structure.

2.2 The Characteristics of the Pyrochlore Structure

Pyrochlores, of general formula $A_2B_2O_7$, are a cubic $2 \times 2 \times 2$ superstructure relative to an underlying fluorite lattice, AO_2 [37]. The superstructure arises due to the regular arrangement of an oxygen (anion) vacancy within the structure at the 8b position ($3/8, 3/8, 3/8$) position (Figure 2.2). This defines the local coordination environment of the cations within the structure, as described by space group $Fd\bar{3}m$, and creates two distinct cation sites [37]. These are represented by A and B in the general formula. With respect to the oxygen anions, the A-site cations are 8 fold coordinated and the B-site cations are

6 fold coordinated [37]. The distortion in the sites are such that the A-site cations are coordinated in a distorted trigonal scalenohedron, and the B-site cations are in a regular octahedron array [38]. The pyrochlore structure comprises of alternating layers of A and B cations which form a face centred cubic array ordered in the $\langle 110 \rangle$ direction [37]. The unit cell parameter ‘ a_P ’ of the pyrochlore structure is twice that of the fluorite structure, $a_P = 2a_F$, as shown in Figure 2.2. The lattice parameters of the ideal pyrochlore structured material are all located in special positions. A-site cations are locations on 16c (0, 0, 0) and B-site cations on 16d (1/2, 1/2, 1/2). The anions are located on two positions, the 8a (1/8, 1/8, 1/8) and 48f (x, 1/8, 1/8) positions [37]. The anion on the 48f position is able to move about the ideal value of $x = 3/8$, due to the vacancy in the 8b (3/8, 3/8, 3/8) position.

Both the A and B-sites offer great chemical flexibility, an ideal pyrochlore has a structure of $A_2^{3+}B_2^{4+}O_7$ [37]. However the structure is not only able to tolerate multiple cations on the A and B-sites, it can also tolerate 8 fold coordinated 2+ cations on the A site, coupled with 6 fold coordinated 5+ cations on the B site [37]. The structure is able to accommodate additional oxygen stoichiometry within the order anion vacancy, however overall the material cannot exceed an oxygen stoichiometry of 8. Although this can destabilise the structure. The pyrochlore structure is most stable with cations of an average oxidation of 3+ on the A-site and 4+ on the B-site [37]. This diversity in the chemical composition of the pyrochlore structure has led to the analysis of over 450 different pyrochlore materials [37]. The pyrochlore structure has been studied and proposed as a wasteform for highly enriched uranium and plutonium disposition due its chemical flexibility, tolerance to radiation induced amorphisation and resistance to dissolution [9, 28, 31, 39-49]. Chemical flexibility is important when looking at the immobilisation of actinide bearing waste streams which contain a vast range of fission products.

This flexibility of the pyrochlore structure means that a variety of elements with different atomic radii and oxidation states can be incorporated within the structure, although there are limitations in the cation radius on the A and B sites, r_A and r_B respectively, see Equation 2.1(a) and (b).

$$r_A = 0.87 - 1.51 \text{ \AA} \quad \text{Equation 2.1(a)}$$

$$r_B = 0.40 - 0.78 \text{ \AA} \quad \text{Equation 2.1(b)}$$

The ratio of these atomic radii, Equation 2.2, was used throughout to describe the stability of the phase, and ultimately the likelihood of a composition forming with the pyrochlore

structure. The description of the position of the 48f oxygen (in the x-direction), Equation 2.3, is also utilised to describe the stability of the B-site co-ordination environment.

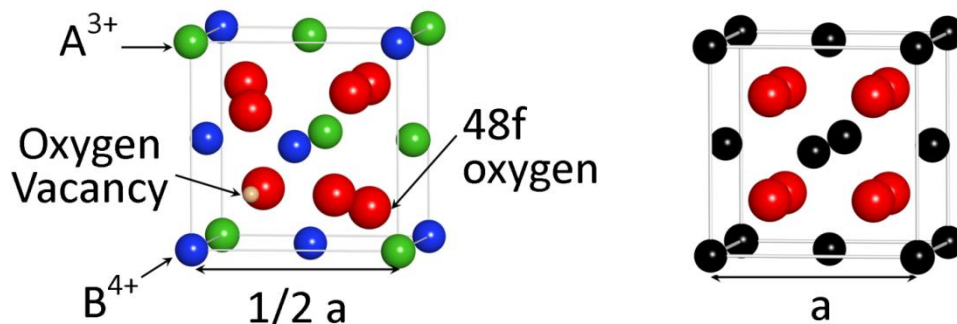


Figure 2.2: (a) 1/8th of the unit cell volume, red are oxygen atoms, green represent the A cations and blue represent the B cations, a key aspect of the pyrochlore structure is the oxygen vacancy within the structure, which if occupied the structure becomes a simple fluorite structure. (b) The fluorite structure, red denotes oxygen anions and black are cations, a defect fluorite is one where there are vacancies in the structure, they tend to disordered.

$$\frac{r_A}{r_B} = 1.46 - 1.78 \quad \text{Equation 2.2}$$

$$0.3125 > 48f \text{ x oxygen} > 0.375 \quad \text{Equation 2.3}$$

For pyrochlore structures at the lower extreme ($r_A/r_B < 1.46$) either a fluorite $(AB)_4O_8$ or defect fluorite $((AB)_4O_7)$ structure is formed, this can also be quantified by the shift in the 48f oxygen x-coordinate, Equation 2.3. A defect fluorite is a fluorite with an unordered oxygen vacancy such that the average anion occupancy is $7/8^{\text{th}}$ of the anion locations, and the average cation coordination is 7. In a defect fluorite the A-site cations arrange into a regular polyhedra cube, and the B site cations into a triagonally flattened octahedra. A defect fluorite shows the greatest distortion in the structure.

Above the upper boundary ($r_A/r_B > 1.78$) a monoclinic structured material is expected to form, an example is the layered perovskite structure of composition $\text{La}_2\text{Ti}_2\text{O}_7$ [50]. This effect can arise if the A site cations is too small or the B site cations are too large for a stable pyrochlore structure to form.

Electron diffraction images of the material, collected in the transmission electron microscope (TEM), aid identification of the presence of the pyrochlore. Figure 2.3 shows the simulated diffraction pattern of the [010] axis of materials with (left) the fluorite

structure, and (right) the pyrochlore structure, with the interstitial reflections of the pyrochlore super lattice indicated by the arrow.

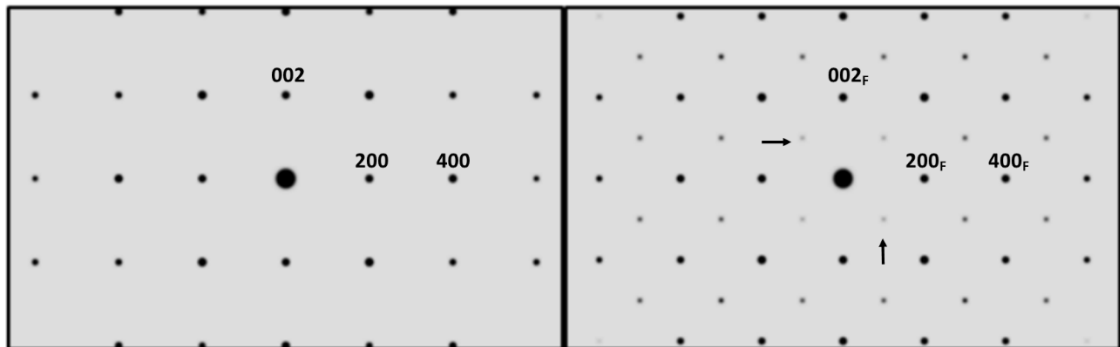


Figure 2.3: The simulated images of the [010] axis of (left) fluorite and (right) pyrochlore. Indexed on the images are the fluorite structure, and the fluorite reflections of the pyrochlore, with the superstructure reflections indicated by the arrows.

2.2.1 Natural Analogues

Pyrochlore structured materials are often found in mined ore containing both naturally occurring radioactive species and rare earth elements (REE), with levels up to 30wt% UO_2 , 9wt% ThO_2 and 16wt% REE_2O_3 [31]. Taking the general pyrochlore formula, $\text{A}_2\text{B}_2\text{O}_6\text{Y}$, it can be seen with synthetic pyrochlores the anion Y is taken as oxygen, although in nature Y could be any of O, OH or F.

Natural pyrochlores can be found with a variety of cations on the A and B-sites (A = Na, Mg, K, Ca, Mn, Fe, Sr, Sb, Cs, Ba, Pb, Bi, Th, U or REE and B= Nb, Ta, Ti, Zr, Sn, W, Fe or Al) [51-54]. The natural analogue of a material with the pyrochlore structure can be taken from zirconolite, ideally $\text{CaZrTi}_2\text{O}_7$. Zirconolite is found in nature to contain up to 33wt% REE including natural U and Th [28]. Naturally occurring minerals with a pyrochlore related structure have been analysed to provide information on radionuclide retention in an environment expected of a geological disposal facility. This includes, but is not limited to, analysis of the material in aqueous environments [14, 15, 29, 31, 41, 55-57] and analysis of the resultant structure due to internal decay modes [21, 44, 47, 54, 58-62].

2.2.2 Promising attributes of the pyrochlore structure

Phases of particular interest include titanate and zirconate pyrochlores, $\text{A}_2\text{Ti}_2\text{O}_7$ and $\text{A}_2\text{Zr}_2\text{O}_7$, respectively. Ion beam irradiation studies on synthesised pyrochlore ceramic

materials have shown that the tolerance to radiation damage in pyrochlores is dependent on the chemical composition. Both variations in the A site and B site cations have an effect on the radiation tolerance of the material.

Varying the lanthanide cation on the A site of titanate pyrochlores, $\text{Ln}_2\text{Ti}_2\text{O}_7$, Lian et al. [63] showed how the critical temperature changes with composition. The critical temperature, T_C , is the minimum temperature at which the material retains the crystalline structure under irradiation simulation of alpha recoil damage. The lower the T_C , the lower the energy required to maintain the crystalline structure. This could be interpreted as a material which is more resistant to damage if the heat from the decay provides sufficient energy to increase the temperature above T_C . Lian et al. found that as the ionic radii of the A-site cation increases, from Lu to Sm, in general composition, $\text{Ln}_2\text{Ti}_2\text{O}_7$, the T_C value increases [64].

Analysis of gadolinium pyrochlore ($\text{Gd}_2\text{B}_2\text{O}_7$) by Wang et al, showed that by varying the B-site cation ($\text{Gd}_2\text{Ti}_2\text{O}_7$ and $\text{Gd}_2\text{Zr}_2\text{O}_7$) the response to radiation damage also varied [47]. The titanate material, with the smaller ionic radii than the zirconium, and hence the smaller r_A/r_B value, became amorphous during heavy ion beam irradiated. However, gadolinium zirconate pyrochlore ($\text{Gd}_2\text{Zr}_2\text{O}_7$) showed greater resistance to radiation damage, even at temperatures as low as 25K [47]. Based on the results of such experiments titanate pyrochlores, such as $\text{Gd}_2\text{Ti}_2\text{O}_7$, containing 10 wt% Pu-239 are projected to remain crystalline for up to 600 years. Whereas the zirconate equivalent, $\text{Gd}_2\text{Zr}_2\text{O}_7$, would be expected to remain crystalline even when irradiated with a dose equivalent to that expect to be received over 30 million years [47]. The gadolinium zirconate pyrochlore is a perfect example of the use of a pyrochlore structure which has an r_A/r_B value close to that of a defect fluorite ($r_A/r_B = 1.46$) but maintains the crystalline properties of a pyrochlore structure [47, 65-72].

The x-coordinate position of the 48f oxygen describes the shape of the B-site cations octahedra, and is used to predict the effect of the heavy ion beam irradiation on the crystal structure. The less distorted the cations on the B site, described by the shift to lower values of the 48f oxygen x-position, the less resistant to radiation damage a ceramic is likely to be as the material is structurally closer to radiation tolerant fluorite.

The effect of radiation damage on a pyrochlore structured materials can exhibit two effects; 1) a transition from a pyrochlore structure to amorphous material via the formation of fluorite / defect fluorite phase or 2) direct transition to an amorphous phase. Irradiation of synthesised materials can provide information on whether an intermediate phase is formed before the material become amorphous. This can be completed on bulk

materials, using heavy ion implantation, or on a small sample of the material using a TEM instrument coupled with an ion beam implanter. In-situ irradiations using the IVEM-TANDEM facility are used to indicate the long term stability of a structure under irradiation (Section 3.4.2). The instrument allows for analysis of the crystalline structure through electron diffraction images at user defined intervals of irradiation, without changing the sample environment. The use of krypton (Kr) is selected to simulating the damage cause by the alpha recoil energy within the parent atom. 1MeV doubly charged Kr is used due the instrument limitations and this it having a similar effect within the structure as 70-100 keV recoil energy of parent atom as the result of alpha decay.

Typical analysis within the IVEM-TANDEM instrument can be seen in Figure 2.4, completed by S.X. Wang et al [73]. This shows the effect of Kr^{2+} 1MeV irradiation, highlighting how the pyrochlore superstructure weakens showing disorder between the two cation sites and the anion vacancy. The appearance of a halo with the electron diffraction images indicates a fraction of amorphous material. The intensity of the amorphous halo increases as the superstructure is lost, resulting in the formation of a fluorite structure with the amorphous fraction. This continues until such a dose that all the material is amorphous. An amorphous material here is defined as the point where no pair of diffraction reflections can be identified within the electron diffraction image (Figure 2.4(d)).

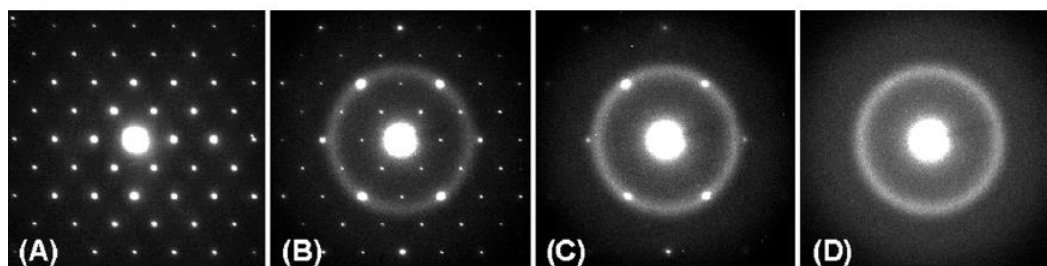


Figure 2.4: Selected Area Electron Diffraction (SAED) images taken with increase dose of 1MeV Kr^{2+} irradiation (A) Pyrochlore crystalline structure, (B) Gradual disappearance of the structure and the formation of amorphous halos (C) The disappearance of the pyrochlore superstructure leaving the fluorite structure and amorphous halos (D) Fully amorphous material[73]

2.3 Titanate Ceramic Materials

Although titanate materials do not offer the same irradiation stability over zirconate materials, titanate ceramics are found in nature to contain large quantities of uranium and thorium [74]. A titanate ceramic is also a key component within the SYNROC multiphase

concept [75-77], and is the bases of Lawrence Livermore composition. Developed by the Australian Nuclear Science and Technology Organisation (ANSTO) and the Lawrence Livermore National Laboratory (LLNL), respectively. The latter is endorsed by the US department of energy (DOE) as their preferred wasteform for excess weapons grade plutonium [5, 6].

2.3.1 Multiphase ceramics systems: Synroc

The multi-component material, SYNROC, is designed to simultaneously host several radioactive elements from a single varied waste stream, within co-existing phases. The component materials are determined by the waste stream [78]. There are several categories of SYNROC depending on the waste stream they are designed for, of interest to this work is the phase formation in the SYNROC F composition. This sees the formation of brannerite as an untargeted phase. Brannerite has been identified when uranium loading is increased within the multiphase synroc material, resulting in insufficient calcium component oxide available to form the targeted perovskite phase. The result is the excess UO_2 precursor reacts with the rutile TiO_2 , forming UTi_2O_6 [76]. The final compositional break down of SYNROC F, as a function of varied UO_2 wt. %, is shown in Table 2.2. Analysis on the durability of the SYNROC material with the presence of brannerite indicated no significant effect on the leach rates, or chemical durability, when compared to those of SYNROC C, whose leach rate is considered satisfactory for GDF requirements [76].

The SYNROC concept overcomes the requirement for reprocessing and separating chemically different elements from spent nuclear fuel. SYNROC is designed to immobilise varied waste streams including; actinides, rare earth elements, strontium (Sr), molybdenum (Mo), caesium (Cs), barium (Ba) and noble metals [7, 78, 79]. However, the interfaces between the different compositions, and the long term stability of the material, needs to be understood. The multiphase assemblage of SYNROC is a unique solution, which is difficult to directly compare to natural analogues of ceramic materials. This limits the information available on the long term stability of the interfaces between the phases of the materials, required for long term disposal in the GDF. Two phases of interest for the immobilisation of separated uranium and plutonium oxides, and heavily utilised within SYNROC are a pyrochlore structured material and the brannerite structure.

Table 2.2: The table shows the percentage of each of the 5 phases present in the composition where the UO₂ precursor is varied [76].

	Wt.% UO ₂			
	30	35	40	45
Pyrochlore	69%	77%	71%	76%
Hollandite	13%	14%	10%	13%
Rutile	4%	5%	15%	7%
Perovskite	14%	4%	0%	0%
Brannerite	0%	0%	4%	4%

2.3.2 Brannerite Structure

The brannerite mineral, (U⁴⁺,REE,Th,Ca)(Ti,Fe⁴⁺,Nb)₂(O,OH)₆, particularly titanate brannerite, (U⁴⁺,REE,Th,Ca)Ti₂O₆ has been seen to be a suitable candidate for hosting actinides, highlighted through its formation in Synroc. Brannerite structure, a titanate based ceramic which becomes amorphous when subject to radiation [32, 36, 80, 81]. However, brannerite can contain high concentrations of uranium and thorium actinides, therefore is useful to study in order to develop materials that can contain similar levels of actinides [82].

Ideal brannerite is an ATi₂O₆ (A = U, Th, Ce) monoclinic structure with space group C2/m. The natural structure is based on layers of TiO₆ edge sharing octahedra linked by AO₆ octahedra, for example UTi₂O₆ (Figure 2.5).

Table 2.3: X-ray lattice parameters (Å) of brannerite structures with composition ATi₂O₆, where A = U, Ce, and Th from [74, 83, 84], respectively.

A	a (Å)	b (Å)	c (Å)	β (°)
Ce	9.8146(5)	3.7022(2)	6.7720(4)	118.69(1)
U	9.812(2)	3.7697(6)	6.9253(9)	118.957(6)
Th	9.822(5)	3.824(2)	7.036(5)	118.84(5)

The brannerite structure is stabilised through the inclusion of uranium, thorium or cerium on the A site of the titanate material. The refined crystal structure of the A site cations within the brannerite structure can be found in Table 2.3. Ionic radii information for the cations are summarised in Table 2.4 [64, 74, 83, 84].

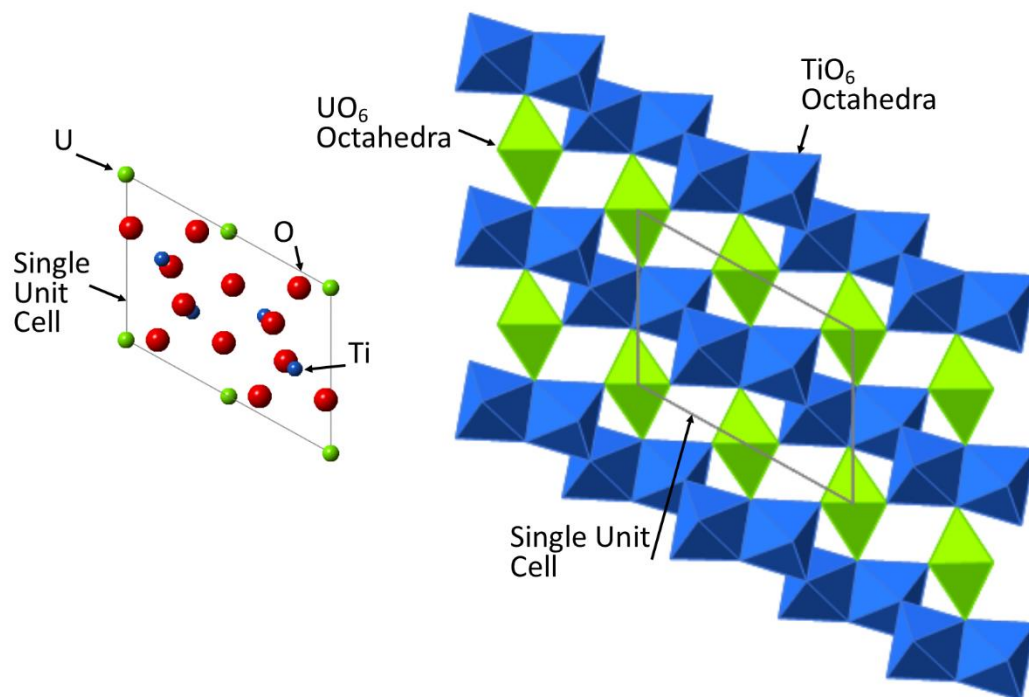


Figure 2.5: The Brannerite structure view down the [010] axis both (left) showing the cations and anions and (right) showing the interaction between the edge sharing TiO_6 octahedra (blue) linked by the UO_6 octahedra (green) for ideal brannerite UTi_2O_6

2.3.3 Natural Analogues

Brannerite is a naturally occurring mineral known to contain radioactive species. Mined minerals for the recovery of uranium are often identified with the brannerite phase [74]. Uranium brannerite, ideally UTi_2O_6 , has been identified to contain high concentrations of UO_2 , making it ideal for mining to achieve high uranium yields for extraction [74]. The chemical flexibility of the structure can be identified from the variable compositions of the ore, with substitutions of Ca, Th, Pb and REE on the uranium A-site and transition metals such as Fe and Al on the titanium B-site [10, 32, 74, 80, 85-88]. The ores are found in a metamict (amorphous) state due to the alpha recoil damage from the uranium and thorium within the material [32]. The once crystalline structure can be synthesised in order to understand the short term behaviour of the material and properties due to recoil damage [32, 81].

Table 2.5: A summary of ionic radii information for cerium, uranium, plutonium and thorium as extraction from Shannon (1976) [64].

Ion	Charge	Coordination	Ionic Radius (Å)
Ce	3	VI	1.01
		VII	1.07
		VIII	1.143
		IX	1.196
		X	1.25
		XII	1.34
	4	VI	0.87
		VIII	0.97
		X	1.07
		XII	1.14
U	3	VI	1.025
	4	VI	0.89
		VII	0.95
		VIII	1.00
		IX	1.05
		XII	1.17
	5	VI	0.76
		VII	0.84
	6	II	0.45
		IV	0.52
		VI	0.73
		VII	0.81
VIII	0.86		
Pu	3	VI	1.00
	4	VI	0.86
		VIII	0.96
	5	VI	0.74
6	VI	0.71	
Th	4	VI	0.94
		VII	1.05
		IX	1.09
		X	1.13
		XI	1.18
		XII	1.21

2.4 Project Aims

Both the pyrochlore and brannerite structures offer chemical flexibility, with natural minerals identified to contain varied cations and large fractions of uranium and thorium. Studies of the chemical flexibility of the two phases are conducted as part of this thesis in order to provide information on the materials ability to tolerate varied waste streams. This would be particularly important should the decision to dispose of uranium and

plutonium stock piles, as well as spent nuclear fuel, be taken within the UK or abroad. To address this shortfall this thesis looks at:

- Analysis of the structural flexibility of the pyrochlore phase of the general formula $A^{2+}A^{3+}B_{1.5}^{5+}B_{0.5}^{3+}O_7$ in order to understand the structural response of the phase with varied compositions.
- Analysis of the compositional dependence of radiation induced damage of materials with target composition $CaLn^{3+}Fe_{0.5}Nb_{1.5}O_7$, where Ln = La, Nd, Sm, Gd, Ho or Yb.
- Exploration of the uranium oxidation state when incorporating of uranium within lanthanum zirconate pyrochlore $La_2Zr_2O_7$ to form materials of the series $La_2Zr_{2-x}U_xO_7$.
- Analysis of the structural flexibility of uranium brannerite with through the substitution of Cr, Fe, Pr, Y or Yb cations in target composition $U_{1-x}M_xTi_2O_6$.

2.5 References

- [1] Ginell WS, Martin JJ, Hatch LP. Ultimate Disposal of Radioactive Wastes. *Nucleonics* 1954; 12:14-18.
- [2] DeGraef M, McHenry ME. Structure of Materials: An Introduction to Crystallography, Diffraction and Symmetry, 2nd Edition. Structure of Materials: an Introduction to Crystallography, Diffraction and Symmetry, 2nd Edition 2012:1-739.
- [3] McCarthy GJ. High Level Waste Ceramics - Materials Considerations, Process Simulation, and Product Characterisation. *Nuclear Technology* 1977; 32:92-105.
- [4] Roy R. Rational Molecular Engineering of Ceramic Materials. *Journal of the American Ceramic Society* 1977; 60:350-363.
- [5] M.W.A. S, Begg BD, Day RA *et al.* Low-Risk Alternative Waste Forms for Actinide Immobilization. In: Proceedings of the Annual Waste Management Symposium 2005: WM'05; 2004.
- [6] Cochran SG, Dunlop WH, Edmunds TA *et al.* Fissile material disposition program-final immobilization form assessment and recommendation. In: Edited by: Energy UDo. 1997.
- [7] Ringwood AE, Kesson SE, Ware NG *et al.* Immobilization of high-level nuclear-reactor wastes in Synroc. *Nature* 1979; 278:219-223.
- [8] Implementing Geological Disposal. In: Edited by: Change DoEC. Crown; 2014.
- [9] Haaker RF, Ewing RC. Naturally Occurring Crystalline Phases: Analogues for Radioactive Waste Forms. In: Battelle Pacific Northwest Labs; 1981.
- [10] Pabst A. The Metamict State. *Am. Mineral.* 1952; 37:137.
- [11] Alonso JIG, Sena F, Arbore P *et al.* Determination of fission- products and actinides in spent nuclear fuel by isotope- dilution ion chromatography inductively-couple plasma-mass spectrometry. *Journal of Analytical Atomic Spectrometry* 1995; 10:381-393.
- [12] Bruno J, Ewing RC. Spent nuclear fuel. *Elements* 2006; 2:343-349.

- [13] Burns PC, Ewing RC, Miller ML. Incorporation mechanisms of actinide elements into the structures of U6+ phases formed during the oxidation of spent nuclear fuel. *Journal of Nuclear Materials* 1997; 245:1-9.
- [14] Burns PC, Deely KM, Skanthakumar S. Neptunium incorporation into uranyl compounds that form as alteration products of spent nuclear fuel: Implications for geologic repository performance. *Radiochimica Acta* 2004; 92:151-159.
- [15] Cachoir C, Gallien JP, Trocellier P. Chemical durability of uranium dioxide stored in geologic medium: Uranium remobilisation. *Annales De Chimie-Science Des Materiaux* 1996; 21:567-592.
- [16] Finch RJ, Buck EC, Finn PA, Bates JK. Oxidative corrosion of spent UO₂ fuel in vapor and dripping groundwater at 90 degrees C. In: *Scientific Basis for Nuclear Waste Management Xxii*. Edited by: Wronkiewicz DJ, Lee JH. 1999. pp. 431-438.
- [17] Finn PA, Hoh JC, Wolf SF *et al.* The release of uranium, plutonium, cesium, strontium, technetium and iodine from spent fuel under unsaturated conditions. *Radiochimica Acta* 1996; 74:65-71.
- [18] Jegou C, Muzeau B, Broudic V *et al.* Effect of external gamma irradiation on dissolution of the spent UO₂ fuel matrix. *Journal of Nuclear Materials* 2005; 341:62-82.
- [19] Rondinella VV, Matzke H, Cobos J, Wiss T. alpha-radiolysis and alpha-radiation damage effects on UO₂ dissolution under spent fuel storage conditions. In: *22nd Symposium on Scientific Basis for Nuclear Waste Management held at the 1998 MRS Fall Meeting*. Boston, Ma: 1998. pp. 447-454.
- [20] Rondinella VV, Matzke H, Cobos J, Wiss T. Leaching behaviour of UO₂ containing alpha-emitting actinides. *Radiochimica Acta* 2000; 88:527-531.
- [21] Weber WJ, Ewing RC, Meldrum A. The kinetics of alpha-decay-induced amorphization in zircon and apatite containing weapons-grade plutonium or other actinides. *Journal of Nuclear Materials* 1997; 250:147-155.
- [22] Ewing RC. Nuclear waste forms for actinides. *Proceedings of the National Academy of Sciences of the United States of America* 1999; 96:3432-3439.
- [23] Ewing RC, Weber WJ, Lian J. Nuclear waste disposal- pyrochlore (A₂B₂O₇): Nuclear waste form for the immobilization of plutonium and "minor" actinides. *Journal of applied Physics* 2004; 95:5949- 5971.
- [24] Balek V, Zelenak V, Benes M, Subrt J. Thermal behaviour of brannerite ceramics and its natural analogue mineral brannerite. *Ceramics-Silikaty* 2009; 53:9-14.
- [25] Calas G, Allard T, Balan E *et al.* Radiation-induced defects in nonradioactive natural minerals: Mineralogical and environmental significance. In: *Radiation Effects and Ion-Beam Processing of Materials*. Edited by: Wang LM, Fromknecht R, Snead LL *et al.* 2004. pp. 81-92.
- [26] Charalambous FA, Ram R, Pownceby MI *et al.* Chemical and microstructural characterisation studies on natural and heat treated brannerite samples. *Minerals Engineering* 2012; 39:276-288.
- [27] Ewing RC. The Metamict State - 1993 - The Centennial. *Nuclear Instruments & Methods in Physics Research Section B-Beam Interactions with Materials and Atoms* 1994; 91:22-29.

- [28] Giere R, Williams CT, Lumpkin GR. Chemical characteristics of natural zirconolite. *Schweizerische Mineralogische Und Petrographische Mitteilungen* 1998; 78:433-459.
- [29] Giere R, Buck EC, Guggenheim R *et al.* Alteration of uranium-rich microlite. In: *Scientific Basis for Nuclear Waste Management XXIV*. Edited by: Hart KP, Lumpkin GR. 2000. pp. 935-944.
- [30] Gilbert MR, Selfslag C, Walter M *et al.* Synthesis and characterisation of Pu-doped zirconolites - $(Ca_{1-x}Pu_x)Zr(Ti_{2-2x}Fe_{2x})O_7$. In: *Actinides Conference*. San Francisco, CA: 2009.
- [31] Lumpkin GR. Alpha-decay damage and aqueous durability of actinide host phases in natural systems. *Journal of Nuclear Materials* 2001; 289:136-166.
- [32] Lumpkin GR, Leung SHF, Ferenczy J. Chemistry, microstructure, and alpha decay damage of natural brannerite. *Chemical Geology* 2012; 291:55-68.
- [33] Lumpkin GR, Gao Y, Giere R *et al.* The role of Th-U minerals in assessing the performance of nuclear waste forms. *Mineralogical Magazine* 2014; 78:1071-1095.
- [34] Sinclair W, Ringwood AE. Alpha recoil damage in natural zirconolite and perovskite. *Geochemical Journal* 1981; 15:229-243.
- [35] Vlcek V, Skala R, Golias V *et al.* Effect of natural irradiation in fluorites: possible implications for nuclear waste management? *Journal of Geosciences* 2012; 57:45-52.
- [36] Zhang Y, Lumpkin GR, Li H *et al.* Recrystallisation of amorphous natural brannerite through annealing: The effect of radiation damage on the chemical durability of brannerite. *Journal of Nuclear Materials* 2006; 350:293-300.
- [37] Subramanian MA, Aravamudan G, Rao GVS. Oxide Pyrochlores- A Review. *Progress in Solid State Chemistry* 1983; 15:55-143.
- [38] Chakoumakos BC. Systematics of the Pyrochlore Structure Type, Ideal $A_2B_2X_6Y$. *Journal of Solid State Chemistry* 1984; 53:120-129.
- [39] Lumpkin GR, Ewing RC, Chakoumakos BC *et al.* Alpha-recoil damage in zirconolite ($CaZrTi_2O_7$). *Journal of Materials Research* 1986; 1:564-576.
- [40] Chakoumakos BC, Murakami T, Lumpkin GR, Ewing RC. Alpha-decay induced fracturing in zircon- the transition from the crystalline to the metamict state. *Science* 1987; 236:1556-1559.
- [41] Lumpkin GR, Ewing RC. Geochemical alteration of Pyrochlore Group Minerals - Microlite Subgroup. *American Mineralogist* 1992; 77:179-188.
- [42] Lumpkin GR, Smith KL, Blackford MG *et al.* Ion Irradiation of Ternary Pyrochlore Oxides. *Chemistry of Materials* 2009; 21:2746-2754.
- [43] Lumpkin GR, Ewing RC, Chakoumakos BC *et al.* Alpha-recoil damage in zirconolite ($CaZrTi_2O_7$). *Journal of Materials Research* 1986; 1:564-576.
- [44] Ewing RC, Wang LM. Amorphization of zirconolite - Alpha decay event damage versus krypton ion irradiation. *Nuclear Instruments & Methods in Physics Research Section B-Beam Interactions with Materials and Atoms* 1992; 65:319-323.

- [45] Wang LM, Ewing RC. Detailed insitu study of ion beam - induced amorphization of zircon. *Nuclear Instruments & Methods in Physics Research Section B-Beam Interactions with Materials and Atoms* 1992; 65:324-329.
- [46] Meldrum A, Boatner LA, Ewing RC. Displacive radiation effects in the monazite- and zircon-structure orthophosphates. *Physical Review B* 1997; 56:13805-13814.
- [47] Wang SX, Begg BD, Wang LM *et al.* Radiation stability of gadolinium zirconate: A waste form for plutonium disposition. *Journal of Materials Research* 1999; 14:4470-4473.
- [48] Lian J, Yudintsev SV, Stefanovsky SV *et al.* Ion beam irradiation of U-, Th- and Ce-doped pyrochlores. *Journal of Alloys and Compounds* 2007; 444:429-433.
- [49] Lang M, Lian J, Zhang J *et al.* Single-ion tracks in $Gd_2Zr_{2-x}Ti_xO_7$ pyrochlores irradiated with swift heavy ions. *Physical Review B* 2009; 79.
- [50] Ishizawa N, Marumo F, Iwai S *et al.* Compounds with pervovskite-type slabs. V. A High-Temperature Modification of $La_2Ti_2O_7$. *Acta Crystallographica Section B-Structural Science* 1982; 38:368-372.
- [51] Stefanovsky SV, Yudintsev SV, Nikonov BS *et al.* Pyrochlore-type phases for actinides and rare earth elements immobilization. In: 22nd Symposium on Scientific Basis for Nuclear Waste Management held at the 1998 MRS Fall Meeting. Boston, Ma: Materials Research Society; 1998. pp. 27-34.
- [52] Chesnokov BV, Eremeev SP. Crystallization of Metamict Pyrochlore Under Natural Conditions. *Doklady Akademii Nauk Sssr* 1962; 146:683-&
- [53] Lumpkin GR, Mariano AN. Natural occurrence and stability of pyrochlore in carbonatites, related hydrothermal systems and weathering environments. In: *Scientific Basis for Nuclear Waste Management Xix*. Edited by: Murphy WM, Knecht DA. 1996. pp. 831-838.
- [54] Lumpkin GR, Ewing RC, Williams CT, Mariano AN. An overview of the crystal chemistry, durability, and radiation damage effects of natural pyrochlore. In: *Scientific Basis for Nuclear Waste Management Xxiv*. Edited by: Hart KP, Lumpkin GR. 2000. pp. 921-934.
- [55] Percy EC, Prikryl JD, Murphy WM, Leslie BW. Alteration of uranite from the Nopal-I deposit, Pena-Blanca district, Chihuahua, Mexico compared to degradation of spent nuclear fuel in the proposed United- States high-Level nuclear waste repository at Yucca Mountain, Nevada. *Applied Geochemistry* 1994; 9:713-732.
- [56] Helean KB, Lutze W, Ewing RC. Surface features and alteration products of natural zirconolite leached in silica-saturated solutions. In: *Scientific Basis for Nuclear Waste Management Xxii*. Edited by: Wronkiewicz DJ, Lee JH. 1999. pp. 157-164.
- [57] Williams CT, Bulakh AG, Giere R *et al.* Alteration features in natural zirconolite from carbonatites. In: 24th International Symposium on Scientific Basis for Nuclear Waste Management. Sydney, Australia: 2000. pp. 945-952.
- [58] Holland HD, Gottfried D. The effect of nuclear radiation on the structure of zircon. *Acta Crystallographica* 1955; 8:291-300.
- [59] Ringwood AE, Oversby V. Radiation stability assessment of naturally-occurring analogues of SYNROC minerals for nuclear waste storage. *American Ceramic Society Bulletin* 1980; 59:395-395.

- [60] Wang LM, Ewing RC. Detailed insitu study of ion beam - induced amorphization of zircon. *Nuclear Instruments & Methods in Physics Research Section B-Beam Interactions with Materials and Atoms* 1992; 65:324-329.
- [61] Lumpkin GR, Smith KL, Blackford MG *et al.* The crystalline-amorphous transformation in natural zirconolite: Evidence for long-term annealing. In: *Scientific Basis for Nuclear Waste Management Xxi*. Edited by: McKinley IG, McCombie C. 1998. pp. 215-222.
- [62] Meldrum A, White CW, Keppens V *et al.* Irradiation-induced amorphization of $\text{Cd}_2\text{Nb}_2\text{O}_7$ pyrochlore. *Physical Review B* 2001; 63:104109.
- [63] Lian J, Chen J, Wang LM *et al.* Radiation-induced amorphization of rare-earth titanate pyrochlores. *Physical Review B* 2003; 68.
- [64] Shannon R. Revised effective ionic radii and systematic studies of interatomic distances in halides and chalcogenides. *Acta Crystallographica Section A* 1976; 32:751-767.
- [65] Jafar M, Phapale SB, Mandal BP *et al.* Preparation and Structure of Uranium-Incorporated $\text{Gd}_2\text{Zr}_2\text{O}_7$ Compounds and Their Thermodynamic Stabilities under Oxidizing and Reducing Conditions. *Inorganic Chemistry* 2015; 54:9447-9457.
- [66] Begg BD, Hess NJ, McCready DE *et al.* Heavy-ion irradiation effects in $\text{Gd}_2(\text{Ti}_{2-x}\text{Zr}_x)\text{O}_7$ pyrochlores. *Journal of Nuclear Materials* 2001; 289:188-193.
- [67] Chen J, Lian J, Wang LM *et al.* X-ray photoelectron spectroscopy study of disordering in $\text{Gd}_2(\text{Ti}_{1-x}\text{Zr}_x)_2\text{O}_7$ pyrochlores. *Physical Review Letters* 2002; 88.
- [68] Icenhower JP, Weber WJ, Hess NJ *et al.* Experimental determination of dissolution kinetics of Zr-substituted Gd-Ti pyrochlore ceramics: Influence of chemistry on corrosion resistance. In: *Scientific Basis for Nuclear Waste Management Xxvi*. Edited by: Finch RJ, Bullen DB. 2003. pp. 227-234.
- [69] Nachimuthu P, Thevuthasan S, Shutthanandan V *et al.* Near-edge x-ray absorption fine-structure study of ion-beam-induced phase transformation in $\text{Gd}_2(\text{Ti}_{1-y}\text{Zr}_y)_2\text{O}_7$. *Journal of Applied Physics* 2005; 97.
- [70] Zhang FX, Lian J, Becker U *et al.* High-pressure structural changes in the $\text{Gd}_2\text{Zr}_2\text{O}_7$ pyrochlore. *Physical Review B* 2007; 76.
- [71] Zhang FX, Wang JW, Lian J *et al.* Phase stability and pressure dependence of defect formation in $\text{Gd}_2\text{Ti}_2\text{O}_7$ and $\text{Gd}_2\text{Zr}_2\text{O}_7$ pyrochlores. *Physical Review Letters* 2008; 100.
- [72] Lang M, Zhang FX, Ewing RC *et al.* Structural modifications of $\text{Gd}_2\text{Zr}_{2-x}\text{Ti}_x\text{O}_7$ pyrochlore induced by swift heavy ions: Disorder and amorphization. *Journal of Materials Research* 2009; 24:1322-1334.
- [73] Wang SX, Wang LM, Ewing RC. Nano-scale glass formation in pyrochlore by heavy ion irradiation. *Journal of Non-Crystalline Solids* 2000; 274:238-243.
- [74] Szymanski JT, Scott JD. A crystal-structure refinement of synthetic brannerite, UTi_2O_6 , and its bearing on rate of alkaline-carbonate leaching of brannerite in ore. *Canadian Mineralogist* 1982; 20:271-280.
- [75] Vance ER. Development of titanate ceramic wasteforms and crystal chemistry of incorporated uranium and plutonium. In: *Environmental Issues and Waste Management Technologies in the Ceramic and Nuclear Industries Viii*. Edited by: Sundaram SK, Spearing DR, Vienna JD. 2003. pp. 301-311.

- [76] Carter ML, Li H, Zhang Y *et al.* Titanate ceramics for immobilisation of uranium-rich radioactive wastes arising from Mo-99 production. *Journal of Nuclear Materials* 2009; 384:322-326.
- [77] Vance ER, Stewart MWA, Moricca SA. Progress at ANSTO on SYNROC. *Journal of the Australian Ceramic Society* 2014; 50:38-48.
- [78] Ringwood AE, Kesson SE, Ware NG *et al.* SYNROC Process- Geochemical approach to nuclear waste immobilization. *Geochemical Journal* 1979; 13:141-165.
- [79] Lumpkin GR, Smith KL, Blackford MG. Partitioning of uranium and rare-earth elements in SYNROC - effects of impurities, metal additive, and waste loading. *Journal of Nuclear Materials* 1995; 224:31-42.
- [80] Hess FL, Wells RC. Brannerite, a new uranium mineral. *Journal of the Franklin Institute* 1920; 189:225-237.
- [81] Lian J, Wang LM, Lumpkin GR, Ewing RC. Heavy ion irradiation effects of brannerite-type ceramics. *Nuclear Instruments & Methods in Physics Research Section B-Beam Interactions with Materials and Atoms* 2002; 191:565-570.
- [82] Huynh LT, Eger SB, Walker JDS *et al.* How temperature influences the stoichiometry of CeTi₂O₆. *Solid State Sciences* 2012; 14:761-767.
- [83] Ruh R, Wadsley AD. Crystal structure of ThTi₂O₆ (Brannerite). *Acta Crystallographica* 1966; 21:974-&.
- [84] Vales V, Matejova L, Matej Z *et al.* Crystallization kinetics study of cerium titanate CeTi₂O₆. *Journal of Physics and Chemistry of Solids* 2014; 75:265-270.
- [85] Pabst A. Brannerite from California. *American Mineralogist* 1954; 39:109-117.
- [86] Hewett DF, Stone J, Levine H. Brannerite from San-Bernardino Country, California. *American Mineralogist* 1957; 42:30-38.
- [87] Finch R, Murakami T. Systematics and Paragenesis of Uranium Minerals. *Reviews in Mineralogy* 1999; 38:91-179.
- [88] Burns PC. The Crystal Chemistry of Uranium. *Reviews in Mineralogy* <D> 1999; 38:23-90.

Chapter 3 Analytical Techniques

3.1 X-ray diffraction

Powder X-ray diffraction (XRD) analysis was used throughout in order to determine the crystalline phase assemblage of materials. While a complete introduction to X-ray diffraction theory is impractical, here the basic principles of XRD, and the setup of the diffractometers used are discussed.

3.1.1 Basic principles of X-ray diffraction for crystalline materials

X-ray diffraction (XRD) uses the interaction between electromagnetic radiation and atoms of a material to determine the materials structure. This requires electromagnetic radiation with a wavelength comparable to the scale of the structure being analysed.

In order to produce X-rays a cathode ray tube must first be heated in order to produce electrons. These electrons are then accelerated by a voltage towards a target material. When the electrons have sufficient energy, an electron is dislodged from the inner shell of an atom of the target material, resulting in an atom with an excited state. X-rays are produced when an electron from a higher energy state drops down to a lower energy state to fill the created vacancy, returning the atom to its ground energy state. These X-rays are characteristic of the target material. For a target material of copper (Cu) metal, two wavelengths, ideal for crystal structure analysis, are observed from the K shell ($K\alpha_1=1.5408\text{\AA}$ and $K\alpha_2=1.5443\text{\AA}$). As the wavelengths are similar, but the two peaks distinguishable, they are referred to as a $K\alpha$ doublet [1]. The intensity of the K emission lines are dependent on the acceleration voltage used of the electrons. A minimum energy is required for the electron to be dislodged from the target material, this is termed the threshold energy. Above the threshold energy the wavelength remains constant, but the intensity increases.

For XRD analysis a monochromatic beam of a single energy is desirable. To achieve this a monochromator is used to remove the unwanted energies. For a Cu target, a germanium (Ge) monochromator is used to remove any X-rays that do not have a wavelength of the $K\alpha_1=1.5408\text{\AA}$.

A crystalline material is defined by a regular arrangement of atoms in 3-dimensional space with a repeatable unit cell. The crystal structure is described by the lattice

parameters. These consist of the crystallographic axis of the unit cell which describe the minimum repeatable structure (in angstroms, Å) in 3-dimensional space (a, b, c). Coupled with definition of the angles (in degrees, °) between the axis, termed α, β and γ . Atomic positions relative to the a, b and c axis are described as fractional coordinates along the respective lengths using the notation of (x, y, z) . Planes of the unit cell describe the connection between the atoms of a unit cell, and vary depending on the crystal structure. Planes are described by Miller indices ($h k l$), which have both direction and a fixed angle of 90° between them [2]. The Miller indices are proportional to the reciprocal of lattice vectors, and therefore describe the intercept of the plane on the axis. Miller indices use the notation of $(h k l)$. The lattice vectors describe the line from the origin of the unit cell to the Miller indices point [1]. Negative indices are written as a number with a bar above. When vectors are related by symmetry then the indices are bounded within angular brackets, $\langle h k l \rangle$ [3].

Planes within a crystal structure are repeatable, this arises due to the long range ordering of the reoccurring unit cell, from the arbitrary position of the origin of the crystal structure. The sets of planes are equally spaced relative to each other, this is termed the d-spacing [3]. The relationship between the plane indices ($h k l$) and the d-spacing is dependent on the crystal structure symmetry, described by the crystal system, examples can be found in Table 3.1 [2, 3]. There are 7 crystal systems (cubic, tetragonal, hexagonal, orthorhombic, monoclinic and triclinic). All crystalline materials adopt one of the systems [3].

Table 3.1: Relationship between the Miller indices ($h k l$) and the d-spacing between lattice planes for structures with a cubic, tetragonal or hexagonal structure [2].

Cubic	Tetragonal	Hexagonal
$\frac{1}{d^2} = \frac{h^2 + k^2 + l^2}{a^2}$	$\frac{1}{d^2} = \frac{h^2 + k^2}{a^2} + \frac{l^2}{c^2}$	$\frac{1}{d^2} = \frac{4}{3} \left(\frac{h^2 + hk + k^2}{a^2} \right) + \frac{l^2}{c^2}$

When the wavelength of the incident X-rays (from the source) are smaller than the d-spacing within the target crystal structure, information on the atomic positions can be interpreted from the interactions. The X-rays are diffracted from the planes of atoms within the structure. The deflection of the incident X-rays is measured as 2θ due to the movement of the detector through 2θ , see Figure 3.1. The combination results in specific characteristics of the material being reflected in the diffracted X-rays [2]. The angle and intensity of the diffracted X-rays provide information the atom placements enabling

identification of the structure of the material. This is described by the Bragg equation (Equation 3.1).

$$n\lambda = 2d\sin\theta \quad \text{Equation 3.1}$$

Where the wavelength of the incident X-rays, λ (Å), is defined by the instrument, and the diffracted angle θ , is interpreted from the data collected. The diffracted angle is characteristic of the constructive interference of the X-rays as they scatter off of the planes in the crystal structure. This enables the calculation of the d-spacing (d) within the crystal structure, which is constant between planes of a crystalline material. XRD analysis of powdered materials results in the measurement of multiple crystals, at various orientations, which enables the diffraction from multiple planes, as described by Table 3.1, depending on the crystal structure [2].

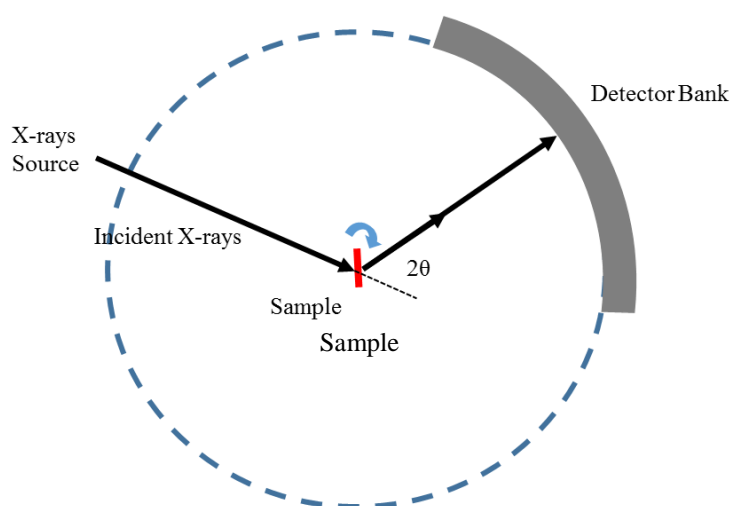


Figure 3.1: Schematic of the geometric arrangement of the Stoe Stadi P in transmission mode. In incident X-rays pass through a thin film of material dispersed on a film using PVA glue. The deflection of the X-rays from the incident beam gives rise to the 2θ angle. The detector bank simultaneously collects data from multiple scattering events.

3.1.2 X-ray Diffraction Instruments Used

Several instruments are used for X-ray analysis in this thesis, below are the specifications of each machine.

3.1.2.1 STOE- Image Plate and Stadi P Diffractometer

The STOE- Image Plate (IP) and STOE-Stadi P Diffractometer (PSD) both use a copper target, with electrons accelerated at 40.0 kV.

The Cu-STOE-IP works in transmission geometry where the sample is rotated to minimise the effect of preferential orientation, which could potentially be created by the sample preparations. Fitted with a germanium-111 (Ge-(111)) monochromator, an intense X-ray beam with a single wavelength of $K\alpha_1=1.5408\text{\AA}$ is produced, with a smallest possible step size of $0.2^\circ 2\theta$. Finely powdered samples were glued to acetate films and placed in the sample holders. Initial characterisation was performed in transmission mode on a STOE Image Plate diffractometer operating at a working voltage and current of 40kV and 35mA, respectively. The curved detector simultaneously collects data between $\sim 6^\circ \leq 2\theta \leq 125^\circ$ for ~ 7 minutes. This measurement is repeated 8 times in order to improve the counting statistics.

For materials, which were not analysed by neutron diffraction analysis, analysis on the Cu Stoe PSD diffractometer was completed. The Cu Stoe-PSD was a position sensitive detector also using a Cu source and Ge-(111) monochromator with operating conditions of 40kV and 40mA. The detector collects at a single 2θ angle, for defined period of time, before moving in defined step sizes through a 2θ range. The source and receiving slits are fixed at 6mm.

The advantage of this instrument over the Cu Stoe IP is that it can collect over a wider range of angles, $\sim 3^\circ \leq 2\theta \leq 130^\circ$, with a high degree of resolution (FWHM $\sim 0.08^\circ 2\theta$). The set up conditions for the instrument used a step size of 0.03 over $\sim 5^\circ \leq 2\theta \leq 80^\circ$. The collect time was material dependant on the absorption of the elements within the composition.

3.2 Scanning electron microscopy and energy dispersive spectroscopy

Scanning electron microscopy uses electrons, under vacuum, to image the surface of a material. Back-scattered electron (BSE) images highlight contrast within the surface of the material, indicating either a surface which is uneven, or a multiphase assemblage with different chemical compositions [4]. Energy dispersive X-ray spectroscopy (EDS) is used to provide localised chemical information, providing quantitative information on the cation elements present within a particular target area.

Materials were analysed on a Hitachi TM3030 instrument, a table top SEM / EDS analysis instrument. This was operated under a low vacuum, at a voltage of 15keV, with a working distance of 8.5mm. EDS analysis was completed through the Burker Quantax 70 software. Calibration of the TM3030 instrument was completed using copper standard to ensure regular instrument and detector calibration.

3.2.1 SEM and EDS Theory

A tungsten filament was used to generate electrons. The electrons were then accelerated by a magnetic field, whose voltage can be varied, dependant on the instrument. The intensity of the incident beam of electrons is increased through the use of condenser lenses to focus the beam, before interacting with the material surface [5]. The electrons of the incident beam interact with the sample surface, producing several signals including: secondary electrons, back scattered electrons and X-rays, see Figure 3.2 [5].

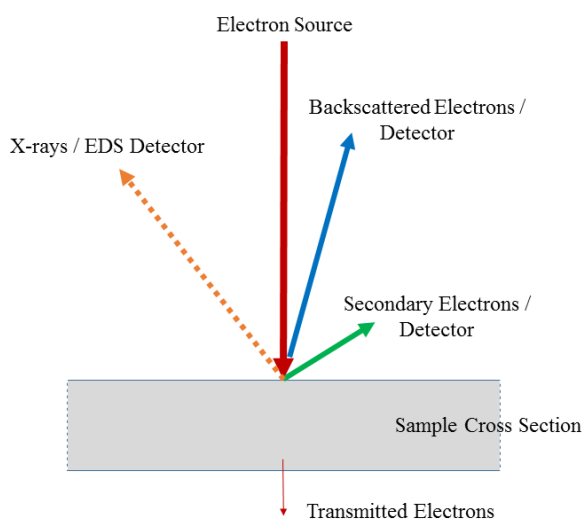


Figure 3.2: Schematic of the electron interactions within a scanning electron microscope (SEM), including secondary and back scattered electrons with detectors and X-rays and corresponding EDS detector indicated.

The interaction with the surface of the material results in the release of secondary electrons. Secondary electrons interact with a scintillator-photomultiplier system, emitting light. A charged metal grid accelerator is used to attract the secondary electrons, increasing the electron energy. This results in an increase in the number of interactions detected, and a higher intensity of data is observed. As the electrons interact with the scintillator the light is emitted. The emitted photons are converted into pulses of electrons and amplified [6].

Secondary electron images enables analysis of the microstructure of the materials surface. The surface topology is highly dependent on the preparation technique. Various preparation techniques were utilised for analysis.

1. Materials were synthesised, cold pressed uniaxially, and sintered to form a dense solid. The sintered pellet was then cut to ensure a flat surface with parallel sides, polished to a 1 micron optical finish. After polishing pellets were thermally etched to aid emphasis of the grain structure. After thermal etching the pellet was mounted onto a metallic stub using silver paint as the adhesive.
2. Materials were synthesised, cold uniaxially pressed, and sintered to form a dense solid. The sintered pellet was then mounted in an epoxy resin, cured, and polished to a 1 micron optical finish. Thermal etching could not be completed due to the resin, so instead the surface was washed with isopropanol alcohol to remove any dirt accumulated on the sample during polishing. Silver paint was used to aid charge dissipation on the sample surface prior to analysis.
3. Powdered material was dispersed on a carbon, double sided adhesive disc, which itself was mounted on a metallic specimen mount. This preparation technique does not ensure a flat surface for analysis, however for radioactive compositions, with minimal material, it enabled analysis without the destruction of large quantities of material within an epoxy resin mount.

Back scattered electrons are produced from the elastic scattering of the incident electron beam, providing information on the elements they interact with, shown in the contrast of the image generated. This enabled identification of the atomic composition of the material and the phase assemblage. The phase assemblage is determined by the contrast between grains within the image. A single contrast indicates a material with comparable reflection energies, interpreted as a material with a single phase assemblage. Cations with a higher atomic number have a greater scattering effect on the energy of the incident electron. The energy is directly proportional to the brightness in the image [5]. Therefore a material with a higher atomic number appears brighter within the image.

Where powders were analysed as dispersed powder on carbon adhesive surface different heights of grains would also vary the contrast in the back scattered electron diffraction images therefore analysis was completed on large grains which have a flat surface to aid the identification of multiple phases through contrast.

The X-rays are emitted when the incident electrons ionise an electron from the inner shell of an atom within the material, this is promptly replaced by an electron from a higher energy shell in order to fill the vacancy [7]. The energy of the X-ray emitted is characteristic of the atom, and is detected by the energy dispersive X-ray spectrometer. Collecting atom information using Energy Dispersive X-ray Spectroscopy (EDS) can be coupled with information gather by the BSE detector to determine the average

composition of a material, or where a multiphase assemblage is identified, the composition of the individual phases.

3.3 Neutron Diffraction

Neutrons have a mass (m_n) of 1.675×10^{-27} kg and are charge neutral. Through providing energy to the neutron it can be utilised to determine atomistic and magnetic structures of solid, liquid or gaseous materials [8]. The De Broglie equation, Equation 3.2, relates the velocity (v) and the wavelength of the neutron (λ) through the Planck constant (h).

$$\lambda = \frac{h}{mv} \quad \text{Equation 3.2}$$

The neutron wavelength is required to be of similar order of magnitude as the spacing within the crystal structure for analysis [8, 9]. Neutrons are scattered by the atomic nuclei within the crystalline structure. Each elemental isotope has a scattering and absorption length which is characteristic of the nucleus. The scattering length of neutrons is not linearly dependant on the nuclei [10].

3.3.1 Neutron diffraction theory: ISIS spallation source

A spallation source utilises the interaction of protons with a heavy-metal target in order to produce neutrons [11]. In detail, as taken from [12] H^- ions are produced by an ion source and are accelerated by a radio frequency quadrupole accelerator. This divides the H^- ions into bunches [13]. The H^- bunches are then transferred to a linear accelerator (linac) until they have a speed of ca.37% of the speed of light [12]. The linac consists of four 10m long tanks which use a copper liner as an electromagnetic resonator to progressively accelerate the H^- bunches [12]. The ions then pass into a synchrotron where, upon entry, thin aluminium foil remove the electrons in order to produce a proton beam, which undergoes further acceleration. The synchrotron has a 163 meters circumference, and after 10,000 circuits the protons have reach a velocity of ~84% of the speed of light, and an energy of ~800MeV [12]. During the circuits the protons divide into two bunches, which both are extracted from the synchrotron by magnets into a tungsten target. The interaction between the protons and the tungsten target produces neutrons through spallation. Spallation is the process by which, upon bombardment of protons, sufficient energy is provided to drive neutrons off of the target atoms [12]. The neutrons require

moderation in order to enable the analysis of material, this is provided by a hydrogen moderator. Neutrons then travel to instruments around the source, including the high resolution powder diffractometer (HRPD).

3.3.2 High resolution powder diffractometer (HRPD), ISIS, Oxford.

Neutron diffraction analysis was completed on powdered samples on the **High Resolution Powder Diffractometer (HRPD)** at the ISIS spallation source, which utilises time of flight neutrons [12]. HRPD is the highest resolution powder diffractometer in the world, housed approximately 100 meters away from the target material [12]. The fixed distance, L (m), between the source and the detector, enables quantification of the velocity (v (m/sec)) through direct measurement of the time (t (sec)) it takes the neutron to travel the distance, Equations 3.3. Substituting this into the De Broglie equation (Equation 3.2) and the Bragg equation (Equation 3.1), Equation 3.4 is formed in order to relate the velocity of the neutron to the relative position (θ) of the planes within the crystal structure.

$$v = \frac{L}{t} \quad \text{Equation 3.3}$$

$$\lambda = \frac{h}{mv} = \frac{ht}{mL} = 2d \sin \theta \quad \text{Equation 3.4}$$

The key characteristic of time of flight (TOF) neutrons is that the neutrons arrive at the sample chamber at different times [14]. This enables analysis of the crystal structure through multiple planes, quantified by the d-spacing, due to the variable wavelengths [8]. The resolution in d-space is inversely proportional to the path length, L , therefore longer distance provides higher resolution [15].

The HRPD instruments has three banks of detectors: the back scattered detectors, the 90° detectors and low angle detectors. The back scattered detectors have the greatest resolution, $\Delta d / d \sim 4 \times 10^{-4}$, and have been used to analyse the spacing between 0.7-2.4Å [15]. The 90° detectors can distinguish between neutrons and non-neutron event, such as gamma (γ) rays [13]. The low angle detectors enable analysis of long d-spacing within the crystalline structure, allowing for the identification of any long range ordering within the structure [13].

For data collection the samples have been loaded into vanadium cans. Vanadium has a low coherent scattering value with neutrons within a temperature range of 2-1273K [16].

This means that the can does not contribute any Bragg reflections of significant intensity to the neutron diffraction pattern.

Rietveld fitting of structural models to the data was completed using the GSAS software. Background removal was completed and refined parameters of the crystalline structure established [17, 18].

3.3.3 The Rietveld Method

The Rietveld method provides information on the structural properties of a material using powder diffraction data [17]. In this thesis, powder diffraction data was acquired from XRD or neutron diffraction analysis, where instrument access was granted. The reflections of the powder diffraction describe the underlying crystal structure. The quality of refinement is based on comparing a model of the ideal structure to the acquired data, taking information from the reflection shape, height and width [17]. The basic principle of the Rietveld method analyses the fit between the experimentally gathered data and the proposed model of the crystalline structure. The model is subsequently refined in order to improve the fitting [17].

The quality of the fitting is obtained by minimising the residual (S_y) simultaneously between all data points (i) [17]. This is completed using Equation 3.5, where the difference between the intensity of the observed data point (y_{oi}) and the calculated data point (y_{ci}) is multiplied by the weighting factor (w_i , the reciprocal of y_{oi}) [17].

$$S_y = \sum_i w_i (y_{oi} - y_{ci}) \quad \text{Equation 3.5}$$

In order to minimise the residual a complex mathematical procedure is adopted by the GSAS software, the details of which are beyond the scope of this thesis.

The key parameters, which are refined in order to improve the fit in Rietveld analysis for this work, are summarised in **Error! Reference source not found.** [17].

The quality of the fit after an iteration of refinement is best quantified by the parameters χ^2 and R_{wp} . R_{wp} (or wRp) is the weighted profile R-factor and provides information on the quality, or goodness, of the fit including the function of the residual (Equation 3.5) [19]. χ^2 is a statistical value which describes the ratio between R_{wp} and R_{exp} , where the R_{exp} parameter describes the value of R_{wp} if only counting statistics are considered within the fitting [19]. R_{wp} alone could be increased due to unindexed

reflections within the powder diffraction pattern. Similarly χ^2 can be artificially small if the error within the counting statistics (R_{exp}) are greater than the weighted profile of the model (R_{wp}) [17]. In order to analysis the fit of the model a magnification of the fitting at low d-spacing is included within figures to enable identification of any systematic errors within the peak fitting. This could be due to incorrect space group or refined structural parameters.

Table 3.2: Key parameters refined during the Rietveld method.

Instrument parameters	The features of the collected powder diffraction which are due to the instrument set up are included in the refinement to ensure that their effect is eliminated.
Profile asymmetry / parameters	The shape of the profile due to contributions from the instrument and the sample preparation are varied. The profile functions are dependent on the powder diffraction technique (XRD or neutron diffraction).
Background function	The background intensity is modelled and the contribution to the observed data (y_{oi}) calculated.
Absorption	Refinement of the element effects on the data point intensity.
Scale factor	Allows the intensities of the calculated data points to vary to provide a better match to those experimentally observed.
Unit cell parameters	Lattice parameter (a , b , and c) and angles (α , β and γ) refinement. Atomic coordinate positions, which the crystal structures symmetry allows to vary, described using Wyckoff notation ($h k l$).
Thermal parameters	The thermal parameters describe vibration of the crystalline lattice, which in turn describes the volume in which the atom can occupy while still maintaining the refined crystal structure. Ideally all thermal parameters would be nearly spherical (isotropic), however the elongation along one axis (high U_{iso} values) shows an anisotropic behaviour. Large U_{iso} values could be the result of the refined atomic positions being assigned to incorrect atoms, highlighting disorder within the structure.

3.4 Transmission Electron Microscopy

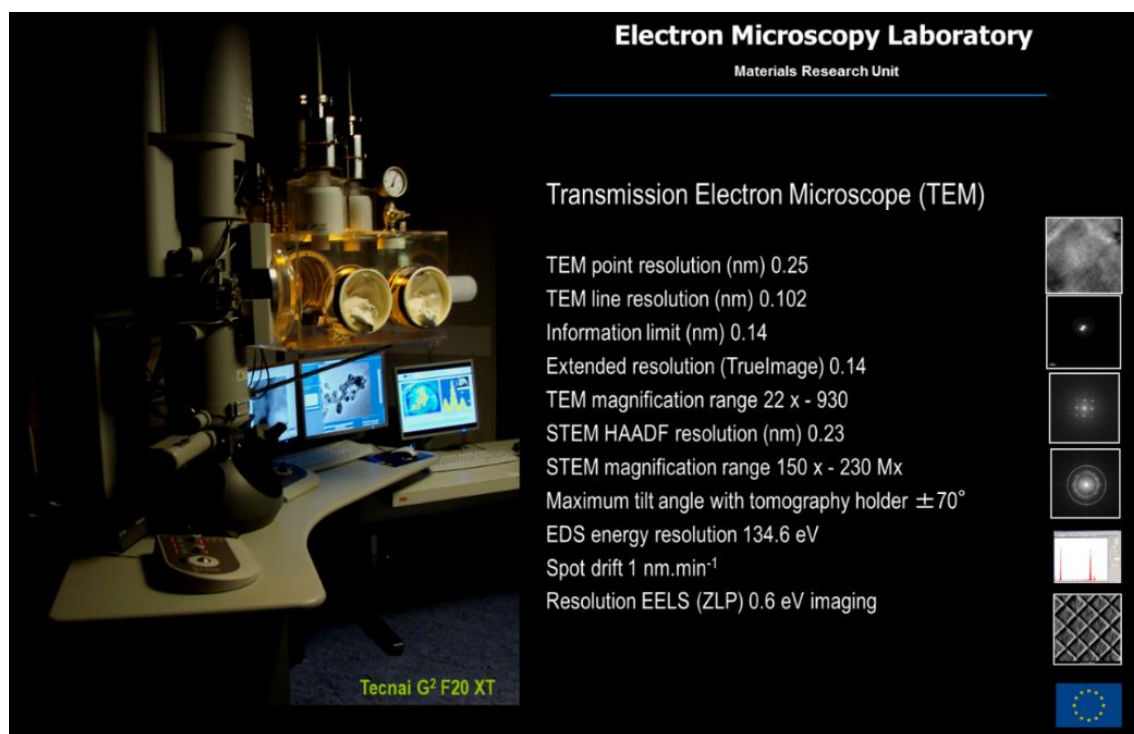
Transmission electron microscopy (TEM) was used to gain crystallographic data on key zone axis of structures using Select Area Electron Diffraction (SAED) patterns. TEM

analysis requires materials to be electron transparent. The electrons interact to provide information on the atomic positions within the material. Materials were prepared by crushing within a pestle and mortar and dispersed within ethyl alcohol. Holey carbon copper grids were used to collect material held in suspension within the alcohol.

A high voltage (typically 100-300 kV) is applied to a tungsten filament in order to produce a beam of electrons. The electron beam is focused through a series of electromagnetic lenses. The condensed and focused beam of electrons is then passed through the fine grains of powdered material. Electrons are either scattered off the material or transmitted through. The un-scattered electrons are mechanically Fourier transformed in order to give rise to an image below the sample using a photographic film or CCD camera.

3.4.1 Technai G2 F20 XT, Institute of Transuranium Elements

The Technai G2 F20 XT instrument, at the Institute for Transuranium Elements (ITU) (Karlsruhe, Germany) is modified to enable TEM analysis of radioactive materials. This includes the addition of a dedicated glove box for loading and unloading the samples into the instrument.



Electron Microscopy Laboratory
Materials Research Unit

Transmission Electron Microscope (TEM)

- TEM point resolution (nm) 0.25
- TEM line resolution (nm) 0.102
- Information limit (nm) 0.14
- Extended resolution (TrueImage) 0.14
- TEM magnification range 22 x - 930
- STEM HAADF resolution (nm) 0.23
- STEM magnification range 150 x - 230 Mx
- Maximum tilt angle with tomography holder $\pm 70^\circ$
- EDS energy resolution 134.6 eV
- Spot drift 1 nm.min⁻¹
- Resolution EELS (ZLP) 0.6 eV imaging

Tecnai G² F20 XT

European Union flag

Figure 3.3: Information slide as provided by The Institute of Transuranium Elements, a European Commission facility, Karlsruhe, Germany.

Materials were loaded on a copper holey carbon grid by suspending finely crushed particulate within ethyl alcohol and submerging the grid. The copper grid was then mounted into a double tilt sample holder and loaded into the microscope through glove

box to glove box transfer. The instrument was operated at 200keV in diffraction mode to determine the crystalline structure of the materials. Due to the nature of the facility only official images released upon request can be used for the instrument, the unmodified image is included within Figure 3.3.

3.4.2 Hitachi H-9000NAR TEM (IVEM-Tandem), Argonne National Laboratory

Radiation damage, as a result of the decay of radioactive isotopes, was experimentally simulated at the Intermediate Voltage Electron Microscopy (IVEM) TANDEM facility. The IVEM-TANDEM facility at Argonne National Laboratory (ANL) was used to irradiate a selection of materials, analysed using the attached Hitachi 9000-NAR transmission electron microscope, with an accelerating voltage of 300kV. This is fitted with a Danfysik ion implanter at a 30° angle to the electron beam, used to irradiate the materials. The ion beam uses 1 MeV Kr²⁺ ions with a flux of 6.125 x 10¹¹ ions cm⁻² sec⁻¹. The samples, prepared by loading crushed powders, suspended in ethyl alcohol, onto holey carbon films on a copper grids. For high temperature experiments, temperatures >500°C, a molybdenum grid was used due to the evaporation of the copper grid at 820°C [20, 21]. A single tilt specimen holder was used. However, due to the shadowing effect, caused by the ion beam entering the TEM instrument at a 30° angle to the electron beam, the tilt on the specimen holder was fixed at 15° angle. A schematic of this can be found in Figure 3.4.

Ions were implanted into samples with enough energy, or mass, to displace atoms within the structure. This simulates the effect of recoil energy within the parent atom of an alpha-decay events, which have an energy of 70-100 keV [22].

The instrument enables incremental addition of fluence (ions per unit area, ions cm⁻²) until the material is fully amorphous. The fluence required to form a fully amorphous material is termed the critical amorphisation fluence (F_C). Amorphisation here is defined using selected area zone axis diffraction pattern, where no pair of Bragg reflections are visible in the diffraction image of an amorphous material. The IVEM-Tandem instrument enables this to be determined experimentally, at specific temperatures (T). The extrapolation of the F_C at zero Kelvin is noted by F_{C0} . The loss of crystallinity of the material during incremental addition of fluence enables identification of the destabilisation of the crystalline structure of the material under irradiation. The application of variable temperatures during the analysis enables the effects of temperature

on damage / recovery to be described. Equation 3.6 was developed by Weber et al. to describe the relationship of fluence and temperature [23-25]:

$$F_c = \frac{F_{c0}}{1 - \exp\left[\left(\frac{E_a}{k_b}\right)\left(\frac{1}{T_c} - \frac{1}{T}\right)\right]}$$

Equation 3.6

Where the critical temperature (T_c) is defined as the temperature at which the recovery rate and the damage rate are equal. At temperatures in excess of T_c the material recovers the crystalline structure during this analysis, irrespective of fluence and the radiation induced damage. The energy required for recovery is denoted as the activation energy (E_a), and described the thermal energy for the recovery of damage in the material (in eV). Finally k_b is Boltzmann's constant ($8.617 \times 10^{-5} \text{ eV K}^{-1}$).

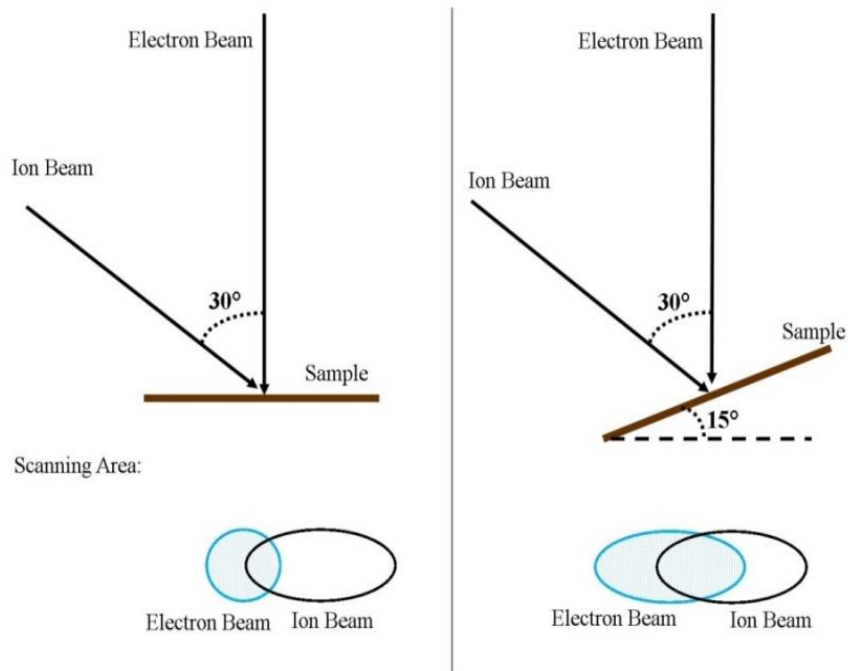


Figure 3.4: Schematic of the ion beam and electron beam set up within the Hitachi 300kV TEM and ion beam accelerator at Argonne National Laboratory.

The variable temperature of the sample is selected and held prior to irradiation, in order to determine the effects temperature on the recovery of the material. This is completed by electrically heating or cryogenically cooling the sample stage within the microscope. For analysis, five individual grains are selected and electron diffraction images taken throughout irradiation in order to analysis the effect of increasing irradiation. The electron

beam is turned off during irradiation, and vice versa, in order to ensure interaction kinetics between electron and ion beam are eliminated.

3.5 X-ray Absorption Spectroscopy

X-ray Absorption Spectroscopy (XAS) uses synchrotron X-rays, an electromagnetic energy, to excite electrons from electron shells within an atom [26].

Each atom consists of neutrons (with a zero charge) and protons (with a positive charge) in a dense nucleus. A nucleus is surrounded by orbitals of electrons (with a negative charge), termed shells. Shells have a defined electron occupancy, with innermost orbitals populated first, and referred to as core electrons, which have the lowest energy. Electrons fill orbitals in order of increasing energy. Electrons in the outermost electron shell are termed valence electrons. Electrons closer to the core shell are more tightly bound to the atom, termed the electron binding energy. The energy required to remove an electron is dependent on the electron binding energy.

Synchrotron X-rays are used to induce the photoelectric effect, where X-rays are absorbed by an electron within the core of the atom [26]. This results in the excitation of the electron, which moves to an unoccupied higher energy orbital. The hole within the core is re-occupied by an electron from a higher orbital, either by the decay of the excited electron or by another higher orbital electron [26]. This is coupled with the release of an X-ray equivalent to the energy difference between the two orbitals. The energies are characteristic of the atom, and therefore the X-ray energy released is dependent on the element [26]. A schematic of the first three shells of an atom (K, L and M) is shown in Figure 3.5. Each shell can be further subdivided (Table 3.3) and each sub-shell has a unique characteristic energy [27].

Specifically XAS measured the linear absorption coefficient, $\mu(E)$, as a function of energy, collected in transmission mode [26]. When an electron is released from the shell the $\mu(E)$ will rapidly increase, this is referred to as the leading or absorption edge. This occurs when the energy of the incoming X-ray corresponds to the energy of the shell of the analysed atom. X-ray Absorption Near Edge Spectroscopy (XANES) is the analysis of the absorption edge of the $\mu(E)$ data. The value of E_0 is used to describe the absorption edge, where E_0 is the inflection point of the first derivative of the collected energy spectrum [26].

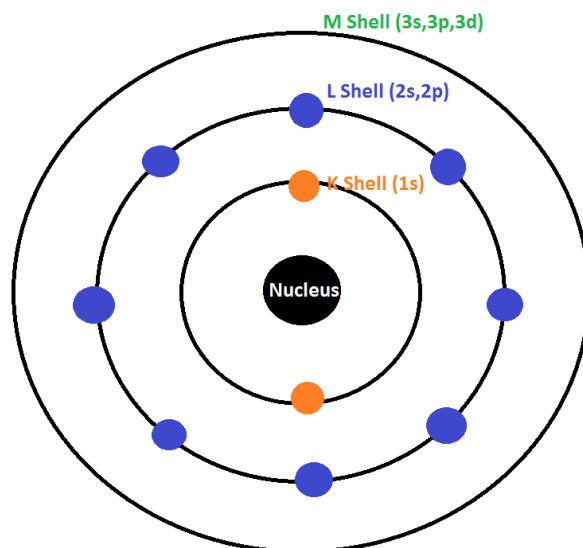


Figure 3.5: Schematic representation of the electron configuration of the K and L shells surrounding the nucleus. The M shell contains 18 electrons, although not drawn in this diagram.

X-ray absorption near edge structure spectroscopy is used to provide information on an elements oxidation and coordination within the material [28]. Figure 3.6 is an example of the data collected using this technique, highlighted is the XANES data region.

For completeness the Extended X-ray Absorption Fine Structure (EXAFS) region provides information on the atomic distances within the structure, as well as coordination number [26]. However, the EXAFS region was not analysed in this thesis.

Table 3.3: Examples of electron shell and sub-shell electron numbers.

Shell Name	Sub-shell Name	Sub-shell maximum number of electrons	Shell maximum electrons
K	1s	2	2
L	2s	2	8
	2p	6	
M	3s	2	18
	3p	6	
	3d	10	

3.5.1 XANES Experimental set up

Analysis of the uranium average oxidation quantified throughout this thesis is defined from analysis of the U L_{III}-edge XANES data. Data were collected in transmission mode using a finely ground specimens dispersed in polyethylene glycol to achieve a thickness of one absorption length. The data was acquired on beam line X23A2 of the National

Synchrotron Light Source (NSLS), Brookhaven National Laboratory (BNL), Upton (USA). The experimental apparatus consisted of a radiation hutch, ion chambers for transmission and fluorescence measurements, sample translation stage and adjustable (horizontal and vertical) exit slits. The beam line can operate between 4.9 – 30 keV, using a Si (311) monochromator crystal, with a resolution of 2×10^{-4} and a flux of 1×10^{10} photons per second. The spot size of 25 mm (horizontal) \times 1.0 mm (vertical) and a total angular acceptance of 4mrad was used. Data analysis was performed using the programs Athena, Artemis and Hephaestus [29]. Data acquisition was performed by Dr Martin Stennett.

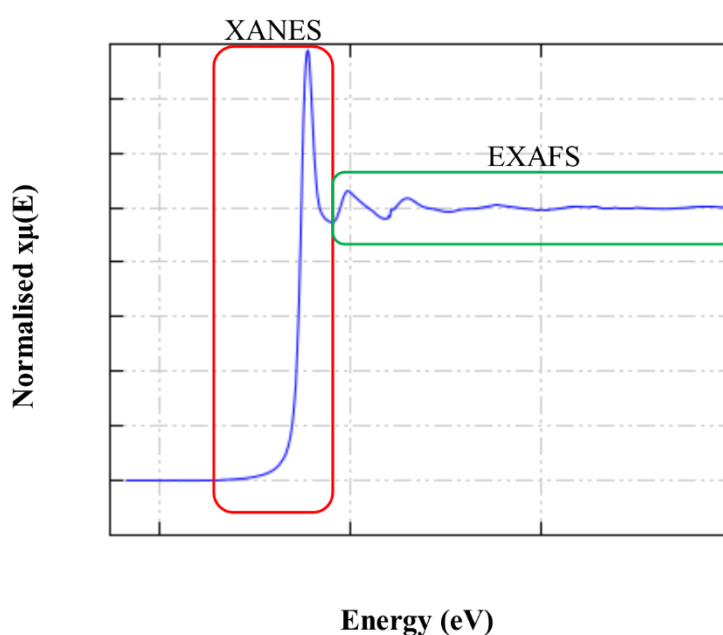


Figure 3.6: A complete XAS Spectra with the XANES and EXAFS regions highlighted.

3.6 References

- [1] Cullity BD. Elements of X-ray Diffraction. Addison-Wesley Publishing Company, Inc.; 1956.
- [2] DeGraef M, McHenry ME. Structure of Materials: An Introduction to Crystallography, Diffraction and Symmetry, 2nd Edition. Structure of Materials: an Introduction to Crystallography, Diffraction and Symmetry, 2nd Edition 2012:1-739.
- [3] West AR. Basic solid state chemistry. John Wiley & Sons; 1999.
- [4] Goodhew PJ, Humphreys J, Beanland R. Electron Microscopy and Analysis, Third Edition. CRC Press; 2000.
- [5] Egerton RF. Physical Principles of Electron Microscopy: An Introduction to TEM, SEM and AEM. Springer US; 2005.

- [6] Goodhew PJ, Humphreys J, Beanland R. *Electron Microscopy and Analysis*. Taylor & Francis; 2001.
- [7] Lilley J. *Nuclear Physics: Principles and Applications*. John Wiley & Sons, Ltd.; 2001.
- [8] Hannon AC. Neutron Diffraction, Theory. *Encyclopedia of Spectroscopy and Spectrometry*; 1999.
- [9] Dinnerbier RE, Billinge SJL, Bruce PG *et al.* *Powder Diffraction: Theory and Practice*. Royal Society of Chemistry; 2008.
- [10] Sears VF. Neutron scattering lengths and cross sections. In: *Neutron News*. 1992. pp. 26-37.
- [11] Chou W. Spallation Neutron Source and Other High Intensity Proton Sources. In: Fermi National Accelerator Laboratory.
- [12] ISIS Web Site. In: Science and Technology Facilities Council; 2017.
- [13] Council SaTF. Neutron Training Course. In: <http://www.isis.stfc.ac.uk/learning/neutron-training-course/downloads/general/neutron-training-course---manual13577.pdf>: Unknown.
- [14] Steichele E, Arnold P. High-Resolution Neutron Time of Flight Diffractometer. *Physics Letters A* 1973; A 44:165-166.
- [15] HRPD User Manual. In: <http://www.isis.stfc.ac.uk/instruments/hrpd/documents/hrpd-manual6735.pdf>.
- [16] ISIS STFC. Vanadium cans. In: <http://www.isis.stfc.ac.uk/sample-environment/sample-containers/vanadium/vanadium-cans8939.html>.
- [17] Larson AC, Von Dreele RB. General Structure Analysis System (GSAS). In: Los Alamos National Laboratory Report LAUR. 2004. pp. 86-748.
- [18] Toby BH. EXPGUI, a graphical user interface for GSAS. *J. Appl. Cryst.* 2001; 34:210-213.
- [19] Toby BH. R factors in Rietveld analysis: How good is good enough? *Powder Diffraction* 2006; 21:67-70.
- [20] Liu ZW, Bando Y. A novel method for preparing copper nanorods and nanowires. *Advanced Materials* 2003; 15:303-305.
- [21] Zhang ZL, Su DS. Behaviour of TEM metal grids during in-situ heating experiments. *Ultramicroscopy* 2009; 109:766-774.
- [22] Weber WJ, Ewing RC, Catlow CRA *et al.* Radiation effects in crystalline ceramics for the immobilization of high-level nuclear waste and plutonium. *Journal of Materials Research* 1998; 13:1434-1484.
- [23] Ewing RC, Wang LM. Amorphization of zirconolite - Alpha decay event damage versus krypton ion irradiation. *Nuclear Instruments & Methods in Physics Research Section B-Beam Interactions with Materials and Atoms* 1992; 65:319-323.
- [24] Wang SX, Wang LM, Ewing RC. Nano-scale glass formation in pyrochlore by heavy ion irradiation. *Journal of Non-Crystalline Solids* 2000; 274:238-243.
- [25] Meldrum A, White CW, Keppens V *et al.* Irradiation-induced amorphization of Cd₂Nb₂O₇ pyrochlore. *Physical Review B* 2001; 63:104109.

- [26] Rehr JJ, Kas JJ, Vila FD, Newville M. Theory and Analysis of XAFS. In: XAFS Techniques for Catalysts, Nanomaterials, and Surfaces. Springer Link; 2016. pp. 13-50.
- [27] Ashcroft NW, Mermin DN. Solid State Physics. 1976.
- [28] Rehr JJ. Theory and calculations of X-ray spectra: XAS, XES, XRS, and NRIXS - ScienceDirect. Radiation Physics and Chemistry 2006; 75:1547-1558.
- [29] Ravel B, Newville M. ATHENA, ARTEMIS, HEPHAESTUS: data analysis for X-ray absorption spectroscopy using IFEFFIT. Journal of Synchrotron Radiation 2005; 12:537-541.

Chapter 4 Systematic substitutions of the calcium niobate pyrochlore system

4.1 Introduction

The long term performance of a ceramic material must be demonstrated in a variety of situations for the immobilisation of actinide materials. One aspect of this is the analysis of the structural flexibility of the ceramic phase. I have completed this through minor variations in composition of the general pyrochlore composition $\text{CaLn}^{3+}\text{M}^{3+}_{0.5}\text{Nb}_{1.5}\text{O}_7$, where Ln = La, Nd, Sm, Gd, Ho or Yb and M = Al, Fe, Cr, Sc or Y.

When considering a geological disposal facility (GDF), the physical and chemical alterations to the wastefrom from the local environment must be understood. To inform this the physical development of the material with time requires analysis. Radiation induced damage is a mechanism by which the material can be physically altered therefore simulation of the damage has been completed on materials with target composition $\text{CaLn}^{3+}\text{Fe}_{0.5}\text{Nb}_{1.5}\text{O}_7$, where Ln = La, Nd, Sm, Gd, Ho or Yb. Other mechanisms which contribute to physical changes within the material include: the leaching of radioactive species in ground water, chemical alteration of the materials due to both the natural and engineered environment. In terms of the long term evolution of the material due to the radioactive nature of the cations they are designed to retain this is compositional and structurally dependant.

Pyrochlore materials have been studied historically as a potential waste form for the immobilisation of radioactive species such as uranium and plutonium. Analysis of a wide range of chemical compositions in a variety of environments have been completed within the field, showing great potential for the materials. This includes studies on the corrosion behaviours in natural and simulated environments [1-9], the material properties with varying chemical composition [10-24], and when subject to high levels of radiation [25-40].

Naturally occurring minerals with a pyrochlore, or pyrochlore related structures, have been identified to retain radioactive species for time scales comparable to those required for the GDF [41-46]. The minerals are found in a metamict state which is a radiation induced amorphous state of a previously crystalline material [47]. Studies on these materials provide information which can be utilised to help underpin the criticality safety

case of highly active species post closure in the GDF. An appreciation of the development of the material with time is required. The behaviour of pyrochlore structured materials can be placed into two broad categories; those that transition from crystalline to amorphous state or, those that transition from a crystalline to amorphous state via an intermediate crystal structure. Information from naturally occurring pyrochlores can be utilised to provide information on the long term behaviour of materials which transition directly from a pyrochlore to amorphous state [48-50].

The pyrochlore structure, of general composition $A_2B_2O_7$, has space group $Fd\bar{3}m$. This is a superstructure described relative to the fluorite subcell, AO_2 with space group $Fm\bar{3}m$ [51]. The superstructure arises from the formation of a regular array of oxygen vacancies in the $(3/8, 3/8, 3/8)$ coordinate position, creating a structure with two distinct cation sites, denoted as A and B [51]. The two sites are defined by their coordination environment, such that A-site cations are 8-fold coordinated whereas the B-site cations are in 6-fold coordination [51]. The crystallographic positions for the pyrochlore structure are defined and restricted, with the exception of the oxygen on the 48f position $(x, 1/8, 1/8)$ where the ordered anion vacancy permits flexibility in the 48f oxygen x-coordinate [51]. The potential for the relaxation of the 48f oxygen due to the anion vacancy enables the accommodation of variable cation sizes within the structure, however as a result the structure distorts [51]. The shift in the 48f oxygen x-position can be utilised to predict the distortion and the structural response. For a crystalline material with a pyrochlore structure the 48f oxygen x-parameter is described by Equation 4.1 [27]:

$$0.3125 > 48f \text{ oxygen } x\text{-parameter} > 0.3750 \quad \text{Equation 4.1}$$

An ideal pyrochlore structure ($x=0.3125$), general formula $A_2B_2O_7$, consists of a corner sharing BO_6 octahedra edge sharing with A cation distorted cubic polyhedra, the exact shape of these are defined by the shift in the 48f oxygen x-parameter [52]. At $x=0.3750$, the BO_6 octahedra are distorted to form a triagonally flattened octahedra, in response the A-site polyhedron becomes a regular cubic polyhedra, typically indicative of a fluorite structure [27]. When a defect fluorite structure, $(AB)_4O_7$, is identified it would indicate disordering of the cations across the A and B sites. The two cations mixed across the A and B site with an average coordination of 7 and the presence of an oxygen vacancy leads to the formation of a defect fluorite. The consequence of disorder within the defect fluorite structure means specific A and B cation locations are not defined. An advantage to the use of a ceramic material is the ability to identify the cation ordering within the structure.

This is important when trying to ensure a material is passively safe within the GDF. This is achieved by selecting a ceramic composition which immobilises radioactive cations with neutron absorbing rare earth elements.

This work looks at the formation and structural analysis of 24 new pyrochlore compositions, based on the systematic substitutions of calcium niobate pyrochlore, to form the target compositions $\text{CaLnM}_{0.5}\text{Nb}_{1.5}\text{O}_7$ where Ln= La, Nd, Gd, Sm, Ho or Yb and M = Al, Fe, Sc or Y. A selection of these with target compositions $\text{CaLnFe}_{0.5}\text{Nb}_{1.5}\text{O}_7$ (where Ln = La, Nd, Gd, Sm, Ho or Yb) have been subject to in-situ irradiation at the IVEM-Tandem Facility, Argonne National Laboratory, Chicago (see Section 3.4.2 for full experimental set up). The facility includes a transmission electron microscope (TEM) coupled to an ion beam accelerator, this enables the use of heavy ion bombardment while examining the structural response using electron diffraction analysis. By incrementally increasing the fluence to the material, the changes in the crystalline structure in a high radiation environment were documented and the effect with chemical composition was studied.

The likelihood of a material forming the pyrochlore structure is governed by the r_A/r_B ratio, the ratio of the atomic radii on the A and B sites. [27]. Generally the ionic radii ratio is applied to pyrochlores of general composition $\text{A}_2\text{B}_2\text{O}_7$. The materials studied here have the general composition $\text{A}^{2+}\text{A}^{3+}\text{B}_{1.5}^{5+}\text{B}_{0.5}^{3+}\text{O}_7$, therefore the extent to which this is appropriate to predict the material formation is unclear [53]. The difference in the cation size and the effect on the polyhedra of the pyrochlores structure can be described by the tolerance factor, Equation 4.4 [54].

The tolerance factor is determined from the derived formula of the unit cell parameter (Equation 4.2) [55], and the description of the XA_4 polyhedra of the pyrochlore structure (Equation 4.3) [56].

$$a = \frac{8}{3^{1/2}} \left[1.43373(R_A + R_O) - 0.42931 \frac{(R_A + R_O)^2}{R_B + R_O} \right] \quad \text{Equation 4.2}$$

$$t_2 = a \frac{3^{1/2}}{[8(R_A + R_O)]} \quad \text{Equation 4.3}$$

$$t = 1.43373 - 0.42931 \left(\frac{R_A + R_O}{R_B + R_O} \right) \quad \text{Equation 4.4}$$

The values for the r_A/r_B values and the tolerance factor, t, values for the measured compositions are included in Table 4.2. The range of tolerance factors for a pyrochlore material falls within the range $0.84 \leq t \leq 0.98$ [54].

The design of the waste form can be explored while simultaneously tuning the r_A/r_B ratio of the material by variations in the rare earth element (REE). For pyrochlores of composition $A_2^{3+}B_2^{4+}O_7$ these values generally fall within the range $r_A/r_B = 1.46 - 1.78$. Beyond the lower boundary (<1.46) a fluorite, with general crystalline structure $(AB)_4O_8$, or defect fluorite structure with generic structure $(AB)_4O_7$, is expected to form. Above the upper boundary a monoclinic structure is expected to form, this has a layered perovskite type structure, for example $La_2Ti_2O_7$ [57].

4.2 Experimental Methods

Materials were prepared from carbonate and oxide precursors according to the stoichiometric masses in Tables 4.2(a)-(d), measured to 3d.p. Chemical reagent information for the precursor materials can be found in Table 4.1.

Batches of 10 grams were homogenised using a Fritsch Pulverisette 7 planetary mill for 4 minutes, at approximately 300 rpm. This was completed in a sialon milling pot containing spherical sialon milling media. The homogenised material was then cold isostatically pressed and reacted by solid state reaction in air at 1450°C with a dwell time of 48 hours, and heating and cooling rates of 5°C min^{-1} in alumina crucibles.

Table 4. 1: Chemical reagent information of the carbonate and oxide precursors.

Chemical Reagent	Chemical Formula	Supplier	Purity (%)
Calcium Carbonate	CaCO_3	Sigma Aldrich	>99.00
Niobium (V) Oxide	Nb_2O_5	Sigma Aldrich	>99.90
Lanthanum (III) Oxide	La_2O_3	Sigma Aldrich	>99.99
Neodymium (III) Oxide	Nd_2O_3	Sigma Aldrich	>99.99
Samarium (III) Oxide	Sm_2O_3	Sigma Aldrich	>99.99
Gadolinium (III) Oxide	Gd_2O_3	Sigma Aldrich	>99.99
Holmium (III) Oxide	Ho_2O_3	Sigma Aldrich	>99.99
Ytterbium (III) Oxide	Yb_2O_3	Sigma Aldrich	>99.99
Aluminium (III) Oxide	Al_2O_3	Sigma Aldrich	>99.00
Scandium (III) Oxide	Sc_2O_3	Sigma Aldrich	>99.00
Iron (III) Oxide	Fe_2O_3	Sigma Aldrich	>99.00
Yttrium (III) Oxide	Y_2O_3	Sigma Aldrich	>99.99

Table 4.2: Tables (a)-(d) show the weighed stoichiometry's of materials utilised for the synthesis of the ceramic compositions, generally $\text{CaLnM}_{0.5}\text{Nb}_{1.5}\text{O}_7$ where Ln= La, Nd, Sm, Gd, Ho or Yb and M= Al, Sc, Fe or Y.

(a) $\text{CaLnAl}_{0.5}\text{Nb}_{1.5}\text{O}_7$

Ln	Mass CaCO_3 (g)	Mass Ln_2O_3 (g)	Mass Al_2O_3 (g)	Mass Nb_2O_5 (g)
La	2.052	3.339	0.523	4.087
Nd	2.029	3.411	0.517	4.042
Sm	2.005	3.492	0.511	3.993
Gd	1.977	3.581	0.504	3.938
Ho	1.948	3.677	0.496	3.880
Yb	1.918	3.775	0.488	3.819

(b) $\text{CaLnSc}_{0.5}\text{Nb}_{1.5}\text{O}_7$

Ln	Mass CaCO_3 (g)	Mass Ln_2O_3 (g)	Mass Sc_2O_3 (g)	Mass Nb_2O_5 (g)
La	2.015	3.279	0.694	4.013
Nd	1.993	3.350	0.687	3.970
Sm	1.969	3.430	0.678	3.922
Gd	1.943	3.518	0.669	3.870
Ho	1.914	3.613	0.659	3.813
Yb	1.885	3.711	0.649	3.755

(c) $\text{CaLnFe}_{0.5}\text{Nb}_{1.5}\text{O}_7$

Ln	Mass CaCO_3 (g)	Mass Ln_2O_3 (g)	Mass Fe_2O_3 (g)	Mass Nb_2O_5 (g)
La	1.993	3.243	0.795	3.969
Nd	1.972	3.314	0.787	3.927
Sm	1.948	3.394	0.777	3.881
Gd	1.923	3.481	0.767	3.829
Ho	1.895	3.576	0.756	3.774
Yb	1.866	3.673	0.744	3.717

(d) $\text{CaLnY}_{0.5}\text{Nb}_{1.5}\text{O}_7$

Ln	Mass CaCO_3 (g)	Mass Ln_2O_3 (g)	Mass Y_2O_3 (g)	Mass Nb_2O_5 (g)
La	1.929	3.140	1.088	3.843
Nd	1.910	3.210	1.077	3.804
Sm	1.888	3.288	1.065	3.760
Gd	1.863	3.374	1.051	3.711
Ho	1.837	3.468	1.036	3.659
Yb	1.810	3.564	1.021	3.605

4.3 Results

4.3.1 Scanning electron microscopy and energy dispersive spectroscopy

Micro-structural and micro-chemical analyses was performed on pellets of material polished to a $1\mu\text{m}$ optical finish, on the Hitachi TM3030 SEM (see section 3.2 for instrument set up). Images were collected in backscattered electron (BSE) imaging mode to determine phase purity. Semi quantitative energy dispersive X-ray spectroscopy (EDS) provided information on the ratio of cations present in each phase identified within the

material. The data was collected at 30,000x magnification at 5 different points within the BSE image. The reported composition is an average of the 5 measured point compositions. Where a multiphase composition was identified within the BSE image then the composition of each phase was determined using the average composition of 5 measured points. The technique utilises scattered X-rays in order to ascertain chemical information of the material [58]. Information from the scattering of X-rays from the anions (in this case oxygen) within the structure is limited due to the dominance of X-rays scattering from heavy cations, therefore anion content cannot accurately be determined. The oxygen stoichiometry has been calculated under the assumption that the material is charge neutral, with both trivalent lanthanides (Ln) and transition metals (M), divalent calcium and pentavalent niobium cations. The chemical compositions, including inferred oxygen content, for all materials are summarised in Table 4.3.

For each composition BSE and secondary electron images have been collected. Figure 4.3 shows materials of target composition $\text{CaLnFe}_{0.5}\text{Nb}_{1.5}\text{O}_7$, where Ln = La, Nd, Gd, Sm, Ho or Yb. The contrast within the BSE images defines areas with variable average atomic numbers, this can be inferred as multiple phases of the assemblage of the material. A lack of variation in the contrast of the BSE image is indicative of a material containing only a single phase assemblage. Secondary electron images, and BSE images for other samples (whose compositional analysis is included within Table 4.3) can be found in Appendix A.

EDS analysis generally showed all the materials were chemically homogeneous. Three of the samples prepared contained additional phases which were identified (Figure 4.1). Cation ratios were measured for each phase using EDS analysis. The target composition $\text{CaLaAl}_{0.5}\text{Nb}_{1.5}\text{O}_7$ showed the presence of 3 phases; all phases were present in apparently equal amounts. For the target composition $\text{CaHoY}_{0.5}\text{Nb}_{1.5}\text{O}_7$, phase A was found to be the predominant phase within the material, within minor contributions from phase B. For material with target composition $\text{CaYbY}_{0.5}\text{Nb}_{1.5}\text{O}_7$ a secondary phase was identified within the phase assemblage but in such small quantities that it was not possible to isolate the phase for EDS analysis. Calculated values for the r_A/r_B ratio and the tolerance factor for the single phase materials are included within Table 4.2. The r_A/r_B ratio and the tolerance factor for multiphase materials was calculated using the target compositions in order to establish if this provides information as to why the material was unable to form a single phase pyrochlore. The values calculated for the multiphase compositions did not indicate that these materials would sit outside the pyrochlore stability range. The phase

assemblage of multiphase materials was studied by X-ray diffraction and neutron diffraction (Sections 4.3.2 and 4.3.3, respectively).

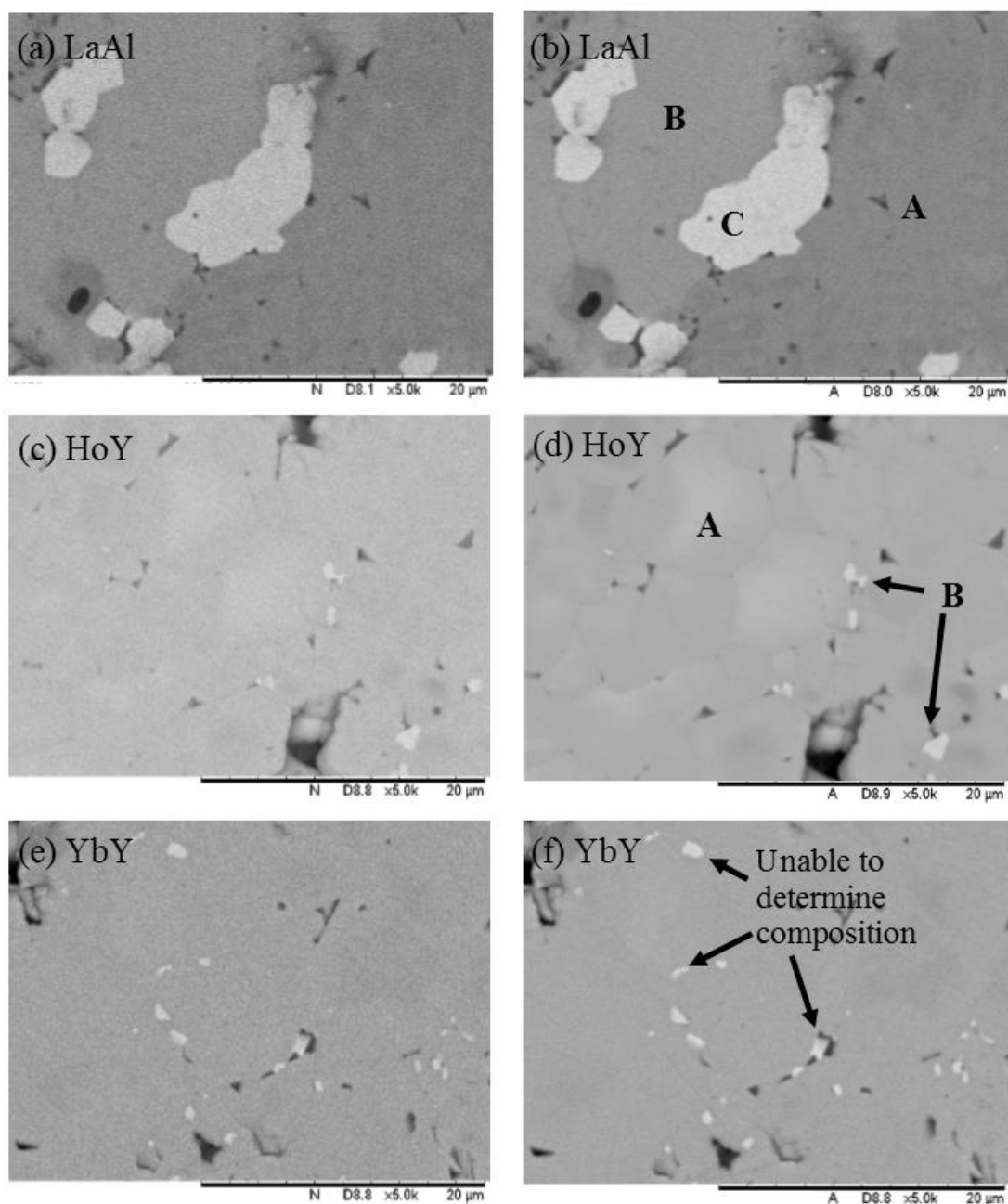


Figure 4.1: SEM secondary electron and back scattered images of materials with (a) and (b) showing target composition $\text{CaLaAl}_{0.5}\text{Nb}_{1.5}\text{O}_7$, (c) and (d) showing target composition $\text{CaHoY}_{0.5}\text{Nb}_{1.5}\text{O}_7$ and (e) and (f) showing target composition $\text{CaYbY}_{0.5}\text{Nb}_{1.5}\text{O}_7$.

In addition, the series materials with general composition $\text{CaLnCr}_{0.5}\text{Nb}_{1.5}\text{O}_7$ (where Ln= La, Nd, Sm, Gd, Ho or Yb) were reacted, however, despite numerous attempts single phase material could not be synthesised, these results are included within Appendix A to support this chapter of work.

Table 4.3: Semi-quantitative EDS results as collected. Oxygen stoichiometry was inferred from the assumed valence of cations ($\text{Ln}^{3+} / \text{Ca}^{2+} / \text{Nb}^{5+}$) charge compensation within the oxide material. *Values calculated using idealised target compositions.

Target Composition	Composition- as determined by EDS	r _A /r _B	t, tolerance factor
Al Series			
CaLaAl _{0.5} Nb _{1.5} O ₇	A - Ca _{1.43(5)} La _{0.50(6)} Al _{1.17(5)} Nb _{0.68(7)} O _{5.64(39)}	1.86*	0.89*
	B - Ca _{1.45(5)} La _{0.28(3)} Al _{0.13(1)} Nb _{1.47(14)} O _{4.93(46)}		
	C - Ca _{0.08(1)} La _{1.13(11)} Al _{0.06(1)} Nb _{1.44(11)} O _{5.47(47)}		
CaNdAl _{0.5} Nb _{1.5} O ₇	Ca _{1.08(5)} Nd _{0.99(10)} Al _{0.49(2)} Nb _{1.52(3)} O _{7.10(31)}	1.87	0.90
CaSmAl _{0.5} Nb _{1.5} O ₇	Ca _{1.14(11)} Sm _{1.00(6)} Al _{0.53(1)} Nb _{1.66(5)} O _{7.59(34)}	1.75	0.90
CaGdAl _{0.5} Nb _{1.5} O ₇	Ca _{1.04(10)} Gd _{1.01(11)} Al _{0.51(2)} Nb _{1.56(6)} O _{7.22(45)}	1.75	0.90
CaHoAl _{0.5} Nb _{1.5} O ₇	Ca _{1.10(12)} Ho _{0.92(10)} Al _{0.57(6)} Nb _{1.43(5)} O _{6.91(49)}	1.78	0.91
CaYbAl _{0.5} Nb _{1.5} O ₇	Ca _{1.05(11)} Yb _{1.01(7)} Al _{0.51(2)} Nb _{1.49(9)} O _{6.92(47)}	1.76	0.91
Sc Series			
CaLaSc _{0.5} Nb _{1.5} O ₇	Ca _{1.08(2)} La _{1.01(8)} Sc _{0.49(1)} Nb _{1.42(9)} O _{6.88(38)}	1.87	0.89
CaNdSc _{0.5} Nb _{1.5} O ₇	Ca _{1.18(3)} Nd _{1.00(9)} Sc _{0.54(1)} Nb _{1.52(11)} O _{7.29(46)}	1.77	0.90
CaSmSc _{0.5} Nb _{1.5} O ₇	Ca _{1.08(3)} Sm _{0.97(10)} Sc _{0.52(1)} Nb _{1.42(11)} O _{6.87(47)}	1.74	0.90
CaGdSc _{0.5} Nb _{1.5} O ₇	Ca _{1.13(3)} Gd _{1.00(10)} Sc _{0.49(2)} Nb _{1.45(11)} O _{6.99(49)}	1.79	0.90
CaHoSc _{0.5} Nb _{1.5} O ₇	Ca _{1.12(4)} Ho _{1.02(11)} Sc _{0.50(1)} Nb _{1.46(11)} O _{7.05(49)}	1.75	0.90
CaYbSc _{0.5} Nb _{1.5} O ₇	Ca _{1.21(5)} Yb _{0.97(12)} Sc _{0.54(2)} Nb _{1.51(10)} O _{7.25(51)}	1.69	0.91
Fe Series			
CaLaFe _{0.5} Nb _{1.5} O ₇	Ca _{1.06(4)} La _{1.08(10)} Fe _{0.68(10)} Nb _{1.48(6)} O _{7.40(49)}	1.76	0.90
CaNdFe _{0.5} Nb _{1.5} O ₇	Ca _{1.03(8)} Nd _{0.93(11)} Fe _{0.49(2)} Nb _{1.63(10)} O _{7.24(53)}	1.61	0.92
CaSmFe _{0.5} Nb _{1.5} O ₇	Ca _{0.94(10)} Sm _{0.99(11)} Fe _{0.49(1)} Nb _{1.51(5)} O _{6.94(41)}	1.65	0.92
CaGdFe _{0.5} Nb _{1.5} O ₇	Ca _{1.04(7)} Gd _{1.01(9)} Fe _{0.49(2)} Nb _{1.58(4)} O _{7.24(34)}	1.68	0.90
CaHoFe _{0.5} Nb _{1.5} O ₇	Ca _{0.98(9)} Ho _{1.06(6)} Fe _{0.50(2)} Nb _{1.57(4)} O _{7.25(31)}	1.64	0.92
CaYbFe _{0.5} Nb _{1.5} O ₇	Ca _{1.01(11)} Yb _{1.04(8)} Fe _{0.54(5)} Nb _{1.56(5)} O _{7.28(43)}	1.60	0.92
Y Series			
CaLaY _{0.5} Nb _{1.5} O ₇	Ca _{1.06(10)} La _{0.95(11)} Y _{0.54(4)} Nb _{1.53(4)} O _{7.02(43)}	1.56	0.92
CaNdY _{0.5} Nb _{1.5} O ₇	Ca _{1.02(4)} Nd _{0.96(10)} Y _{0.49(2)} Nb _{1.53(6)} O _{7.02(37)}	1.55	0.92
CaSmY _{0.5} Nb _{1.5} O ₇	Ca _{0.90(12)} Sm _{0.93(11)} Y _{0.49(1)} Nb _{1.40(5)} O _{6.58(43)}	1.50	0.93
CaGdY _{0.5} Nb _{1.5} O ₇	Ca _{1.03(10)} Gd _{1.03(10)} Y _{0.51(2)} Nb _{1.47(2)} O _{6.97(33)}	1.60	0.92
CaHoY _{0.5} Nb _{1.5} O ₇	A - Ca _{1.23(3)} Ho _{0.64(7)} Y _{0.44(3)} Nb _{1.38(10)} O _{6.30(43)}	1.51*	0.93*
	B - Ca _{1.35(3)} Ho _{0.71(7)} Y _{0.53(4)} Nb _{1.63(11)} O _{7.29(47)}		
CaYbY _{0.5} Nb _{1.5} O ₇	Ca _{0.99(8)} Yb _{0.98(4)} Y _{0.54(2)} Nb _{1.49(6)} O _{7.00(32)}	1.44	0.94

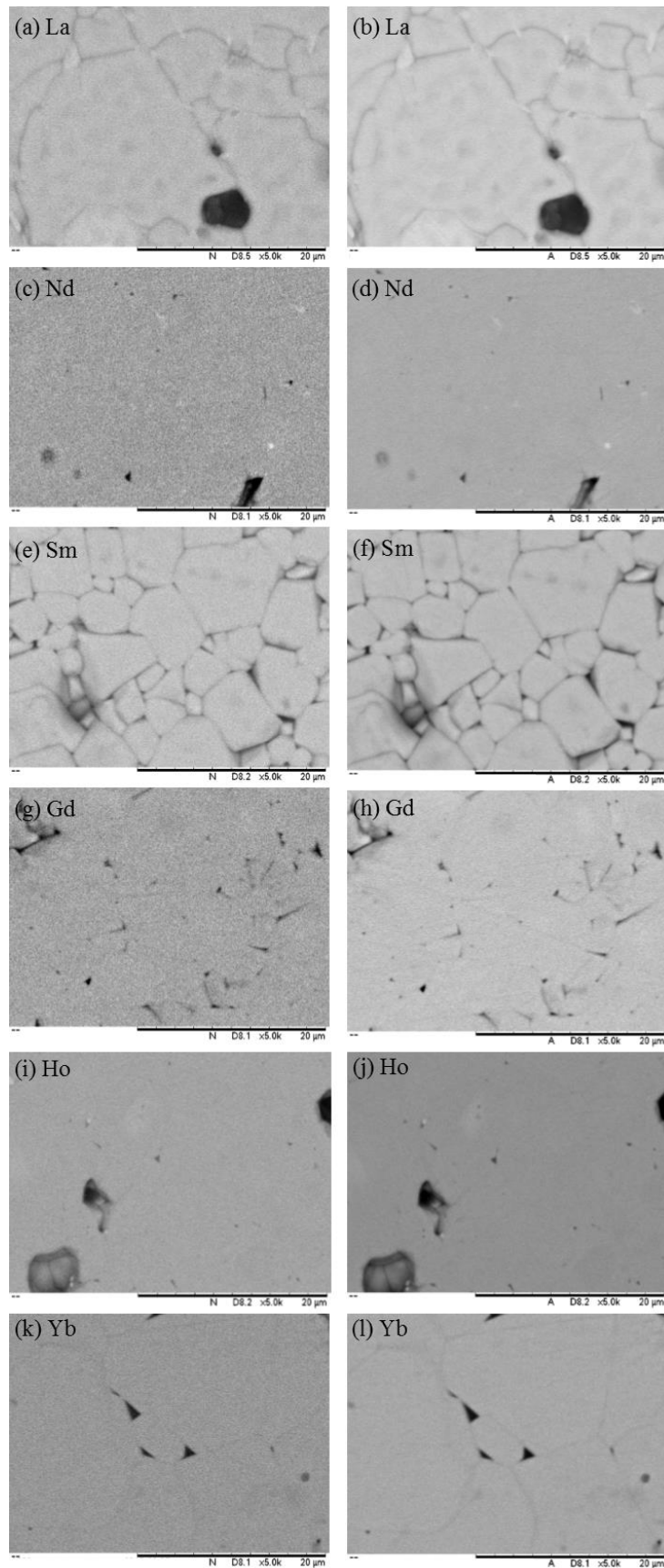


Figure 4.2: SEM images of samples with target composition $\text{CaLnFe}_{0.5}\text{Nb}_{1.5}\text{O}_7$ where Ln = La for images (a) and (b), Ln = Nd for (c) and (d), Ln = Sm for (e) and (f), Ln = Gd for (g) and (h), Ln = Ho for (i) and (j) and Ln = Yb for images (k) and (l). Images on the left are the secondary electron images and the right hand side showing the back-scattered electron micrographs of compositions.

4.3.2 X-ray Diffraction

Characterisation using X-ray diffraction was completed on the STOE STADI P, Image Plate (IP) diffractometer with a Cu $K\alpha_1$ radiation ($\lambda=1.5408\text{\AA}$) source, operating with a working voltage and current of 40kV and 35mA, respectively (see section 3.1.2.1 for full instrument details).

X-ray diffraction (XRD) describes the crystalline structure by elastic scattering of incoming X-rays on planes of the crystalline structure [59]. X-rays are insensitive to anions within the structure [59], so quantification of the 48f oxygen position of the pyrochlore structure was not determined via this technique. When the electron density of the cations on the A-site are comparable to the electron density of the cations on the B-site the X-rays are scattered similarly[51]. Due to this interaction mechanism XRD is susceptible to being unable to distinguish between cations on the A and B sites, and hence unable to identify the pyrochlore ordering. The intensity of the associated pyrochlore supercell reflections are quantified by the difference in the electron density between the two sites. For all materials the difference between the electronic density of the A and B sites have been calculated, see Table 4.5, from values summarised in Table 4.4. A small difference between the electron density means that the cations scatter the X-rays similarly and cannot be distinguished from one another.

Table 4.4: Electron density and ionic radii values for rare earth elements (REE) and transition metal cations taken from [60, 61]. Scattering and absorption cross sections for each element with thermal neutrons are also included as taken from [61].

	Ion	Charge	Ionic Radii (\AA)	Electrons	Coherent Scattering Length (barn)	Absorption cross section for 2200 M/s neutrons (barn)
Ln (VIII)	La	3+	1.160	54	9.66	8.97
	Nd		1.109	57	16.60	50.50
	Sm		1.079	59	39.00	5922.00
	Gd		1.053	61	180.00	49700.00
	Ho		1.015	64	8.42	64.70
	Yb		0.985	67	23.40	34.80
M (VI)	Al	3+	0.535	10	1.50	0.23
	Fe		0.645	23	11.62	2.56
	Sc		0.745	18	23.50	27.50
	Y		0.900	36	7.70	1.28
	Ca	2+	1.120	20	2.83	0.43
	Nb	5+	0.640	41	6.26	1.15
	O	2-	1.400	8	4.23	0.0002

Any cation ordering present is therefore not observed due to the effectively zero intensity. This may result in the material being identified as having a fluorite cell, although this is not confirmation that the pyrochlore superstructure is not present.

XRD analysis provided initial structural information for the materials, an example of the experimental data for general compositions $\text{CaLnFe}_{0.5}\text{Nb}_{1.5}\text{O}_7$ (where Ln= La, Nd, Gd, Sm, Ho or Yb) are shown in Figures 4.3. In general, all materials are indexed with the pyrochlore supercell, space group $Fd\bar{3}m$, full XRD data can be found in Appendix A. The reflections of the crystalline structure within Figure 4.3 have been indexed with respect to the pyrochlore cell. Reflections indicative of the pyrochlore structure have been highlighted through the use of an arrow. Minor additional intensities were identified but could not be indexed to an additional phase.

Table 4.5: The electron density differences calculated between the cations expected to reside on the A and B sites, Z_A and Z_B respectively, of each of the target compositions. Quoted are the valence shell for the cations as substituted on the B site within the structure.

	Target Composition	Electron Number Difference	M Cation Valence Shell
Al	$\text{CaLaAl}_{0.5}\text{Nb}_{1.5}\text{O}_7$	13.0	3p
	$\text{CaNdAl}_{0.5}\text{Nb}_{1.5}\text{O}_7$	14.5	
	$\text{CaSmAl}_{0.5}\text{Nb}_{1.5}\text{O}_7$	15.5	
	$\text{CaGdAl}_{0.5}\text{Nb}_{1.5}\text{O}_7$	16.5	
	$\text{CaHoAl}_{0.5}\text{Nb}_{1.5}\text{O}_7$	18.0	
	$\text{CaYbAl}_{0.5}\text{Nb}_{1.5}\text{O}_7$	19.5	
Fe	$\text{CaLaFe}_{0.5}\text{Nb}_{1.5}\text{O}_7$	6.5	3d
	$\text{CaNdFe}_{0.5}\text{Nb}_{1.5}\text{O}_7$	8.0	
	$\text{CaSmFe}_{0.5}\text{Nb}_{1.5}\text{O}_7$	9.0	
	$\text{CaGdFe}_{0.5}\text{Nb}_{1.5}\text{O}_7$	10.0	
	$\text{CaHoFe}_{0.5}\text{Nb}_{1.5}\text{O}_7$	11.5	
	$\text{CaYbFe}_{0.5}\text{Nb}_{1.5}\text{O}_7$	13.0	
Sc	$\text{CaLaSc}_{0.5}\text{Nb}_{1.5}\text{O}_7$	9.0	3d
	$\text{CaNdSc}_{0.5}\text{Nb}_{1.5}\text{O}_7$	10.5	
	$\text{CaSmSc}_{0.5}\text{Nb}_{1.5}\text{O}_7$	11.5	
	$\text{CaGdSc}_{0.5}\text{Nb}_{1.5}\text{O}_7$	12.5	
	$\text{CaHoSc}_{0.5}\text{Nb}_{1.5}\text{O}_7$	14.0	
	$\text{CaYbSc}_{0.5}\text{Nb}_{1.5}\text{O}_7$	15.5	
Y	$\text{CaLaY}_{0.5}\text{Nb}_{1.5}\text{O}_7$	0.0	4d
	$\text{CaNdY}_{0.5}\text{Nb}_{1.5}\text{O}_7$	1.5	
	$\text{CaSmY}_{0.5}\text{Nb}_{1.5}\text{O}_7$	2.5	
	$\text{CaGdY}_{0.5}\text{Nb}_{1.5}\text{O}_7$	3.5	
	$\text{CaHoY}_{0.5}\text{Nb}_{1.5}\text{O}_7$	5.0	
	$\text{CaYbY}_{0.5}\text{Nb}_{1.5}\text{O}_7$	6.5	

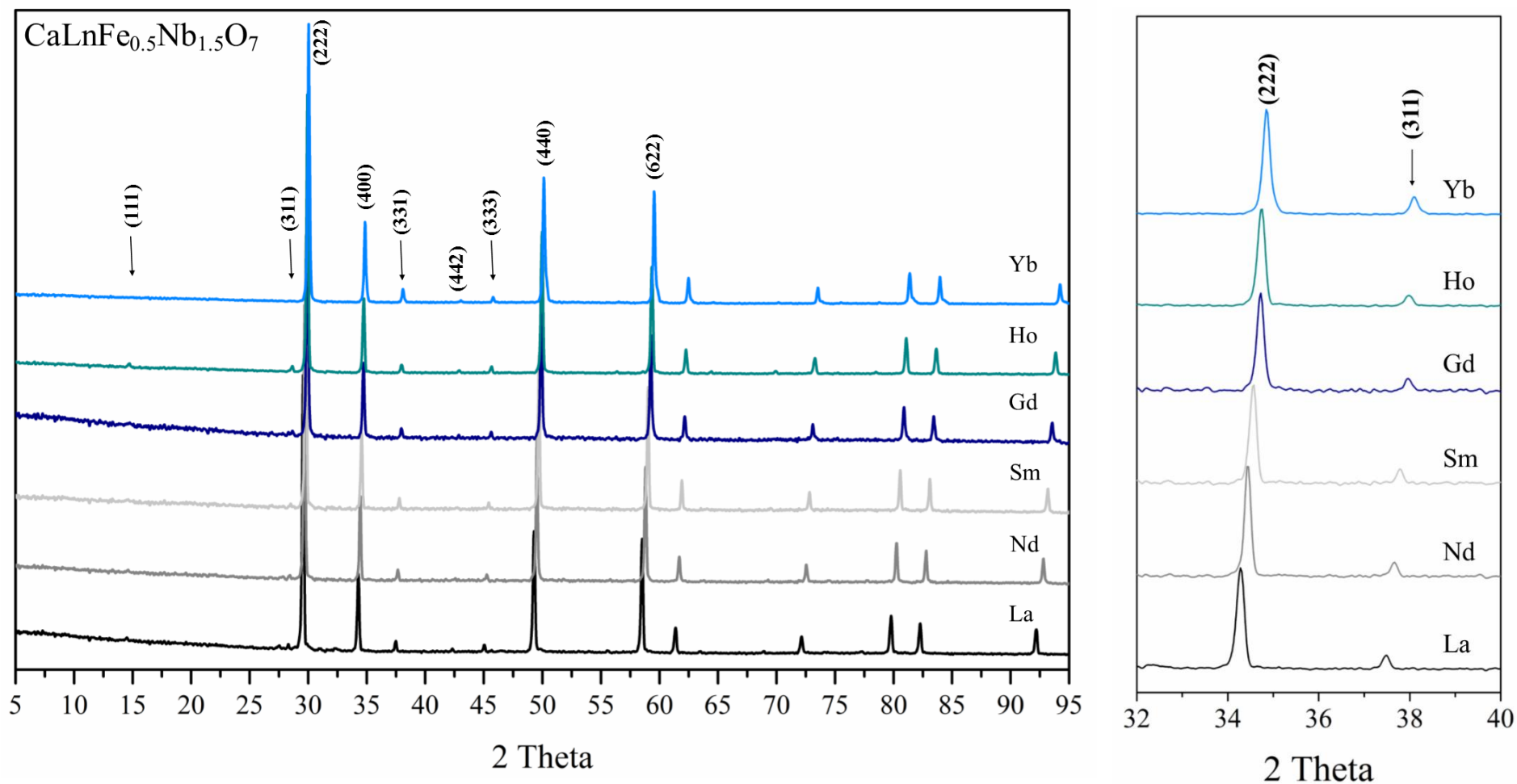


Figure 4.3: X-ray diffraction data for materials with target compositions $\text{CaLnFe}_{0.5}\text{Nb}_{1.5}\text{O}_7$, where Ln= La, Nd, Sm, Gd, Ho or Yb, Reflections indicative of the pyrochlore superstructure are highlighted by the arrow in the figure. (Right) magnification of the (311) pyrochlore reflection within the materials.

4.3.3 Neutron Diffraction

Neutron diffraction analysis enabled both the identification of the two distinct cation sites and analysis of the 48f oxygen position. This is due to the fact that the neutrons scatter directly off the nucleus of the atom. This also means that neutron diffraction is sensitive to locating both cations and anions within the material. Scattering cross sections (Table 4.4) show the comparative scattering cross section of oxygen with heavier lanthanide (Ln) cations. This enables analysis of the shift in the 48f oxygen x-parameter with the compositional variations. The highly absorbing nature of gadolinium and samarium rare earth elements (REE) in a neutron rich environment is an advantage when discussing the long term passively safe storage of actinide materials. However, as a result neutron diffraction analysis could not be completed on materials containing these cations, and they have therefore been excluded from neutron diffraction measurements.

4.3.3.1 Lattice parameter analysis

Accurate structural analysis requires the use of a high resolution technique such as neutron diffraction. Analysis was completed on the High Resolution Powder Diffractometer (HRPD) instrument at ISIS, Harwell. Time of flight (TOF) neutron diffraction data were acquired at room temperature in a cylindrical vanadium can with a 15mm diameter. The collection chamber is evacuated prior to analysis, this reduces the probability of neutrons scattering prior to interaction with the sample. Rietveld refinement analysis was completed on data collected using the backscattered detector which has a d-spacing range of $\sim 0.6\text{-}4.6\text{\AA}$ (TOF 30-230ms) and a resolution ($\Delta d/d$) of up to $\sim 5 \times 10^{-4}$.

The pyrochlore structural model has been refined in GSAS to fit the data collected [62, 63]. An example of the fitting of the model to the data achieved is shown in Figure 4.4. This is representative of all materials identified to have a single phase assemblage. The neutron diffraction patterns can be found in Appendix A. Refined structural parameters are summarised in Table 4.7. The refinement has been taken from the theoretical model of composition $(\text{CaNd})^{2.5+}\text{Nb}^{5+}_2\text{O}_7$, values have been included in Table 4.6 [64]. Cation sites with shared occupancy have had their thermal parameters constrained to be equal due to sharing the same crystallographic site.

Analysis of the samples within Table 4.5 show that as the ionic radii of the substituted cation A-site decreases, the a-parameter decreases. Figure 4.5 shows the change in the refined cell for materials with target compositions $\text{CaLnFe}_{0.5}\text{Nb}_{1.5}\text{O}_7$ where Ln = La, Nd, Ho or Yb.

The pyrochlore structure is cubic, and described entirely by a single lattice parameter (the a-parameter) and the x-parameter of the 48f oxygen. Figure 4.5 shows refined neutron diffraction data of the materials with compositions $\text{Ca}(\text{Ln})\text{Fe}_{0.5}\text{Nb}_{1.5}\text{O}_7$ (where Ln = La, Nd, Ho, or Yb). This indicated that as the size of the lanthanide decreases, between 1.16 Å (La) and 0.985 Å (Yb), the unit cell contracts. Further analysis of the variation in the refined parameters as a function of chemical composition for all materials can be found in Section 4.3.3.2.

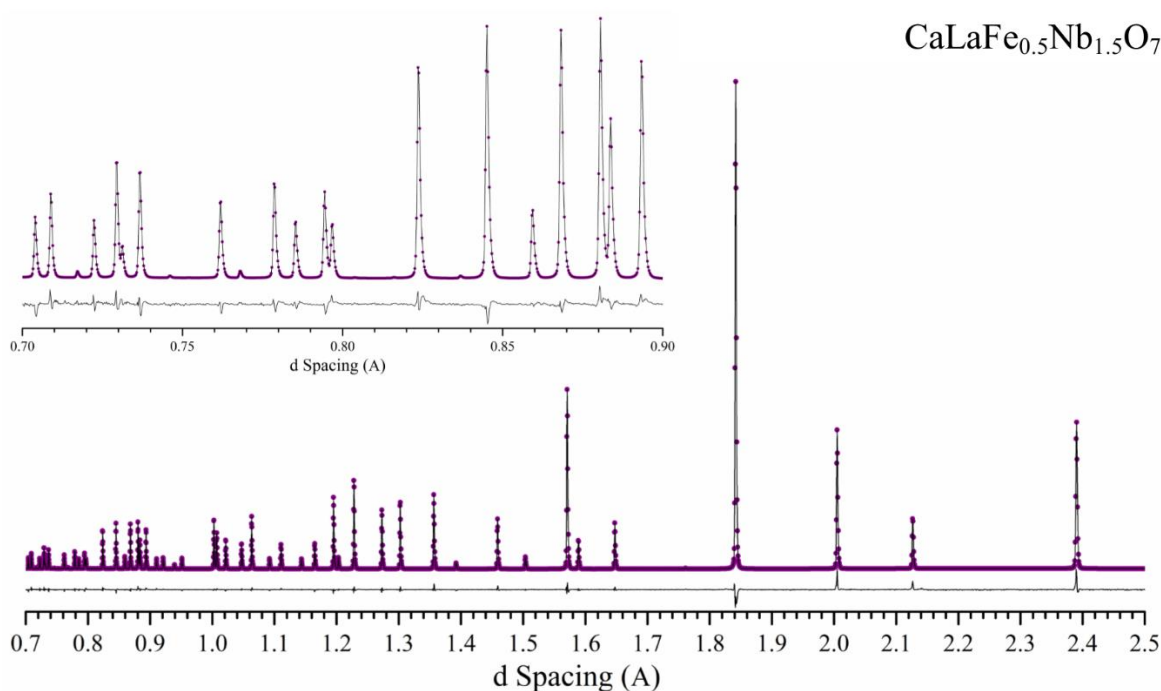


Figure 4.4: Rietveld refinement fitting to neutron diffraction data collected on the sample $\text{CaLaFe}_{0.5}\text{Nb}_{0.5}\text{O}_7$ on the High Resolution Powder Diffractometer (HRPD). The figure shows the pyrochlore model fitted to the data. The difference trace is also shown within the figure to highlight the quality of the fit (actual-calculated). Insert: Magnification of low d-spacing to highlight the fitting quality.

For a cubic system, the position in d-space of the reflections are related to the unit cell parameter by Equation 4.5:

$$\frac{1}{d^2} = \frac{h^2 + k^2 + l^2}{a^2} \quad \text{Equation 4.5}$$

Where h, k, l are the miller indices of the reflections. This describes the relationship between the a-parameter and d spacing in the crystal structure of a cubic cell; as the a-parameter is reduced, there will be a systematic decrease in the d-spacing.

Reference material for the refinement was taken from Istomin et al. [64] of composition $\text{CaNdNb}_2\text{O}_7$, a material with a refined pyrochlore structure. All compositions were refined from the starting parameters of the $\text{CaNdNb}_2\text{O}_7$ material, including multiphase materials.

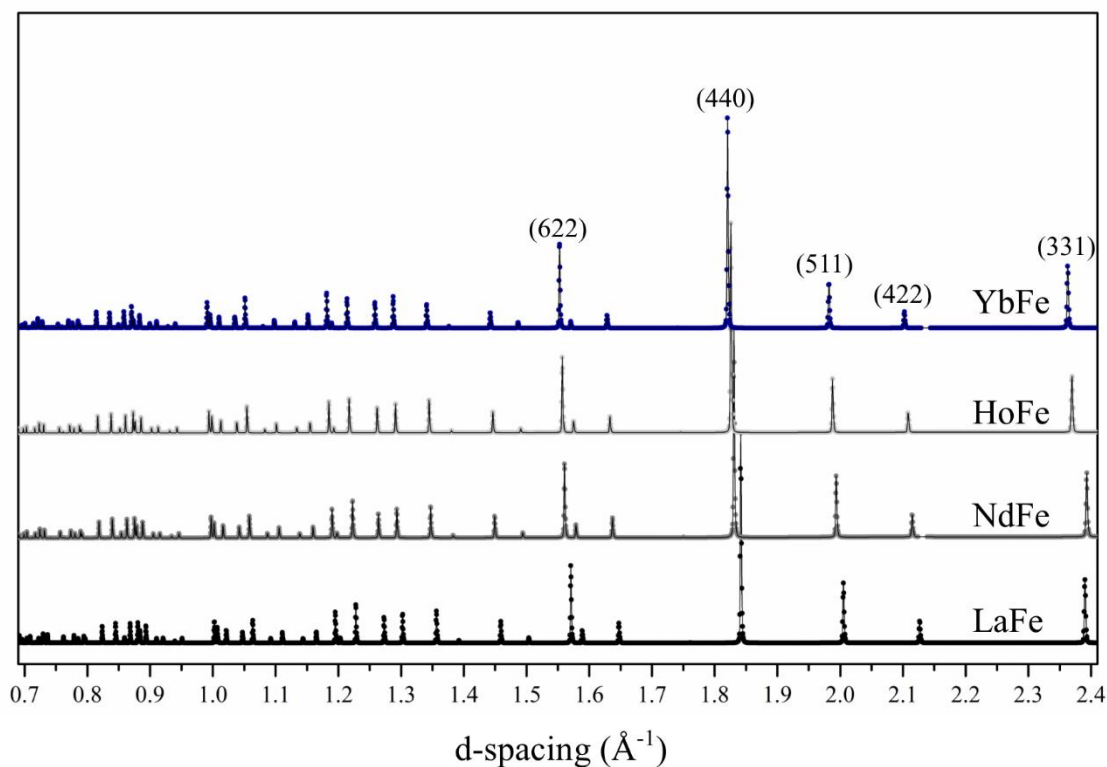


Figure 4.5: Rietveld refinement fitting of neutron diffraction data collected on the Fe series, compositions $\text{Ca}(\text{La}, \text{Nd}, \text{Ho} \text{ or } \text{Yb})\text{Fe}_{0.5}\text{Nb}_{1.5}\text{O}_7$ on the High Resolution Powder Diffractometer (HRPD) collected at ISIS, Harwell.

4.3.3.2 Tuning the structure through the r_A/r_B ratio

By systematic substitution on both the A-site and B-site it is possible to tune the pyrochlore structure. All materials synthesised with a single phase pyrochlore structure have been analysed. As a function of composition, analysis of the variation in the a-parameter (Figure 4.6 and Figure 4.7) and the 48f oxygen x-parameter (Figure 4.8) have been conducted.

The r_A/r_B ratios were calculated based on the measured composition which was obtained from the EDS analysis in Table 4.3. Trends have been extracted from the analysis of single phase materials only; multiphase materials were excluded from the analysis. The pyrochlore structure has the general formula $\text{A}^{3+}_2\text{B}^{4+}_2\text{O}_7$ and is stable when the r_A/r_B ratio is within the range, 1.46-1.78. For materials with general composition $\text{A}^{2+}\text{A}^{3+}\text{B}_{1.5}^{5+}\text{B}_{0.5}^{3+}\text{O}_7$ the r_A/r_B ratios from compositions may not follow the same trend, with materials synthesised here falling within a r_A/r_B range of 1.50-1.87. The mixed cation

site occupancy, resulting in the need to take an average ionic radii / charge to represent the A and B sites, may not be compatible with the ionic radius ratio range. EDS analysis showed a single phase material with a r_A/r_B ratio out width of the boundary. Alternatively, the tolerance factor, which describes the polyhedra of the pyrochlore structure (Equation 4.4) was used. This established if the ionic radii on the A and B-sites would result in the distortion of the polyhedra indicative of the pyrochlore structure (Table 4.3).

Analysis of the a-parameter (Figure 4.6) shows the correlation between the r_A/r_B ratio and the a-parameter. Similarly, Figure 4.7 shows the correlation between the tolerance factor and the a-parameter. Both of these indicated a dependence on the B-site cation (M= Al, Sc, Fe, Y). Included in Table 4.5 are the valence shells of the B-site cation, it is noted that Fe and Sc have the same valence shell. Figure 4.6 shows elements iron and scandium, both with a 3d valence shell, following the same linear trend when describing the relationship of the a-parameter to r_A/r_B . A similar trend was identified in Figure 4.7, however, generally as the size of the cation on the A site decreases (lanthanum to ytterbium), the tolerance factor increases and the a-parameter decreases.

The same relationship between 48f oxygen x-parameter (Figure 4.8) and r_A/r_B ratio is not observed. There is a discrete linear relationship and an increase in the 48f oxygen x-parameter is seen with an increase in the r_A/r_B ratio. Materials with a larger A-site cation and smaller B-site cation have the largest 48f oxygen x-parameter; materials with the smallest A-site cation and the largest B-site cation have the smallest 48f oxygen x-parameter.

The linear relationship between the lanthanide, the a-parameter and 48f oxygen x-parameter have been used to calculate approximate structural parameters of the gadolinium and samarium containing materials. This was calculated with consistent metal cation (Al, Fe, Sc, or Y) in order to ensure the crystallographic changes are solely down to the change in the A-site cation. This has been calculated assuming, with a singular change within the composition, the a-parameter and 48f oxygen x-parameter will behave linearly (as shown in Figures 4.6, 4.7 and 4.8). Figure 4.9 shows the relationship for the Fe containing materials, with Table 4.7 summarising the calculated values for all compositions.

It is noted that the error within the r_A/r_B values is a product of the error in the measured cation ratios from EDS analysis and the error within the ionic radii value (taken from Shannon [60]). The error was not included within figures which use the r_A/r_B values as these dominate the graph.

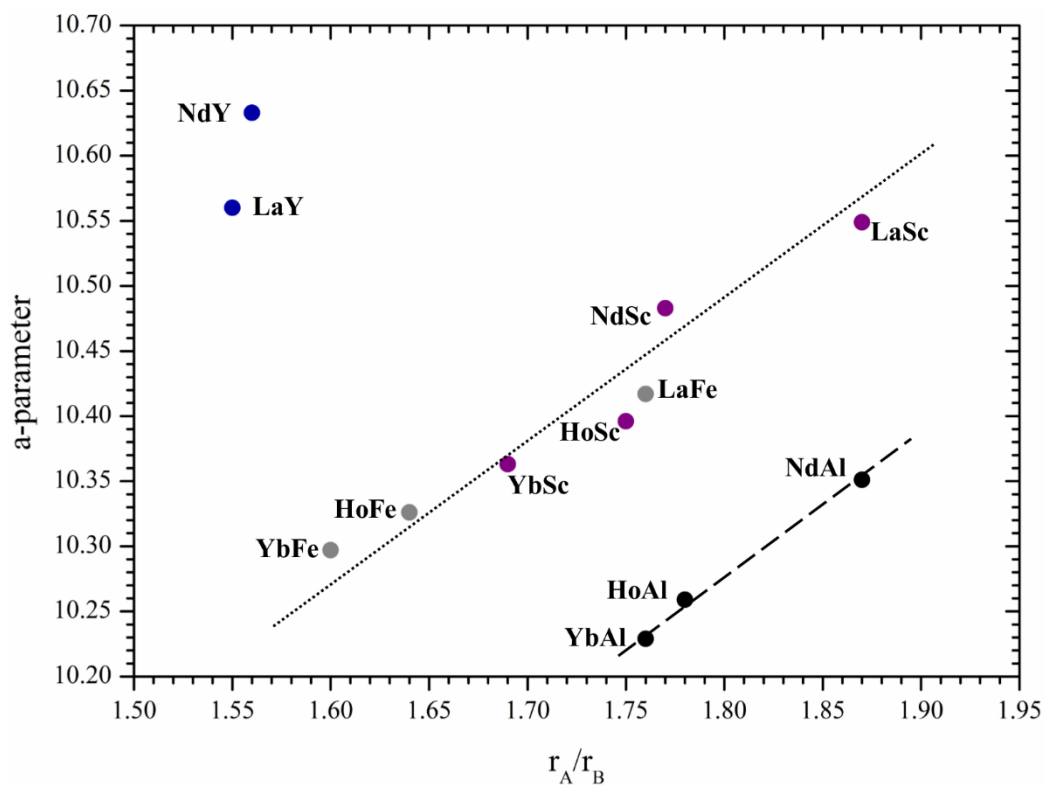


Figure 4.6: A graph of the r_A/r_B ratio plotted against the a-parameter of materials as refined from the Rietveld refinement of the pyrochlore model to High Resolution Powder Diffractometer (HRPD) data using the GSAS software. The error within the a-parameter are to small to be seen on the scale of the figure.

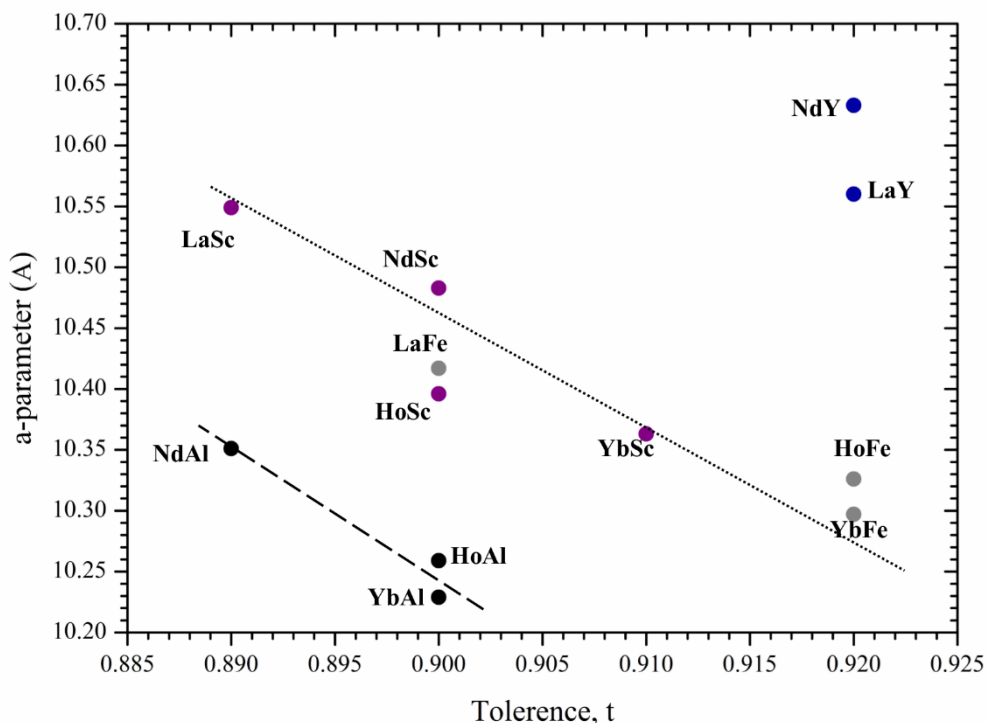


Figure 4.7: A graph of the tolerance factor (t) plotted against the a-parameter of materials as refined from the Rietveld refinement of the pyrochlore model to High Resolution Powder Diffractometer (HRPD) data using the GSAS software. The error within the a-parameter are to small to be seen on the scale of the figure.

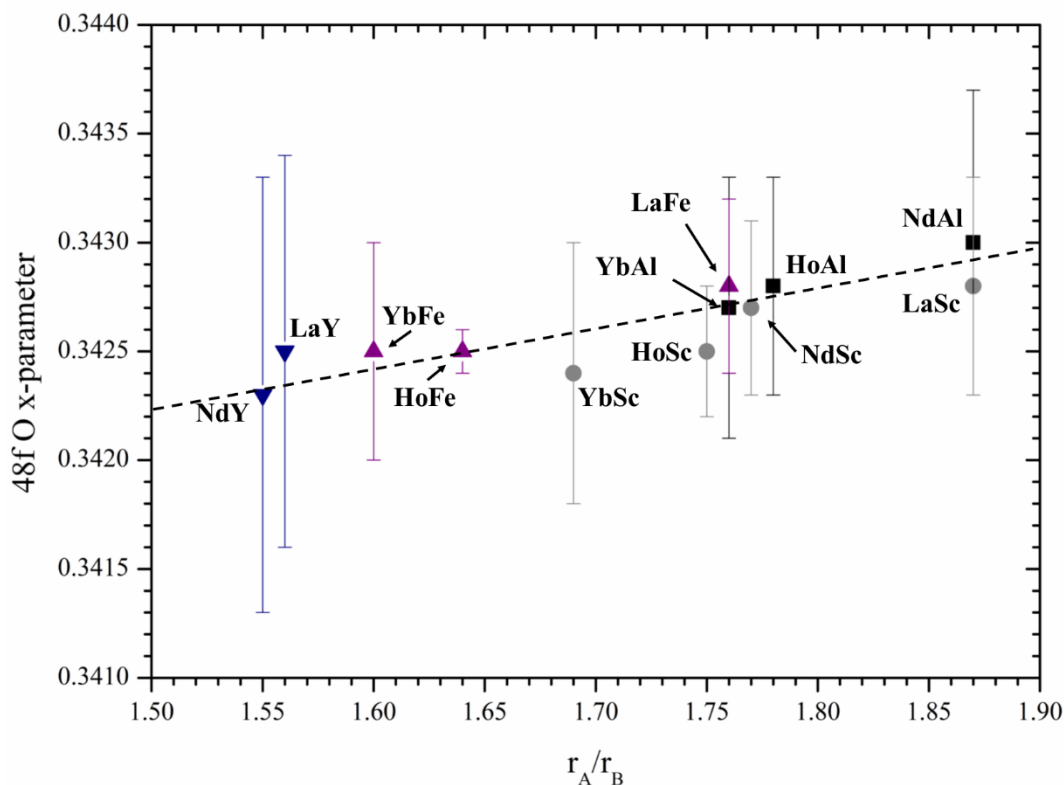


Figure 4.8: r_A/r_B ratio plotted against the x-parameter of the 48f oxygen. Values are taken from the Rietveld refinement of neutron diffraction data.

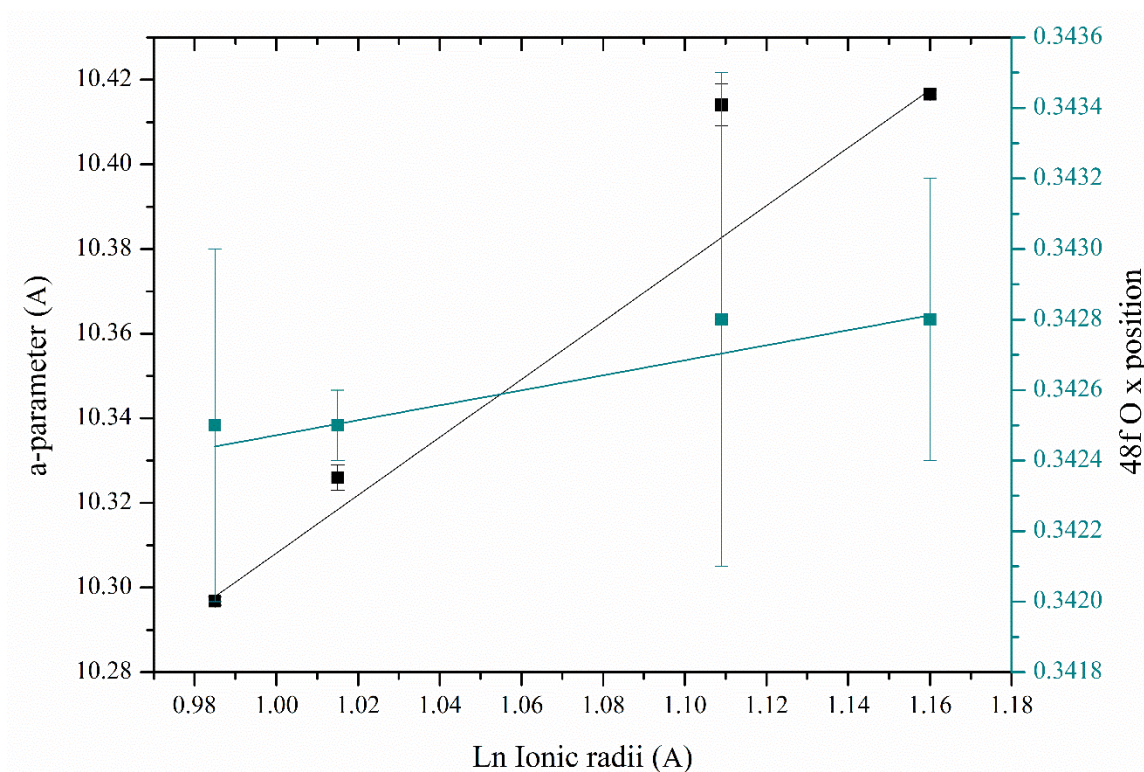


Figure 4.9: Linear relationship between the refined 48f oxygen x-parameter and a-parameter for compositions the in $\text{CaLnFe}_{0.5}\text{Nb}_{1.5}\text{O}_7$ system, where Ln=La, Nd, Ho or Yb.

Table 4.6: Unit cell parameter ‘a’ and 48f oxygen x-position, and structural parameters U_{iso} and bond lengths, as determined from neutron diffraction analysis of data collected on the HRPD instrument. Rietveld refinement was performed using the GSAS software package. The errors for the parameters are as determined using standard deviation estimations in the results calculated by the GSAS software[62, 63]. Reference material is taken from [64].

Ln	M	a-parameter (Å)	48f-O x- parameter	χ^2	wRp	U_{iso} (x100Å ²)				Bond Length (Å)		
						Ca & Ln	M & Nb	O ₁	O ₂	A-O ₁ (x2)	A-O ₂ (x6)	B-O ₂ (x6)
La	Al	10.32(2)	0.3429(3)	1.101	0.060	7.79(3)	1.61(1)	1.56(2)	1.60(1)	2.597(2)	2.234(1)	1.966(1)
Nd		10.351(2)	0.3430(7)	2.774	0.066	1.06(2)	1.08(2)	1.06(1)	0.50(4)	2.609(1)	2.241(1)	1.969(3)
Ho		10.259(1)	0.3428(5)	2.275	0.047	1.17(2)	1.20(3)	1.14(2)	0.63(3)	2.570(3)	2.221(1)	1.960(2)
Yb		10.229(1)	0.3427(6)	2.171	0.051	1.19(2)	0.90(2)	0.93(1)	0.47(3)	2.559(4)	2.215(1)	1.956(2)
La	Fe	10.417(1)	0.3428(4)	2.670	0.049	1.29(2)	1.00(2)	0.97(2)	0.66(3)	2.611(3)	2.255(1)	1.989(2)
Nd		10.413(5)	0.3428(7)	3.488	0.064	1.14(5)	0.87(4)	1.01(3)	0.73(4)	2.611(5)	2.255(1)	1.989(3)
Ho		10.326(3)	0.3425(1)	2.592	0.043	1.08(2)	1.01(2)	1.13(2)	0.65(3)	2.572(3)	2.236(1)	1.981(2)
Yb		10.297(1)	0.3425(5)	3.190	0.054	1.41(2)	1.07(2)	1.29(1)	0.86(3)	2.560(4)	2.229(1)	1.978(2)
La	Sc	10.549(2)	0.3428(5)	2.338	0.055	1.17(3)	0.87(3)	1.07(3)	0.60(3)	2.649(4)	2.284(1)	2.012(2)
Nd		10.483(1)	0.3427(4)	3.188	0.047	1.14(2)	1.06(1)	1.266(9)	0.696(3)	2.621(3)	2.270(1)	2.006(2)
Ho		10.396(6)	0.3425(3)	1.259	0.055	1.02(4)	0.88(2)	1.39(1)	0.50(4)	2.592(6)	2.251(1)	1.998(3)
Yb		10.363(1)	0.3424(6)	2.469	0.053	1.46(3)	1.04(2)	1.72(3)	0.72(4)	2.567(5)	2.244(1)	1.996(3)
La	Y	10.633(8)	0.3425(9)	2.476	0.051	1.12(2)	1.14(2)	2.69(2)	0.50(4)	2.648(6)	2.302(1)	2.041(4)
Nd		10.560(9)	0.342(1)	2.152	0.048	1.21(5)	0.69(5)	2.94(6)	0.29(6)	2.609(1)	2.286(1)	2.038(5)
Ho		*See Appendix A										
Yb		*See Appendix A										
Reference		10.437	0.3259	-	-	1.7	0.8	1.1	1.0	2.590	2.260	2.008

Table 4.7: Calculated 48f oxygen x-parameter and a-parameter for samarium and gadolinium containing materials from linear fitting of measured materials, graphs within Appendix A. *These fittings have been calculated from two data point only and therefore no standard deviation is presented.

Ln	M	a-parameter (Å)	48f oxygen x-parameter
Sm	Al	10.352(9)	0.3429(5)
Gd		10.326(9)	0.3429(5)
Sm	Sc	10.5(1)	0.3426(3)
Gd		10.4(1)	0.3426(3)
Sm	Fe	10.4(3)	0.3426(5)
Gd		10.4(3)	0.3425(5)
Sm	Y*	10.517	0.3422
Gd		10.480	0.3421

4.4 In-situ irradiation of materials with composition $\text{CaLnFe}_{0.5}\text{Nb}_{1.5}\text{O}_7$

Radiation damage in target compositions $\text{CaLnFe}_{0.5}\text{Nb}_{1.5}\text{O}_7$ (where Ln = La, Nd, Sm, Gd, Ho or Yb), as a result of the natural decay of radioactive species, has been experimentally simulated. The aim of this work is to establish the response of the materials due to the in-situ irradiation with a single change in the A-site cation. Ions were implanted into samples with enough energy to displace atoms within the structure. This simulates the effect of recoil energy within the parent atom of an alpha-decay event, which typically have an energy of 70-100 keV [65].

The fluence (ions per unit area, ions cm^{-2}) required to render a material fully amorphous, termed the critical amorphisation fluence (F_C), has been determined experimentally at specific temperatures (T). The extrapolation of the F_C at zero kelvin is denoted as F_{C0} . Though incremental addition of fluence the change in the crystallinity of the material is monitored using electron diffraction, until a fully amorphous material is identified. Amorphisation here is defined as the point at which no pair of Bragg reflections are visible in the selected area zone axis diffraction pattern. This indicates a complete loss of crystalline ordering. The effects of temperature on damage / recovery are described by Equation 4.6, as developed by Weber, Wang and Meldrum [66-68]:

$$F_C = \frac{F_{C0}}{1 - \exp\left[\left(\frac{E_a}{k_b}\right)\left(\frac{1}{T_C} - \frac{1}{T}\right)\right]}$$

Equation 4.6

Where T_C , the critical temperature, is defined as the temperature at which the recovery rate is equal to the damage rate. Hence, above this temperature the material remains crystalline even when subjected to radiation induced damage. The activation energy for recovery is denoted as E_a (thermal recovery of the material in eV), and k_b is Boltzmann's constant ($1.381 \times 10^{-23} \text{ m}^2 \text{ kg s}^{-2} \text{ K}^{-1}$). For the data analysed here, T_C , F_{C0} and E_a were determined using least square numerical analysis of the obtained F_c and T results, Table 4.8.

4.4.1 Experimental Set Up

Samples of material were irradiated at the IVEM-TANDEM facility, Argonne National Laboratory, using a Hitachi 9000-NAR transmission electron microscope (TEM), operating at an accelerating voltage of 300kV, coupled to a Danfysik ion implanter. The sample stage of the TEM was able to electrically heat or cryogenically cool samples to a specific temperature prior to the analysis. A 1 MeV Kr^{2+} ion beam with a flux of $6.125 \times 10^{11} \text{ ions cm}^{-2} \text{ sec}^{-1}$ was used for the irradiations. Samples were prepared by loading crushed powders onto holey carbon films supported by a copper grid for analysis at low temperature. A molybdenum grid was used at high temperatures $>800\text{K}$. This was in order to prevent copper contamination on the sample. Controlling and maintaining the temperature during irradiation ensured that the thermal kinetics of recovery in the material were stabilised.

The Danfysik ion implanter was angled at 30° to the vertical to the electron beam, with the sample stage angled at 15° , reducing the shadowing effect and maximise the area which the ion beam and electron beam both interact on the sample surface (see Figure 4.10).

Analysis was performed on individual grains, with electron diffraction images taken on each of the selected grains at incremental steps during the irradiation. An example of this can be seen for a single grain of $\text{CaGdFe}_{0.5}\text{Nb}_{1.5}\text{O}_7$ in Figure 4.11. The response of five individual grains in each sample were studied at each temperature. Data in Table 4.8 shows the average fluence at which all 5 grains became amorphous, with the errors reflecting the standard deviation in the values. During irradiation the electron beam was turned off to ensure any interactions between electron and ion beams were eliminated. Similarly, electron diffraction images were taken in the absence of the ion beam.

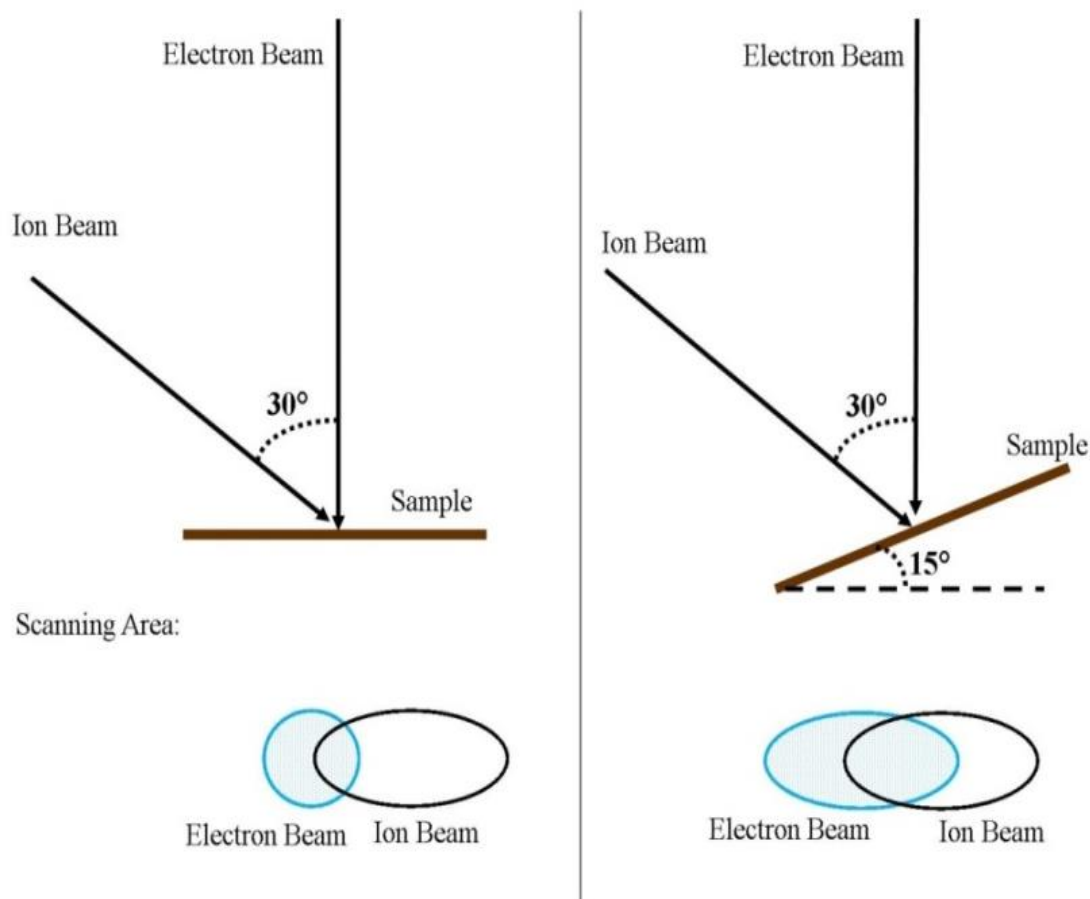


Figure 4.10: (Not to scale) Schematic image of the Danfysik ion beam and Hitachi 300kV TEM electron beam set relative to the sample stage.

4.4.2 Material Analysis

Electron diffraction images were collected on axis which enabled the identification of both the fluorite subcell and pyrochlore supercell, Figure 4.11 shows the $[331]_F$ zone axis of material with target composition $\text{CaGdFe}_{0.5}\text{Nb}_{1.5}\text{O}_7$. The fluorite sub-lattice is identified by the F subscript in the annotated TEM image. The presence of sharp reflections, such as those labelled in Figure 4.11, indicate the presence of the ordered fluorite substructure. These reflections describe the reciprocal lattice of the general fluorite matrix, G_F . They are surrounded by additional sharp reflections highlighting an ordered cation / anion super-lattice, indicative of the pyrochlore super cell. These additional reflections are described using the modulation vector 'q', relating the additional scattered energy to the underlying super-lattice through the use of $G_F \pm q$. The sharp reflections indicated by the arrows in Figure 4.11, are at the $G_F \pm 1/2(2-20)^*$ pyrochlore super lattice positions, as observed down the $[331]_F$ zone axis. Prior to irradiation electron diffraction analysis on multiple grains was completed. This confirmed

that the material being analysed had the pyrochlore structure, and this was identifiable in the fixed sample holder position. For imaging quality the transmitted beam has been shielded to aid the visibility of the long range structure reflections. A loss of intensity in the reflections indicates the likely loss of ordering in the crystal structure. The appearance of a halo around the primary transmitted reflection is consistent with the formation of amorphous material, as shown by Wang et al. [69]. A complete loss of crystal structure is identified by a lack of paired Bragg reflections, this is associated with a critical fluence, F_c . Fluence is increased in order to monitor the structural development as a functions of induced damage. Analysis of the materials respective electron diffraction patterns highlight that as damage is induced, the crystal structure is replaced by a region of amorphous material. Damage induced in a crystalline material with the pyrochlore structure can result in either a loss in the reflections related to the pyrochlore super lattice and a pyrochlore to fluorite transition occurs, or a complete loss of crystallinity with a direct pyrochlore to amorphous transition [11, 26, 70-73].

Table 4.8: Critical fluence calculated from an average of 5 individual grains of each composition.

Target Composition	Critical Fluence ($\times 10^{14}$ ions cm^{-2}) at indicated temperature (K)					
	300K	500K	900K	1050K		
CaLaFe _{0.5} Nb _{1.5} O ₇	2.44 ± 0.31	2.34 ± 0.47	5.38 ± 0.63	9.69 ± 0.72		
CaNdFe _{0.5} Nb _{1.5} O ₇	3.69 ± 0.31	6.25 ± 0.63	7.88 ± 1.38			
CaSmFe _{0.5} Nb _{1.5} O ₇	3.31 ± 0.56	3.94 ± 0.31	4.44 ± 0.31	10.30 ± 1.25	16.60 ± 1.88	
CaGdFe _{0.5} Nb _{1.5} O ₇	2.50 ± 1.25	2.94 ± 0.31				
CaHoFe _{0.5} Nb _{1.5} O ₇	3.13 ± 0.63	2.75 ± 0.75	4.13 ± 0.63	10.50 ± 1.41	16.30 ± 1.33	
CaYbFe _{0.5} Nb _{1.5} O ₇	3.13 ± 0.31	4.79 ± 0.63	3.75 ± 0.63	5.00 ± 1.25	6.75 ± 1.25	∞

Analysis of materials CaLnFe_{0.5}Nb_{1.5}O₇ (where Ln = La, Nd, Sm, Gd, Ho or Yb) showed a transition from a pyrochlore to amorphous structure without an intermediate fluorite

structure. This was identified by the weakening of the reflection intensities simultaneously (pyrochlore supercell and fluorite), and the formation of an amorphous halo.

In-situ irradiation analysis was completed on samples of material with target compositions $\text{CaLnFe}_{0.5}\text{Nb}_{1.5}\text{O}_7$ (where Ln = La, Nd, Gd, Sm, Ho or Yb). Materials were all irradiated first at 300K, the progression (step size) of the temperature (T) varied depending on the materials response to the irradiation at 300K. The critical fluence at each temperature was determined, see Table 4.8. The critical temperature, T_c has been extrapolated from the curve fitting for the systems where Ln = La, Sm, Ho or Yb using Equation 4.6. The variables E_a , T_c and F_{c0} are shown in Table 4.9 for the fitted curves in Figure 4.12. Critical temperature values (T_c) were calculated by taking a tangent to the vertical part of the fitted curve. The critical fluence at T=0K (T_{c0}) has been calculated by taking a tangent to the horizontal part of the curve.

Figure 4.13 shows the structural changes, as a function of composition, described using the refined parameters within Table 4.6, as a function of the critical temperature. The a-parameter and the 48f oxygen x-parameter for the Sm containing sample have been taken from the calculated parameters in Table 4.7. It can be seen that there is a small correlation between the a-parameter and the critical temperature determined for the materials. With an increase in the a-parameter a corresponding increase in the critical temperature was observed. However, there is minimal variation in the 48f oxygen x-parameter and therefore no correlation with the critical temperature.

Table 4.9: Critical temperature (T_c), critical fluence at zero kelvin (F_{c0}) and activation energy (E_a) as calculated for target compositions $\text{CaLnFe}_{0.5}\text{Nb}_{1.5}\text{O}_7$ (where Ln= La, Sm, Ho, or Yb).

Target Composition	Measured r_A/r_B	48f oxygen x-parameter	a-parameter (Å)	T_c (K)	F_{c0} (ions cm^{-2})	E_a (eV)
$\text{CaLaFe}_{0.5}\text{Nb}_{1.5}\text{O}_7$	1.76	0.3428(4)	10.417(1)	1269 (17)	2.24 (27)	0.15 (3)
$\text{CaSmFe}_{0.5}\text{Nb}_{1.5}\text{O}_7$	1.65	0.3428(7)	10.4(3)	1102 (15)	3.31 (30)	0.20 (4)
$\text{CaHoFe}_{0.5}\text{Nb}_{1.5}\text{O}_7$	1.64	0.3425(1)	10.326(3)	755 (9)	2.79 (25)	0.15(2)
$\text{CaYbFe}_{0.5}\text{Nb}_{1.5}\text{O}_7$	1.60	0.3425(5)	10.297(1)	682 (10)	3.68 (22)	0.24(4)

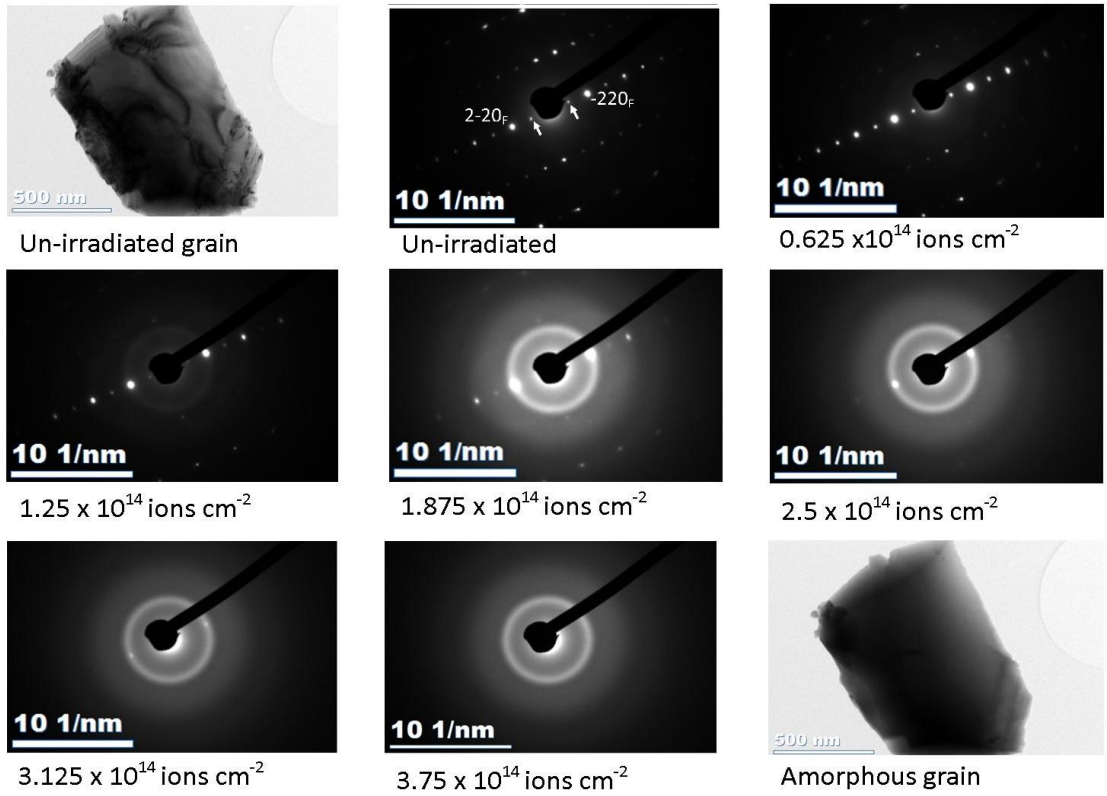


Figure 4.11: [311] zone axis diffraction pattern from a grain of $\text{CaGdFe}_{0.5}\text{Nb}_{1.5}\text{O}_7$ with irradiation transitions at a constant temperature of 300K. Images show the effect on the crystalline structure in the electron diffraction images within increasing fluence (ions cm^{-2}).

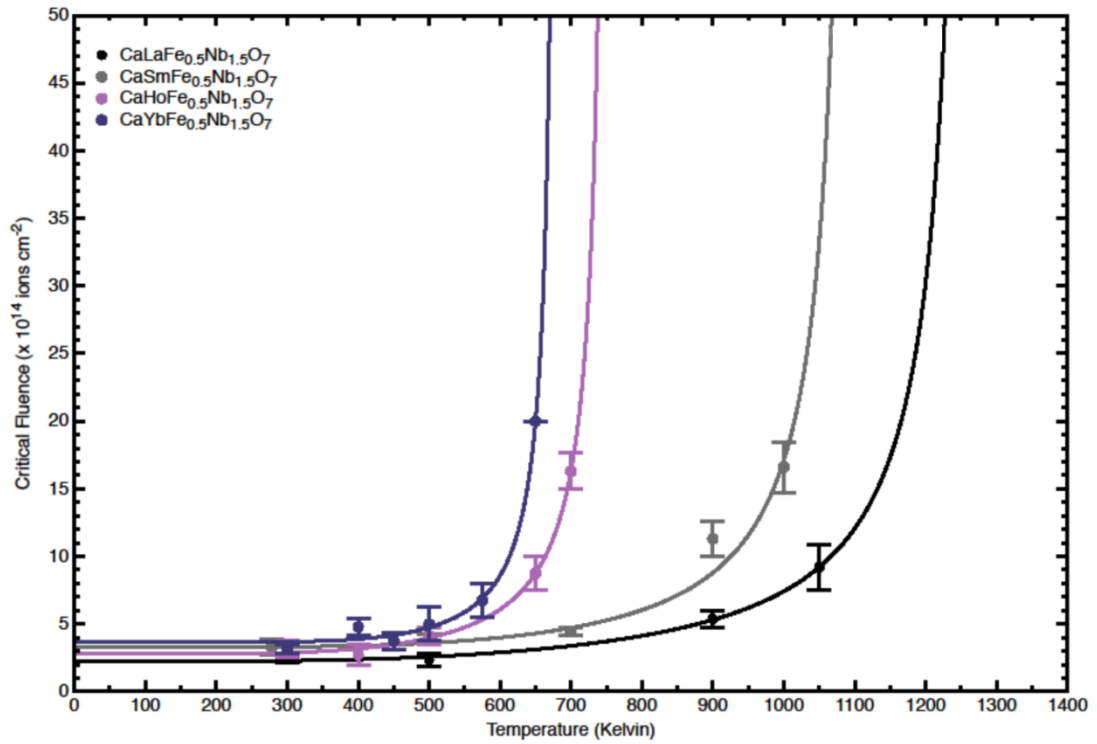


Figure 4.12: Critical temperature (T_c) curves for materials of target compositions $\text{CaLnFe}_{0.5}\text{Nb}_{1.5}\text{O}_7$ (where $\text{Ln} = \text{La, Sm, Ho, or Yb}$).

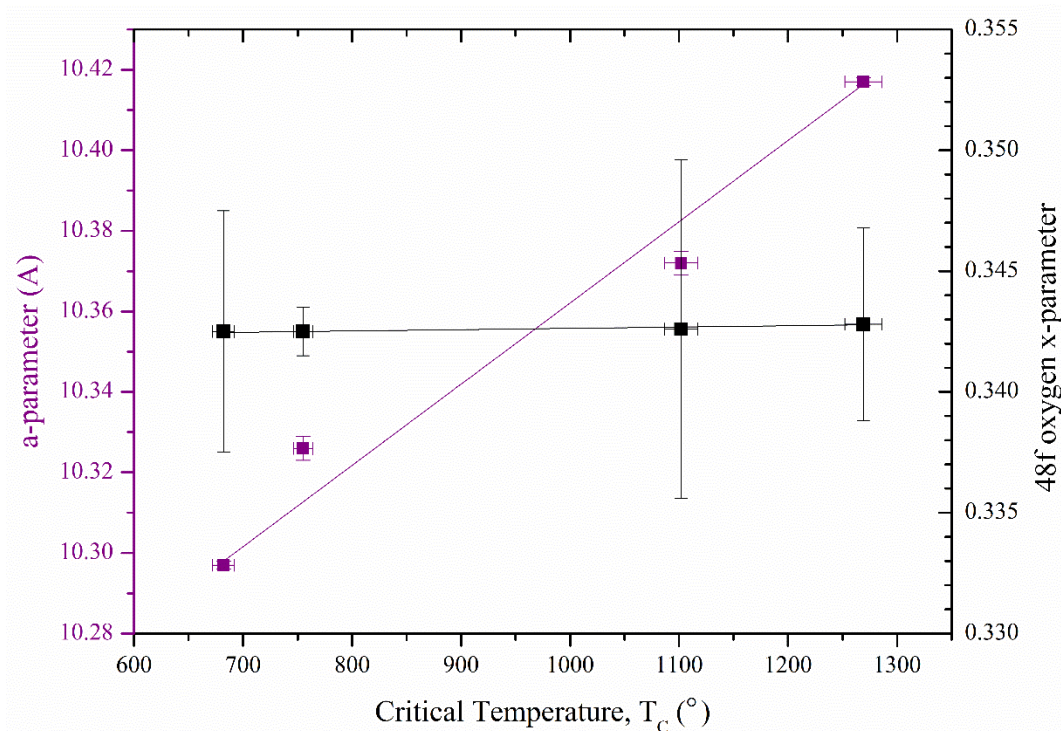


Figure 4.13: The critical temperatures of the measured samples plotted as a function of 48f oxygen x-position values with linear line of best fit included.

4.5 Discussion

Materials with target composition $\text{CaLnM}_{0.5}\text{Nb}_{1.5}\text{O}_7$, where Ln = La, Nd, Sm, Gd, Ho or Yb and M = Al, Sc, Cr, Fe or Y, were synthesised through solid state reaction of oxide and carbide precursors. Generally, materials where M = Al, Sc, Fe and Y formed a single phase assemblage with a crystalline structure indicative of a pyrochlore. This was initially confirmed by XRD and EDS analysis (Table 4.3). Under the assumption that the calcium and lanthanide (Ln) are located on the A-site, of the pyrochlore general formula $\text{A}_2\text{B}_2\text{O}_7$, and the metal (M) cation and niobium on the B-site, the r_A/r_B ionic radius ratios have been calculated for the measured compositions (Table 4.3). A r_A/r_B ratio range of 1.46-1.78 would be expected to adopt the pyrochlore structure. However, these materials have an ideal composition of $\text{A}^{2+}\text{A}^{3+}\text{B}_{1.5}^{5+}\text{B}_{0.5}^{3+}\text{O}_7$, so may not be defined by this stability range for the radius ratio of the pyrochlore structure. Materials with a single phase assemblage were analysed within the r_A/r_B ratio range of 1.50-1.87, beyond the expected range. The r_A/r_B values of 1.87 were defined for materials with compositions $\text{Ca}_{1.08(5)}\text{Nd}_{0.99(10)}\text{Al}_{0.49(2)}\text{Nb}_{1.52(3)}\text{O}_{7.10(31)}$ and $\text{Ca}_{1.08(2)}\text{La}_{1.01(8)}\text{Sc}_{0.49(1)}\text{Nb}_{1.42(9)}\text{O}_{6.88(38)}$. Analysis by SEM / EDS, XRD, and neutron diffraction shows them to have an assemblage of a single phase pyrochlore. Structural refinement, completed on high resolution neutron diffraction data collected for all materials showed a good fit could be achieved to the

pyrochlore structural model, including materials with an r_A/r_B values of 1.87; $\text{Ca}_{1.08(5)}\text{Nd}_{0.99(10)}\text{Al}_{0.49(2)}\text{Nb}_{1.52(3)}\text{O}_{7.10(31)}$ and $\text{Ca}_{1.08(2)}\text{La}_{1.01(8)}\text{Sc}_{0.49(1)}\text{Nb}_{1.42(9)}\text{O}_{6.88(38)}$ (Table 4.5). This indicated that the hypothesis that the family of materials with general formula $\text{A}^{2+}\text{A}^{3+}\text{B}_{1.5}^{5+}\text{B}_{0.5}^{3+}\text{O}_7$, are not wholly described by the r_A/r_B ratio, used to describe the pyrochlore range of general formula $\text{A}^{3+}_2\text{B}^{4+}_2\text{O}_7$. This highlights the chemical flexibility of the pyrochlore structure, even beyond the ionic radius ratio, r_A/r_B and emphasised the structural ability to accommodate multiple charged cations on a single crystallographic site.

The r_A/r_B value has been used as a descriptor of the structural stability in analysis of the a-parameter (Figure 4.6) with composition. The tolerance factors of the pyrochlore structure (Equation 4.5) are included within Table 4.3. Tolerance factors are also used to describe the stability of the pyrochlore structure, with Figure 4.7 highlighting the use of the tolerance factor to describe the change in a-parameter with composition. A similar trend within the a-parameter data was observed for both r_A/r_B and the tolerance factor. However, the range of calculated tolerance factor values for all materials, while within the defined range (0.84-0.98), was narrow (0.89-0.94) therefore the r_A/r_B value was used going forward [54]. The linear relationship between the a-parameter and the r_A/r_B (Figure 4.6), as a function of the variable B-site cation, cannot be explained with the available information. However, the refined 48f oxygen x-parameter, as a function of r_A/r_B , did not exhibit the same relationship with the B-site cation (Figure 4.8). A single linear relationship was identified in Figure 4.8 with the 48f oxygen x-parameter and the r_A/r_B value. There is a seemingly direct relationship between the increase in the r_A/r_B ratio, and an increased value of the 48f oxygen x-parameter. This shows that there is shift towards a defect fluorite ($x > 0.3750$) with increased r_A/r_B value, away from the ideal pyrochlore value at $x = 0.3125$ with smaller B-site M-cation and larger A-site Ln-cation.

Attempts were made to refine a structure indicative of a pyrochlore to the neutron diffraction data of the multiphase materials with target compositions; $\text{CaLaAl}_{0.5}\text{Nb}_{1.5}\text{O}_7$, $\text{CaHoY}_{0.5}\text{Nb}_{1.5}\text{O}_7$ and $\text{CaYbY}_{0.5}\text{Nb}_{1.5}\text{O}_7$.

The refined structural parameters for the material with target composition $\text{CaLaAl}_{0.5}\text{Nb}_{1.5}\text{O}_7$, were indicative of a pyrochlore material. The inclusion of a secondary pyrochlore structure did not improve the statistics of the fitting. No reflections within the crystalline structure remained unindexed. In addition to this, the U_{iso} values for the A-site (Ca and La) was notably larger than those refined for the other analysed materials (Table 4.6). The U_{iso} values are a measurement of the volume of the scattering density of an atom, a larger rare earth cation, such as the lanthanides (La, Nd etc.), will occupy a greater

volume. During refinement the U_{iso} value is an indicator of the stability of the cation within the defined position. The smaller the value then the more accurate the definition of the cation location. The large U_{iso} value for target composition $\text{CaLaAl}_{0.5}\text{Nb}_{1.5}\text{O}_7$ highlights the instability of the cation sites explained by the multiphase material observed in SEM analysis.

Rietveld refinement of the pyrochlore structure to the neutron diffraction data of multiphase materials with target compositions $\text{CaHoY}_{0.5}\text{Nb}_{1.5}\text{O}_7$ and $\text{CaYbY}_{0.5}\text{Nb}_{1.5}\text{O}_7$, indicated a secondary phase not modelled by the pyrochlore supercell. This was seen by a series of weak unindexed reflections within the data. However, a series of attempts to identify the additional phase(s), including the use of the Inorganic Structures Chemical Database (ICSD), were unsuccessful. It was therefore decided that the structural parameters for the materials with target compositions $\text{CaHoY}_{0.5}\text{Nb}_{1.5}\text{O}_7$ and $\text{CaYbY}_{0.5}\text{Nb}_{1.5}\text{O}_7$ were to be excluded from both Table 4.5 and subsequent analysis of the data. This was based upon the fact that the composition of the materials did not show the structural stability of the pyrochlore structure as desired.

In addition to the target compositions $\text{CaLaAl}_{0.5}\text{Nb}_{1.5}\text{O}_7$, $\text{CaHoY}_{0.5}\text{Nb}_{1.5}\text{O}_7$ and $\text{CaYbY}_{0.5}\text{Nb}_{1.5}\text{O}_7$, materials with general composition $\text{CaLnCr}_{0.5}\text{Nb}_{1.5}\text{O}_7$, where Ln = La, Nd, Sm, Gd, Ho or Yb, were synthesised. Despite numerous attempts a single phase assemblage was not formed, analysis of these materials are within Appendix A.

4.5.1 Discussions on the in-situ irradiations of $\text{CaLnFe}_{0.5}\text{Nb}_{1.5}\text{O}_7$ materials

In-situ irradiations were completed on systematically substituted iron containing materials, $\text{CaLnFe}_{0.5}\text{Nb}_{1.5}\text{O}_7$ where Ln = La, Nd, Sm, Gd, Ho or Yb. This was completed in order to analyse the response of the materials to radiation damage, simulating the recoil of the parent atoms during alpha decay. Composition was described using the refined structural parameter, the a-parameter, and the x-position of the 48f oxygen, as determined through GSAS analysis of neutron diffraction data, Table 4.6. The critical temperature (T_C) parameter was used to represent the materials response to the irradiation and was determined for materials where Ln = La, Sm, Ho or Yb (Figure 4.12). Where T_C is defined as the temperature at which there is sufficient energy for the material to not exhibit any radiation induced damage, defined as the loss of the long range ordering within the crystalline structure. Instrument availability limited the number of materials which could be analysed, as such insufficient statistical data was collected to determine the T_C for neodymium and gadolinium containing materials.

Analysis showed that as the *a*-parameter increased, so does the critical temperature (Figure 4.13). However, Figure 4.13 highlights despite the variation in the *a*-parameters of the materials there is minimal variation in the 48f oxygen *x*-parameter, and therefore minimal trend as a function of the critical temperature. Within the literature there are few comparative studies with systematic A-site lanthanide substitutions. With none found for direct comparison, analysis of general materials with the pyrochlore supercell, irradiated at the IVEM-Tandem facility, are used to understand the effect of changes in the chemical composition with T_C [11, 37, 38, 40, 74, 75]. Results show that with a decrease in the average ionic radii on the A-site (decreasing the r_A/r_B ratio), of the general pyrochlore formula $A_2B_2O_7$, the critical temperature is reduced. Similarly, studies analysing an increasing in the size of the average ionic radii on the B-site of the pyrochlore structure (decreasing the r_A/r_B ratio), was also found to have a tendency to reduce the critical temperature [38]. In terms of the r_A/r_B ratio, Figure 4.9 highlights the increase in the *a*-parameter corresponds to an increase in the Ln ionic radii, which in turn indicates a decrease in the r_A/r_B ratio. This indicates that the data here is consistent with that observed elsewhere.

The shift in the 48f *x*-parameter is minimal. The 48f oxygen is coordinated by two B site cations and two A site cations [33]. Therefore it would be expected that by varying the size of the average ionic radii of the A-site, through changing the lanthanide cation, there would be a shift in the *x*-parameter in order to accommodate the larger cation. The minimal changes in the refined 48f oxygen *x*-parameter indicate stability in the 8a oxygen vacancy, which is coordinated by four B site cations which remain unchanged in the materials. The irradiations show that the pyrochlore supercell is maintained throughout the irradiation of all materials until the crystalline structure is lost, with no intermediate fluorite phase observed (Figure 4.11). The comparable 48f oxygen *x*-position indicate stability in the 8a oxygen vacancy, which gives rise to the ordering in the A and B site cations, in all materials. This is a possible explanation for the consistency in the response of the materials despite the changes in the r_A/r_B ratio values and the changes in the T_C values.

This information will support the wider objective to understand and enable the long term prediction of a materials response to radiation damage when incorporating actinide species for geological disposal.

4.6 Conclusions

The chemical flexibility of the pyrochlore structure, general formula, $A_2B_2O_7$, was analysed through the tuning of the r_A/r_B ionic radius ratio. This was achieved using the general formula $A^{2+}A^{3+}B^{3+}_{0.5}B^{5+}_{1.5}O_7$, with chemical compositions of $Ca^{2+}Ln^{3+}M^{3+}_{0.5}Nb^{5+}_{1.5}O_7$, where $Ln = La, Nd, Sm, Gd, Ho$ or Yb and $M = Al, Sc, Fe$ or Y . Materials were largely synthesised with a crystallographic structure indicative of a pyrochlore. The r_A/r_B ionic radius ratio, for materials analysis by EDS analysis (Table 4.3), showed the measured compositions provided a r_A/r_B ionic radius ratio range of 1.50 to 1.87, where a single phase pyrochlore material was synthesised. Materials were synthesised beyond the theoretical r_A/r_B ionic radius ratio range (1.46-1.78). This is attributed to the fact that the theoretical range of the r_A/r_B values were established from pyrochlores with the general formula $A^{3+}_2B^{4+}_2O_7$.

Analysis of the refined parameters, from the Rietveld refinement of neutron diffraction data collected on the HRPD instrument, ISIS (Table 4.6) have been analysed as a function of the r_A/r_B ionic radius ratio (Figure 4.6). The unit cell a-parameter of the cubic superstructure was found to increase linearly with increasing lanthanide (Ln) substitution, when the M-cation remains constant. The relationship of between the 48f oxygen x-parameter and the r_A/r_B ratio is not dependent on the lanthanide (Ln) or metal cation (M), and a single linear relationship is seen, Figure 4.8.

In-situ irradiation of materials with target composition $CaLnFe_{0.5}Nb_{1.5}O_7$, where $Ln = La, Nd, Gd, Sm, Ho$ or Yb was completed at the IVEM-Tandem facility, Argonne National Laboratory. A direct relationship was found between the r_A/r_B ionic radius ratio and the critical temperature, T_C . Where T_C is defined as the temperature at which sufficient energy is provided to eliminate the loss of the crystallinity from the radiation induced damage. With decreasing r_A/r_B the critical temperature reduced. It was also observed, during in-situ irradiation experiments at the IVEM-Tandem facility that all materials transitioned directly from a material with pyrochlore crystalline phase to an amorphous material, with no intermediate phase identified. This was determined through the simultaneous disappearance of the pyrochlore supercell with the fluorite reflections, and the formation of an amorphous halo.

4.7 Future Work

Further work for this chapter should be undertaken in the following areas:

- Completion of the in-situ irradiation work on the samples with target composition $\text{CaNdFe}_{0.5}\text{Nb}_{1.5}\text{O}_7$ and $\text{CaGdFe}_{0.5}\text{Nb}_{1.5}\text{O}_7$.
- Further studies on the material response with variation of the B site cation in $\text{CaLnM}_{0.5}\text{Nb}_{1.5}\text{O}_7$ where Ln= La, Nd, Sm, Gd, Ho or Yb and M = Al, Sc and Y, in order to further understand the effect of the chemical variation on the materials response to in-situ irradiation of pyrochlores with general composition $\text{A}^{2+}\text{A}^{3+}\text{B}^{3+}_{0.5}\text{B}^{5+}_{1.5}\text{O}_7$. This will also enable confirmation of the pyrochlore supercell via TEM analysis.

4.8 References

- [1] Bakel AJ, Zyryanov VN, Mertz CJ *et al.* Corrosion behavior of pyrochlore-rich titanate ceramics for plutonium disposition; Impurity effects. In: Scientific Basis for Nuclear Waste Management Xxii. Edited by: Wronkiewicz DJ, Lee JH. 1999. pp. 181-188.
- [2] Fortner JA, Kropf AJ, Finch RJ *et al.* Crystal chemistry of uranium (V) and plutonium (IV) in a titanate ceramic for disposition of surplus fissile material. *Journal of Nuclear Materials* 2002; 304:56-62.
- [3] Fischer C, Finkeldei S, Brandt F *et al.* Direct Measurement of Surface Dissolution Rates in Potential Nuclear Waste Forms: The Example of Pyrochlore. *Acs Applied Materials & Interfaces* 2015; 7:17857-17865.
- [4] Helean KB, Navrotsky A, Lian J, Ewing RC. Thermochemical investigations of zirconolite, pyrochlore and brannerite: Candidate materials for the immobilization of plutonium. In: 27th Symposium on Scientific Basis for Nuclear Waste Management. Kalmar, SWEDEN: Materials Research Society; 2003. pp. 297-302.
- [5] Icenhower JP, Weber WJ, Hess NJ *et al.* Experimental determination of dissolution kinetics of Zr-substituted Gd-Ti pyrochlore ceramics: Influence of chemistry on corrosion resistance. In: Scientific Basis for Nuclear Waste Management Xxvi. Edited by: Finch RJ, Bullen DB. 2003. pp. 227-234.
- [6] Icenhower JP, Strachan DM, McGrail BP *et al.* Dissolution kinetics of pyrochlore ceramics for the disposition of plutonium. *American Mineralogist* 2006; 91:39-53.
- [7] Jitta RR, Gundeboina R, Veldurthi NK *et al.* Defect pyrochlore oxides: as photocatalyst materials for environmental and energy applications - a review. *Journal of Chemical Technology and Biotechnology* 2015; 90:1937-1948.
- [8] Xu HF, Wang YF, Zhao PH *et al.* Investigation of pyrochlore-based U-bearing ceramic nuclear waste: Uranium leaching test and TEM observation. *Environmental Science & Technology* 2004; 38:1480-1486.
- [9] Zhang Y, Hart K, Begg BD *et al.* Durability of Pu-doped titanate and zirconate ceramics designed for Pu immobilisation. In: Scientific Basis for Nuclear Waste Management Xxv. Edited by: McGrail BP, Cragnolino GA. 2002. pp. 389-395.
- [10] Cleave A, Grimes RW, Sickafus K. Plutonium and uranium accommodation in pyrochlore oxides. *Philosophical Magazine* 2005; 85:967-980.

- [11] de los Reyes M, Whittle KR, Zhang Z *et al.* The pyrochlore to defect fluorite phase transition in $Y_2Sn_{2-x}Zr_xO_7$. *Rsc Advances* 2013; 3:5090-5099.
- [12] Giere R, Hatcher C, Reusser E, Buck EC. Element partitioning in a pyrochlore-based ceramic nuclear waste form. In: 25th Symposium on Scientific Basis for Nuclear Waste Management. Boston, Ma: Materials Research Society; 2001. pp. 303-310.
- [13] Gregg DJ, Zhang YJ, Middleburgh SC *et al.* The incorporation of plutonium in lanthanum zirconate pyrochlore. *Journal of Nuclear Materials* 2013; 443:444-451.
- [14] Gregg DJ, Zhang ZM, Thorogood GJ *et al.* Cation antisite disorder in uranium-doped gadolinium zirconate pyrochlores. *Journal of Nuclear Materials* 2014; 452:474-478.
- [15] Harvey EJ, Whittle KR, Lumpkin GR *et al.* Solid solubilities of $(La,Nd)_2(Zr,Ti)_2O_7$ phases deduced by neutron diffraction. *Journal of Solid State Chemistry* 2005; 178:800-810.
- [16] Jafar M, Phapale SB, Mandal BP *et al.* Preparation and Structure of Uranium-Incorporated $Gd_2Zr_2O_7$ Compounds and Their Thermodynamic Stabilities under Oxidizing and Reducing Conditions. *Inorganic Chemistry* 2015; 54:9447-9457.
- [17] James M, Carter ML, Zhang Z *et al.* Crystal Chemistry and Structures of (Ca,U) Titanate Pyrochlores. *Journal of the American Ceramic Society* 2010; 93:3464-3473.
- [18] Jiang C, Stanek CR, Sickafus KE, Uberuaga BP. First-principles prediction of disordering tendencies in pyrochlore oxides. *Physical Review B* 2009; 79.
- [19] Kulkarni NK, Sampath S, Venugopal V. Preparation and characterisation of Pu-pyrochlore: $(La_{1-x}Pu_x)_2Zr_2O_7$ ($x=0-1$). *Journal of Nuclear Materials* 2000; 281:248-250.
- [20] Kumari R, Kulriya PK, Grover V *et al.* Radiation stability of $Gd_2Zr_2O_7$: Effect of stoichiometry and structure. *Ceramics International* 2016; 42:103-109.
- [21] Reid DP, Stennett MC, Hyatt NC. Synthesis and Structures of $Gd_2Zr_{2-x}Ce_xO_7$: A model ceramic system for plutonium disposition. In: *Advances in Materials Science for Environmental and Nuclear Technology*. Edited by: Fox K, Hoffman E, Manjooran N, Pickrell G. 2010. pp. 11-20.
- [22] Reid DP, Stennett MC, Hyatt NC. The fluorite related modulated structures of the $Gd_2(Zr_{2-x}Ce_x)O_7$ solid solution: An analogue for Pu disposition. *Journal of Solid State Chemistry* 2012; 191:2-9.
- [23] Shu XY, Lu XR, Fan L *et al.* Design and fabrication of $Gd_2Zr_2O_7$ -based waste forms for U_3O_8 immobilization in high capacity. *Journal of Materials Science* 2016; 51:5281-5289.
- [24] Stefanovsky SV, Yudinsev SV, Nikonov BS *et al.* Pyrochlore-type phases for actinides and rare earth elements immobilization. In: 22nd Symposium on Scientific Basis for Nuclear Waste Management held at the 1998 MRS Fall Meeting. Boston, Ma: Materials Research Society; 1998. pp. 27-34.
- [25] Crawford CL, Biddle CR, Bibler NE, Ans. Durability testing of heavy-ion irradiated crystalline ceramics. *Proceedings of the Embedded Topical Meeting on Spent Nuclear Fuel and Fissile Material Management* 2000:449-456.
- [26] Ewing RC, Lian J, Wang LM. Ion beam-induced amorphization of the pyrochlore structure-type: A review. In: *Radiation Effects and Ion-Beam Processing of Materials*. Edited by: Wang LM, Fromknecht R, Snead LL *et al.* 2004. pp. 37-48.

- [27] Ewing RC, Weber WJ, Lian J. Nuclear waste disposal- pyrochlore ($A_2B_2O_7$): Nuclear waste form for the immobilization of plutonium and "minor" actinides. *Journal of applied Physics* 2004; 95:5949- 5971.
- [28] Lang M, Zhang F, Zhang J *et al.* Review of $A_2B_2O_7$ pyrochlore response to irradiation and pressure. *Nuclear Instruments & Methods in Physics Research Section B-Beam Interactions with Materials and Atoms* 2010; 268:2951-2959.
- [29] Lang M, Toulemonde M, Zhang J *et al.* Swift heavy ion track formation in $Gd_2Zr_{2-x}Ti_xO_7$ pyrochlore: Effect of electronic energy loss. *Nuclear Instruments & Methods in Physics Research Section B-Beam Interactions with Materials and Atoms* 2014; 336:102-115.
- [30] Lang M, Lian J, Zhang J *et al.* Single-ion tracks in $Gd_2Zr_{2-x}Ti_xO_7$ pyrochlores irradiated with swift heavy ions. *Physical Review B* 2009; 79.
- [31] Lian J, Zu XT, Kutty KVG *et al.* Ion-irradiation-induced amorphization of $La_2Zr_2O_7$ pyrochlore. *Physical Review B* 2002; 66.
- [32] Lian J, Chen J, Wang LM *et al.* Radiation-induced amorphization of rare-earth titanate pyrochlores. *Physical Review B* 2003; 68.
- [33] Lian J, Wang L, Chen J *et al.* The order-disorder transition in ion-irradiated pyrochlore. *Acta Materialia* 2003; 51:1493-1502.
- [34] Lian J, Wang LM, Haire RG *et al.* Ion beam irradiation in $La_2Zr_2O_7$ - $Ce_2Zr_2O_7$ pyrochlore. *Nuclear Instruments & Methods in Physics Research Section B-Beam Interactions with Materials and Atoms* 2004; 218:236-243.
- [35] Lian J, Helean KB, Kennedy BJ *et al.* Effect of structure and thermodynamic stability on the response of lanthanide stannate-pyrochlores to ion beam irradiation. *Journal of Physical Chemistry B* 2006; 110:2343-2350.
- [36] Lumpkin GR, Whittle KR, Rios S *et al.* Radiation damage in pyrochlore and related compounds. In: *Scientific Basis for Nuclear Waste Management XXIX*. Edited by: VanIseghem P. 2006. pp. 549-558.
- [37] Lumpkin GR, Pruneda M, Rios S *et al.* Nature of the chemical bond and prediction of radiation tolerance in pyrochlore and defect fluorite compounds. *Journal of Solid State Chemistry* 2007; 180:1512-1518.
- [38] Lumpkin GR, Smith KL, Blackford MG *et al.* Ion Irradiation of Ternary Pyrochlore Oxides. *Chemistry of Materials* 2009; 21:2746-2754.
- [39] Strachan DM, Scheele RD, Buck EC *et al.* Radiation damage effects in candidate titanates for Pu disposition: Zirconolite. *Journal of Nuclear Materials* 2008; 372:16-31.
- [40] Whittle KR, Blackford MG, Aughterson RD *et al.* Ion irradiation of novel yttrium/ytterbium-based pyrochlores: The effect of disorder. *Acta Materialia* 2011; 59:7530-7537.
- [41] Giere R, Williams CT, Lumpkin GR. Chemical characteristics of natural zirconolite. *Schweizerische Mineralogische Und Petrographische Mitteilungen* 1998; 78:433-459.
- [42] Giere R, Buck EC, Guggenheim R *et al.* Alteration of uranium-rich microlite. In: *Scientific Basis for Nuclear Waste Management Xxiv*. Edited by: Hart KP, Lumpkin GR. 2000. pp. 935-944.
- [43] Lumpkin GR, Gao Y, Giere R *et al.* The role of Th-U minerals in assessing the performance of nuclear waste forms. *Mineralogical Magazine* 2014; 78:1071-1095.

- [44] Meldrum A, Boatner LA, Ewing RC. Displacive radiation effects in the monazite- and zircon-structure orthophosphates. *Physical Review B* 1997; 56:13805-13814.
- [45] Sinclair W, Ringwood AE. Alpha recoil damage in natural zirconolite and perovskite. *Geochemical Journal* 1981; 15:229-243.
- [46] Vlcek V, Skala R, Golias V *et al.* Effect of natural irradiation in fluorites: possible implications for nuclear waste management? *Journal of Geosciences* 2012; 57:45-52.
- [47] Pabst A. The Metamict State. *Am. Mineral.* 1952; 37:137.
- [48] Chesnokov BV, Eremeev SP. Crystallization of Metamict Pyrochlore Under Natural Conditions. *Doklady Akademii Nauk Sssr* 1962; 146:683-&.
- [49] Lumpkin GR, Mariano AN. Natural occurrence and stability of pyrochlore in carbonatites, related hydrothermal systems and weathering environments. In: *Scientific Basis for Nuclear Waste Management Xix*. Edited by: Murphy WM, Knecht DA. 1996. pp. 831-838.
- [50] Lumpkin GR, Ewing RC, Williams CT, Mariano AN. An overview of the crystal chemistry, durability, and radiation damage effects of natural pyrochlore. In: *Scientific Basis for Nuclear Waste Management Xxiv*. Edited by: Hart KP, Lumpkin GR. 2000. pp. 921-934.
- [51] Chakoumakos BC. Systematics of the Pyrochlore Structure Type, Ideal $A_2B_2X_6Y$. *Journal of Solid State Chemistry* 1984; 53:120-129.
- [52] Ewing RC, Weber WJ, Lian J. Nuclear waste disposal- pyrochlore ($A_2B_2O_7$): Nuclear waste form for the immobilization of plutonium and "minor" actinides Nuclear waste disposal- pyrochlore ($A_2B_2O_7$): Nuclear waste form for the immobilization of plutonium and "minor" actinides. *Journal of applied Physics* 2004; 95:5949- 5971.
- [53] Subramanian MA, Aravamudan G, Rao GVS. Oxide Pyrochlores- A Review. *Progress in Solid State Chemistry* 1983; 15:55-143.
- [54] Mouta R, Silva RX, Paschoal CWA. Tolerance factor for pyrochlores and related structures. *Acta Crystallographica Section B-Structural Science* 2013; 69:439-445.
- [55] Brik MG, Srivastava AM. Pyrochlore Structural Chemistry: Predicting the Lattice Constant by the Ionic Radii and Electronegativities of the Constituting Ions. *Journal of the American Ceramic Society* 2012; 95:1454-1460.
- [56] Cai L, Arias AL, Nino JC. The tolerance factors of the pyrochlore crystal structure. *Journal of Materials Chemistry* 2011; 21:3611-3618.
- [57] Ishizawa N, Marumo F, Iwai S *et al.* Compounds with perovskite-type slabs. V. A High-Temperature Modification of $La_2Ti_2O_7$. *Acta Crystallographica Section B-Structural Science* 1982; 38:368-372.
- [58] Egerton RF. *Physical Principles of Electron Microscopy: An Introduction to TEM, SEM and AEM*. Springer US; 2005.
- [59] Dinnerbier RE, Billinge SJL, Bruce PG *et al.* *Powder Diffraction: Theory and Practice*. Royal Society of Chemistry; 2008.
- [60] Shannon R. Revised effective ionic radii and systematic studies of interatomic distances in halides and chalcogenides. *Acta Crystallographica Section A* 1976; 32:751-767.
- [61] Sears VF. Neutron scattering lengths and cross sections. In: *Neutron News*; 1992. pp. 29-37.

- [62] Larson AC, Von Dreele RB. General Structure Analysis System (GSAS). In: Los Alamos National Laboratory Report LAUR. 2004. pp. 86-748.
- [63] Toby BH. EXPGUI, a graphical user interface for GSAS. *J. Appl. Cryst.* 2001; 34:210-213.
- [64] Istomin SY, Dyachenko OG, Antipov EV, Svensson G. Synthesis and characterization of reduced niobates $\text{CaLnNb}_2\text{O}_7$, Ln=Y, Nd with a pyrochlore structure. *Materials Research Bulletin* 1997; 32:421-430.
- [65] Weber WJ, Ewing RC, Catlow CRA *et al.* Radiation effects in crystalline ceramics for the immobilization of high-level nuclear waste and plutonium. *Journal of Materials Research* 1998; 13:1434-1484.
- [66] Ewing RC, Wang LM. Amorphization of zirconolite - Alpha decay event damage versus krypton ion irradiation. *Nuclear Instruments & Methods in Physics Research Section B-Beam Interactions with Materials and Atoms* 1992; 65:319-323.
- [67] Wang SX, Wang LM, Ewing RC. Nano-scale glass formation in pyrochlore by heavy ion irradiation. *Journal of Non-Crystalline Solids* 2000; 274:238-243.
- [68] Meldrum A, White CW, Keppens V *et al.* Irradiation-induced amorphization of $\text{Cd}_2\text{Nb}_2\text{O}_7$ pyrochlore. *Physical Review B* 2001; 63:104109.
- [69] Wang SX, Begg BD, Wang LM *et al.* Radiation stability of gadolinium zirconate: A waste form for plutonium disposition. *Journal of Materials Research* 1999; 14:4470-4473.
- [70] Sickafus KE, Minervini L, Grimes RW *et al.* A comparison between radiation damage accumulation in oxides with pyrochlore and fluorite structures. *Radiation Effects and Defects in Solids* 2001; 155:133-137.
- [71] Lang M, Zhang FX, Ewing RC *et al.* Structural modifications of $\text{Gd}_2\text{Zr}_{2-x}\text{Ti}_x\text{O}_7$ pyrochlore induced by swift heavy ions: Disordering and amorphization. *Journal of Materials Research* 2009; 24:1322-1334.
- [72] Tabira Y, Withers RL, Barry JC, Elcoro L. The Strain-Driven Pyrochlore to “Defect Fluorite” Phase Transition in Rare Earth Sesquioxide Stabilized Cubic Zirconias. 2001; 159:121–129.
- [73] Withers R, Thompson J, Barlow P, Barry J. The Defect Fluorite Phase in the ZrO_2 - $\text{PrO}_{1.5}$ System and Its Relationship to the Structure of Pyrochlore. *Australian Journal of Chemistry* 1992; 45:1375-1395.
- [74] Lumpkin GR, Whittle KR, Rios S *et al.* Temperature dependence of ion irradiation damage in the pyrochlores $\text{La}_2\text{Zr}_2\text{O}_7$ and $\text{La}_2\text{Hf}_2\text{O}_7$. Temperature dependence of ion irradiation damage in the pyrochlores $\text{La}_2\text{Zr}_2\text{O}_7$ and $\text{La}_2\text{Hf}_2\text{O}_7$. *Journal of Physics-Condensed Matter* 2004; 16:8557-8570.
- [75] Whittle KR, Lumpkin GR, Blackford MG *et al.* Ion-beam irradiation of lanthanum compounds in the systems La_2O_3 - Al_2O_3 and La_2O_3 - TiO_2 . *Journal of Solid State Chemistry* 2010; 183:2416-2420.

Chapter 5 Uranium Substituted Lanthanum Zirconate Pyrochlores

5.1 Introduction

Lanthanum zirconate pyrochlores, $\text{La}_2\text{Zr}_2\text{O}_7$, with a general formula $\text{A}_2\text{B}_2\text{O}_7$ and space group $Fd\bar{3}m$, have been studied as a potential disposal matrices for nuclear materials, as part of a wider zirconate family of materials [1-21]. This includes a number of studies on the radiation tolerance and the chemical flexibility of the lanthanum zirconate material, as an analogue to the incorporation of actinides [6, 7]. It is interesting to note that whilst the substitution of an actinide on the A-site of the structure [2, 22] have been investigated, there has been little work on the incorporation of actinides on the B-site. This work focuses on developing an understanding of the solid solubility of uranium on the B-site of the lanthanum zirconate pyrochlore. Through analysis of the uranium oxidation state, as a function of processing atmosphere, combined with elucidation of structural changes by scanning electron microscopy (SEM) and transmission electron microscopy (TEM). This has direct relevance to both the disposal of uranium oxide but also tetravalent actinide species such as Pu^{4+} where U^{4+} is an active analogue.

The general pyrochlores structure, $\text{A}_2\text{B}_2\text{O}_7$, has a cubic $2 \times 2 \times 2$ superstructure relative to an underlying fluorite, AO_2 , cell with space group ($Fm\bar{3}m$) [23]. The superstructure, space group $Fd\bar{3}m$, is formed through the creation of a regular array of oxygen vacancies yielding a structure with 2 distinct cation sites, denoted as A and B [23]. With respect to the oxygen cations, the A cations are 8-fold coordinated and the B cations are 6-fold coordinated. The lattice parameters of the ideal pyrochlore structure material are all located on special crystallographic positions, with the exception of the oxygen on the 48f position ($x, 1/8, 1/8$), where the ordered anion vacancy at $(3/8, 3/8, 3/8)$, the 8b position, enables flexibility in the 48f oxygen x-position [23]. Section 2.2 includes further information on the pyrochlore structure.

The ratio of the atomic radii of cations on the A and B sites (r_A/r_B), can be used to predict the likelihood of a composition forming the pyrochlore structure. For pyrochlore structures to form the radius ratio (r_A/r_B) is bound by the range of 1.46 - 1.78 [9]. Beyond the lower boundary a fluorite ($(\text{AB})_4\text{O}_8$) or defect fluorite structure ($(\text{AB})_4\text{O}_7$) is expected to form [9]. A defect fluorite is a disordered fluorite with at least 2 cations randomly

arranged and un-ordered oxygen vacancy. Above the upper boundary a monoclinic structure is expected to form, this has a layered perovskite structure, for example $\text{La}_2\text{Ti}_2\text{O}_7$ [24].

$\text{La}_2\text{Zr}_2\text{O}_7$ has a r_A/r_B value of 1.611, which lies well within the bounds of a pyrochlore structure. From inspection of the ionic radii values given in Table 5.1, it can be hypothesised that with increasing substitution of uranium onto the B site of the $\text{La}_2\text{Zr}_{2-x}\text{U}_x\text{O}_7$ pyrochlore structure the r_A/r_B value would decrease. The decrease will be dependent on the oxidation state of the uranium, this effect, for the materials synthesised here, is highlighted in Table 5.6.

Table 5.1: Table of ionic radii according to Shannon Radii database, ‘X’ indicates coordination/charge combination not found within the literature. [25]

Ion		Zr	La	U			Pu			
Charge		4+	3+	4+	5+	6+	3+	4+	5+	6+
Coordination	VI	0.72	-	0.89	0.76	0.73	0.86	0.74	0.71	1
	VIII	-	1.16	1.00	-	0.86	0.96	-	-	-

Uranium substitution is complicated by the fact that it can exist in a number of different oxidation states. In this work the uranium precursor was in the oxide form of UO_3 . Hexavalent uranium, UO_3 , is found to have a greater solubility than other uranium forms, including tetravalent UO_2 and triuranium octoxide U_3O_8 . Due to the decision to prepare the materials using a sol gel method, in order to encourage intimate mixing of the precursor materials prior to reacting, UO_3 was ideal for dissolution. Different processing atmospheres were employed to investigate the effect of uranium oxidation state and inclusion of the cation in the pyrochlore structure. In order to accommodate cations of a higher valence state than the tetravalent zirconium on the B-site, the structure must be able to charge compensate. This could include the addition of oxygen, possibly in the ordered anion vacancy within the structure, however this could result in the loss of the pyrochlore structure.

Radiation damage studies have been completed on zirconate pyrochlores, of the general composition $\text{A}_2\text{Zr}_2\text{O}_7$. Of particular interest to this work is the studies reported by Lian et al [1, 6, 7], which considered the effect of changes in A-site cation on radiation damage recovery. It was shown that with neodymium (Nd), samarium (Sm) and gadolinium (Gd) on the A-site of a zirconate pyrochlore, the materials did not become

amorphous when subject to heavy ion irradiation. Instead the crystalline structure loses the ordering within the oxygen vacancies resulting in a transition to a fluorite structure. This was maintained, even when subject to 1.5 MeV Xe⁺ irradiations at room temperature (293K) a level of 7dpa, 7.3dpa and 36dpa, respectively [7]. In contrast, the lanthanum containing analogue became amorphous when subject to irradiation under the same conditions. The La₂Zr₂O₇ phase showed that, the material transitioned from pyrochlore, to a defect fluorite, finally to an amorphous material. However, analysis completed at slightly elevated temperatures of >310K, the crystalline structure was retained, irrespective of the dose. Both HLW and actinides produce heat, this means that materials bearing HLW / actinides with sufficient heat energy available, should maintain a crystalline structure. However the long term behaviour, once the heat has dissipated, requires analysis for the lifetime of the GDF facility. The temperature required to provide sufficient energy to enable a material to retain its crystallinity is referred to as the critical amorphisation temperature (T_c). Above this temperature there is enough thermal energy provided for recovery from the damage caused by the irradiation process. The critical amorphisation dose, D_C, the dose where the material is fully amorphous, at room temperature of the sample La₂Zr₂O₇ was ~5.5dpa [7]. A transition from a crystalline to an amorphous material, when insufficient thermal energy is available, offers the advantage that the long term behaviour, and end state, can be inferred through the analysis of naturally occurring zirconate materials found within rock formations containing uranium and thorium [26]. See section 2.2.1 for naturally occurring analogues with the pyrochlore structure. In summary, these results suggest that, after 10⁴ years, the original pyrochlore structure is lost and an amorphous material is formed yet the radioactive species are still retained. Naturally occurring materials with the pyrochlore structure also exhibit good resistance to leaching [26-30]. A secondary phase as the end state within a waste form would have to be subject to extensive studies to determine the response to long term storage in a geological environment. The Lian et al. study [6] also showed that the material became more resistant to irradiation as the r_A/r_B ratio decreased, with decreasing A cation size. The substitution of uranium for zirconium in lanthanum zirconate will decrease the r_A/r_B ratio and therefore could potentially have a positive effect of the recovery mechanisms within the material, although this is beyond the scope of this work.

5.2 Experimental Method

5.2.1 Material Synthesis

A sol-gel method has been adopted in order to ensure a homogeneous mixing of the precursor oxides prior to high temperature synthesis. All oxide precursors, UO_3 and La_2O_3 , were measured according the relevant stoichiometry after drying at 600°C in air overnight. As ZrO_2 is insoluble in acid, $\text{ZrO}(\text{NO}_3)_2$ was used. Chemical reagent information for the precursor materials can be found in Table 5.2.

Table 5. 2: Chemical reagent information of precursors.

Chemical Reagent	Chemical Formula	Supplier	Purity (%)
Uranium trioxide	UO_3	-	-
Zirconium (IV) Oxynitrate Hydrate	$\text{ZrO}(\text{NO}_3)_2 \cdot x\text{H}_2\text{O}$	Sigma Aldrich	>99.99
Lanthanum (III) Oxide	La_2O_3	Sigma Aldrich	>99.99

Materials were measured according to the stoichiometries within Table 5.3. Zirconium oxynitrate hydrate stoichiometry is calculated from the required quantity of zirconium oxide (ZrO_2). The water fraction within the zirconium oxynitrate hydrate is determined through heating 1g of $\text{ZrO}(\text{NO}_3)_2 \cdot x\text{H}_2\text{O}$ to 1000°C for 12 hours to form ZrO_2 . The final product is weighed and the fraction of water lost calculated.

In order to ensure a homogeneous product is formed all the precursors were dissolved in a combination of de-ionised water and nitric acid. The $\text{ZrO}(\text{NO}_3)_2$ was initially dissolved in 10ml of de-ionised water on a magnetic stirring plate. Once the $\text{ZrO}(\text{NO}_3)_2$ had dissolved, the La_2O_3 was dissolved in 5ml of de-ionised water and 1ml nitric acid (69 %). The UO_3 was also dissolved in 5ml de-ionised water and 1 ml nitric acid and combined with the La_2O_3 solution, prior to all three solutions being mixed. An excess of ammonia was added, forming a yellow 'gel' precipitate. The pH of the solution was tested to ensure the solution was highly alkaline (pH 14) and then the precipitate was filtered under vacuum using a Buchner flask and a 0.45 micron filter paper. Once filtered the solid precipitate was dried overnight at 100°C to remove any excess moisture. Finally the dry precipitate was ground in a pestle and mortar and quantities of loose powder, ~0.5g, were fired at 1400°C under different atmospheric conditions. Materials were formed in a hydrogen / nitrogen atmosphere with flowing H_2/N_2 , in a tube furnace for 4

hrs with heating and cooling rates of 3 °C min⁻¹. Materials were also formed in an air atmosphere in a muffle furnace for 4 hrs with heating and cooling rates of 5 °C min⁻¹.

Materials were prepared with target composition La₂(Zr_{2-x}U_x)O_{7+δ}, with 0.1 ≤ x ≤ 0.9 in hydrogen / nitrogen atmosphere, and with 0.1 ≤ x ≤ 0.6 in air. These materials were initially characterised using the STOE-PSD X-ray diffractometer, followed by scanning electron microscopy and energy dispersive X-ray spectroscopy completed on the Hitachi TM3030, full experimental set up can be found in Section 3.1.2.1 and 3.2.1, respectively. Further analysis was completed using X-ray absorption Near Edge Spectroscopy (XANES) to determine the average uranium oxidation state and Transmission Electron Microscopy (TEM) to analyse the pyrochlore supercell.

Table 5. 3: Stoichiometry of precursor materials utilised for the synthesis of the ceramic compositions where La₂(Zr_{2-x}U_x)O_{7+δ}, with 0.1 ≤ x ≤ 0.9.

x	La₂O₃	UO₃	ZrO₂	ZrO(NO₃)₂.xH₂O
0.0	0.5694	0.0000	0.4306	1.1333
0.1	0.5536	0.0486	0.3978	1.0468
0.2	0.5387	0.0946	0.3667	0.9650
0.3	0.5246	0.1382	0.3373	0.8875
0.4	0.5112	0.1795	0.3093	0.8140
0.5	0.4984	0.2188	0.2828	0.7441
0.6	0.4863	0.2562	0.2575	0.6776
0.7	0.4748	0.2918	0.2334	0.6143
0.8	0.4638	0.3257	0.2105	0.5539
0.9	0.4533	0.3581	0.1886	0.4962

5.3 Results

5.3.1 Scanning Electron Microscopy and Energy Dispersive X-ray Spectroscopy

SEM / EDS analysis was conducted on the Hitachi TM3030 microscope, see Section 3.2.1 for instrument set up. Materials were ground after formation and cold uniaxially pressed within a dedicated glove box. They were then sintered in their respective atmospheres and mounted within an epoxy resin. The resin was allowed to set for 24 hours within a fume cupboard. The materials were initially polished using an 800 grit silicon carbide paper, working to a 2400 grit paper. Finally a 3 and 1 micron polishing paper is used to achieve a 1 micron optical finish. Images were collected in back scattered electron (BSE)

diffraction mode prior to elemental analysis using the energy dispersive X-ray spectroscopy (EDS) within the instrument.

5.3.1.1 Materials formed in an air atmosphere

Semi-quantitative EDS analysis was completed on all materials to determine the cation composition at 30,000x magnification. A lack of variation in the contrast (grey scale) for materials $\text{La}_2\text{Zr}_{(2-x)}\text{U}_x\text{O}_{7+\delta}$ ($0.1 < x < 0.5$), Figure 5.1(a)-(e), is indicative of a material with a single composition. It should be noted that porosity/cracks within a sintered material under the EDS analysis will show as black areas. The black regions within Figure 5.1 and Figure 5.2 are a combination of pores and cracks within the surface.

The material with target composition $\text{La}_2(\text{Zr}_{1.4}\text{U}_{0.6})\text{O}_{7+\delta}$, Figure 5.1(f), showed two distinct variations in the contrast, labelled '1' and '2', indicating two distinct compositions within the material. Semi-quantitative EDS analysis has been completed on both of these phases in isolation, see Table 5.4.

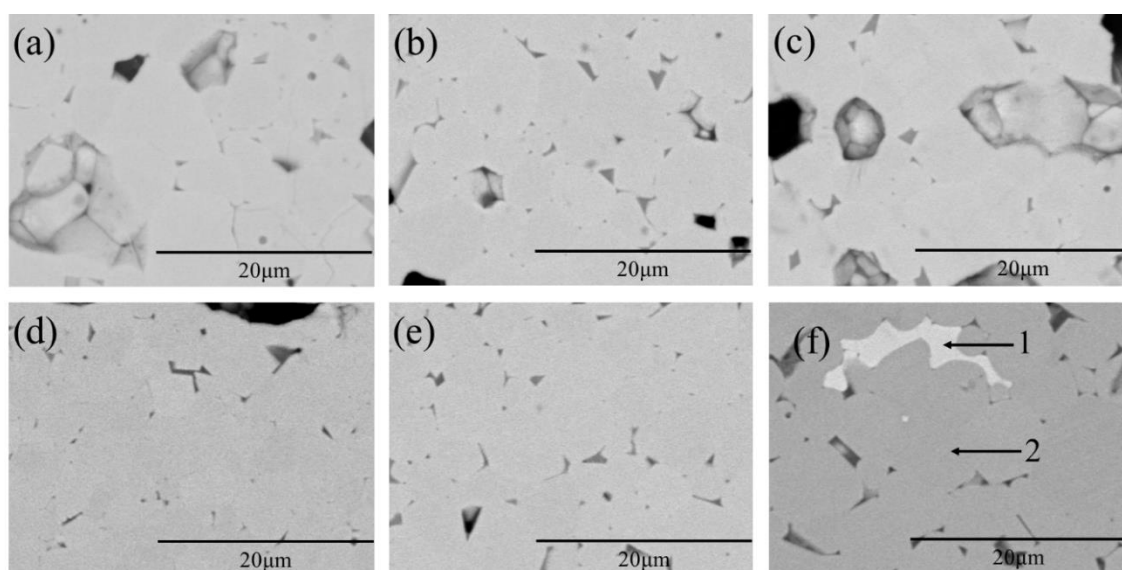


Figure 5.1: Back Scattered Electron (BSE) diffraction images of materials of the system $\text{La}_2\text{Zr}_{2-x}\text{U}_x\text{O}_{7+\delta}$, where $x = 0.1$ to 0.6 , (a)-(f), respectively. These materials were formed in a muffle furnace with an air atmosphere.

In general the semi-quantitative EDS results, Table 5.4, showed a close correlation to the target compositions, with the exception of the material with the target composition $\text{La}_2\text{Zr}_{1.4}\text{U}_{0.6}\text{O}_7$. A two phase assemblage for material with target composition $\text{La}_2\text{Zr}_{1.4}\text{U}_{0.6}\text{O}_7$ was observed, Figure 5.1(f), dominated by the phase highlighted '2', with minor contributions from the phase highlighted '1'. To show the material has the correct ratios of cations an average composition from the bulk of this material was measured

using EDS analysis, with the resultant composition of $\text{La}_{2.06(2)}\text{Zr}_{1.35(1)}\text{U}_{0.58(1)}\text{O}_{7+\delta}$ measured, showing the correct stoichiometry of precursor oxides were reacted.

Table 5.4: Semi-quantitative results from EDS analysis using the back scattered detector of the Hitachi TM3030 instrument for compositions in the system $\text{La}_2\text{Zr}_{2-x}\text{U}_x\text{O}_{7+\delta}$, where $x = 0.1$ to 0.6 , formed in an air atmosphere. For compositions (a)-(e) the oxygen stoichiometries were inferred from measurement of the U L_3 edge during XANES analysis of average uranium oxidation state, and summarised within Table 5.12. Taking the oxygen for both phases in (f) from the oxygen as measured by XANES of the bulk material.

	Target Composition	Semi-Quantitative EDS
(a)	$\text{La}_2\text{Zr}_{1.9}\text{U}_{0.1}\text{O}_{7+\delta}$	$\text{La}_{2.10(2)}\text{Zr}_{1.87(2)}\text{U}_{0.10(1)}\text{O}_{7.19(1)}$
(b)	$\text{La}_2\text{Zr}_{1.8}\text{U}_{0.2}\text{O}_{7+\delta}$	$\text{La}_{2.01(3)}\text{Zr}_{1.75(2)}\text{U}_{0.20(1)}\text{O}_{7.11(1)}$
(c)	$\text{La}_2\text{Zr}_{1.7}\text{U}_{0.3}\text{O}_{7+\delta}$	$\text{La}_{2.05(3)}\text{Zr}_{1.72(2)}\text{U}_{0.32(1)}\text{O}_{7.46(2)}$
(d)	$\text{La}_2\text{Zr}_{1.6}\text{U}_{0.4}\text{O}_{7+\delta}$	$\text{La}_{2.11(2)}\text{Zr}_{1.58(1)}\text{U}_{0.38(1)}\text{O}_{7.42(3)}$
(e)	$\text{La}_2\text{Zr}_{1.5}\text{U}_{0.5}\text{O}_{7+\delta}$	$\text{La}_{2.06(2)}\text{Zr}_{1.51(1)}\text{U}_{0.48(1)}\text{O}_{7.45(3)}$
(f)	$\text{La}_2\text{Zr}_{1.4}\text{U}_{0.6}\text{O}_{7+\delta}$	1- $\text{La}_{1.94(1)}\text{Zr}_{0.55(1)}\text{U}_{1.52(1)}\text{O}_{8.2(1)}$
		2- $\text{La}_{1.94(1)}\text{Zr}_{1.51(1)}\text{U}_{0.53(1)}\text{O}_{7.40(4)}$
		Bulk- $\text{La}_{2.06(2)}\text{Zr}_{1.35(1)}\text{U}_{0.58(1)}\text{O}_{7.39(4)}$

Overall, the results indicate that single phase material of a composition comparable to that of the target composition is formed up to and including the substitution of $x=0.5$, or 25% substitution of uranium for zirconium. Above this solid solution limit, the structure de-stabilises and a second, uranium rich, minor phase is formed. The upper limit of the substitution can be described by the boundary $0.5 < x < 0.6$ in $\text{La}_2\text{Zr}_{2-x}\text{U}_x\text{O}_{7+\delta}$. The oxygen content reported in Table 5.4 was calculated under the assumption that cation / anion adopt their usual oxidation state, with uranium adopting the bulk oxidation state defined by XANES, Table 5.12, including for target composition $\text{La}_2\text{Zr}_{1.4}\text{U}_{0.6}\text{O}_{7+\delta}$. The structural analysis of the materials have been confirmed using X-ray diffraction analysis, see Figure 5.4.

5.3.1.2 Materials formed in a hydrogen / nitrogen atmosphere

Phase assemblage has been analysed through the use of SEM / EDS on all compositions formed in a hydrogen / nitrogen atmosphere. A lack of contrast in Figure 5.2 highlights a single phase material has been formed in compositions up to, and including, the

substitution of $x=0.8$, with target composition $\text{La}_2\text{Zr}_{1.2}\text{U}_{0.8}\text{O}_{7+\delta}$. Full compositional analysis by EDS are reported in Table 5.5.

Table 5.5: Semi-quantitative results from EDS analysis using the back scattered detector of the Hitachi TM3030 instrument for samples of composition system $\text{La}_2\text{Zr}_{2-x}\text{U}_x\text{O}_{7+\delta}$, where $x = 0.1$ to 0.9 , formed in a hydrogen/nitrogen atmosphere. The oxygen stoichiometries were defined from the average uranium oxidation state, measured by U L_3 edge XANES analysis, as summarised in Table 5.13 and Table 5.14.

	Target Composition	Semi-Quantitative EDS
(a)	$\text{La}_2\text{Zr}_{1.9}\text{U}_{0.1}\text{O}_{7+\delta}$	$\text{La}_{2.19(3)}\text{Zr}_{1.91(2)}\text{U}_{0.08(1)}\text{O}_{7.33(1)}$
(b)	$\text{La}_2\text{Zr}_{1.8}\text{U}_{0.2}\text{O}_{7+\delta}$	$\text{La}_{2.17(3)}\text{Zr}_{1.83(2)}\text{U}_{0.15(1)}\text{O}_{7.38(3)}$
(c)	$\text{La}_2\text{Zr}_{1.7}\text{U}_{0.3}\text{O}_{7+\delta}$	$\text{La}_{2.13(2)}\text{Zr}_{1.74(1)}\text{U}_{0.26(1)}\text{O}_{7.40(4)}$
(d)	$\text{La}_2\text{Zr}_{1.6}\text{U}_{0.4}\text{O}_{7+\delta}$	$\text{La}_{2.16(2)}\text{Zr}_{1.59(1)}\text{U}_{0.36(1)}\text{O}_{7.46(7)}$
(e)	$\text{La}_2\text{Zr}_{1.5}\text{U}_{0.5}\text{O}_{7+\delta}$	$\text{La}_{1.99(2)}\text{Zr}_{1.49(1)}\text{U}_{0.49(1)}\text{O}_{7.28(7)}$
(f)	$\text{La}_2\text{Zr}_{1.4}\text{U}_{0.6}\text{O}_{7+\delta}$	$\text{La}_{2.02(2)}\text{Zr}_{1.44(1)}\text{U}_{0.57(1)}\text{O}_{7.5(1)}$
(g)	$\text{La}_2\text{Zr}_{1.3}\text{U}_{0.7}\text{O}_{7+\delta}$	$\text{La}_{2.16(2)}\text{Zr}_{1.27(1)}\text{U}_{0.64(1)}\text{O}_{7.5(1)}$
(h)	$\text{La}_2\text{Zr}_{1.2}\text{U}_{0.8}\text{O}_{7+\delta}$	$\text{La}_{1.94(2)}\text{Zr}_{1.20(1)}\text{U}_{0.81(1)}\text{O}_{7.4(1)}$
(i)	$\text{La}_2\text{Zr}_{1.1}\text{U}_{0.9}\text{O}_{7+\delta}$	1- $\text{La}_{1.51(2)}\text{Zr}_{0.29(1)}\text{U}_{2.20(3)}\text{O}_{8.4(3)}$
		2- $\text{La}_{2.13(4)}\text{Zr}_{0.89(2)}\text{U}_{0.98(1)}\text{O}_{7.5(2)}$
		3- $\text{La}_{3.13(5)}\text{Zr}_{0.24(1)}\text{U}_{0.63(2)}\text{O}_{6.77(9)}$

The variation in the contrast exhibited in the BSE images of the target composition $\text{La}_2\text{Zr}_{1.1}\text{U}_{0.9}\text{O}_{7+\delta}$ evidenced a multiphase assemblage in Figure 5.2(i), three phases, denoted as phase 1, 2 and 3 from the EDS investigation. Semi-quantitative EDS analysis was performed at 30,000x magnification for all materials, including the three regions distinctive in contrast seen within Figure 5.2(i), the results are summarised in Table 5.5. The average composition of the material with target composition $\text{La}_2\text{Zr}_{1.1}\text{U}_{0.9}\text{O}_{7+\delta}$ (i.e. covering all three regions of contrast) was measured by EDS to be $\text{La}_{2.01(4)}\text{Zr}_{1.13(2)}\text{U}_{0.89(2)}\text{O}_{7.5(1)}$, again in line with the target stoichiometry. The oxygen stoichiometry of the compositions summarised in Table 5.5 were estimated from determination of the bulk uranium oxidation state by the U L_3 edge XANES analysis (see Figure 5.9 and Table 5.14).

The crystallographic structure of these phases were explored using X-ray diffraction, as summarised in Section 5.3.2.2.

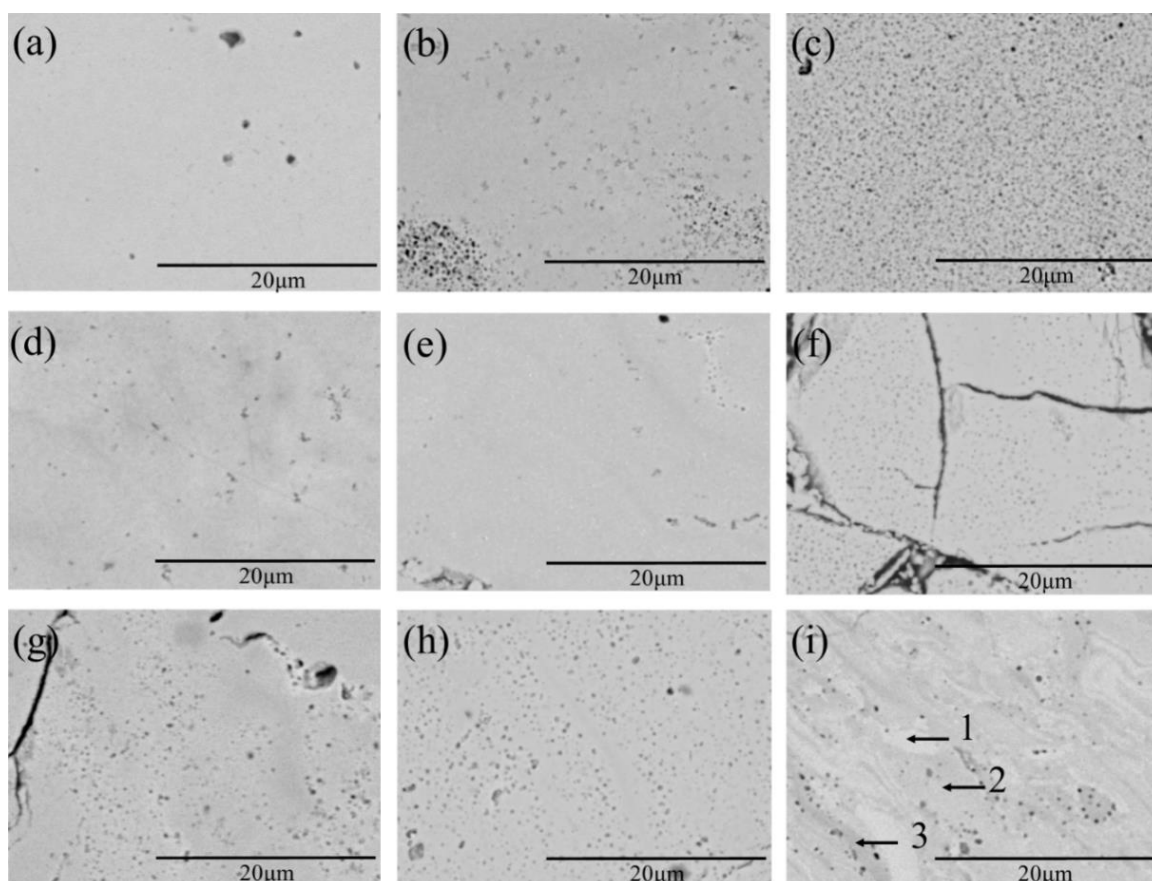


Figure 5.2: Back scattered electron diffraction image (a)-(i) for composition $\text{La}_2\text{Zr}_{2-x}\text{U}_x\text{O}_{7+\delta}$ with $x=0.1-0.9$, respectively. The black areas within the images are indicative of porosity / cracks within the surface. EDS on the surface of (i) indicates the formation of 3 phases closely mixed, these have been labelled as Phase 1, 2 and 3.

5.3.2 X-ray diffraction

X-ray diffraction (XRD) analysis was performed in transmission mode on a STOE-PSD diffractometer, using a $\text{Cu K}\alpha_1$ radiation ($\lambda=1.5408 \text{ \AA}$) source operating at a working voltage and current of 40kV and 35mA, respectively. Sample preparation was performed within a dedicated fume cupboard. Finely powdered samples were glued to acetate films and placed into the relevant STOE sample holder. Data were collected between $4.00 \leq 2\theta \leq 94.00^\circ$ with a step size of 0.02, total collection time was ~ 1.5 hours per sample. A model of a pyrochlore structure was fitted to the data, and refined using the GSAS graphic user interface [31, 32], an example of the quality of the fitted model is in Figure 5.3. The complete set of refinement data are included as Appendix B.

5.3.2.1 Materials formed in an air atmosphere

X-ray diffraction was completed on the 5 single phase materials, for compositions up to, and including, the substitution $x=0.5$, and the multiphase system, as determined by SEM,

with $x=0.6$. Figure 5.4 shows the X-ray diffraction patterns acquired for the composition range $0.1 \leq x \leq 0.6$. The diffraction patterns were indexed using the pyrochlore supercell ($Fd\bar{3}m$, $a = 2a_F$) with the diagnostic supercell reflections highlighted by an arrow. The insert in Figure 5.4 shows the pyrochlore (111) reflection, highlighting the changes in the intensity of this reflection with increased uranium substitution. It can be seen that as the substitution of uranium increases the intensity of the pyrochlore supercell reflections decreases. The intensity of the pyrochlore supercell in XRD reflections are sensitive to the difference in the electron density of the each of the A and B sites of the $A_2B_2O_7$ structure. Assuming the A site to be exclusively occupied by La and the B site to be exclusively occupied by the Zr and U, then the difference in electron density, reduced from 36 electrons at $x = 0.0$, to near 0 electrons at $x = 0.6$ (Table 5.6). Consequently, the intensity of the pyrochlore supercell reflections decreases monotonically with increasing uranium content (x). The absence of appreciable intensity the super cell reflections of compositions $x = 0.5$ and $x = 0.6$, could be interpreted as a transformation from the pyrochlore to a defect fluorite structure. In fact, electron diffraction, which is a more sensitive probe of small differences in the A and B site electron density, confirmed the presence of the pyrochlore supercell reflections in material where $x = 0.5$, as discussion in Section 5.3.1.1.

Table 5.6: Electron density difference between the ideal A and B site cations within composition $La_2(Zr_{2-x}U_x)O_{7+\delta}$ across the two extreme charges of U^{4+} and U^{6+} , with the possible U^{5+} residing within the middle of the two.

Composition, x	Difference of Electron Density between the A and B sites		r_A/r_B Range	
	U^{4+}	U^{6+}		
0.0	36		1.611	
0.1	30.8	31	1.592	1.610
0.2	25.6	26	1.574	1.609
0.3	20.4	21	1.556	1.608
0.4	15.2	16	1.538	1.607
0.5	10	11	1.521	1.606
0.6	4.8	6	1.505	1.604
0.7	0.4	1	1.488	1.603
0.8	5.6	4	1.472	1.602
0.9	10.8	9	1.456	1.601

For the material with substitution $x=0.6$, the supercell pyrochlore reflections did not have an appreciable intensity in the XRD patterns, see Figure 5.4 insert. Close inspection of the XRD pattern of the composition $x = 0.6$, revealed the reflection full width at half height to be greater than for the composition $x = 0.5$. This suggested the presence of

multiple phases, of distinct composition, consistent with SEM / EDX data, Figure 5.1(f). The chemical composition of each of the component phases was quantified through the use of EDS, see Table 5.4. These compositions were utilised for the refinement of the pyrochlore structure, therefore it was possible to calculate the electronic density differences between the A and B sites and the r_A/r_B ratios for the refined compositions, see Table 5.7.

Table 5.7: Electronic density difference calculations for the bulk phase assemblage, as identified using BSE, and the components identified in Figure 5.1(f), for the target composition $\text{La}_2\text{Zr}_{1.4}\text{U}_{0.6}\text{O}_{7+\delta}$, and the corresponding range of r_A/r_B values. Calculations made under the assumption that as the lanthanum orientates on the A site and the uranium and zirconium on the B site at the ratios determined by EDS, see Table 5.4.

Semi-Quantitative EDS		Difference of Electron Density between the A and B sites		r_A/r_B Range	
		U^{4+}	U^{6+}		
(f)	1- $\text{La}_{1.94(1)}\text{Zr}_{0.55(1)}\text{U}_{1.52(1)}\text{O}_{8.2(1)}$	46.3	48.8	1.287	1.495
	2- $\text{La}_{1.94(1)}\text{Zr}_{1.51(1)}\text{U}_{0.53(1)}\text{O}_{7.40(4)}$	3.8	4.8	1.444	1.527
BULK	$\text{La}_{2.06(2)}\text{Zr}_{1.35(1)}\text{U}_{0.58(1)}\text{O}_{7.39(4)}$	11.6	12.76	1.606	1.712

Table 5.8: Unit cell parameters and thermal, U_{iso} , parameters as refined in the GSAS software from x-ray diffraction data collected on the Stoe PSD instrument for materials of general composition $\text{La}_2\text{Zr}_{2-x}\text{U}_x\text{O}_{7+\delta}$ with $0.1 \leq x \leq 0.6$ and formed in an air atmosphere. ^{*1} as taken from reference [33].

x	a (Å)	48f O-x	χ^2	wRp	U_{iso}		
					La (Å ²)	Zr & U (Å ²)	O ₁ & O ₂ (Å ²)
0.0 ^{*1}	10.779(1)	0.331(1)	-	-	-	-	-
0.1	10.812(1)	0.332(1)	1.002	0.120	2.246(1)	1.701(1)	2.796(4)
0.2	10.812(1)	0.335(1)	1.014	0.142	3.085(1)	3.142(1)	3.325(4)
0.3	10.821(2)	0.336(2)	0.945	0.201	3.204(2)	2.734(2)	3.585(6)
0.4	10.832(1)	0.336(2)	1.208	0.152	2.770(2)	2.239(2)	3.453(6)
0.5	10.827(4)	0.340(2)	0.996	0.146	2.113(2)	2.667(2)	3.701(6)
0.6₁	10.833(5)	0.354(1)	0.912	0.232	-	-	-
0.6₂	10.836(2)	0.342(5)			-	-	-

The refined parameters from the GSAS software for the fitting of the pyrochlore model to the data are summarised in Table 5.8 for the single phase compositions $\text{La}_2\text{Zr}_{2-x}\text{U}_x\text{O}_{7+\delta}$ $0.1 \leq x \leq 0.5$ formed in air. The a-parameter and the 48f oxygen x-position have been refined for both phase 1 and 2 in the x=0.6 composition. The a-parameter for the air formed materials, in Table 5.8, generally show an increase in the a-parameter with an increased substitution of uranium. The 48f oxygen x-parameter also shifts to higher values with increased substitution of uranium, see Figure 5.5.

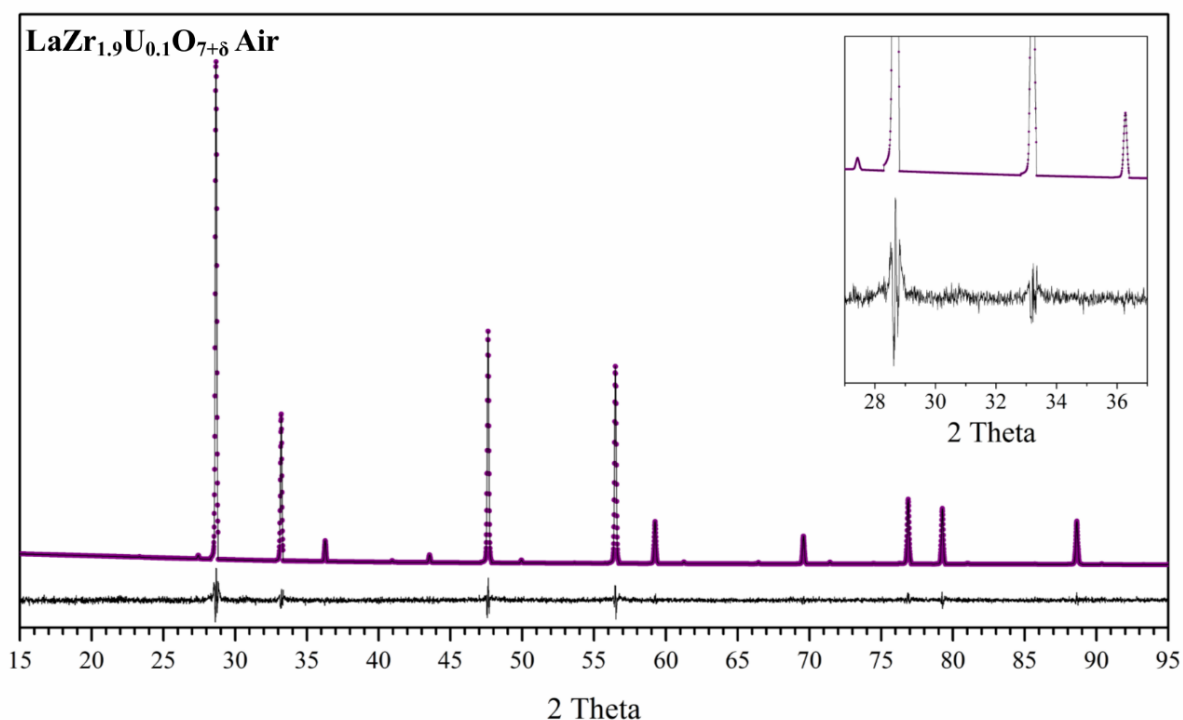


Figure 5.3: The refinement model of material with ideal composition $\text{La}_2\text{Zr}_{1.9}\text{U}_{0.1}\text{O}_{7+\delta}$ formed in an air atmosphere. The pyrochlore models has been refined to the data using the GSAS software. The model fitted is shown in the purple trace, the quality of the fitting to the data are shown by the observed minus calculated difference trace (black).

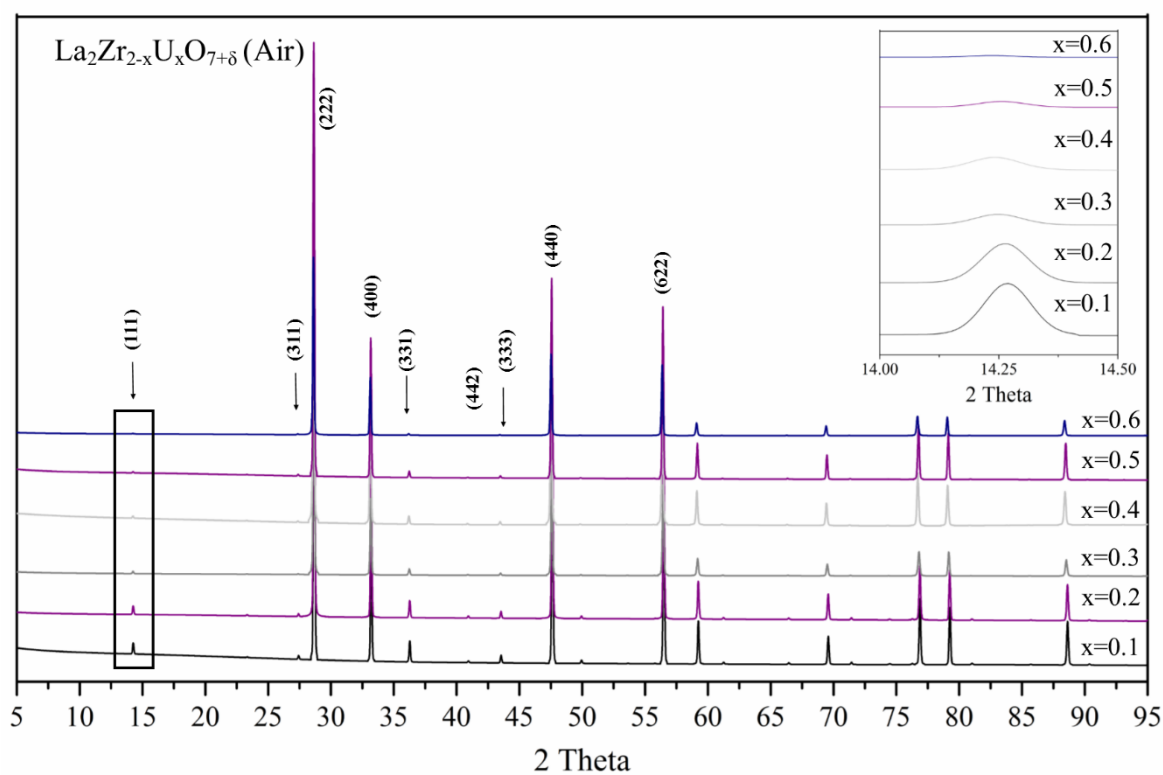


Figure 5.4: GSAS refined structure fitted to X-ray diffraction data collected on the Stoe PSD instrument on samples of the system $\text{La}_2\text{Zr}_{2-x}\text{U}_x\text{O}_{7+\delta}$ with $0.1 \leq x \leq 0.6$ formed in an air atmosphere. Insert shows enlargement of the boxed area, the (111) pyrochlore reflection.

The isotropic thermal parameters of the U and Zr cations, which were assumed to share occupancy of the B site, were constrained to be equal. The isotropic thermal parameters of the oxygen within the structure, O₁ and O₂, were also constrained to be equal. This was due to the interaction of X-rays, in powder XRD analysis, only weakly scattering by the oxygen anions within the structure, and therefore unable to distinguish between the two anion sites.

The refined bond lengths in Table 5.9 generally show a linear response to the increased substitution of uranium. Independent from the general trend is Phase 1, La_{1.94(1)}Zr_{0.55(1)}U_{1.52(1)}O_{8.2(1)}, in the x=0.6 composition. With Phase 1 the La-O₁ length has contracted at a greater fraction to the pure lanthanum zirconate than other materials. Phase 1 is a uranium rich material, where uranium is expected to situate on the B-site. The B-site bond length, B-O₂, is greater than the general trend within the data.

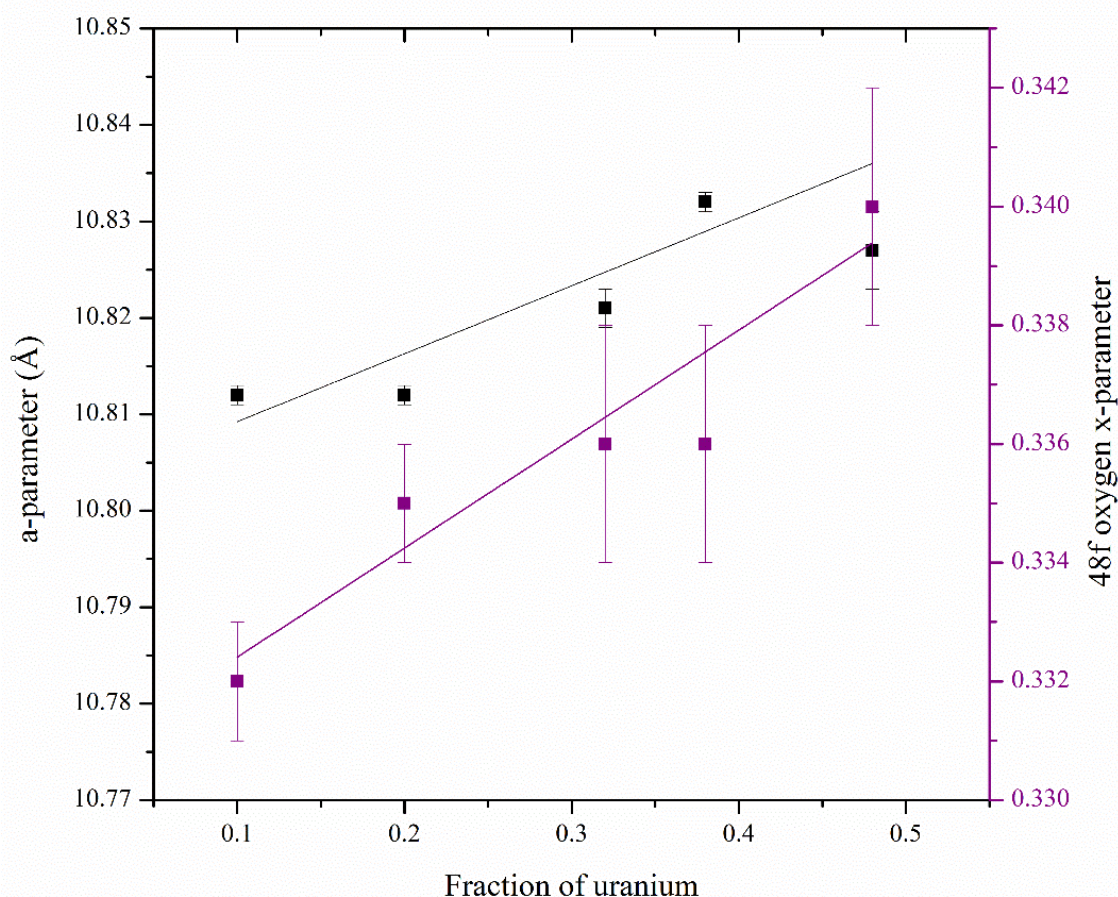


Figure 5.5: Linear relationship observed between the 48f oxygen x-parameter and the a-parameters, as refined in Table 5.8 for single phase pyrochlore materials of the system La₂Zr_{2-x}U_xO_{7+δ} with x=0.1 - 0.5 formed in air. The fraction of uranium is as measured by EDS analysis.

Table 5.9: Key bond lengths for materials with target composition $\text{La}_2\text{Zr}_{2-x}\text{U}_x\text{O}_7$ formed in an air atmosphere, as refined from Rietveld analysis of the XRD data. *As taken from reference [33].

Bond		Length (Å)		
		La-O ₁	La-O ₂	B-O ₂
Bond Multiplicity		(x2)	(x6)	(x6)
Composition, x	0.0*	2.643	2.338	2.099
	0.1	2.635(8)	2.341(2)	2.108(5)
	0.2	2.610(7)	2.341(2)	2.124(5)
	0.3	2.61(1)	2.343(2)	2.129(8)
	0.4	2.61(1)	2.345(2)	2.133(9)
	0.5	2.58(1)	2.344(1)	2.15(1)
	0.6₁	2.56(3)	2.346(7)	2.23(2)
	0.6₂	2.580(8)	2.346(3)	2.163(6)

5.3.2.2 Materials formed in a hydrogen / nitrogen atmosphere

Figure 5.7 shows the XRD patterns of compositions fabricated in a 5% H_2 / N_2 atmosphere. The pyrochlore supercell reflections, highlighted by an arrow, were generally of a very weak intensity, with the (111) reflection apparently absent. Figure 5.7(b) shows, as an example, the (311) reflection. The decrease intensity of the supercell with increasing content of uranium (x). Unit cell parameters from the refinement of the pyrochlore structure for each composition, as taken from the EDS analysis in Table 5.5, are summarised in Table 5.10, with bond lengths determined by the refinement summarised in Table 5.11.

Considering the composition $\text{La}_2\text{Zr}_{1.1}\text{U}_{0.9}\text{O}_{7+\delta}$, a model of a pyrochlore structure could not be fitted to the data, however, a model using the fluorite sub cell was successfully refined to the data. To improve the fit, and considering the observations in the BSE / EDS data, Figure 5.2(i), a phase assemblage with 3 individual fluorite structures were fitted to the data, the a-parameters of which are included within Table 5.10. In order to compare the lattice parameter of the fluorite structures which make up the phase assemblage of $x=0.9$, to that of the pyrochlore super cell, the a-parameters are reported as $2a_F$ (where $a_P=2a_F$).

Summarised within Table 5.11 are the bond length from the Rietveld refinement of the pyrochlore model fitted to the X-ray diffraction data. Unlike the materials formed in air, there is only a weak linear relationship in the 48f oxygen x-parameter, and no linearity of the calculated bond lengths. However there is a linear relationship in the a-parameter, with increased uranium the a-parameter increases indicating a constant increase in the unit cell volume ($V=a^3$), see Figure 5.6.

In general, as seen with the air formed materials, when uranium is substituted into the composition the B-O₂ bond length increases compared to the reference material, La₂Zr₂O₇. The La-O₁ length has also contracted from the same reference and the La-O₂ bond length is similar but slightly larger than the reference.

Table 5.10: Unit cell parameters and thermal, U_{iso} , parameters as refined in the GSAS software from X-ray diffraction data collected on the Stoe PSD instrument for materials of composition La₂Zr_{2-x}U_xO_{7+δ} with $0.1 \leq x \leq 0.9$ and formed in a hydrogen/nitrogen atmosphere. Composition with $x=0.9$ has been fitted using a fluorite structure, however for comparison the lattice parameter has been doubled. *₁ as taken from reference [33].

x	$U_{iso} \times 100$						
	a (Å)	48f O-x	χ^2	wRp	La (Å ²)	Zr & U (Å ²)	O ₁ & O ₂ (Å ²)
0.0* ₁	10.779(1)	0.331(1)	-	-	-	-	-
0.1	10.808(2)	0.334(1)	0.951	0.133	1.470(1)	1.722(1)	1.957(5)
0.2	10.818(2)	0.332(1)	0.999	0.149	2.110(1)	1.879(2)	1.575(5)
0.3	10.837(2)	0.338(2)	0.915	0.140	2.017(2)	1.960(2)	2.590(5)
0.4	10.851(2)	0.345(3)	0.889	0.128	1.210(2)	2.189(2)	4.296(7)
0.5	10.843(3)	0.335(2)	0.997	0.125	1.512(2)	2.283(3)	1.581(7)
0.6	10.863(2)	0.344(3)	0.878	0.118	1.341(2)	2.420(2)	3.046(7)
0.7	10.896(3)	0.339(3)	0.876	0.251	3.225(4)	0.892(3)	1.568(14)
0.8	10.891(3)	0.342(2)	0.791	0.335	1.947(2)	6.316(3)	8.035(12)
0.9 ₁	10.522 (6)	-	0.881	0.296	-	-	-
0.9 ₂	10.488(6)	-			-	-	-
0.9 ₃	10.456(12)	-			-	-	-

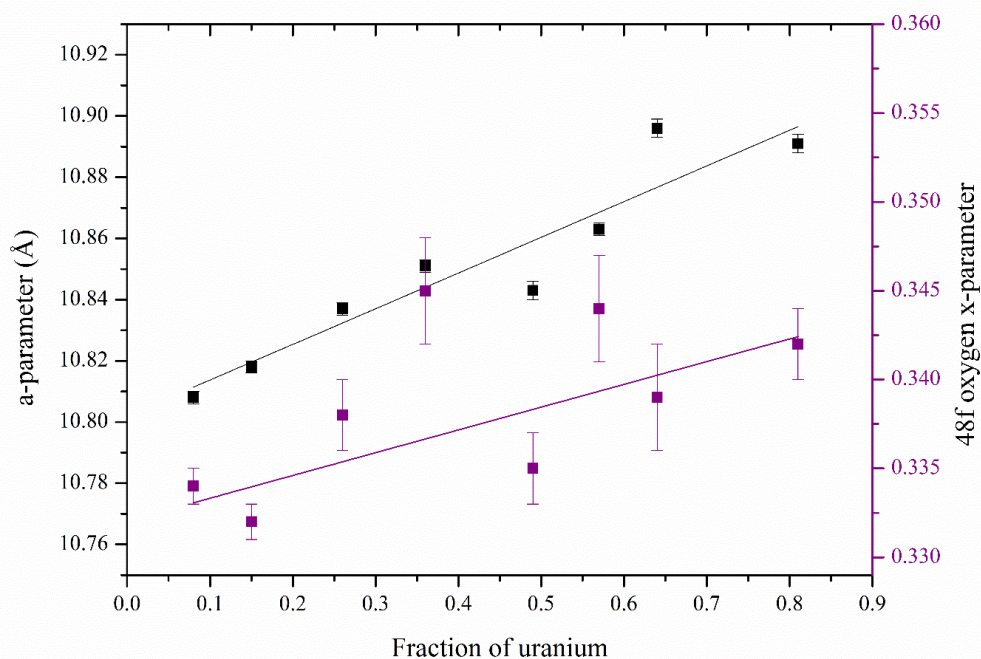


Figure 5.6: Relationship observed between the 48f oxygen x-parameter and the a-parameters, as refined in Table 5.8 for single phase pyrochlore materials of the system La₂Zr_{2-x}U_xO_{7+δ} with $x=0.1 - 0.8$ formed in a hydrogen / nitrogen. The fraction of uranium is as measured by EDS analysis.

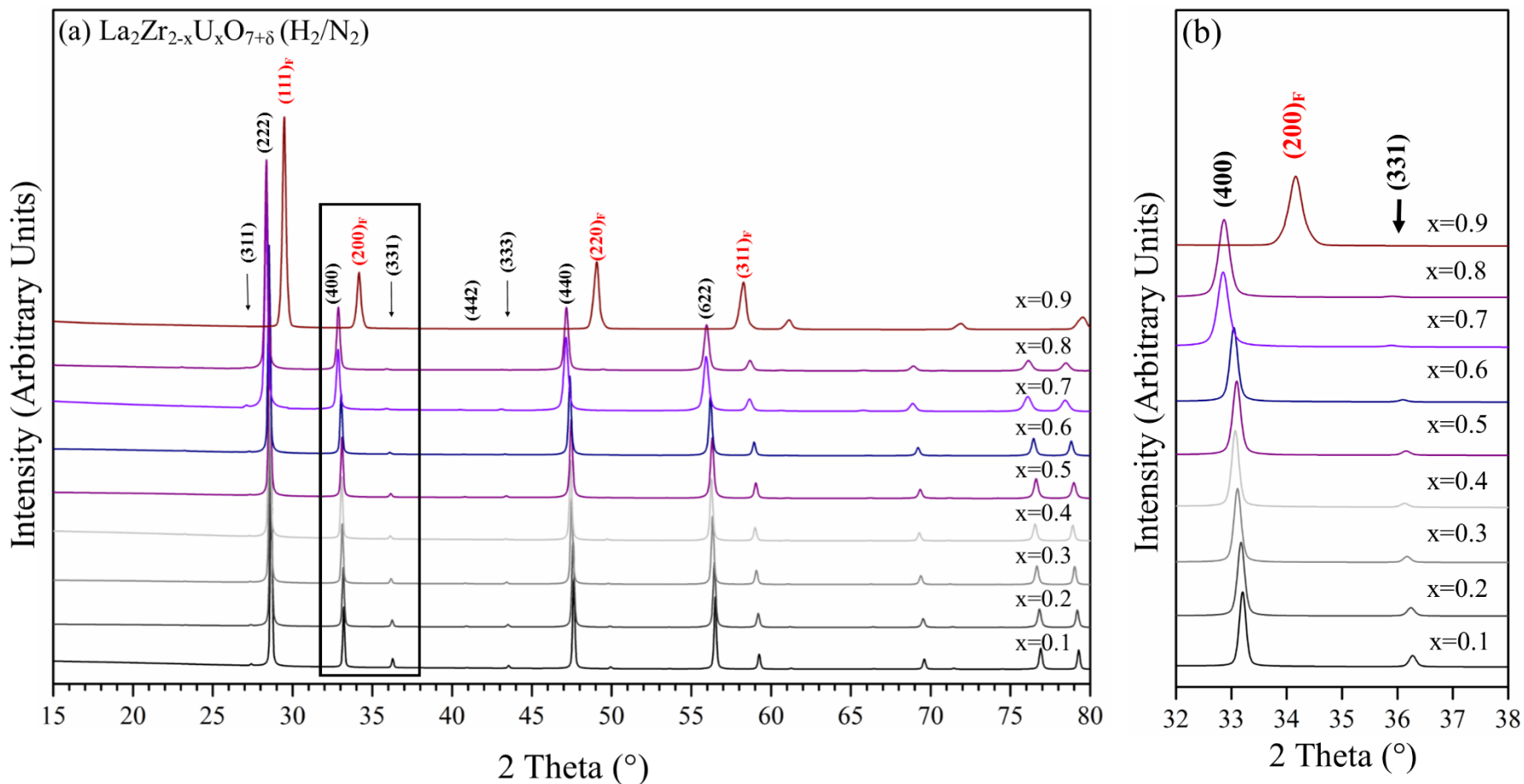


Figure 5.7: (a) X-ray diffraction of materials from the system $\text{La}_2\text{Zr}_{2-x}\text{U}_x\text{O}_{7+\delta}$ with $x=0.1-0.9$ formed in a reducing hydrogen/nitrogen atmosphere and (b) the magnification of the (400) and (331) pyrochlore reflections area highlights in (a) and their development with increasing substitution of uranium up to, and including composition $\text{La}_2\text{Zr}_{1.2}\text{U}_{0.8}\text{O}_{7+\delta}$. The material with composition $\text{La}_2\text{Zr}_{1.1}\text{U}_{0.9}\text{O}_{7+\delta}$ has been modelled to a fluorite structured material using the GSAS software. The fluorite indices are highlighted in red with the 'F' fluorite subscript.

Table 5.11: Key bond lengths for materials with target composition $\text{La}_2\text{Zr}_{2-x}\text{U}_x\text{O}_7$ formed in a hydrogen/ nitrogen atmosphere, as refined from Rietveld analysis of the X-ray diffraction data. *As taken from reference [33]

Bond		Length (Å)		
		La-O ₁	La-O ₂	B-O ₂
Bond Multiplicity		(x2)	(x6)	(x6)
Composition, x	0.0*	2.643	2.338	2.099
	0.1	2.623(10)	2.340(1)	2.114(6)
	0.2	2.639(9)	2.342(1)	2.108(6)
	0.3	2.601(12)	2.346(1)	2.138(8)
	0.4	2.553(19)	2.349(1)	2.177(13)
	0.5	2.624(16)	2.348(1)	2.126(10)
	0.6	2.563(20)	2.352(1)	2.174(14)
	0.7	2.616(32)	2.359(1)	2.150(21)
	0.8	2.580(80)	2.358(1)	2.170(50)

5.3.3 X-ray Absorption Near Edge Structure Spectroscopy

X-ray Absorption Near Edge Structure (XANES) analysis was completed in transmission mode on the X23A2 beamline at the National Synchrotron Light Source (NSLS), Brookhaven National Laboratory (BNL), USA. Finely ground specimens were dispersed in polyethylene glycol to achieve a thickness of one absorption length, full experimental set up can be found in Section 3.6.1.1. Target energies to observe the U L₃-edge were selected in order to provide information on the average oxidation state of the uranium within the compositions. This was completed through the comparison of materials to standards $\text{CaU}^{6+}\text{O}_4$, $\text{U}_{0.5}^{5+}\text{Y}_{0.5}\text{Ti}_2\text{O}_6$ and $\text{U}^{4+}\text{Ti}_2\text{O}_6$ with known oxidation states of uranium; U^{6+} , U^{5+} and U^{4+} , respectively [34]. The comparison of the absorption edges of the materials was made. An absorption edge is where there is a sharp rise within the $\mu(\text{E})$ value, at a particular energy, E_0 , due to interaction of the incident X-rays with an electronic shell of the probed atom. E_0 was determined as energy at half of the normalised intensity of the $\mu(\text{E})$ data, this value was calibrated and corrected through the use of the yttrium K-edge of Y_2O_3 as a reference material, collected simultaneously with the data. The energy at half the height of the normalised intensity was selected due to the differing coordination environments of the uranium within the standards compared to the measured materials, artificially effecting the position of the E_0 value. A true E_0 value quantifies the maxima of the first derivative of the $\mu(\text{E})$ data. Background removal and normalisation of the data to $\mu(\text{E})=1$ was performed using the Athena Programme [35].

Analysis of XANES data can be used as a fingerprint to quantify the uranium oxidation state. The full shape of the peak is both determined by the oxidation state and the coordination environment of the absorbent element. The target site of the uranium within the pyrochlore material, the B-site, is a 6-fold coordinated site, this will influence the shape of the peak of the $\mu(E)$ curve. The crystal structure of the uranium in $U^{4+}Ti_2O_6$, the U^{4+} standard, and $U^{5+}_{0.5}Y_{0.5}Ti_2O_6$, the U^{5+} standard, dictate that the uranium has a 6-fold coordinated local environment, whereas the uranium for the U^{6+} standard, $CaU^{6+}O_4$, is found in an 8-fold coordination environment. The linear deconvolution feature of the Athena software enables the proportions of U^{4+} , U^{5+} and U^{6+} within the materials to be calculated from the standards could have been utilised [36]. However, the standards would be required to have the same coordination environment of the target element in order to provide an accurate analysis. For this reason the alternative methodology of using the energy at half the height of the normalised intensity for E_0 values, to approximate the average oxidation state of the uranium species within the materials was used.

5.3.3.1 Materials formed in an Air Atmosphere

Figure 5.8 show the XANES data for the U L_3 -edge of materials with ideal compositions $La_2Zr_{2-x}U_xO_{7+\delta}$ ($x=0.1-0.6$) formed in an air atmosphere. Each data set has been normalised to an absorption edge step of $\mu(E)=1$.

The XANES data within Figure 5.8 were utilised to ascertain the E_0 values, summarised in Table 5.12, showing the change in uranium oxidation state with increasing substitution. As the fraction of uranium in the ideal compositions increases the oxygen stoichiometry required to charge balance the material increases.

For the air formed materials, the average uranium oxidation state >5.5 , this is evidence that uranium oxidation state is dominated by U^{6+} with an average uranium oxidation state formed from a combination of either U^{4+} or U^{5+} with U^{6+} . Therefore, a partial reduction in the average uranium oxidation state was effected, despite the materials being formed in air where oxygen was readily available.

For composition $x = 0.6$ has an average uranium oxidation state has been calculated on the bulk material (Table 5.7). The XANES technique is unable to distinguish between the two phases, therefore analysis of the oxygen stoichiometry for multiphase material, based on the cation stoichiometries measured by EDS analysis (Table 5.4), was completed under the assumption that the uranium oxidation state of each phase is equivalent and represented by the XANES measurement. Oxygen stoichiometries for the multiphase material (Table 5.12) have been calculated based on the average uranium oxidation state

of the bulk material. However, the refined XRD analysis (Figure 5.4), indicates a secondary phase with the structure of a pyrochlore (Table 5.8). The pyrochlore structure would be unable to accommodate an oxygen stoichiometry >8 , therefore this suggests that the average uranium oxidation state is not representative of both phases within the material.

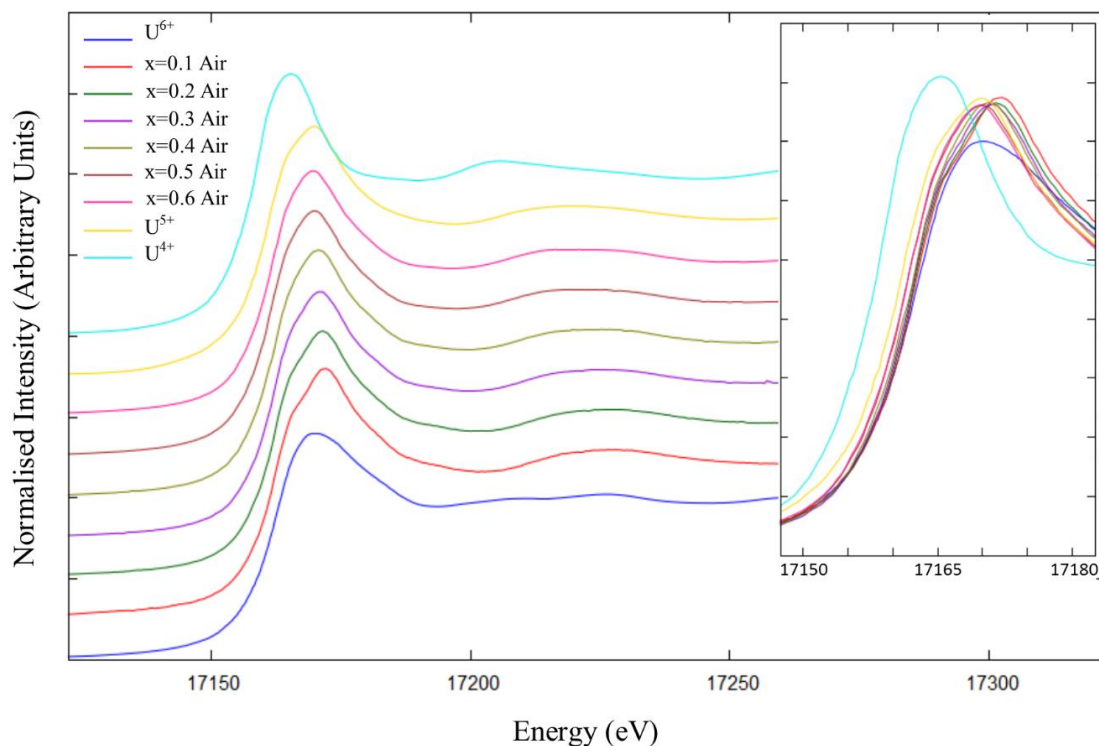


Figure 5.8: X-ray Absorption Near Edge Structure (XANES) data of the uranium completed on all samples of composition series $\text{La}_2(\text{Zr}_{2-x}\text{U}_x)\text{O}_7$ formed in air up to and including $x = 0.5$. Data reduction was performed using the Athena software. Data from uranium standards for U^{4+} , U^{5+} and U^{6+} are also shown.

For composition $x = 0.6$ has an average uranium oxidation state has been calculated on the bulk material (Table 5.7). The XANES technique is unable to distinguish between the two phases, therefore analysis of the oxygen stoichiometry for multiphase material, based on the cation stoichiometries measured by EDS analysis (Table 5.4), was completed under the assumption that the uranium oxidation state of each phase is equivalent and represented by the XANES measurement. Oxygen stoichiometries for the multiphase material (Table 5.12) have been calculated based on the average uranium oxidation state of the bulk material. However, the refined XRD analysis (Figure 5.4), indicates a secondary phase with the structure of a pyrochlore (Table 5.8). The pyrochlore structure would be unable to accommodate an oxygen stoichiometry >8 , therefore this suggests

that the average uranium oxidation state is not representative of both phases within the material.

Table 5.12: Summary of the uranium oxidation state for each composition formed in an air atmosphere, as determined from the linear fitting of the E_0 values extracted from the Athena fitting of the data.

Target composition	E_0 energy (eV)	U average oxidation state –calculated (error)	Oxygen Stoichiometry (error)
$\text{La}_2(\text{Zr}_{1.9}\text{U}_{0.1})\text{O}_{7+\delta}$	17158.8	5.97(13)	7.19 (1)
$\text{La}_2(\text{Zr}_{1.8}\text{U}_{0.2})\text{O}_{7+\delta}$	17158.7	5.93(13)	7.11(1)
$\text{La}_2(\text{Zr}_{1.7}\text{U}_{0.3})\text{O}_{7+\delta}$	17158.6	5.88(13)	7.46(2)
$\text{La}_2(\text{Zr}_{1.6}\text{U}_{0.4})\text{O}_{7+\delta}$	17158.3	5.75(13)	7.42(3)
$\text{La}_2(\text{Zr}_{1.5}\text{U}_{0.5})\text{O}_{7+\delta}$	17157.9	5.57 (13)	7.42(3)
$\text{La}_2(\text{Zr}_{1.4}\text{U}_{0.6})\text{O}_{7+\delta}$	1	17157.8	8.2(1)
	2		7.40(4)
	bulk		7.39(4)

5.3.3.2 Material formed in a Hydrogen / Nitrogen atmosphere

Figure 5.9 show the XANES data collected on the U L_3 -edge for materials of ideal composition $\text{La}_2\text{Zr}_{2-x}\text{U}_x\text{O}_{7+\delta}$ ($x=0.2, 0.4, 0.6$ and 0.8) formed in a reducing hydrogen/nitrogen atmosphere. Each data set has been normalised to $\mu(E)=1$.

The energy value at $\mu(E)=0.5$ was used to approximate the average oxidation state of the uranium species within the material using measured standards as comparison. Analysis of the measured compositions average uranium oxidation state, and the corresponding oxygen stoichiometry for the measured compositions (Table 5.5), can be seen in Table 5.13.

Due to restrictions on the instrument schedule not all materials formed in a hydrogen/nitrogen atmosphere have been investigated by U L_3 XANES, just alternate compositions. In order to gain information on the non-measured materials the calculated uranium oxidation states for the measured materials were plotted against uranium substitution level (Figure 5.10) to establish a linear line of best fit. The uranium oxidation state of non-measured materials have been estimated from the equation of this line of best fit in Figure 5.10. The calculated values are quoted within Table 5.14.

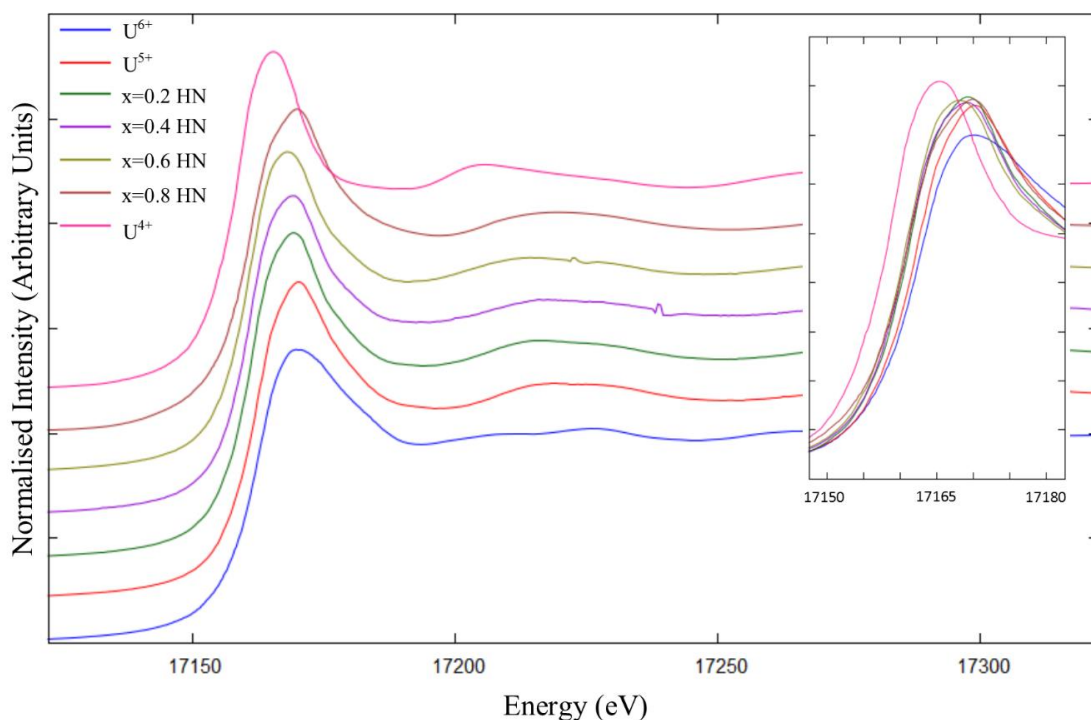


Figure 5.9: X-ray Absorption Near Edge Structure (XANES) data fitting of the Uranium completed on alternate materials of composition series $\text{La}_2(\text{Zr}_{2-x}\text{U}_x)\text{O}_7$ formed in hydrogen/nitrogen, up to and including $x=0.8$, using the Athena software. The figure includes the fitting for U^{4+} , U^{5+} and U^{6+} standards, as measured and used to quantify the oxidation state of the samples.

Table 5.13: Summary of the uranium oxidation state for each measured composition formed in a hydrogen/nitrogen atmosphere, as determined from the linear fitting of the E_0 values extracted from the Athena fitting of the data. The oxygen stoichiometry has been calculated from the measured compositions within the EDS analysis, Table 5.5.

Target composition	E_0 Energy (eV)	Average U Oxidation State (error)	Oxygen Stoichiometry (error)
$\text{La}_2(\text{Zr}_{1.8}\text{U}_{0.2})\text{O}_{7+\delta}$	17158.1	5.66(4)	7.38(3)
$\text{La}_2(\text{Zr}_{1.6}\text{U}_{0.4})\text{O}_{7+\delta}$	17157.6	5.44(4)	7.46(7)
$\text{La}_2(\text{Zr}_{1.4}\text{U}_{0.6})\text{O}_{7+\delta}$	17157.3	5.31(4)	7.5(1)
$\text{La}_2(\text{Zr}_{1.2}\text{U}_{0.8})\text{O}_{7+\delta}$	17156.9	5.13(4)	7.6(2)

For materials formed in a hydrogen / nitrogen atmosphere there is an inverse relationship between the increased uranium substitution and the average uranium oxidation state measured. This results in a non-linear relationship between the oxygen stoichiometry required to charge balance the compositions. As the fraction of uranium (x) increases for the hydrogen / nitrogen formed materials, then E_0 values generally shift closer towards a lower average uranium oxidation states. The calculated oxidation states for the higher substitutions of uranium ($x=0.6$ and $x=0.8$ in H_2/N_2) have a calculated average uranium

oxidation state close to U^{5+} . This shows that under a reducing atmosphere a greater fraction of the uranium must have reduced from U^{6+} , to equate to the lower average oxidation states.

Table 5.14: Calculated uranium oxidation state based on the linear fitting of the measured uranium average oxidation state and the inferred oxygen stoichiometry within the structure.

x	Average U Oxidation State (calculated)	Oxygen Stoichiometry (calculated)
0.1	5.69(3)	7.33(1)
0.2	5.64(3)	7.34(2)
0.3	5.55(3)	7.40(4)
0.4	5.47(3)	7.41(5)
0.5	5.37(3)	7.28(7)
0.6	5.31(3)	7.42(9)
0.7	5.25(3)	7.5(1)
0.8	5.12(3)	7.4(1)
0.9	5.06(3)	8.4(3)
1		7.5(2)
2		6.77(9)
3		7.5(1)
bulk		

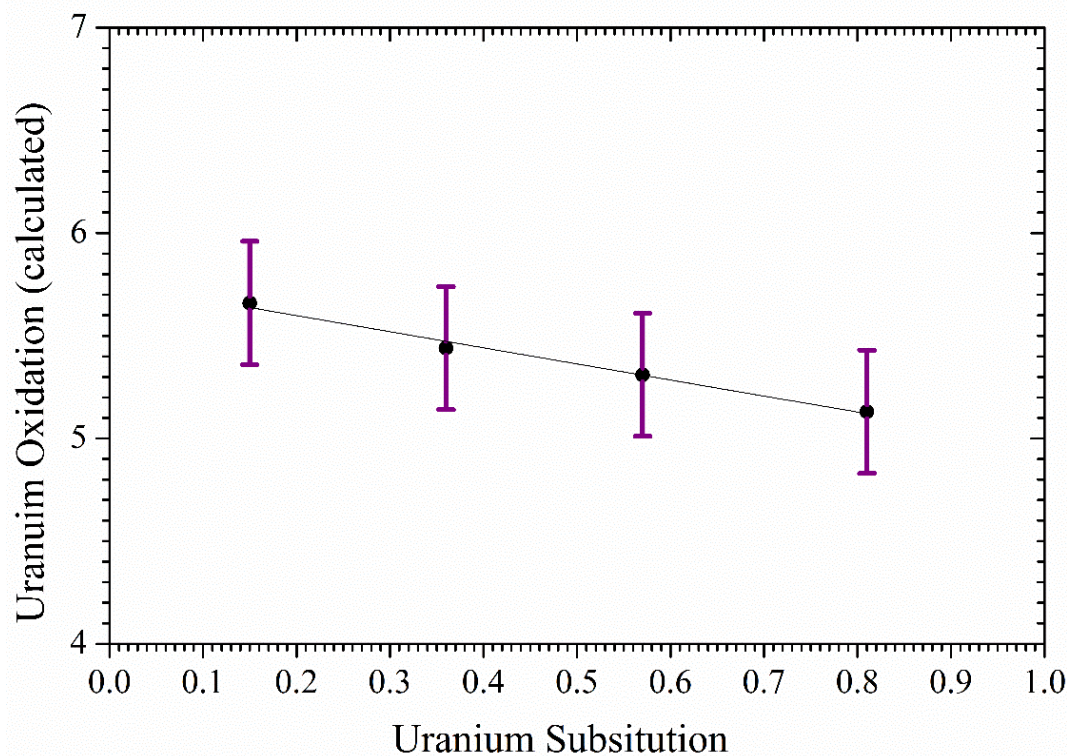


Figure 5.10: Linear fitting of the uranium oxidation state as a function of uranium fraction, as measured in the EDS analysis for general composition $La_2(Zr_{2-x}U_x)O_{7+\delta}$.

5.3.4 Transmission Electron Microscopy

TEM investigations were completed on single grains of material, ground from the bulk composition and mounted on a holey carbon-copper grid, the full experimental set up can be found in Section 3.4.1.

Electron diffraction images were collected using the Technai G² F20 XT TEM instrument at The Institute of Transuranium Elements (ITU), Karlsruhe, Germany. Analysis was completed on the [110]_F and [112]_F zone axis in order to enable the identification of the pyrochlore superstructure on the fluorite sub-lattice, whose cell is identified by the F subscript in the annotated TEM images. The presence of sharp Bragg reflections, such as those labelled in Figures 5.11 and 5.12 for the air and hydrogen / nitrogen formed materials, respectively, indicate the presence of the ordered fluorite substructure. These reflections describe the reciprocal lattice of the general fluorite matrix, G_F. These are surrounded by additional sharp intensities highlighting a cation/anion super-lattice. These additional intensities are described using the modulation vector 'q', relating the additional scattered energy to the underlying super-lattice through the use of G_F±q. The presence of the sharp intensities at G_F±½(001)* positions, observed down the [110]_F zone axis, and G_F±½(111)* positions, observed down both the [110]_F and [112]_F zone axis, as shown in Figures 5.11 and 5.10, are indicative of the presence of the pyrochlore superstructure. Due to time constraints on access to the instrument the full set of electron diffraction patterns could not be collected but a representative example have been analysed.

5.3.3.1 Materials formed in an air atmosphere

For the air formed materials, electron diffraction data from samples with target compositions La₂Zr_{2-x}U_xO_{7+δ}, with x=0.1, 0.3 and 0.5 was collected and analysed. Figure 5.11 (a) and (b) show a typical [110]_F and [112]_F zone axis diffraction pattern for the materials with ideal composition La₂Zr_{1.9}U_{0.1}O_{7+δ} (x=0.1) formed in an air atmosphere. Indexed are the fluorite sub-lattice of the structure with the presence of sharp reflections at positions G_F±½(111) highlighted with the arrows in (a) and (b) and the G_F±½(001) intensity highlighted with the arrow in (a), indicating the presence of the ordered pyrochlore superstructure. Similar super lattice reflections, indicated by the arrows, are observed in all analysed materials, up to, and including, substitution of x=0.5, with ideal compositions La₂Zr_{1.7}U_{0.3}O_{7+δ} and La₂Zr_{1.5}U_{0.5}O_{7+δ} also shown in Figure 5.11. The intensity of the pyrochlore supercell reflections highlighted appear to be consistent

relative to the fluorite reflections indexed. The definition, or sharpness, of the pyrochlore supercell reflections are also retained.

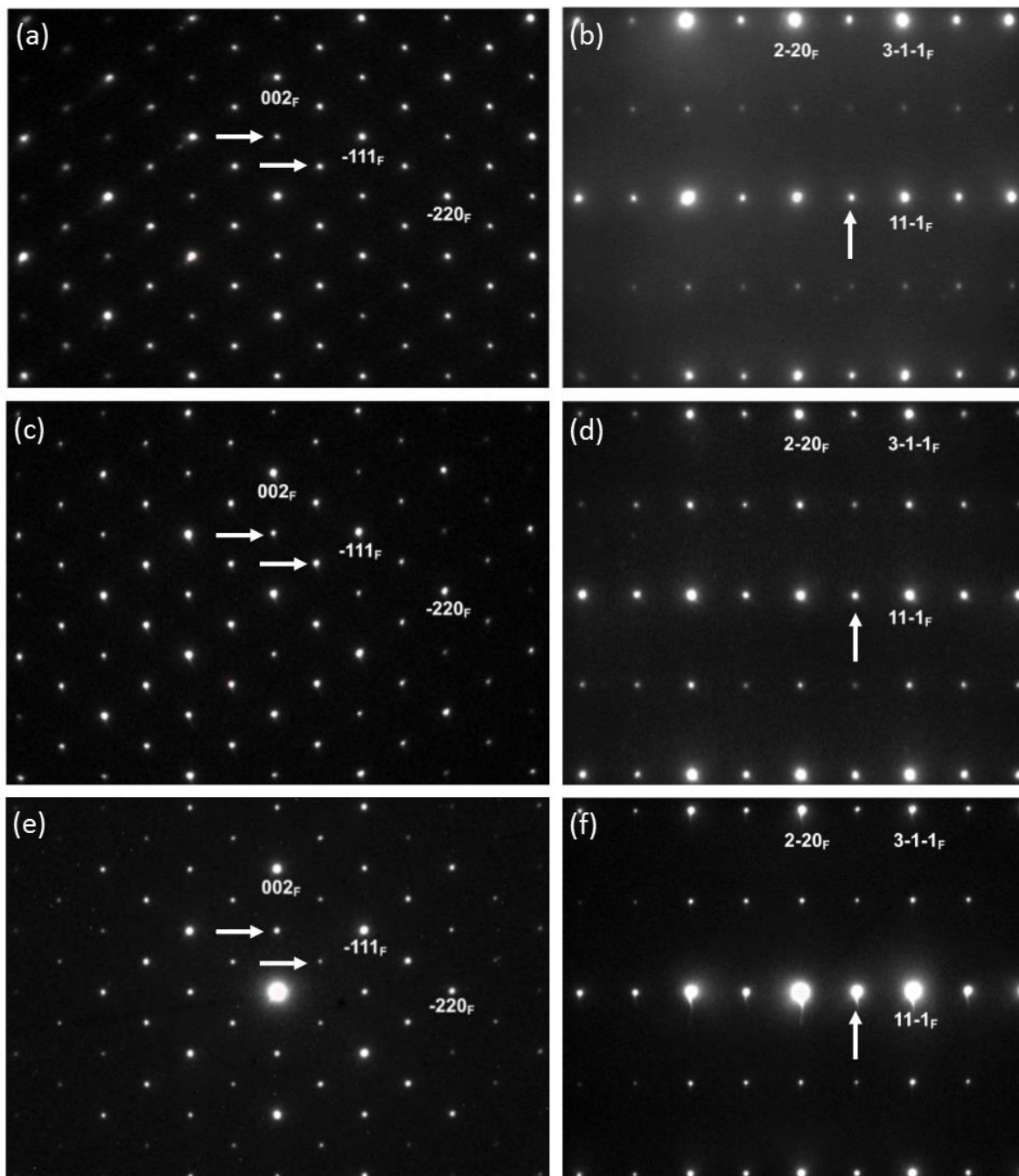


Figure 5.11: Electron diffraction images, indexed with respect to the fluorite substructure, of materials from the series $\text{La}_2\text{Zr}_{2-x}\text{U}_x\text{O}_{7+\delta}$ formed in air atmosphere with (a) $[110]_F$ and (b) $[112]_F$ zone axis diffraction patterns for $\text{La}_2\text{Zr}_{1.9}\text{U}_{0.1}\text{O}_{7+\delta}$, (c) $[110]_F$ and (d) $[112]_F$ zone axis diffraction patterns for $\text{La}_2\text{Zr}_{1.7}\text{U}_{0.3}\text{O}_{7+\delta}$, (e) $[110]_F$ and (f) $[112]_F$ zone axis diffraction patterns for $\text{La}_2\text{Zr}_{1.5}\text{U}_{0.5}\text{O}_{7+\delta}$.

5.3.3.2 Materials formed in a reducing hydrogen/nitrogen atmosphere

Figure 5.12 shows images collected from the materials with composition $\text{La}_2\text{Zr}_{2-x}\text{U}_x\text{O}_{7+\delta}$, with $x=0.2, 0.4, 0.6$ and 0.8 formed in a hydrogen / nitrogen atmosphere. Electron diffraction images have been collected on the $[110]_F$ and $[112]_F$ zone axis. Indexed within the images are the fluorite sub-lattice of the structure. The presence of sharp reflections at positions $G_F \pm \frac{1}{2}(111)$ highlighted with the arrows on both axis and the $G_F \pm \frac{1}{2}(001)$ intensity highlighted with the arrow on the images of the $[110]_F$ axis, indicates the presence of the ordered pyrochlore superstructure. Similar super lattice reflections, indicated by the arrows, are observed in all the materials analysed, up to and including substitution of $x=0.8$, as shown in Figure 5.12(g) and (h). The definition, or sharpness, of the pyrochlore diffraction reflections are retained throughout the compositions and the ratio of the intensity of the indexed fluorite cell to the highlighted pyrochlore supercell appear constant.

5.4 Discussion

5.4.1 Discussions on Air formed Materials

Materials with the general composition $\text{La}_2\text{Zr}_{2-x}\text{U}_x\text{O}_{7+\delta}$ where $0.1 \leq x \leq 0.6$, were formed in an air atmosphere, and have undergone crystallographic and chemical analysis. The diffractions patterns at $x \leq 0.5$ were indexed to the pyrochlore super cell. For target composition $\text{La}_2\text{Zr}_{2-x}\text{U}_x\text{O}_{7+\delta}$ where $x = 0.6$, a multiphase assemblage was identified using back scattered electron microscopy, coupled with EDS analysis. EDS analysis showed, in general, a close correlation between the measured and target compositions for all materials. It was also identified that for the materials formed in air it is shown that the upper limit for a single phase uranium substituted lanthanum zirconate material, $\text{La}_2\text{Zr}_{2-x}\text{U}_x\text{O}_{7+\delta}$, is defined by the boundary $0.5 < x < 0.6$. Confirmation of the pyrochlore supercell was possible on all single phase materials, with no indication of cation disorder within the TEM images (Figure 5.11).

For target composition $\text{La}_2\text{Zr}_{1.4}\text{U}_{0.6}\text{O}_7$ a two phase assemblage was identified, with the major phase, Phase 2, having a composition defined as $\text{La}_{1.94(1)}\text{Zr}_{1.51(1)}\text{U}_{0.53(1)}\text{O}_{7.40(4)}$. This is comparable to the composition measured for the target material $\text{La}_2\text{Zr}_{1.5}\text{U}_{0.5}\text{O}_7$, at $\text{La}_{2.06(2)}\text{Zr}_{1.51(1)}\text{U}_{0.48(1)}\text{O}_{7.45(3)}$, full EDS compositional analysis for all the materials formed in an air atmosphere can be found in Table 5.4. The EDS data shows that the limit of the substitution, and the stability of the phase, is close to the $x = 0.5$ composition. As a function of increasing uranium substitution (x), the average uranium oxidation state

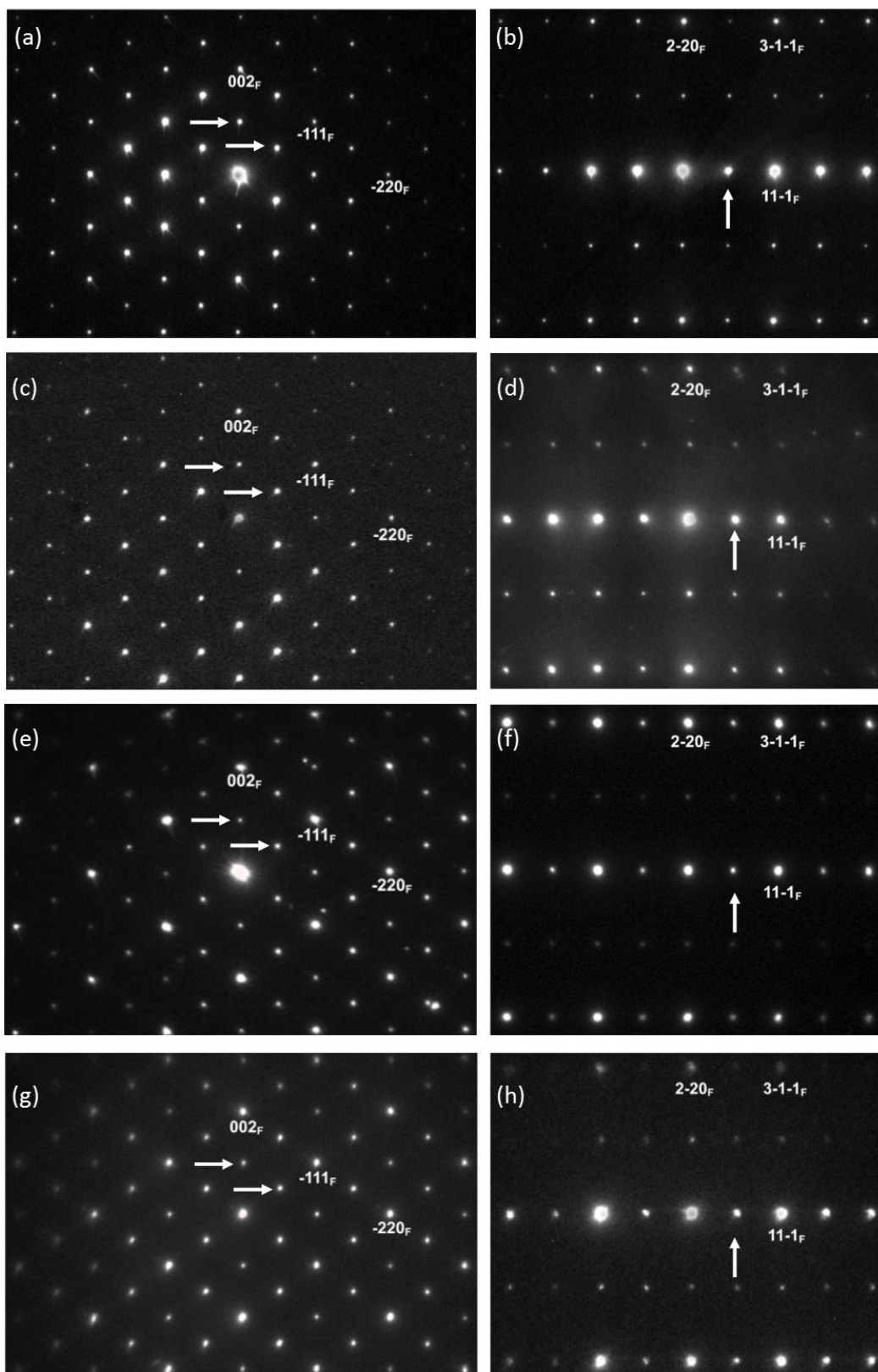


Figure 5.12: Electron diffraction image of sample from the series $\text{La}_2\text{Zr}_{2-x}\text{U}_x\text{O}_{7+\delta}$ formed in H_2/N_2 atmosphere with (a) $[110]_F$ and (b) $[112]_F$ zone axis diffraction patterns for $\text{La}_2\text{Zr}_{1.8}\text{U}_{0.2}\text{O}_{7+\delta}$, (c) $[110]_F$ and (d) $[112]_F$ zone axis diffraction patterns for $\text{La}_2\text{Zr}_{1.6}\text{U}_{0.4}\text{O}_{7+\delta}$, (e) $[110]_F$ and (f) $[112]_F$ zone axis diffraction patterns for $\text{La}_2\text{Zr}_{1.4}\text{U}_{0.6}\text{O}_{7+\delta}$, (g) $[110]_F$ and (h) $[112]_F$ zone axis diffraction patterns for $\text{La}_2\text{Zr}_{1.2}\text{U}_{0.8}\text{O}_{7+\delta}$, Indexed with respect to the fluorite substructure.

measured decreases, despite the availability of oxygen within the forming air atmosphere (Table 5.12). XANES analysis indicates the average uranium oxidation state of material formed in air is $>5.5+$ highlighting that the uranium species is dominated by U^{6+} with a smaller contribution of U^{4+} or U^{5+} . The uranium is assumed to locate on the target tetravalent B-site of the structure, this is postulated to force the uranium to reduce in order to co-exist with the Zr^{4+} cations on the B site. For the target composition $La_2Zr_{1.4}U_{0.6}O_7$ the uranium has reduced to an average oxidation state of $5.53+$ but this is not sufficient to form a single phase material. The EDS measurement completed on the bulk material showed an average composition of $La_{2.06(2)}Zr_{1.35(1)}U_{0.58(1)}O_{7.39(4)}$, highlighting that the precursor materials were combined in the correct stoichiometry. The r_A/r_B value is used as an indicator of the likelihood of a pyrochlore structure forming, using the ionic radii of the cations. Analysis of this value (Table 5.6) indicates from the ionic radii ratio between the two cation sites, a single phase material should have formed. Rietveld refinement of two pyrochlore structures was successfully applied to the data of the $La_2Zr_{1.4}U_{0.6}O_7$ target material. Both the a-parameter and the x-position in the 48f oxygen for Phase 1 and Phase 2 are larger than for the single phase materials, although Phase 2 is comparable to target composition $La_2Zr_{1.5}U_{0.5}O_7$ highlighting the solid solution limit must be close to the $x = 0.5$ composition. XANES samples were prepared from the bulk material through grinding into a fine power, prior to the correct quantities being taken for the sample preparation, this is to ensure that a representative sample is taken of the phase assemblage. XANES analysis on the multiphase composition, both identified to contain uranium, only provides information on the average uranium oxidation state, therefore the uranium oxidation state of each phase was not defined. Both phases were analysed to exhibit the pyrochlore superstructure, see Figure 5.4 and Rietveld refinement results in Tables 5.8 and 5.9. However, the oxygen stoichiometry calculated, from the average uranium oxidation state, show the minor phase, a uranium rich material with composition $La_{1.94(1)}Zr_{0.55(1)}U_{1.52(1)}O_{8.2(1)}$ to have an unusually high oxygen stoichiometry for a pyrochlore materials. This oxygen stoichiometry has been derived in order to maintain charge neutrality across the oxide material. Accumulation of oxygen would be assumed in the ordered oxygen vacancy inherent in the pyrochlore structure. This level of oxygen accumulation within the minor secondary pyrochlore phase observed would be expected to destabilise the pyrochlore structure. An oxygen stoichiometry of 8 would result in all vacant position being occupied, the loss of the order anion vacancy, and the formation of a fluorite structured material. Rietveld refinement with a combination of pyrochlores and fluorite structures was attempted but was unsuccessful, as was refinement with 2 fluorite

structures. Initial refinement did indicate the presence of two pyrochlore structures. Therefore an oxygen stoichiometry of 8 would not be expected, an oxygen stoichiometry >8 with a pyrochlore structure would not be possible due to a lack of crystallographic sites for the additional oxygen to locate.

Analysis of the materials with normalised compositions from the EDS measured materials can be found in Table 5.15. These are normalised to ~7 oxygen, as expected for the ideal pyrochlore structure. For target composition $\text{La}_2\text{Zr}_{1.4}\text{U}_{0.6}\text{O}_7$ the normalised compositions for the bulk material can be compared to the normalised composition of Phase 2, the predominant phase within the material. It can be seen that the bulk material is deficient in zirconium and rich in uranium compared to Phase 2. In contrast, the minor secondary pyrochlore material (Phase 1) formed is deficient in cations, indicating the formation on cation vacancies within the structure.

Table 5. 15: Summary of semi-quantitative results from EDS analysis (Table 5.2) with the inclusion of the normalised cation calculations to ~4 cations and the corresponding oxygen stoichiometry based on the XANES analysis of bulk uranium oxidation state, summarised in Table 5.12.

Target Composition	Semi-Quantitative EDS	Normalised Compositions
(a) $\text{La}_2\text{Zr}_{1.9}\text{U}_{0.1}\text{O}_{7+\delta}$	$\text{La}_{2.10(2)}\text{Zr}_{1.87(2)}\text{U}_{0.10(1)}\text{O}_{7.19(1)}$	$\text{La}_{2.01(2)}\text{Zr}_{1.78(2)}\text{U}_{0.10(1)}\text{O}_{7.00(1)}$
(b) $\text{La}_2\text{Zr}_{1.8}\text{U}_{0.2}\text{O}_{7+\delta}$	$\text{La}_{2.01(3)}\text{Zr}_{1.75(2)}\text{U}_{0.20(1)}\text{O}_{7.11(1)}$	$\text{La}_{2.00(3)}\text{Zr}_{1.74(2)}\text{U}_{0.20(1)}\text{O}_{7.00(1)}$
(c) $\text{La}_2\text{Zr}_{1.7}\text{U}_{0.3}\text{O}_{7+\delta}$	$\text{La}_{2.05(3)}\text{Zr}_{1.72(2)}\text{U}_{0.32(1)}\text{O}_{7.46(2)}$	$\text{La}_{1.93(3)}\text{Zr}_{1.62(2)}\text{U}_{0.30(1)}\text{O}_{7.00(2)}$
(d) $\text{La}_2\text{Zr}_{1.6}\text{U}_{0.4}\text{O}_{7+\delta}$	$\text{La}_{2.11(2)}\text{Zr}_{1.58(1)}\text{U}_{0.38(1)}\text{O}_{7.42(3)}$	$\text{La}_{1.99(2)}\text{Zr}_{1.49(1)}\text{U}_{0.36(1)}\text{O}_{7.00(3)}$
(e) $\text{La}_2\text{Zr}_{1.5}\text{U}_{0.5}\text{O}_{7+\delta}$	$\text{La}_{2.06(2)}\text{Zr}_{1.51(1)}\text{U}_{0.48(1)}\text{O}_{7.45(3)}$	$\text{La}_{1.94(2)}\text{Zr}_{1.41(1)}\text{U}_{0.46(1)}\text{O}_{7.00(3)}$
(f) $\text{La}_2\text{Zr}_{1.4}\text{U}_{0.6}\text{O}_{7+\delta}$	1- $\text{La}_{1.94(1)}\text{Zr}_{0.55(1)}\text{U}_{1.52(1)}\text{O}_{8.2(1)}$	1- $\text{La}_{1.66(1)}\text{Zr}_{0.47(1)}\text{U}_{1.30(1)}\text{O}_{7.0(1)}$
	2- $\text{La}_{1.94(1)}\text{Zr}_{1.51(1)}\text{U}_{0.53(1)}\text{O}_{7.40(4)}$	2- $\text{La}_{1.84(1)}\text{Zr}_{1.43(1)}\text{U}_{0.50(1)}\text{O}_{7.00(4)}$
	Bulk- $\text{La}_{2.06(2)}\text{Zr}_{1.35(1)}\text{U}_{0.58(1)}\text{O}_{7.39(4)}$	Bulk- $\text{La}_{1.95(2)}\text{Zr}_{1.28(1)}\text{U}_{0.55(1)}\text{O}_{7.00(4)}$

5.4.2 Discussions on Hydrogen / Nitrogen formed Materials

The development of materials of the target compositions $\text{La}_2\text{Zr}_{2-x}\text{U}_x\text{O}_{7+\delta}$, where $0.1 \leq x \leq 0.9$, have been analysed after synthesis in a hydrogen / nitrogen atmosphere. The successful formation of the pyrochlore structure up to, and including, target composition $\text{La}_2(\text{Zr}_{1.2}\text{U}_{0.8})\text{O}_7$, shows that, in a reducing atmosphere, a greater fraction (x) of uranium can be substituted for zirconium and successfully form a single phase assemblage with a pyrochlore crystallographic structure. Rietveld refinement completed on XRD data using the GSAS software (Figure 5.7) provided refined structural parameters for the pyrochlore

supercell (Tables 5.10 and 5.11). SEM and EDS analysis was used to confirm a single phase assemblage (Figure 5.2) and the material compositions are summarised in Table 5.5.

EDS analysis provided measurement of the cation stoichiometries within the materials and indicated that all material compositions were comparable the target stoichiometries. The limit of the substitution with the targeted substitution was measured by EDS analysis at $\text{La}_{1.94(2)}\text{Zr}_{1.20(1)}\text{U}_{0.81(1)}\text{O}_{7.4(1)}$. The presence of the pyrochlore supercell was confirmed through the use of electron diffraction within the TEM instrument.

TEM analysis of the materials on the $[110]_{\text{F}}$ and $[112]_{\text{F}}$ axis enabled the identification of additional diffraction intensities indicative of the pyrochlore supercell. Within Figure 5.12 the pyrochlore supercell intensities are highlighted through the use of the arrow. There are few examples of TEM analysis of actinide bearing pyrochlore materials, however the results of inactive analogues analysed show mixed findings for the development of the phase with increasing concentrations of uranium analogue species [17, 21, 37]. This work shows that with increasing substitution of uranium for zirconium on the B site within the pyrochlore structure, ideal composition $\text{A}_2\text{B}_2\text{O}_7$, are randomly arranged. This can be deduced from the lack of additional intensities to the pyrochlore supercell, showing that no additional cell to the pyrochlore or fluorite cells exists, so the zirconium and uranium cations have not ordered within the structure. In addition to this, the sharp nature of the pyrochlore supercell reflection intensities are consistent, showing that the B site is able to accommodate the substitution without creating crystallographic stresses / strains. Stresses / strains within the crystallographic structure of a pyrochlore would have been identified through the appearance of diffused scattering around the pyrochlore supercell reflections in the electron diffraction images, as observed by Reid et al and De-los-Reyes et al. [17, 21, 37]. The absence of such diffuse intensity, and the maintenance of the intensity of the supercell reflections, show a disordered B site arrangement of the uranium and zirconium cations maintaining the pyrochlore superstructure with the underlying fluorite sub lattice.

Material with the target composition $\text{La}_2\text{Zr}_{1.1}\text{U}_{0.9}\text{O}_7$, $x=0.9$, was synthesised in a hydrogen / nitrogen atmosphere with a bulk composition measured of $\text{La}_{2.01(4)}\text{Zr}_{1.13(2)}\text{U}_{0.89(2)}\text{O}_{7.5(1)}$. Back scattered electrons showed an assemblage consisting of three phases, shown in Figure 5.2(i), with compositional analysis of the three phases are included in Table 5.3. Rietveld analysis on the XRD data on the material showed the formation of 3 phases each with the structure of a fluorite. Attempts to refine a single pyrochlore structure, in isolation and in combination with a fluorite structure, were not

successful. Figure 5.7 (b) shows the model of the material as refined to the data, for composition with $x=0.9$ there is a distinct shift within the data to higher 2θ angles, symptomatic of a reduction in the volume of the unit cell. In order to analysis this, the refined a -parameter for the 3 fluorite structures, in Table 5.10, are reported as $2a_F$, where $a_P=2a_F$. It can be seen that for all 3 phases the unit cell parameter is smaller than those measured for the pyrochlore materials ($x \leq 0.8$).

The XANES analysis of the series formed in hydrogen / nitrogen showed that as the fraction of uranium increases, then the average uranium oxidation state decreases. This relationship is utilised in Figure 5.10 in order to determine the average oxidation state of the non-measured materials within the series ($x = 0.1, 0.3, 0.5, 0.7, 0.9$), respectively. Materials formed in an oxygen deprived atmosphere are able to incorporate a greater fraction of uranium within the pyrochlore structure, and still maintain a single phase assemblage. For the substituted limit of $\text{La}_{1.94(2)}\text{Zr}_{1.20(1)}\text{U}_{0.81(1)}\text{O}_{7.4(1)}$ the oxygen stoichiometry has been determined by XANES analysis, and is comparable to the oxygen stoichiometry measured for the air formed material. This suggests that the limit of substitution driven by the structures ability to incorporate oxygen in order to maintain charge neutrality. In the absence of an oxygen rich atmosphere the uranium is able to reduce and therefore less oxygen is assumed to accumulate within the anion vacancy of the structure. However, a complete substitution was not possible, with the limit of substitution reached between the boundary $0.8 < x < 0.9$ in $\text{La}_2\text{Zr}_{2-x}\text{U}_x\text{O}_7$ for hydrogen/nitrogen materials. The XANES analysis (Table 5.13 and Table 5.14) shows that the uranium has not been fully reduced to U^{4+} , however an average uranium oxidation state close to U^{5+} was quantified, indicating the dominate average oxidation state of U^{5+} , or has a larger fraction of U^{4+} .

The bulk material with target composition $\text{La}_2\text{Zr}_{1.1}\text{U}_{0.9}\text{O}_7$ has a chemical makeup of $\text{La}_{2.01(4)}\text{Zr}_{1.13(2)}\text{U}_{0.89(2)}\text{O}_{7.5(1)}$. The oxygen stoichiometry has been determined assuming the uranium oxidation state has continued to reduce linearly in the multiphase material. The average uranium oxidation state of the material is assumed to represent the uranium species within all three phases, however this may not be the case. Establishing the oxidation state of each phase is beyond the scope of this work. Phase 2 and 3 have been successfully refined to the structure of a fluorite, space group $\text{Fm}\bar{3}\text{m}$ (Figure 5.7). The oxygen stoichiometry of the material for Phase 2 and 3, based on the calculated average uranium oxidation state, has less than 8 oxygens, as required by the ideal fluorite material, $(\text{AB})_4\text{O}_8$. This could be an indicator that a defect fluorite, $(\text{AB})_4\text{O}_7$, structure, with a disordered anion vacancy, has formed. TEM was not completed on this material due to

time restrictions, but TEM on the material would provide information on the underlying crystal structure. Phase 1, also successfully refined to the fluorite space group, has a calculated oxygen stoichiometry of 8.4(3). The error within the oxygen stoichiometry has been calculated from the uranium oxidation state, however, the error on the composition, as determined by EDS analysis will influence the oxygen stoichiometry therefore the error maybe underestimated. The general formula of the pyrochlore structure includes 4 formula units of cations, split evenly across the two cation sites, A and B. Cation ratios for phases 1-3 in the multiphase assemblage with target composition $\text{La}_2\text{Zr}_{1.1}\text{U}_{0.9}\text{O}_{7+\delta}$ (assuming lanthanum sits on the A-site, and zirconium / uranium on the B-site) have been assessed from Table 5.5. Phase 1 is A site deficient or B site rich. Phase 2 has a slight excess of cations on the A site and is deficient on the B site. Phase 3 has a >50% excess of cations on the A site and would be highly deficient on the B site. All 3 phases have a 4 formula units of cations. The refined fluorite structures, and the instability of the cations on the A and B-sites, indicate the cations on the A and B-sites have mixed in order to stabilise the fluorite structure.

5.5 Conclusions

This work shows the chemical flexibility of lanthanum zirconate pyrochlore, $\text{La}_2\text{Zr}_2\text{O}_7$, through the incorporation radioactive species of variable oxidation state onto the tetravalent zirconium B-site. Using uranium, both for direct disposal and as an analogue for plutonium oxide immobilisation, ceramic materials have been prepared. Materials were formed in an air or reducing hydrogen / nitrogen atmosphere to determine the phase assemblage, with the target phase a single pyrochlore structure of space group $\text{Fd}\bar{3}\text{m}$. Materials were successfully synthesised with compositions up to, and including, $\text{La}_{2.06(2)}\text{Zr}_{1.51(1)}\text{U}_{0.48(1)}\text{O}_{7.45(3)}$ and $\text{La}_{1.94(2)}\text{Zr}_{1.20(1)}\text{U}_{0.81(1)}\text{O}_{7.4(1)}$, in air and hydrogen / nitrogen, respectively. The limit of the substitution of uranium within the pyrochlore material $\text{La}_2\text{Zr}_2\text{O}_7$, has been determined as dependent on the availability of oxygen within the forming atmosphere.

The inability for the uranium to reduce sufficiently in the air formed materials results in the substitution limit being driven by the structures ability to incorporate an excess oxygen anions. This is caused by replacing Zr^{4+} cations with uranium cations with an average oxidation state of >5.5+, hence dominated by U^{6+} . This assumption is based on creating a charge neutral material. At the limit of substitution in air a two phase assemblage is formed, a major phase with a pyrochlore structure and composition of

$\text{La}_{1.94(1)}\text{Zr}_{1.51(1)}\text{U}_{0.53(1)}\text{O}_{7.40(4)}$, and a minor uranium rich phase of composition $\text{La}_{1.94(1)}\text{Zr}_{0.55(1)}\text{U}_{1.52(1)}\text{O}_{8.2(1)}$. The uranium oxidation state for both materials has been calculated based on the average uranium oxidation state of the bulk material. The excess of oxygen in the minor phase, and the average oxidation state calculated on the bulk material ($\text{La}_{2.06(2)}\text{Zr}_{1.35(1)}\text{U}_{0.58(1)}\text{O}_{7.39(4)}$) leads to the conclusion that the oxidation state of the uranium within each phase is independent and the average is not representative.

When materials were synthesised in an oxygen free, or reducing hydrogen / nitrogen, atmosphere the uranium cations are able to reduce further. This is assumed due to the lack of available oxygen within the forming atmosphere. The reduced oxygen results in a greater fraction of uranium being included within the structure. However it was noted that the oxygen stoichiometry for both air and hydrogen / nitrogen atmosphere were comparable, indicating that the accumulation of oxygen within the ordered oxygen vacancy of structures limits the substitution of uranium.

5.6 Future Work

Further work for this chapter should be undertaken in the following areas:

- Complete TEM analysis of materials in order to understand the complete development of the materials within increasing substitution in air and hydrogen / nitrogen.
- Complete XANES analysis on the hydrogen / nitrogen single phase materials in order to gain further information of the uranium average oxidation state.
- Undertake analysis using neutron diffraction to enable Rietveld refinement of the structure, including the x-coordinate position of the 4f oxygen.

5.7 References

[1] Lian J, Wang LM, Haire RG *et al.* Ion beam irradiation in $\text{La}_2\text{Zr}_2\text{O}_7$ - $\text{Ce}_2\text{Zr}_2\text{O}_7$ pyrochlore. Nuclear Instruments & Methods in Physics Research Section B-Beam Interactions with Materials and Atoms 2004; 218:236-243.

[2] Gregg DJ, Zhang Y, Middleburgh SC *et al.* The incorporation of plutonium in lanthanum zirconate pyrochlore. Journal of Nuclear Materials 2013; 443:444-451.

[3] Xiao HY, Jiang M, Zhao FA *et al.* Thermal and mechanical stability, electronic structure and energetic properties of Pu-containing pyrochlores: $\text{La}_{2-y}\text{Pu}_y\text{Zr}_2\text{O}_7$ and $\text{La}_2\text{Zr}_{2-y}\text{Pu}_y\text{O}_7$ ($0 \leq y \leq 2$). Journal of Nuclear Materials 2015; 466:162-171.

[4] Wang SX, Begg BD, Wang LM *et al.* Radiation stability of gadolinium zirconate: A waste form for plutonium disposition. Journal of Materials Research 1999; 14:4470-4473.

- [5] Williford RE, Weber WJ. Computer simulation of Pu³⁺ and Pu⁴⁺ substitutions in gadolinium zirconate. *Journal of Nuclear Materials* 2001; 299:140-147.
- [6] Lian J, Wang LM, Chen J *et al.* Heavy ion irradiation of zirconate pyrochlores. In: *Scientific Basis for Nuclear Waste Management XXV*. Edited by: McGrail BP, Cragolino GA. 2002. pp. 507-512.
- [7] Lian J, Zu XT, Kutty KVG *et al.* Ion-irradiation-induced amorphization of La₂Zr₂O₇ pyrochlore. *Physical Review B* 2002; 66.
- [8] Zhang Y, Hart K, Begg BD *et al.* Durability of Pu-doped titanate and zirconate ceramics designed for Pu immobilisation. In: *Scientific Basis for Nuclear Waste Management Xxv*. Edited by: McGrail BP, Cragolino GA. 2002. pp. 389-395.
- [9] Ewing RC, Weber WJ, Lian J. Nuclear waste disposal-pyrochlore A₂B₂O₇: Nuclear waste form for the immobilization of plutonium and "minor" actinides. *Journal of Applied Physics* 2004; 95:5949-5971.
- [10] Liu Z-G, Ouyang J-H, Zhou Y *et al.* Influence of ytterbium- and samarium-oxides codoping on structure and thermal conductivity of zirconate ceramics. *Journal of the European Ceramic Society* 2009; 29:647-652.
- [11] Martin PM, Belin RC, Valenza PJ, Scheinost AC. EXAFS study of the structural phase transition in the americium zirconate pyrochlore. *Journal of Nuclear Materials* 2009; 385:126-130.
- [12] Merkushkin AO, Aung T, U ZEM. Ceramic based on REE zirconates, titanates and stannates. *Glass and Ceramics* 2011; 67:347-350.
- [13] Gregg DJ, Zhang ZM, Thorogood GJ *et al.* Cation antisite disorder in uranium-doped gadolinium zirconate pyrochlores. *Journal of Nuclear Materials* 2014; 452:474-478.
- [14] Jafar M, Phapale SB, Mandal BP *et al.* Preparation and Structure of Uranium-Incorporated Gd₂Zr₂O₇ Compounds and Their Thermodynamic Stabilities under Oxidizing and Reducing Conditions. *Inorganic Chemistry* 2015; 54:9447-9457.
- [15] Stennett MC, Hyatt NC, Reid DP *et al.* Characterisation of Ion Beam Irradiated Zirconolite for Pu Disposition. In: *32nd Symposium on Scientific Basis for Nuclear Waste Management held at the 2008 MRS Fall Meeting*. Boston, MA: 2008. pp. 243-248.
- [16] Gilbert MR, Selfslag C, Walter M *et al.* Synthesis and characterisation of Pu-doped zirconolites - (Ca_{1-x}Pu_x)Zr(Ti_{2-2x}Fe_{2x})O₇. In: *Actinides Conference*. San Francisco, CA: 2009.
- [17] Reid DP, Stennett MC, Hyatt NC. Synthesis and Structures of Gd₂Zr_{2-x}Ce_xO₇: A model ceramic system for plutonium disposition. In: *Advances in Materials Science for Environmental and Nuclear Technology*. Edited by: Fox K, Hoffman E, Manjooran N, Pickrell G. 2010. pp. 11-20.
- [18] Reid DP, Stennett MC, Ravel B *et al.* The structure of ion beam amorphised zirconolite studied by grazing angle X-ray absorption spectroscopy. *Nuclear Instruments & Methods in Physics Research Section B-Beam Interactions with Materials and Atoms* 2010; 268:1847-1852.
- [19] Reid D, Hyatt N, Stennett M, Maddrell ER. Immobilising plutonium. *Materials World* 2011; 19:26-28.

- [20] Squire J, Maddrell ER, Hyatt NC, Stennett MC. Developing the plutonium disposition option: Ceramic processing concerns. *Advances in Materials Science for Environmental and Nuclear Technology* 2011; 227:241-249.
- [21] Reid DP, Stennett MC, Hyatt NC. The fluorite related modulated structures of the $Gd_2(Zr_{2-x}Ce_x)O_7$ solid solution: An analogue for Pu disposition. *Journal of Solid State Chemistry* 2012; 191:2-9.
- [22] Kulkarni NK, Sampath S, Venugopal V. Preparation and characterisation of Pu-pyrochlore: $(La_{1-x}Pu_x)_2Zr_2O_7$ ($x=0-1$). *Journal of Nuclear Materials* 2000; 281:248-250.
- [23] Subramanian MA, Aravamudan G, Rao GVS. Oxide Pyrochlores- A Review. *Progress in Solid State Chemistry* 1983; 15:55-143.
- [24] Ishizawa N, Marumo F, Iwai S *et al.* Compounds with pervovskite-type slabs. V. A High-Temperature Modification of $La_2Ti_2O_7$. *Acta Crystallographica Section B-Structural Science* 1982; 38:368-372.
- [25] Shannon R. Revised effective ionic radii and systematic studies of interatomic distances in halides and chalcogenides. *Acta Crystallographica Section A* 1976; 32:751-767.
- [26] Lumpkin GR. Alpha-decay damage and aqueous durability of actinide host phases in natural systems. *Journal of Nuclear Materials* 2001; 289:136-166.
- [27] Crawford CL, Biddle CR, Bibler NE, Ans. Durability testing of heavy-ion irradiated crystalline ceramics. *Proceedings of the Embedded Topical Meeting on Spent Nuclear Fuel and Fissile Material Management* 2000:449-456.
- [28] Trocellier P, Delmas R. Chemical durability of zircon. *Nuclear Instruments & Methods in Physics Research Section B-Beam Interactions with Materials and Atoms* 2001; 181:408-412.
- [29] Xu HF, Wang YF, Zhao PH *et al.* Investigation of pyrochlore-based U-bearing ceramic nuclear waste: Uranium leaching test and TEM observation. *Environmental Science & Technology* 2004; 38:1480-1486.
- [30] Lumpkin GR, Gao Y, Gier R *et al.* The role of Th-U minerals in assessing the performance of nuclear waste forms. *Mineralogical Magazine* 2014; 78:1071-1095.
- [31] Larson AC, Von Dreele RB. General Structure Analysis System (GSAS). In: Los Alamos National Laboratory Report LAUR. 2004. pp. 86-748.
- [32] Toby BH. EXPGUI, a graphical user interface for GSAS. *J. Appl. Cryst.* 2001; 34:210-213.
- [33] Tabira Y, Withers RL, Yamada T, Ishizawa N. Annular dynamical disorder of the rare earth ions in a $La_2Zr_2O_7$ pyrochlore via single crystal synchrotron X-ray diffraction. *Zeitschrift Fur Kristallographie* 2001; 216:92-98.
- [34] James M, Carter ML, Watson JN. The synthesis, crystal chemistry and structures of Y-doped brannerite ($U_{1-x}Y_xTi_2O_6$) and thorutite ($Th_{1-x}Y_xTi_2O_{6-\delta}$) phases. *Journal of Solid State Chemistry* 2003; 174:329-333.
- [35] Ravel B, Newville M. ATHENA, ARTENIS, HEPHAESTUS: data analysis for X-ray absorption spectroscopy using IFEFFIT. In: *Journal of Synchrotron Radiation*; 2005.
- [36] Ravel B. Athena: A User's Guide. In: 2.0. <http://bruceravel.github.io/demeter/au/>.

[37] de los Reyes M, Whittle KR, Zhang Z *et al.* The pyrochlore to defect fluorite phase transition in $\text{Y}_2\text{Sn}_{2-x}\text{Zr}_x\text{O}_7$. Rsc Advances 2013; 3:5090-5099.

Chapter 6 Formation of Uranium Titanate Materials

6.1 Introduction

Titanate ceramics have been studied extensively as a candidate material for the long term disposal of actinides. This could comprise of a single phase assemblage, or, as part of a multiphase waste form, such as synthetic rock (SYNROC) [1-7]. This chapter focuses on the brannerite and rutile structured titanate materials, both of which can be found as component phases within SYNROC type system [4, 6, 8-17]. A key advantage of SYNROC is its ability to simultaneously host several radioactive components of a single waste stream. Several formulations have been derived depending on the waste stream in which they target, with SYNROC C and SYNROC F including the formation of a uranium brannerite material. The uranium brannerite material forms when an excess of uranium oxide is added to an immobilisation matrix which includes rutile titanium dioxide as a starting component [1].

The brannerite mineral, $(U^{4+}, REE, Th, Ca)(Ti, Fe^{4+}, Nb)_2(O, OH)_6$, is found in natural environments with uranium, thorium and rare earth element (REE) components with variable compositions. This highlights the structures ability to incorporate actinide cations with impure components in a synthetic brannerite of ideal composition UTi_2O_6 [18-20]. Natural brannerites are found in a metamict state, where the crystal structure has been lost due to damage accumulation from the radioactive decay of component species over time. However, the abundance of natural analogues for ceramic materials enables analysis of the material structure, and its ability to retain radioactive species over long time scales [2, 21-23]. This is a concern for the GDF concept which relies upon multiple engineered barriers, working in conjunction with the properties of the host geological rock, designed to retain the radioactive species for hundreds of thousands of years [24]. Ceramic materials are proposed as the primary barrier to prevent the release of radioactive cations through intimately mixing of actinide materials with inactive components.

The crystalline structure of a brannerite is monoclinic, with general structure $A^{4+}B_2^{4+}O_6$ space group $C2/m$. The structure consists of layers of TiO_6 edge sharing octahedra, linked by UO_6 octahedra, see Figure 6.1. The refinement of synthetic uranium brannerite,

UTi₂O₆ is refined to structural parameters $a = 9.8123(15)\text{\AA}$, $b = 3.7697(6)\text{\AA}$, $c = 6.9253(9)\text{\AA}$ and $\beta = 118.957(6)^\circ$, with crystallographic positions summarised in Table 6.1 [25].

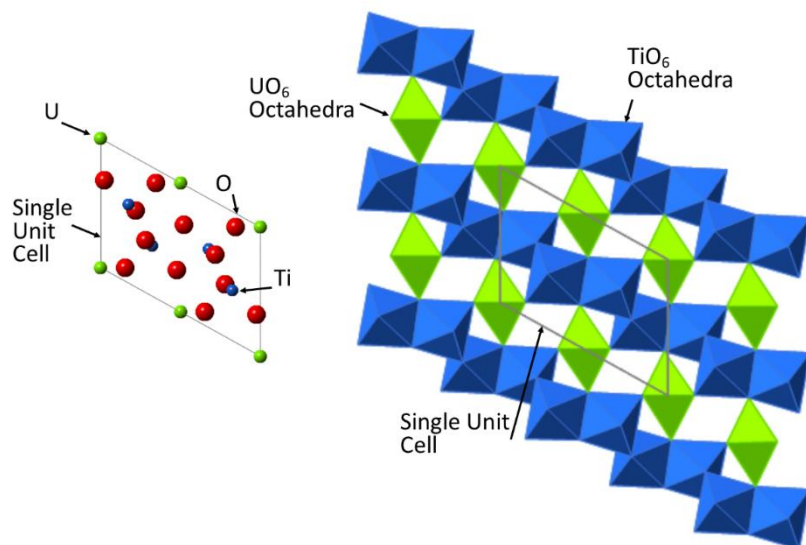


Figure 6.1: The Brannerite structure view of the [010] axis: left, showing the cations and anions, and right, showing the interaction between the edge sharing TiO₆ octahedra (blue) linked by the UO₆ octahedra (green) for ideal brannerite UTi₂O₆

Table 6.1: Crystallographic coordinate positions for the brannerite structure with space group C2/m and composition UTi₂O₆, taken from J.T. Szymanski (1982) [25].

Element	Wyckoff Symbol	x	y	z
U	2a	0	0	0
Ti	4i	0.82356(4)	0	0.39107(6)
O1	4i	0.97718(22)	0	0.30828(31)
O2	4i	0.65272(24)	0	0.10530(33)
O3	4i	0.28053(26)	0	0.40531(38)

The oxidation state of uranium within a ceramic material requires a full understanding for storage within the GDF. The mobility of uranium is dependent on the charge of the uranium cation. Under oxic conditions, uranium will oxidise to form UO₂²⁺ cations, which are mobile in aqueous environments. For this reason a full understanding of the charge compensation mechanism of the composition is required for storage within the GDF. In order to understand this behaviour the stability of a brannerite phase with variable cation substitutions has been completed. The substitution of trivalent cations, M, in place of tetravalent uranium, general composition U_{1-x}M_xTi₂O₆ with M= Cr, Fe, Pr, Y and Yb, have been completed in order to understand the structural response of the material. The chemical flexibility of the brannerite structure with large rare earth element substitutions

in the A site of the structure has been studied by others [13, 14, 17, 26]. Conversely here the use of chromium and iron will enable analysis of the structure with the substitution of smaller transition metal cations, see Table 6.2 for a summary of ionic radii.

Table 6.2: A list of the compositions synthesised. The cation ionic radii of both the substituted element (M) and the ionic radii size of various oxidation states of uranium. Note: titanium cation ionic radii size of 0.605Å was used.

Composition	U Ionic Radii (VI), Å			M ³⁺ Ionic Radii (VI), Å	
	4+	5+	6+		
U _{0.25} Cr _{0.25} Ti _{2.5} O ₆	0.890	0.760	0.730	0.615	
U _{0.5} Cr _{0.5} Ti ₂ O ₆					
U _{0.75} Cr _{0.75} Ti _{1.5} O ₆					
UCrTiO ₆				0.550-0.645	
U _{0.5} Fe _{0.5} Ti ₂ O ₆					
U _{0.54} Y _{0.46} Ti ₂ O ₆					0.900
U _{0.525} Pr _{0.475} Ti ₂ O ₆					0.990
U _{0.5} Yb _{0.5} Ti ₂ O ₆					0.868

Substitutions of chromium, U_{0.50}Cr_{0.50}Ti₂O₆ saw the formation of a single phase assemblage with a structure which could be indexed to the reflections of a rutile. In order to investigate this further compositions of series U_xCr_xTi_{3-2x}O₆ with x = 0.25, 0.50, 0.75 and 1.00 were synthesised.

The rutile structure, TiO₂, is a tetragonal structure with space group P42/mmm. Ideal structure parameters for rutile, TiO₂, are a = b = 4.592Å, c = 2.958Å with α = β = γ = 90° [27]. The structure has a cation crystallographic site defined at position 2a, (0, 0, 0), with flexibility in the oxygen anion position, the 4f oxygen position with (x, y, 0) where x = y = 0.3057 for an ideal TiO₂ rutile [28]. A small unit cell and single cation crystallographic site, may not be desirable for large quantities of actinide materials when designing a ceramic wasteform. Large quantities of fissionable uranium or plutonium oxides within a small volume may lead to a critical event as radiation induced damage results in a loss of crystalline structure. However, the potential formation of the phase in a ceramic material where large quantities of uranium, titanium and chromium oxides are present, warrant an understanding of the materials development.

6.2 Experimental Method

Materials were fabricated from stoichiometric quantities of dried component oxides; UO₂, TiO₂ and M₂O₃ (with M= Cr, Fe, Pr, Yb, Y). Oxide precursors were dried to remove any hydration / carbonation products, and weighed according to the relevant stoichiometries.

These were then homogeneously mixed using a Mini-Mill PULVERISETTE 23 ball mill, in batch sizes of 1g. Materials were reacted in air as powders at 1400°C for 24 hours, allowed to cool to room temperature, reground into a powder and heated for a second treatment at 1400°C for 16 hours. Target compositions $U_{1-x}M_xTi_2O_6$ with $M = Fe, Pr, Yb$ and Y and target compositions $U_xCr_xTi_{3-2x}O_6$ where $x = 0.25, 0.50, 0.75$ and 1.00 have been synthesised.

In order to aid analysis, the materials have been divided into two groups; brannerite, Section 6.3, and chromium substituted materials, Section 6.4. The brannerite sub group divided further into Fe substitutions and substitutions of REE; Y, Yb and Pr. The iron containing materials highlight the substitution of a small cation in the structure. The substitution of REEs highlight the chemical and structural flexibility of the material due to substitutions of cations with ionic radii comparable to those of actinide cations. This enabled the analysis of the uranium response to the large quantities of trivalent cations in its place. A 50:50 tri- and tetra-valent cation on the A site could bring about several changes in the uranium oxidation:

- 1) The uranium could oxidise to U^{5+} , therefore the A-site average charge of 4 will be maintained.
- 2) The uranium could all oxidise to U^{6+} , with the formation of cation vacancies in order to maintain the oxygen stoichiometry of 6.
- 3) The uranium could form a U^{4+} / U^{6+} mix with average uranium oxidation state of U^{5+} , and an average site valence of 5.
- 4) The uranium could remain as U^{4+} with the formation of oxygen vacancies in the structure in order to form a charge neutral material.

The desirable reaction would be for the uranium to all oxidise to U^{5+} . This would ensure a stable phase formation without structural modification to the unit cell. A single uranium with an oxidation state of 5 also mitigates the risk of uranium cations with a oxidation state of 6, which are mobile within the environment [29]. In order to enable the measurement of the uranium oxidation state, and establish the effect with the variable REE cation size, systematic substitutions were completed. However, instrument availability restricted the quantification of the uranium average oxidation state, therefore bond valence sum calculations have been completed using the refined bond lengths determined from neutron diffraction analysis.

6.3 Brannerite Materials Results and Discussions

6.3.1 X-ray Diffraction Analysis

X-ray diffraction (XRD) analysis was performed on a STOE STADI P diffractometer using the set up described in Section 3.1.2.1. XRD samples were prepared within a dedicated fume cupboard whereby finely ground powder was homogeneously dispersed in glue on an acetate film prior to loading into the instrument sample holder.

6.3.1.1 Rare Earth Element (REE) Substitution

Analysis of the synthesised materials found that in order to form a single phase assemblage, minor variations in the original stoichiometries were required. Scanning electron microscopy (SEM) and energy dispersive X-ray spectroscopy (EDS) have been utilised to confirm this, Section 6.3.2. The final target compositions to form a single phase assemblage were; $U_{0.525}Pr_{0.475}Ti_2O_6$, $U_{0.500}Yb_{0.500}Ti_2O_6$ and $U_{0.540}Y_{0.460}Ti_2O_6$. X-ray diffraction data collected to confirm this were indexed to the brannerite structure in Figure 6.2. Full structural refinement of the materials has been completed with neutron diffraction data, Section 6.3.3.

6.3.1.2 Iron (Fe) Substitution

The formation of a single phase assemblage with target composition $U_{0.6}Fe_{0.4}Ti_2O_6$ was formed by Vance et al. [30]. By increasing the fraction of trivalent iron substituted for the uranium, target composition $U_{0.5}Fe_{0.5}Ti_2O_6$, the oxidation of uranium to form U^{5+} was targeted in order to maintain charge neutrality across the material. However, attempts to form a single phase assemblage were unsuccessful. Vance et al. used a nitrate / alkoxide route to form the product in both air and argon atmospheres. In contrast, here, dried oxide powders are utilised due to the difficulties associated with the dissolution of $U^{4+}O_2$ oxide in a nitrate / alkoxide route. In order to understand if the brannerite phase formation in this experiment was due to the

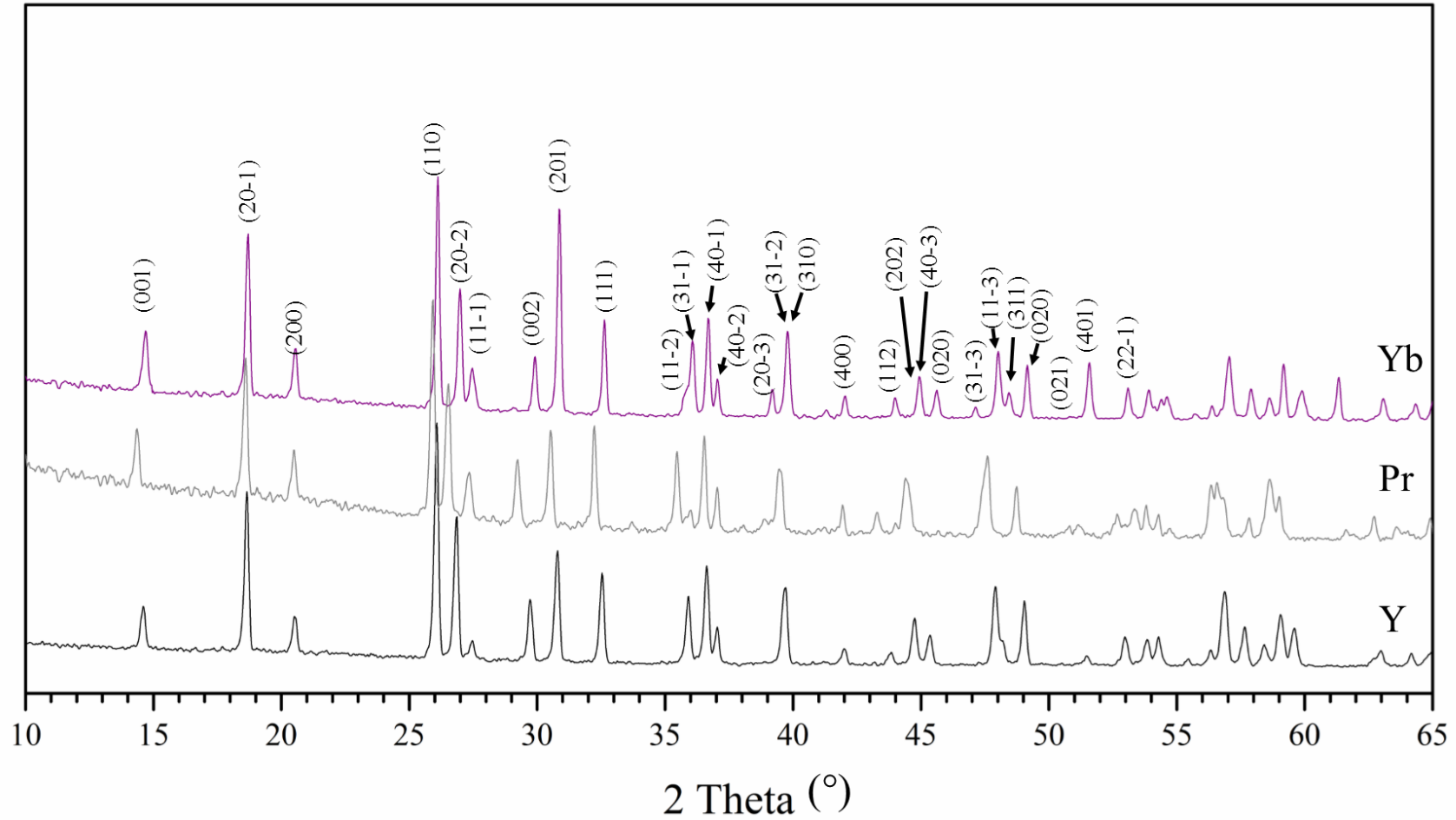


Figure 6.2: X-ray diffraction data collected on the STOE STADI IP for compositions; Pr = $\text{U}_{0.525}\text{Pr}_{0.475}\text{Ti}_2\text{O}_6$, Yb = $\text{U}_{0.500}\text{Y}_{0.500}\text{Ti}_2\text{O}_6$ and Y = $\text{U}_{0.540}\text{Y}_{0.460}\text{Ti}_2\text{O}_6$. Indices of the reflections indicative of the brannerite structure, space group $C2/m$, are included.

increased iron substitution, over the more intimate mixing regime utilised by Vance et al., a smaller fraction of iron was substituted (target composition $U_{0.6}Fe_{0.4}Ti_2O_6$ as formed by Vance et al.) and synthesised using dried oxides. Attempts to form a single phase assemblage proved futile therefore it is concluded that the more intimate mixing regime, and hence the short diffusion distances during sintering, aids the formation of brannerite materials with iron transition metal substituted for uranium. The multiphase assemblage formed during the reaction of the dried oxides with iron substitution are indexed in Figure 6.3.

Crystallographic analysis of XRD data for the target composition, $U_{0.5}Fe_{0.5}Ti_2O_6$, highlighted the presence of brannerite, however, the crystal structure indicative of rutile TiO_2 , with minor contributions of uranium oxide were also indexed. No excess iron was indexed, indicating all the iron has reacted with component oxides. A greater fraction of uranium oxide was required to react with the titanium oxide to form the brannerite phase, therefore the target stoichiometry $U_{0.6}Fe_{0.4}Ti_2O_6$ was synthesised. A greater fraction of the crystal structure indicative of the brannerite phase has been indexed, but an excess of rutile TiO_2 was still identified, with a smaller quantity of unreacted UO_3 . The ionic radii of iron and uranium are dissimilar, see Table 6.2, this could be used to explain the substitution limit of iron for uranium within the structure. This highlights, via this synthesis methodology, the structure is unable to accommodate large quantities of small cations on the A site.

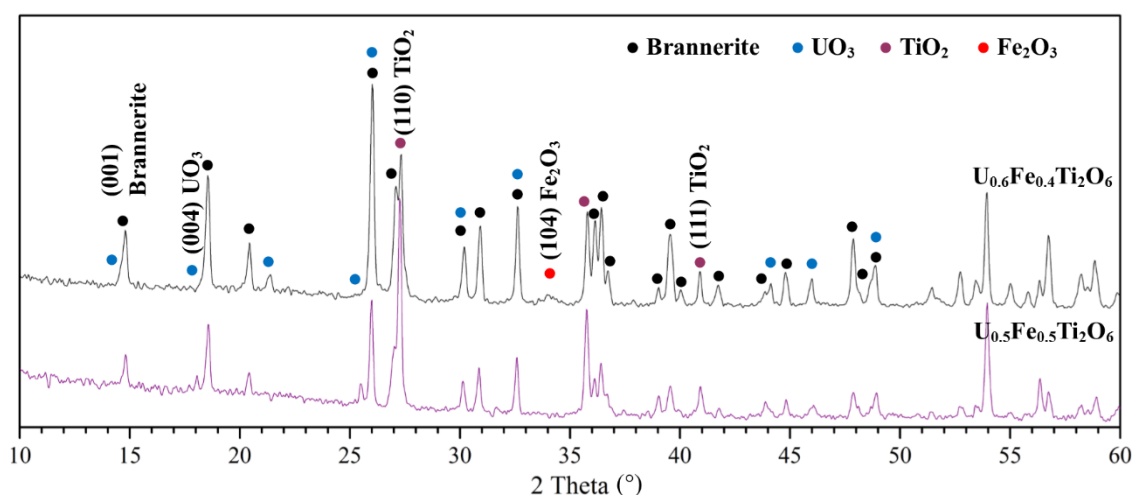


Figure 6.3: Indexed phases identified within target materials of compositions $U_{0.6}Fe_{0.4}Ti_2O_6$ and $U_{0.5}Fe_{0.5}Ti_2O_6$. Reflections indicative of the phase assemblage present are highlighted.

6.3.2 Scanning Electron Microscopy and Energy Dispersive X-ray Spectroscopy of REE Brannerite Materials

Scanning electron microscopy (SEM) and energy dispersive X-ray spectroscopy (EDS) analysis have been used to aid identification of the phase composition of the REE substituted materials on the Hitachi TM 3030 instrument, see Section 3.2 for theory and instrument set up.

Ceramic materials are generally prepared for SEM analysis through sintering a sample of the formed material into pellets, however multiple attempts to press and sinter material resulted in the sample melting. For this reason powders have been analysed as dispersed powder on carbon adhesive surfaces. The black areas are the carbon adhesive film on which to loose powder has been affixed to.

Examination of the materials; $U_{0.525}Pr_{0.475}Ti_2O_6$, $U_{0.540}Y_{0.460}Ti_2O_6$ and $U_{0.500}Yb_{0.500}Ti_2O_6$, using SEM and EDS analysis (Figure 6.4) indicted the material had a single phase assemblage. Semi-quantitative EDS data, as averaged from 5 individual grains for each composition, was analysed at 30,000x magnification and collated in Table 6.3. Oxygen stoichiometry was inferred from the assumption that the material is unable to accommodate an oxygen stoichiometry >6 . Due to the inability to quantify the uranium oxidation state the compositions measured were normalised to 2 titanium cations, as defined by the brannerite structure. Assuming that the lanthanide has a charge of 3+, and the titanium a charge of 4+, the average uranium oxidation state has been inferred from the normalised compositions, see Table 6.3.

Table 6.3: Compositional analysis using semi-quantitative EDS of target composition; $U_{0.525}Pr_{0.475}Ti_2O_6$, $U_{0.540}Y_{0.460}Ti_2O_6$ and $U_{0.500}Yb_{0.500}Ti_2O_6$. Compositions are determined from an average of 5 spot analysis on multiple grains of each phase. The number of oxygen is assumed to be 6 based on the observed brannerite structure, and the normalised compositions are determined from assuming 2 formula units of titanium.

Target Composition	Measured Cation Composition	Normalised composition	U Oxidation
$U_{0.525}Pr_{0.475}Ti_2O_6$	$U_{0.59(4)}Pr_{0.45(2)}Ti_{2.09(8)}O_6$	$U_{0.56(4)}Pr_{0.43(2)}Ti_{2.00(8)}O_6$	4.84(4)
$U_{0.54}Y_{0.46}Ti_2O_6$	$U_{0.56(2)}Y_{0.43(1)}Ti_{2.09(7)}O_6$	$U_{0.54(2)}Y_{0.41(1)}Ti_{2.00(7)}O_6$	5.13(2)
$U_{0.5}Yb_{0.5}Ti_2O_6$	$U_{0.54(4)}Yb_{0.47(3)}Ti_{2.04(3)}O_6$	$U_{0.53(4)}Yb_{0.46(3)}Ti_{2.00(3)}O_6$	4.94(4)

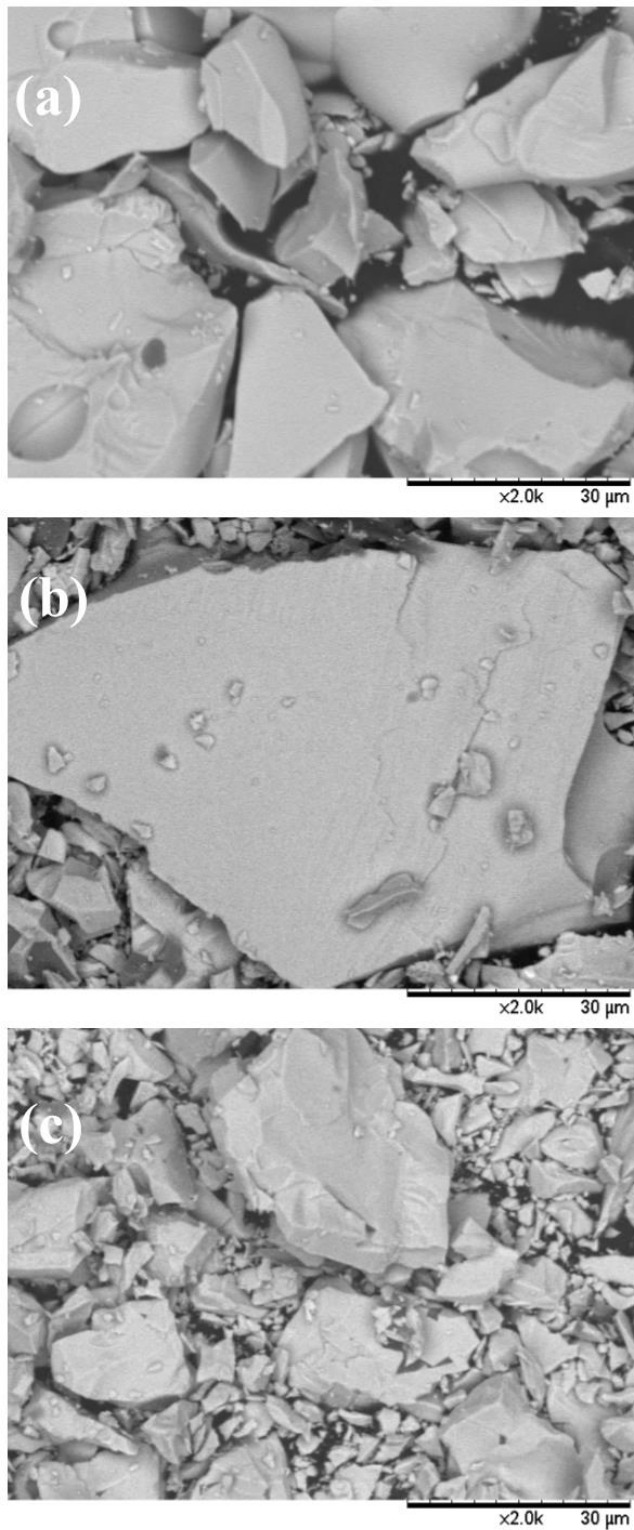


Figure 6.4: Back scattered electron micrograph of samples (a) $U_{0.525}Pr_{0.475}Ti_2O_6$, (b) $U_{0.540}Y_{0.460}Ti_2O_6$ and (c) $U_{0.500}Yb_{0.500}Ti_2O_6$ as collected on the Hitachi TM3030 instrument.

6.3.3 Neutron Diffraction Analysis of REE Brannerite Materials

Accurate structural analysis was completed on the High Resolution Powder Diffractometer (HRPD) instrument at ISIS, Harwell. The ISIS facilities uses time of flight

neutrons (TOF), full facility configuration can be found in Section 3.3.2. Radioactive materials were prepared away from the instrument, at the University of Sheffield, within a dedicated glovebox. Data collected using the backscattered detector was refined using Rietveld refinement analysis, which has a d-spacing range of $\sim 0.6\text{-}4.6\text{\AA}$ (TOF 30-230ms) with a resolution ($\Delta d/d$) of up to $\sim 5 \times 10^{-4}$.

Refinement was undertaken using the Rietveld method through the GSAS software, results shown in Table 6.4 and Table 6.5. [31, 32]. Refinement has been completed using the normalised compositions within Table 6.3 and the starting parameters taken from the refinement of synthetic uranium brannerite (UTi_2O_6) by Szymanski et al. [25]. Figures 6.6 - 6.8 show the refined brannerite structures for target compositions $\text{U}_{0.525}\text{Pr}_{0.475}\text{Ti}_2\text{O}_6$, $\text{U}_{0.540}\text{Y}_{0.460}\text{Ti}_2\text{O}_6$ and $\text{U}_{0.500}\text{Yb}_{0.500}\text{Ti}_2\text{O}_6$, respectively. Cations on the A-site (ATi_2O_6) have a shared occupancy, therefore their thermal parameters have been constrained due to sharing the same crystallographic site.

Analysis of the refined lattice parameters in Figure 6.5, represented by the volume (Table 6.4), show a linear relationship with the ionic radii of the REE cation on the A site of the structure. As the ionic radii increases so does the refined unit cell volume.

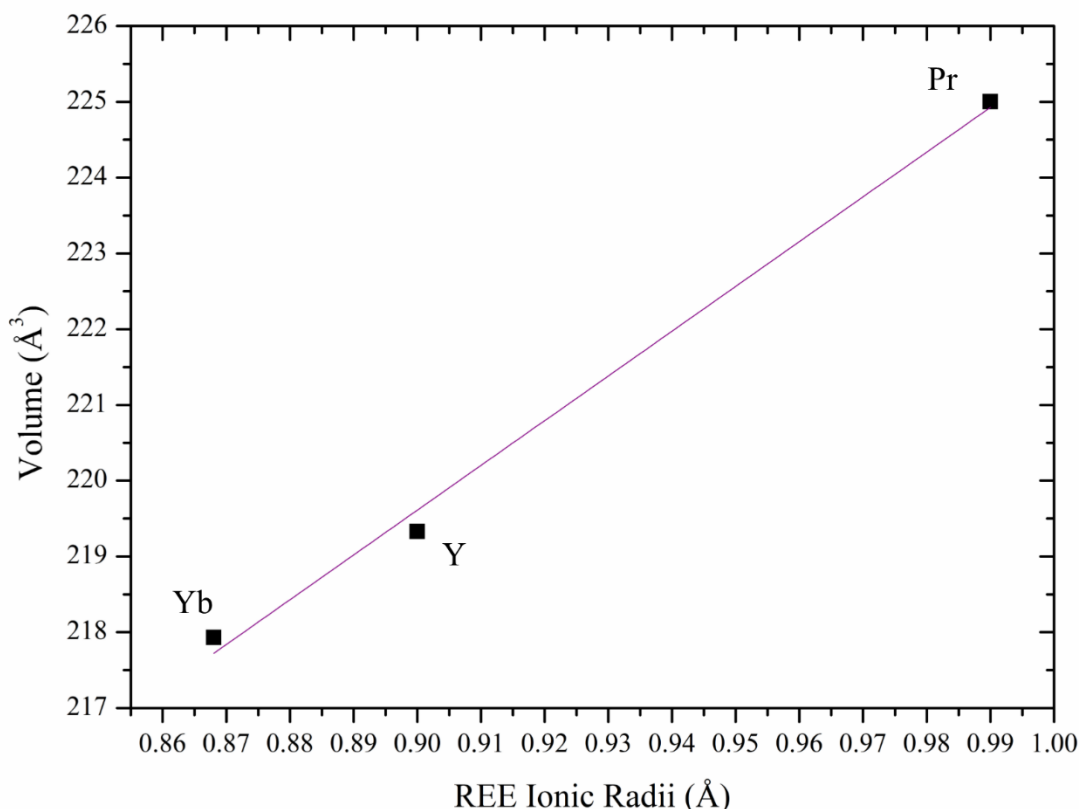


Figure 6.5: The unit cell volume of the brannerite target compositions; $\text{U}_{0.525}\text{Pr}_{0.475}\text{Ti}_2\text{O}_6$, $\text{U}_{0.540}\text{Y}_{0.460}\text{Ti}_2\text{O}_6$ and $\text{U}_{0.500}\text{Yb}_{0.500}\text{Ti}_2\text{O}_6$, plotted against the ionic radii size of the substituted A-site REE cation. The volume is extracted from the Rietveld refinement of the unit cells.

Table 6.4: Refined parameters of single phase brannerite materials analysed by Rietveld refinement of neutron diffraction data collected on the HRPD instrument, ISIS.

Substituted Cation				Pr	Y	Yb	
Refined Parameters	Space Group			C 2/m			
	a (Å)			9.810 (2)	9.809(1)	9.805(4)	
	b (Å)			3.746 (6)	3.722(1)	3.715(1)	
	c (Å)			6.966 (3)	6.842 (3)	6.814(3)	
	β (°)			118.46 (1)	118.601 (7)	118.59 (1)	
	Cell Volume (Å ³)			225.022 (4)	219.328(1)	217.931 (2)	
	χ^2			3.29	1.94	2.25	
	wRp			0.066	0.048	0.063	
U _{iso} (x 100 Å ⁻²)	U & Ln			0.946 (4)	0.678 (4)	1.241 (4)	
	Ti			1.253 (4)	1.383 (5)	1.026 (5)	
	O1			0.841 (3)	0.757 (4)	1.042 (4)	
	O2			1.229 (4)	1.249 (4)	1.295 (4)	
	O3			1.328 (4)	1.234 (4)	1.320 (4)	
Atom coordination	Site	U & Ln	2a	x	0	0	0
				y	0	0	0
				z	0	0	0
		Ti	4i	x	0.839(1)	0.832(1)	0.830(2)
				y	0	0	0
				z	0.410(1)	0.409(3)	0.405(2)
		O ₁	4i	x	0.986(1)	0.981(1)	0.980(1)
				y	0	0	0
				z	0.310(1)	0.309(1)	0.305(2)
		O ₂	4i	x	0.662(2)	0.660(1)	0.657(2)
				y	0	0	0
				z	0.109(1)	0.107(2)	0.104(2)
		O ₃	4i	x	0.290(1)	0.286(2)	0.281(2)
				y	0	0	0
				z	0.416(1)	0.410(1)	0.409(1)

Table 6.5: Key bond lengths for the brannerite structure, as determined from Rietveld refinement of high resolution neutron diffraction data for each of the target compositions.

Bond	Multiplicity	Length (Å)		
		Pr	Y	Yb
U & M-O ₁	x2	2.239(2)	2.231(4)	2.229(5)
U & M-O ₂	x4	2.289(4)	2.283(3)	2.278(3)
Ti-O ₁	x1	1.852(4)	1.849(3)	1.843(1)
Ti-O ₁	x1	2.019(2)	2.012(3)	2.008(2)
Ti-O ₂	x1	1.899(3)	1.892(1)	1.889(1)
Ti-O ₃	x1	2.121(2)	2.115(3)	2.106(3)
Ti-O ₃	x2	1.949(1)	1.942(2)	1.939(1)

6.3.5 REE Brannerite Bond Valence Summations

Rietveld refinement of neutron diffraction data enabled the analysis of the bond lengths within the crystal structure for each of the REE compositions, Table 6.5. The bond lengths were used to for bond valence sum (BVS) calculations.

The valence of a cation is an expression of the number of electrons gained or lost in order to stabilise the bond of the atom, and is given in valence units (v.u.). A bond is created with the valence electrons, the electrons within the outer most shell of an atom, between two atoms, this also described the charge of the cation. The valence electrons of a cation is equivalent to the charge of the cation, valence electrons also require the least energy to form a bond within the structure. Bond valence sum (BVS) calculations were completed through analysis of the measured bond length of a structure and the reference bond length of the cation, multiplied by the number of bonds and the products summed. Bond valence sum calculations have been used as a comparative tool to understand the stability of the refined crystal structures with U^{4+} , U^{5+} and U^{6+} . Each cation valence has been calculated using the bond valence summation (BVS) methodology, Equation 6.1.

The BVS has also been calculated for the Ti^{4+} and metal cation, Pr^{3+} , Y^{3+} and Yb^{3+} in order to validate the refined cation location with known valency but highlighting any abnormal behaviours.

$$\text{Valence} = V = \sum v_i$$
$$v_i = \exp\left(\frac{R_0 - R_i}{b}\right) \quad \text{Equation 6.1}$$

Empirical constant b is determined as $b = 0.37$ for oxides, R_0 is the tabulated reference bond lengths taken from Brese and O'Keefe [33] and R_i is the observed bond length, taken from the refinement of the structures using high resolution neutron diffraction analysis, Table 6.5. A valence with a difference of $>10\%$ to target valence indicates that the atom is over or under bonded, depending on whether the value is greater or smaller, respectively. The valence is dependent on the atom in the material. For these materials it was expected that the titanium would have a valence of 4, the REE would have a valence of 3, and the valence of the uranium is explored by varying the R_0 value for U^{4+} , U^{5+} and U^{6+} . However, studies of the theoretical values of R_0 for U^{5+} are limited, and therefore the R_0 value for U^{5+} must be determined uniquely. X-ray Absorption Near Edge Spectroscopy (XANES) analysis previously completed on yttrium bearing uranium brannerite material (Stennett et al.) quantified the average oxidation state of uranium at U^{5+} .

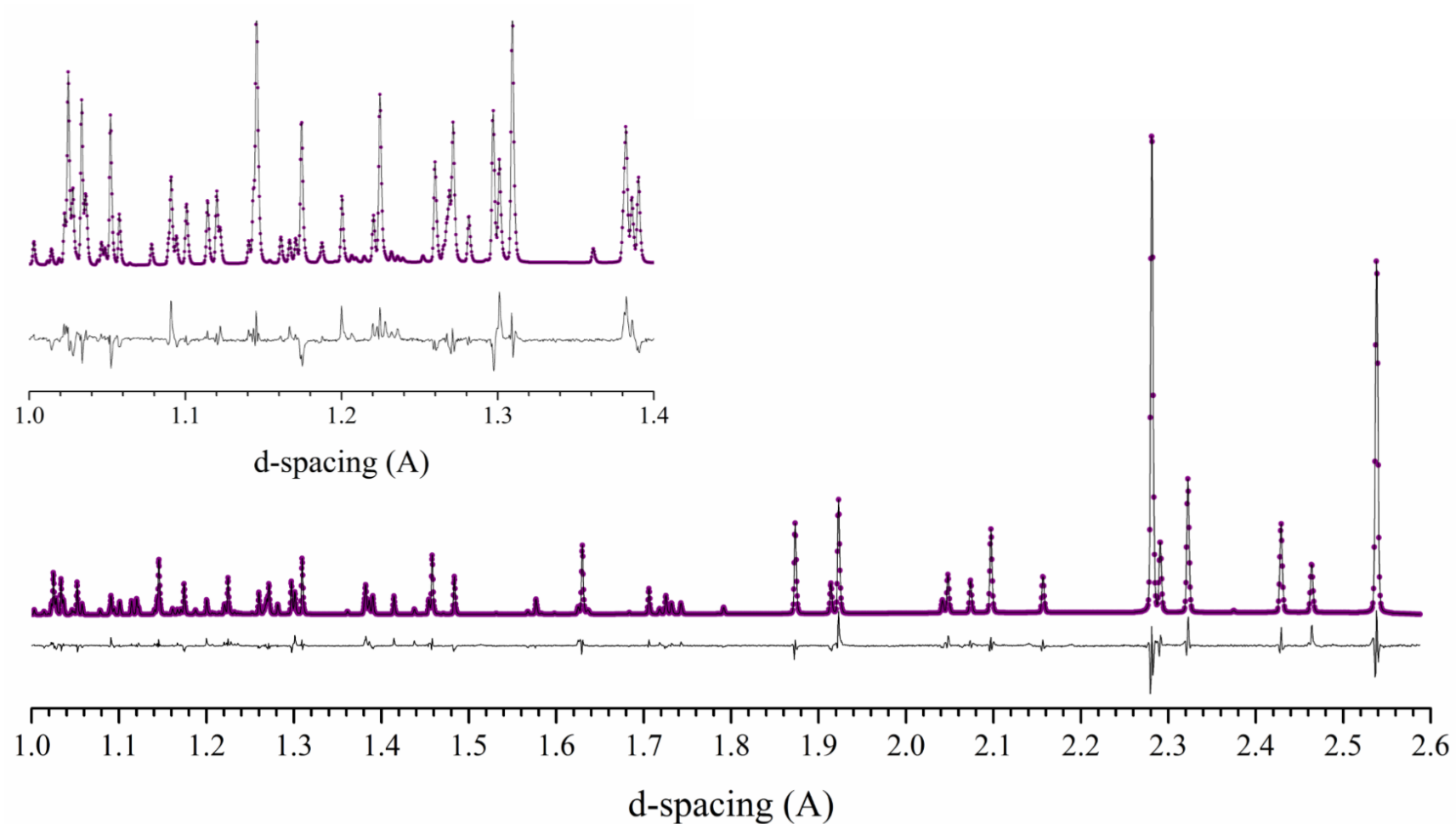


Figure 6.6: The refinement of the brannerite model of material with target composition $\text{U}_{0.525}\text{Pr}_{0.475}\text{Ti}_2\text{O}_6$. The analysis was completed using neutron diffraction data collected on the HRPD Instrument, ISIS, Harwell using the GSAS software. The model fitting is indicated by the purple trace, and the quality of the fitting to the data is shown by the observed minus calculated difference trace, in black

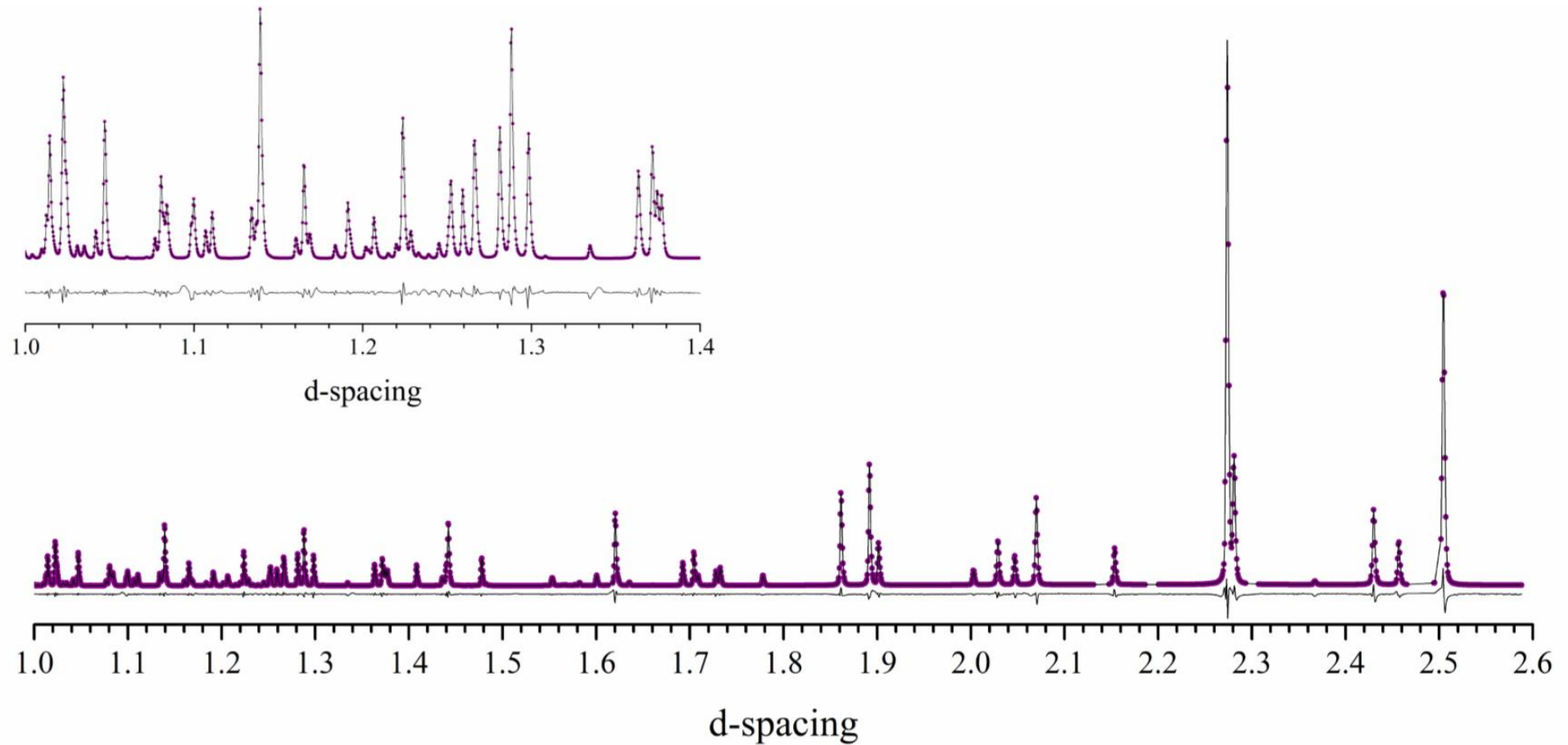


Figure 6.7: The refinement of the brannerite model of material with target composition $\text{U}_{0.540}\text{Y}_{0.460}\text{Ti}_2\text{O}_6$. The analysis was completed using neutron diffraction data collected on the HRPD Instrument, ISIS, Harwell using the GSAS software. The model fitting is indicated by the purple trace, and the quality of the fitting to the data is shown by the observed minus calculated difference trace, in black.

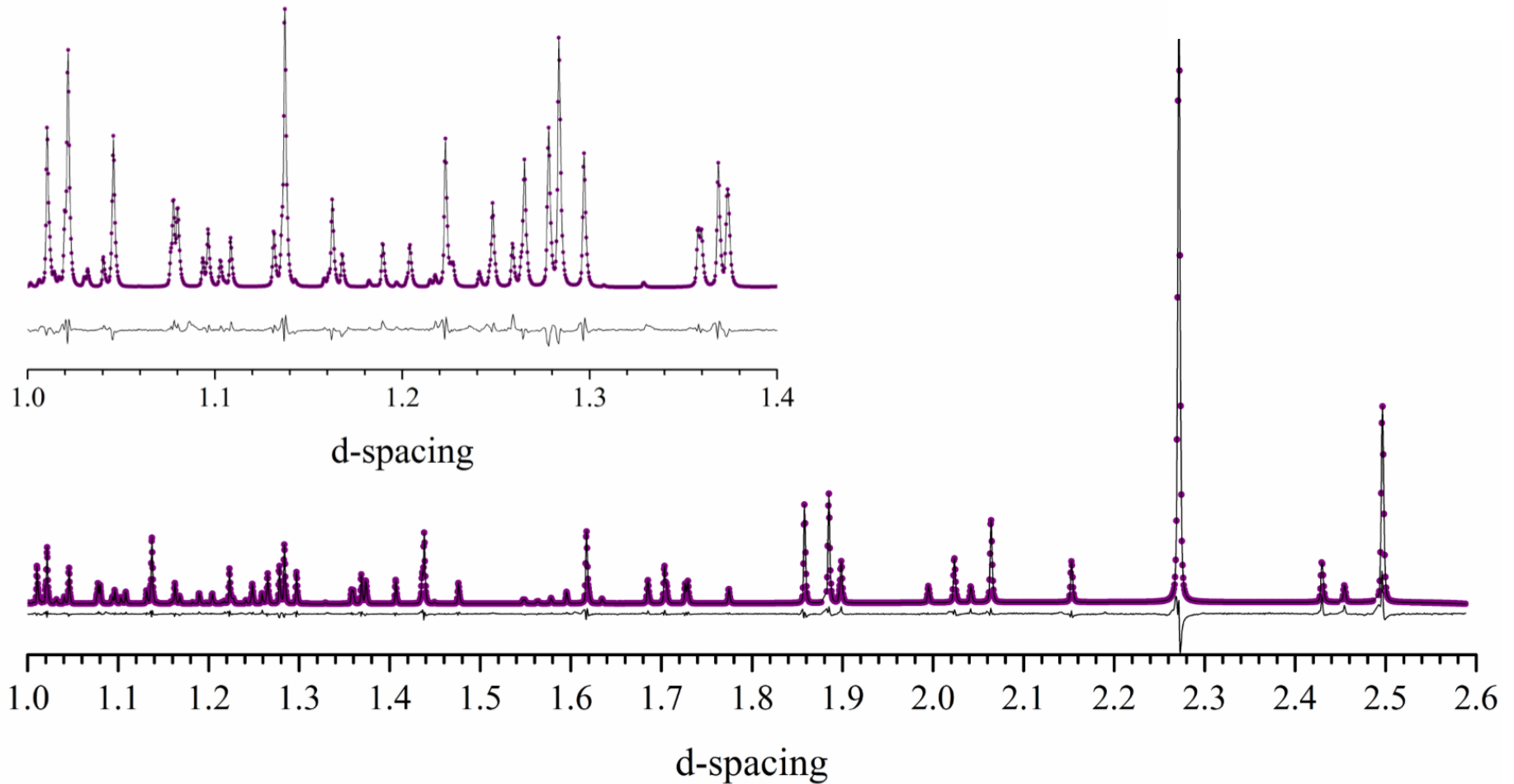


Figure 6.8: The refinement of the brannerite model of material with target composition $\text{U}_{0.500}\text{Yb}_{0.500}\text{Ti}_2\text{O}_6$. The analysis was completed using neutron diffraction data collected on the HRPD Instrument, ISIS, Harwell using the GSAS software. The model fitting is indicated by the purple trace, and the quality of the fitting to the data is shown by the observed minus calculated difference trace, in black.

Therefore the assumption that the uranium within target composition $U_{0.540}Y_{0.460}Ti_2O_6$ is U^{5+} was made. Using the refined uranium / oxygen bond lengths of the $U_{0.540}Y_{0.460}Ti_2O_6$ material (Table 6.5), the reference bond length, R_0 , of U^{5+} within a brannerite structured material was calculated at 2.2\AA .

For all compositions, the calculated valence is summarised in Table 6.6. This was compared to the target valence in order to understand the stability of the structure with the cation. Comparing the BVS calculations for the uranium within the materials it can be seen that both the U^{4+} and U^{5+} have a valence of 4 and 5 respectively, indicating both cations would be stable within the structure. Analysis of the BVS for the U^{6+} highlights an under bonding with this cation, with a discrepancy in the calculated valence to the theoretical valence of $>-35\%$ for all materials. For the yttrium and ytterbium containing materials, target compositions $U_{0.540}Y_{0.460}Ti_2O_6$ and $U_{0.500}Yb_{0.500}Ti_2O_6$ respectively, the REE cation are within 10% of the expected valence. For the compositions $U_{0.540}Y_{0.460}Ti_2O_6$ and $U_{0.500}Yb_{0.500}Ti_2O_6$ the A-site can be considered as stable with the substitution of the rare earth element, with a uranium oxidation state of either U^{4+} or U^{5+} .

For material with target composition $U_{0.525}Pr_{0.475}Ti_2O_6$, the praseodymium has an assumed valence of 3, whereas the BVS calculation gave a value of 4.15, $\sim 38\%$ greater than the theorised value. This highlights that the praseodymium is over bonded within the material, although the explanation for this is beyond the scope of this thesis. However, this could be an indicator that the praseodymium has an average oxidation state of 4. While an oxidation state of 4 for the praseodymium cation was not targeted, the structural formation at high temperature could have led to the stabilisation Pr^{4+} within the structure. The discrepancy within the praseodymium valence highlights a potential instability in the A site of the material. However, with the stabilisation of Pr^{4+} it would be expected that the uranium oxidation state would be maintained at U^{4+} . Further analysis of the uranium and praseodymium average oxidation state via XANES analysis would provide the information to further define the cation stability on the A-site of this material.

6.3.6 Brannerite Conclusions

Materials of target composition $U_{1-x}M_xTi_2O_6$ with $M = Fe, Pr, Yb$ and Y were synthesised in an air atmosphere from dried oxide precursors. Their crystallographic and chemical properties have been analysed through a range of techniques in order to determine the presence of the brannerite structure (space group $C2/m$).

Table 6.6: BVSs for brannerite materials with target compositions $U_{0.525}Pr_{0.475}Ti_2O_6$, $U_{0.540}Y_{0.460}Ti_2O_6$ and $U_{0.500}Yb_{0.500}Ti_2O_6$. Refined bond lengths have been taken from Table 6.5 and reference bond lengths, R_0 taken from Brese and O’Keeffe [33].

Substituted Cation	Space Group	Bond	Multiplicity	R_0	R_{ij}	v_i	Valence
Pr	C 2/m	U ⁴⁺ -O ₁	2	2.11	2.24	0.71	3.90
		U ⁴⁺ -O ₂	4		2.29	0.62	
		U ⁵⁺ -O ₁	2	2.20	2.24	0.89	4.90
		U ⁵⁺ -O ₂	4		2.29	0.78	
		U ⁶⁺ -O ₁	2	2.08	2.24	0.64	3.53
		U ⁶⁺ -O ₂	4		2.29	0.56	
		Pr-O ₁	2	2.14	2.24	0.76	4.15
		Pr-O ₂	4		2.29	0.66	
		Ti-O ₁	1	1.82	1.85	0.91	4.11
		Ti-O ₁	1		2.02	0.58	
		Ti-O ₂	1		1.90	0.80	
		Ti-O ₃	1		2.12	0.44	
		Ti-O ₃	2		1.95	0.70	
Y	C 2/m	U ⁴⁺ -O ₁	2	2.11	2.23	0.73	3.97
		U ⁴⁺ -O ₂	4		2.28	0.63	
		U ⁵⁺ -O ₁	2	2.20	2.23	0.91	4.99
		U ⁵⁺ -O ₂	4		2.28	0.79	
		U ⁶⁺ -O ₁	2	2.08	2.23	0.66	3.59
		U ⁶⁺ -O ₂	4		2.28	0.57	
		Y-O ₁	2	2.01	2.23	0.56	3.05
		Y-O ₂	4		2.28	0.48	
		Ti-O ₁	1	1.82	1.85	0.91	4.18
		Ti-O ₁	1		2.01	0.59	
		Ti-O ₂	1		1.89	0.81	
		Ti-O ₃	1		2.12	0.44	
		Ti-O ₃	2		1.94	0.71	
Yb	C 2/m	U ⁴⁺ -O ₁	2	2.11	2.23	0.73	4.01
		U ⁴⁺ -O ₂	4		2.28	0.64	
		U ⁵⁺ -O ₁	2	2.20	2.23	0.92	5.05
		U ⁵⁺ -O ₂	4		2.28	0.80	
		U ⁶⁺ -O ₁	2	2.08	2.23	0.66	3.63
		U ⁶⁺ -O ₂	4		2.28	0.58	
		Yb-O ₁	2	1.99	2.23	0.57	2.85
		Yb-O ₂	4		2.28	0.45	
		Ti-O ₁	1	1.82	1.84	0.93	4.23
		Ti-O ₁	1		2.01	0.59	
		Ti-O ₂	1		1.89	0.82	
		Ti-O ₃	1		2.11	0.46	
		Ti-O ₃	2		1.94	0.72	

6.3.6.1 Rare Earth Element (REE) Substitution Conclusions

SEM and EDS analysis was utilised in order to define the composition required to form a single phase brannerite material with substitutions of Pr, Y, and Yb in the systems, $U_{1-x}REE_xTi_2O_6$, where REE = Pr, Y or Yb. XRD analysis indicated the formation of a single phase assemblage adopting the crystalline structure of a brannerite for compositions; $U_{0.56(4)}Pr_{0.43(2)}Ti_{2.00(8)}O_6$, $U_{0.54(2)}Y_{0.41(1)}Ti_{2.00(7)}O_6$ and $U_{0.53(4)}Yb_{0.46(3)}Ti_{2.00(3)}O_6$. Material stoichiometries were determined by EDS analysis (Table 6.3). Figure 6.4 shows back scattered electron diffraction images as collected on the materials, indicating a single phase assemblage by a lack of variation in the contrast of the images.

Rietveld refinement of neutron diffraction data provided refined lattice parameters of the brannerite structure for each material. A linear relationship was identified between the size of the substituted REE cation (Pr, Y or Yb) and the volume of the unit cell (Table 6.5). Similarly as the refine volume of the unit cell decreases (Table 6.4) the uranium stoichiometry decreases (Table 6.3). However, there is no linear relationship between the REE cation stoichiometry and the unit cell volume.

Bond valence sums (Table 6.6) were calculated for all cations within the materials using the refined bond lengths from Rietveld refinement of the neutron diffraction data in order to aid identification of the uranium oxidation state through exploration of the stability of the cation through the valence summations. In addition to the uranium the REE and titanium cation BVS were calculated to understand the stability of the material. The BVS for titanium cations are all within 10% of the theoretical value of 4 for all materials. The BVS for the Y and Yb, substituted materials ($U_{0.54(2)}Y_{0.41(1)}Ti_{2.00(7)}O_6$ and $U_{0.53(4)}Yb_{0.46(3)}Ti_{2.00(3)}O_6$, respectively) show the stability of the substituted cations, with an expected valence of 3 and calculated values with 10% of this (Table 6.6). However, the BVS for the praseodymium, in composition $U_{0.56(4)}Pr_{0.43(2)}Ti_{2.00(8)}O_6$, highlight an over bonding by ~38%, at 4.15. However, this could be an indicator that, in order to stabilise the substitution of praseodymium within structure, the praseodymium would be required to oxidise to Pr^{4+} rather than remain at Pr^{3+} . This analysis to quantify the praseodymium oxidation state is beyond the scope of this work, but would require the use of XANES analysis. Uranium BVS calculations indicate that the presence of U^{6+} could be unstable, with under bonding values for all materials at >35% to the theoretical value of 6. The BVS indicate the structure would stabilise with the presence of U^{4+} or U^{5+} , with theoretical bond length of U-O bonds (R_0) for U^{5+} calculated from yttrium containing material, previously analysed (unpublished), to stabilise with an average uranium oxidation state of U^{5+} . In order to gain information on the average uranium oxidation

state, including analysis of material within composition $U_{0.54(2)}Y_{0.41(1)}Ti_{2.00(7)}O_6$ to confirm U^{5+} , XANES analysis would be required.

6.3.6.2 Iron Brannerite Conclusions

Attempts to substitute iron within the target composition, $U_{1-x}Fe_xTi_2O_6$, through the use of dried oxide powders, were unsuccessful. XRD analysis (Figure 6.3) indicated the formation of a multiphase material, with reflections indexed highlighting the formation of brannerite, and presence of unreacted component oxide materials (UO_3 , Fe_2O_3 and TiO_2). Previous work by Vance et al. [30] indicated the formation of material with composition $U_{0.6}Fe_{0.4}Ti_2O_6$ via an nitrate / alkoxide route, however, as attempts via a dried oxide route proved unsuccessful, a more intimate mixing of component oxides is required in order to ensure a single phase assemblage with the brannerite structure forms.

6.4 Chromium Substituted Material Results and Discussions

Synthesis of the composition $U_{0.50}Cr_{0.50}Ti_{2.50}O_6$ was attempted with the aim of establishing the stability of the brannerite material with large quantities of small transition metal cations. Initial characterisation with the use of chromium using XRD highlighted a structure which could be indexed with respect to a rutile structure (space group $P4_2/mnm$). As a result, material of the series $U_xCr_xTi_{3-2x}O_6$ with $x=0.25, 0.50, 0.75$ and 1.00 were synthesised to establish the extent at which uranium and chromium could be substituted into the rutile structure (TiO_2).

6.4.1 X-ray Diffraction Analysis

XRD analysis was completed on a STOE STADI P diffractometer. Operated in transmission mode with a $Cu K\alpha_1$ radiation ($\lambda=1.5408 \text{ \AA}$) source, at a voltage and current of 40kV and 40mA, respectively. Powdered samples were prepared within a dedicated fume cupboard, where finely ground powder was dispersed in glue on an acetate film to form a nominally homogeneous, flat surface. Figure 6.9 shows the resultant crystalline structure of the phase assemblages after equilibrium was reached through synthesis for all materials of the series $U_xCr_xTi_{3-2x}O_6$ with $x=0.25, 0.50, 0.75$ and 1.00 .

A material with structural reflections indicative of the rutile structure can be seen for the target compositions $U_{0.25}Cr_{0.25}Ti_{2.50}O_6$ and $U_{0.50}Cr_{0.50}Ti_{2.00}O_6$. This indicates that both the uranium and chromium cations have substituted for the 6-fold coordinated titanium within the structure, see Figure 6.10(a). For target composition $U_{0.50}Cr_{0.50}Ti_{2.00}O_6$ the

rutile structure is formed, however, upon close inspection of the XRD pattern the full width at half height of the reflections are broader than the reflections of the target composition $U_{0.25}Cr_{0.25}Ti_{2.50}O_6$. This is characteristic of a material with multiple phases with similar chemical compositions and comparable lattice parameters of the same space group. This was analysed in detail using high resolution neutron diffraction data.

For materials with target composition $U_{0.75}Cr_{0.75}Ti_{1.50}O_6$ and $UCrTiO_6$, $x=0.75$ and $x=1.00$ in $U_xCr_xTi_{3-2x}O_6$, respectively, XRD analysis indicated the presence of the rutile structure. However, a second phase was also identified, indexed to the space group $P-31m$. This was identified as a hexagonal uranium dichromate oxide material of composition UCr_2O_6 , or general composition $A^{6+}B_2^{3+}O_6$. Structural parameters for the reference material was taken from A. Collomb et al [34, 35], who have studied the phase formation during high pressure synthesis, Figure 6.10(c). The structure has a trigonal symmetry, with reference structural parameters of $a = b = 4.990(1) \text{ \AA}$, $c = 4.622(1) \text{ \AA}$ and atomic position coordinates of uranium at the 1a site (0, 0, 0), a chromium at the 2d site (1/3, 2/3, 1/2) and an oxygen at the 6k site (0.3405(3), 0, 0.2647(2)). The x and z coordinates of the oxygen anion at the 6k site can be refined within the structure.

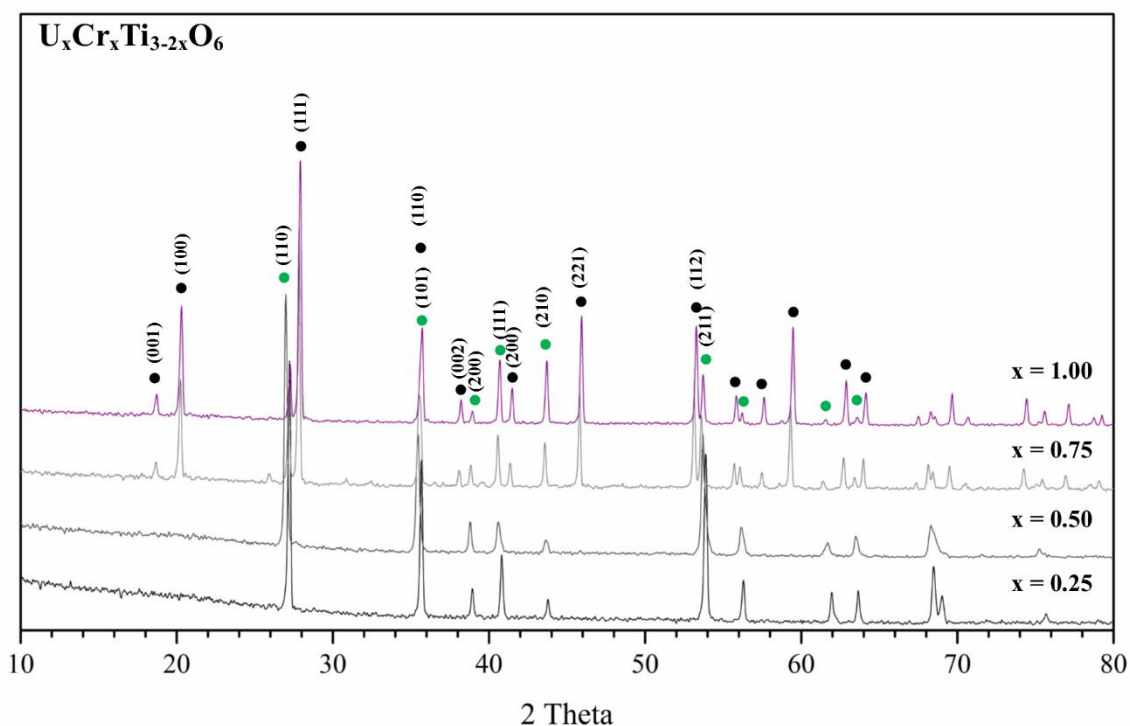


Figure 6.9: XRD data as collected on the STOE-IP instrument of the system $U_xCr_xTi_{3-2x}O_6$, where $x=0.25, 0.50, 0.75, 1.00$. Phase assemblage of the structure has been identified as ●: material with space group $P-31m$ (generic composition AB_2O_6) and ●: rutile, space group $P42/mnm$ (generic composition AO_2)

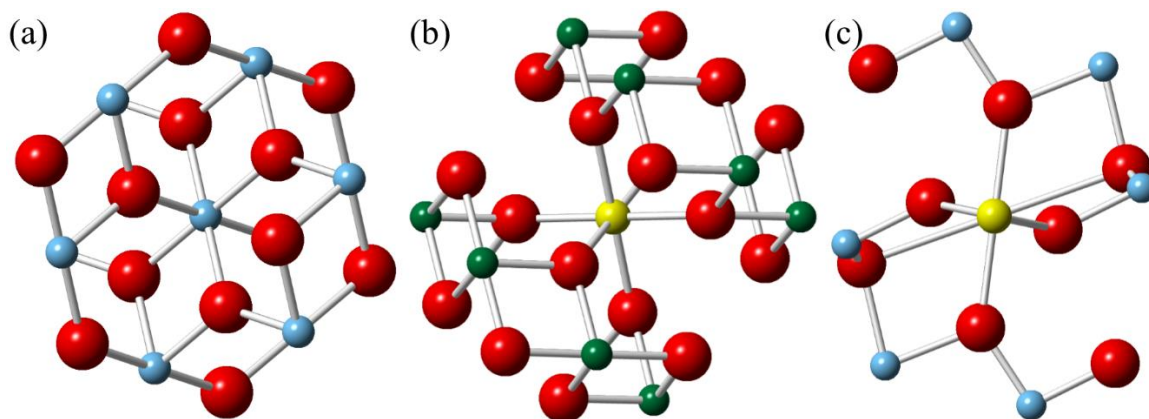


Figure 6.10: (a) rutile, AO_2 (b) uranium dichromate, A_2BO_6 and (c) brannerite, ATi_2O_6 , structure in the [010] direction. Cations are colour coordinated, where blue=titanium, green=chromium, yellow=uranium and red=oxygen.

6.4.2 Scanning Electron Microscopy and Energy Dispersive X-ray Spectroscopy of Chromium Substituted Materials

SEM and EDS analysis using the Hitachi TM 3030 instrument has been implemented, see Section 3.2 for the instrument set up. Synthesised powdered material was cold uniaxially pressed, sintered and mounted within an epoxy resin.

Microstructural and micro-chemical analyses was then performed through the use of backscattered electron (BSE) images (Figure 6.11). Semi-quantitative elemental analysis was completed using the EDS detector within the instrument at 30,000x magnification (Table 6.7). Semi-quantitative EDS analysis (Table 6.7) provided compositional information, however the technique is insensitive to the oxygen anion stoichiometry of the material. Oxygen stoichiometry was defined as 6, as determined by both the rutile (Ti_3O_6) and uranium dichromate (UCr_2O_6) crystal structures. In the absence of complete X-ray Absorption Near Edge Spectroscopy (XANES) for all material, the average uranium oxidation state has been calculated from the normalised composition, where the oxygen stoichiometry is 6, and the materials have 3 formula units (f.u.) of cations, as defined by the reference materials. The assumption that the titanium has an oxidation state of 4, and the chromium an oxidation state of 3, was also used for the calculations. For the materials where two phases have been identified, target compositions $U_{0.75}Cr_{0.75}Ti_{1.50}O_6$ and $UCrTiO_6$, the assumption that the greater proportion of titanium would be associated with the rutile crystal structure was used to infer the space group (Table 6.7).

BSE / EDS analysis of the target composition $U_{0.25}Cr_{0.25}Ti_{2.50}O_6$ and $U_{0.50}Cr_{0.50}Ti_{2.00}O_6$, indicate a material with a single phase assemblage of compositions $U_{0.19(1)}Cr_{0.27(2)}Ti_{2.54(5)}O_6$ and $U_{0.45(2)}Cr_{0.43(2)}Ti_{2.08(4)}O_6$, respectively. This is determined by

the lack of variation in the contrast of the BSE images. The average oxidation state of the uranium of 5.58 was calculated for the material with composition $U_{0.19(1)}Cr_{0.27(2)}Ti_{2.54(5)}O_6$. XRD analysis indicated that material target composition $U_{0.50}Cr_{0.50}Ti_{2.00}O_6$ consisted of multiple rutile compositions with similar lattice parameters. Within the BSE image a single contrast was observed, highlighting the similarity of the chemical composition of the phases within the assemblage. The point EDS analysis of the material did not indicate a variant in the chemical composition, therefore the average of 5 spot analysis has been taken as a representative of the material.

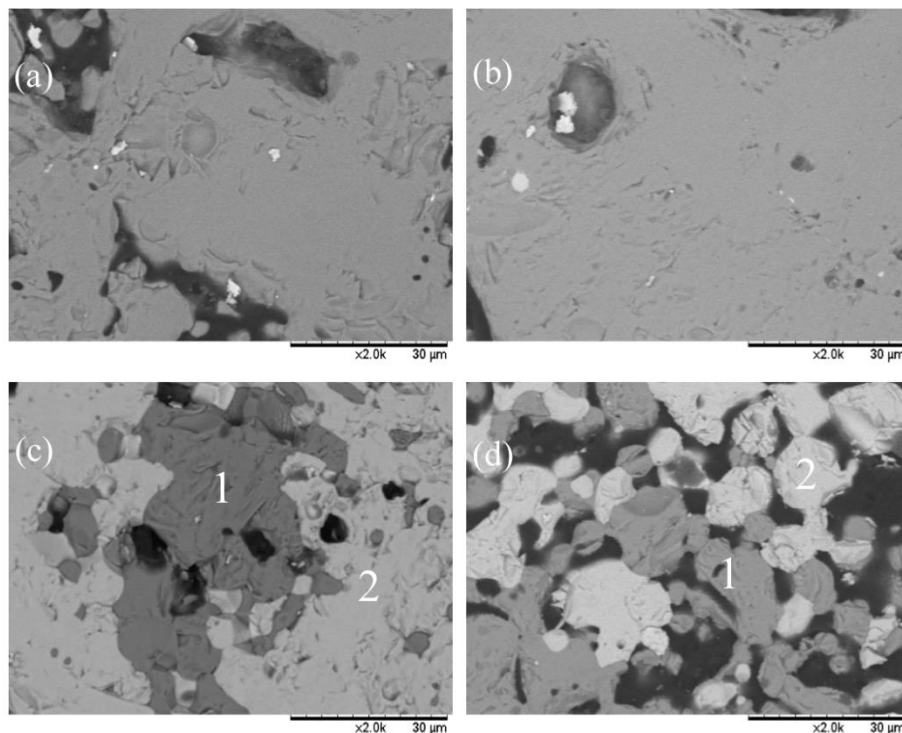


Figure 6.11: Back scattered electron micrograph of target compositions (a) $U_{0.25}Cr_{0.25}Ti_{2.50}O_6$, (b) $U_{0.50}Cr_{0.50}Ti_{2.00}O_6$, (c) $U_{0.75}Cr_{0.75}Ti_{1.50}O_6$ and (d) $UCrTiO_6$. In (c) and (d) ‘1’ highlights the rutile phase and ‘2’ highlights the hexagonal phase. White spots in (a) and (b) are silver contaminants from the use of silver dag to aid charge dissipation on the material during analysis.

Both the materials with target compositions $U_{0.75}Cr_{0.75}Ti_{1.50}O_6$ and $UCrTiO_6$ consisted of a multiphase assemblage. EDS analysis of both target compositions $U_{0.75}Cr_{0.75}Ti_{1.50}O_6$ and $UCrTiO_6$ indicated a phase assemblage of two chemical compositions, which across the materials are comparable. Therefore the average of the measured compositions was taken for both phases of both materials at, $U_{0.29(2)}Cr_{0.46(2)}Ti_{2.27(5)}O_6$ and $Cr_{0.98(4)}Ti_{1.09(3)}U_{0.95(4)}O_6$. Under the assumption that the rutile material will be dominated by titanium the composition $U_{0.29(2)}Cr_{0.46(2)}Ti_{2.27(5)}O_6$ was used for analysis of the rutile phase. It then follows that the composition $Cr_{0.98(4)}Ti_{1.09(3)}U_{0.95(4)}O_6$ has the hexagonal

uranium dichromate structure. BSE images indicated that for target composition $U_{0.75}Cr_{0.75}Ti_{1.50}O_6$ the two phases are approximately equal in proportion, whereas for target composition $UCrTi_5O_6$, the hexagonal uranium dichromate material is predominant. Refinement of the neutron diffraction data enabled the definition of the relative ratios (phase split) between the two phases.

6.4.3 Neutron Diffraction Analysis of Chromium Substituted Materials

The High Resolution Powder Diffractometer (HRPD) instrument at ISIS, Harwell was used to complete accurate structural analysis of the chromium materials of the series $U_xCr_xTi_{3-2x}O_6$, where $x = 0.25, 0.50, 0.75$ and 1.00 . Full instrument set up of the ISIS facility can be found in Section 3.3. The data was collected within an evacuated sample chamber, this reduced the probability of neutrons scattering prior to interacting with the sample. Data was collected using the backscattered detector, with a d-spacing range of ~ 0.6 - 4.6\AA (TOF 30-230ms) with a resolution ($\Delta d/d$) of up to $\sim 5 \times 10^{-4}$.

Lattice parameter and structural bond lengths refined during analysis are summarised in Table 6.8 and Table 6.9, respectively [31, 32]. Refinement has been completed using the normalised compositions within Table 6.7. The model parameters used for the refinement for the rutile and hexagonal dichromate structures were taken from Baur et al. and Collomb et al., respectively [28, 35]. Figures 6.12- 6.14 show the refined structures for target compositions $U_xCr_xTi_{3-2x}O_6$, where $x = 0.25, 0.50, 0.75$ and 1.00 .

The rutile structure has a single crystallographic site. The substitution of chromium and uranium for the titanium cations are expected to share a single crystallographic site, therefore the thermal parameters (U_{iso}) of all cations were constrained. For materials identified with a multiphase assemblage, the U_{iso} values for both cations and anions were constrained at 25\AA , this enabled the stabilisation of the structural refinement within the GSAS software.

The refinement of a structure with parameters indicative of a rutile was successful for all materials. For target compositions where $x=0.25, 0.75$ and 1.00 in $U_xCr_xTi_{3-2x}O_6$ a single rutile structure was required for the refinement. However, for material of composition $U_{0.5}Cr_{0.5}Ti_2O_6$ ($x=0.50$), full width half height of the reflections required a second rutile structure. The addition of a 3rd rutile structure did not improve the fitting statistics of the refinement and was therefore excluded.

Table 6.7: Compositional analysis using semi-quantitative EDS of the phase assemblage identified within the target compositions: (a) $U_{0.25}Cr_{0.25}Ti_{2.5}O_6$, (b) $U_{0.50}Cr_{0.50}Ti_{2.00}O_6$, (c) $U_{0.75}Cr_{0.75}Ti_{1.50}O_6$ and (d) $UCrTiO_6$. Compositions were determined from an average of 5 different analysed areas with the same contrast. (a)- (d) indicated the corresponding BSE image within Figure 6.11.

Target Composition		EDS Measured Composition	Normalised Composition	Calculated Uranium Oxidation State	Inferred Space Group
(a)	$U_{0.25}Cr_{0.25}Ti_{2.5}O_6$	$U_{0.19(1)}Cr_{0.27(2)}Ti_{2.57(5)}O_6$	$U_{0.19(1)}Cr_{0.27(2)}Ti_{2.54(5)}O_6$	5.58(8)	$P4_2/mnm$
(b)	$U_{0.5}Cr_{0.5}Ti_2O_6$	$U_{0.47(2)}Cr_{0.49(2)}Ti_{2.17(4)}O_6$	$U_{0.45(2)}Cr_{0.43(2)}Ti_{2.08(4)}O_6$	5.31(8)	$P4_2/mnm$
(c)	$U_{0.75}Cr_{0.75}Ti_{1.5}O_6$	1 $U_{0.32(2)}Cr_{0.53(1)}Ti_{2.48(2)}O_6$	$U_{0.29(2)}Cr_{0.48(1)}Ti_{2.25(2)}O_6$	5.38(5)	$P4_2/mnm$
		2 $Cr_{1.04(3)}Ti_{1.13(3)}U_{1.00(3)}O_6$	$Cr_{0.98(3)}Ti_{1.07(3)}U_{0.95(3)}O_6$	5.03(9)	$P\bar{3}1m$
(d)	$UCrTiO_6$	1 $U_{0.30(1)}Cr_{0.49(2)}Ti_{2.55(5)}O_6$	$U_{0.27(1)}Cr_{0.44(2)}Ti_{2.29(5)}O_6$	5.63(8)	$P4_2/mnm$
		2 $Cr_{1.03(4)}Ti_{1.17(3)}U_{1.00(4)}O_6$	$Cr_{0.97(4)}Ti_{1.10(3)}U_{0.94(4)}O_6$	5.0(1)	$P\bar{3}1m$

Table 6.8: Unit cell, thermal and atomic coordinate positions as refined parameters of the series $U_xCr_xTi_{3-2x}O_6$, where $x = 0.25, 0.50, 0.75$ or 1.00 , obtained from Rietveld refinement of neutron diffraction data collected on the HRPD instrument, ISIS, Harwell.

		x = 0.25		x = 0.50		x = 0.75		x = 1.00			
Space Group		P42/mnm		1- P42/mnm	2- P42/mnm	P-31m	P42/mnm	P-31m	P42/mnm		
a (Å)		4.6176 (1)		4.6221 (9)	4.6295 (4)	5.0340 (1)	4.6324 (2)	5.0341 (6)	4.6331 (7)		
b (Å)		4.6176 (1)		4.6221 (9)	4.6295 (4)	5.0340 (1)	4.6324 (2)	5.0341 (6)	4.6331 (7)		
c (Å)		2.9947 (1)		3.0059 (9)	3.0143(6)	4.7184 (2)	3.0167 (2)	4.7190 (10)	3.0171 (7)		
α (°)		90		90		90	90	90	90		
β (°)		90		90		90	90	90	90		
γ (°)		90		90		120	90	120	90		
Cell Volume (Å³)		63.805 (1)		64.215 (1)	64.604 (1)	103.549 (1)	64.737 (1)	103.566 (1)	64.762 (2)		
χ^2		4.841		4.767		8.413		4.872			
wRp		0.0718		0.1068		0.0473		0.0508			
Phase Proportions (%)		n/a		n/a		42.7(4)	57.3(4)	95.3(3)	4.7(3)		
U_{iso} ($\times 100 \text{ \AA}^2$)		U, Cr & Ti		0.3281 (36)		0.025					
		O		0.2662 (12)							
Atom Coordination	Site	O	4f	x	0.3055 (1)	0.3065(1)	0.3048(5)	-	0.3097(2)	-	0.3098(2)
				y	0.3055 (1)	0.3065(1)	0.3048(5)	-	0.3097(2)	-	0.3098(2)
				z	0	0	0	-	0	-	0
		O	6k	x	-	-	-	0.3473(1)	-	0.3472(3)	-
				y	-	-	-	0	-	0	-
				z	-	-	-	0.3473(1)	-	0.2710(1)	-

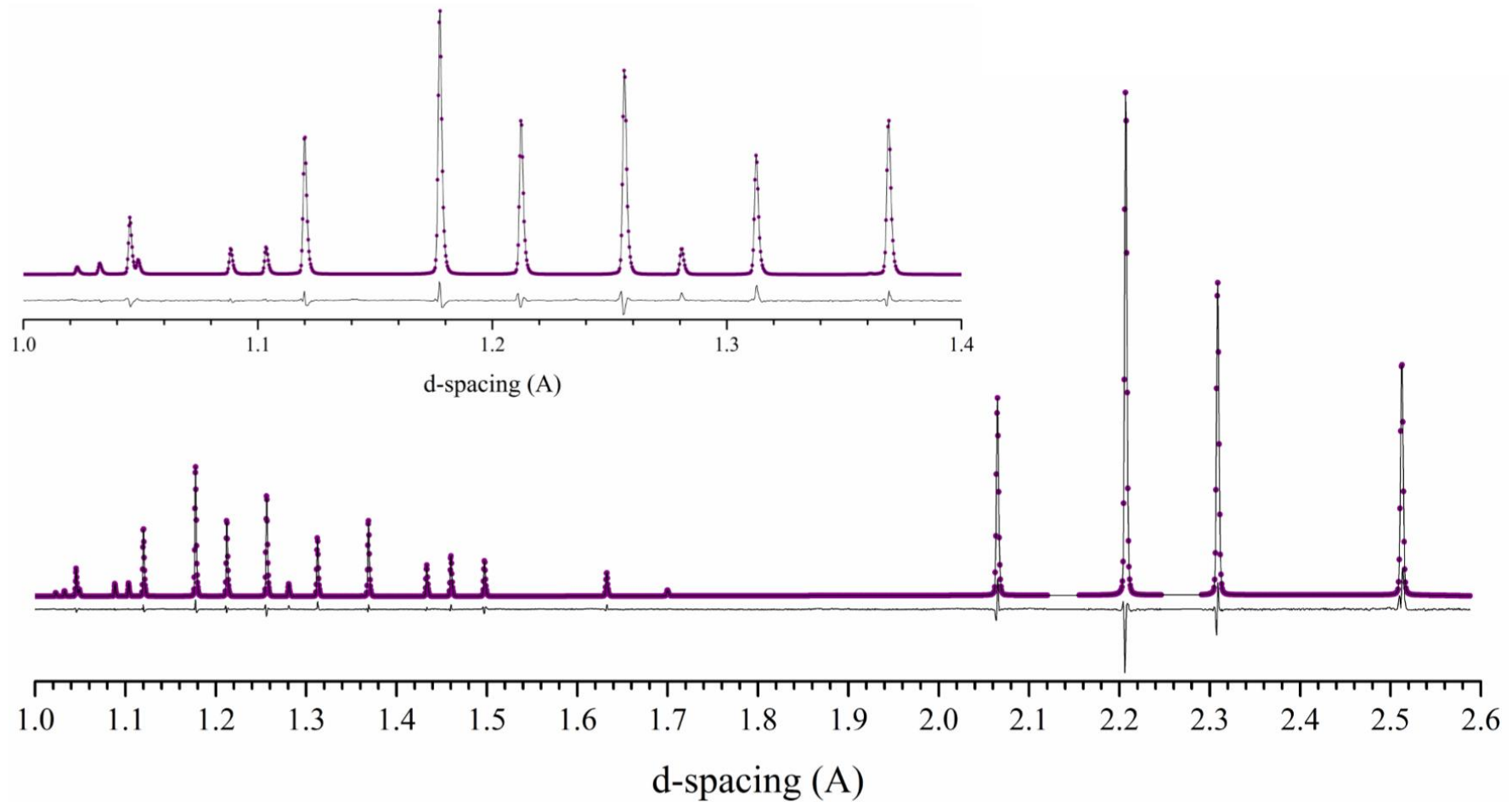


Figure 6.12: The refinement of the rutile model of material with target composition $U_{0.25}Cr_{0.25}Ti_{2.50}O_6$. The analysis was completed using neutron diffraction data collected on the HRPD Instrument, ISIS, Harwell using the GSAS software. The model fitting is indicated by the purple trace, and the quality of the fitting to the data is shown by the observed minus calculated difference trace, in black.

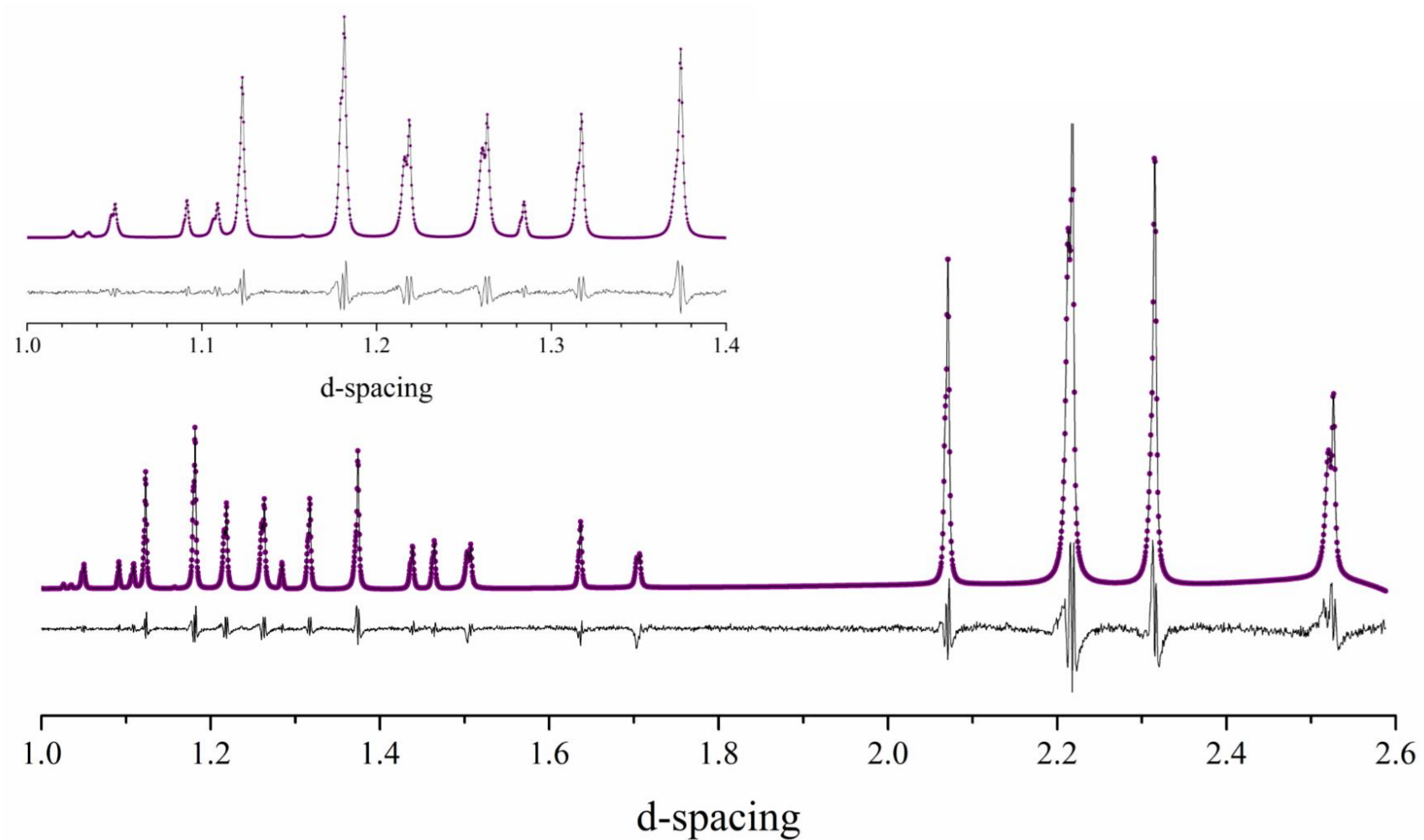


Figure 6.13: The refinement of the rutile model of material with target composition $\text{U}_{0.50}\text{Cr}_{0.50}\text{Ti}_{2.00}\text{O}_6$. The analysis was completed using neutron diffraction data collected on the HRPD Instrument, ISIS, Harwell using the GSAS software. The model fitting is indicated by the purple trace, and the quality of the fitting to the data is shown by the observed minus calculated difference trace, in black.

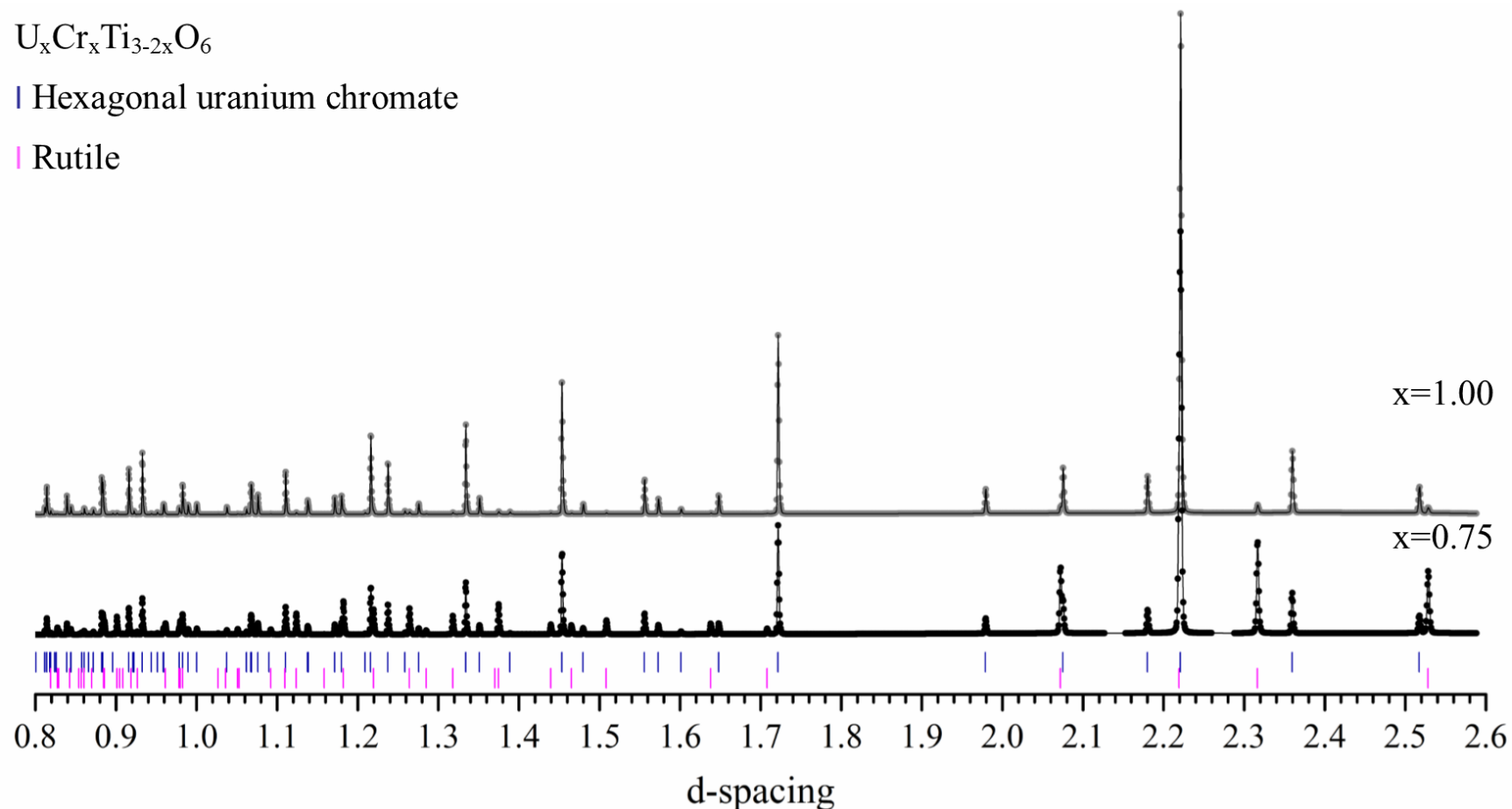


Figure 6.14: Rietveld refinement of materials with target compositions $U_{0.75}Cr_{0.75}Ti_{1.50}O_6$ and $UCrTiO_6$. The refinement of the rutile model and hexagonal uranium dichromate was completed using neutron diffraction data collected on the HRPD Instrument, ISIS, Harwell using the GSAS software. The model fitting is indicated by the purple trace, and the quality of the fitting to the data is shown by the observed minus calculated difference trace, in black. Indicated within the figure are the positions of reflections indicative of the rutile and hexogen structures.

In order to highlight the development of the rutile structure with changing composition Figure 6.15 was plotted. Figure 6.15 shows the refined model and residual background of a single rutile reflection from all compositions, normalised in order to aid direct comparison. For target compositions where $x=0.25$, 0.75 and 1.00 in $U_xCr_xTi_{3-2x}O_6$, the reflections profile and residual background does not indicate the present of any additional intensity. Upon closer inspection of the reflection for the target composition $U_{0.50}Cr_{0.50}Ti_{2.00}O_6$ ($x=0.50$), refined with two rutile phases, the residual background does not indicate the requirement for an additional rutile phase, in agreement with the refinement fitting statistics.

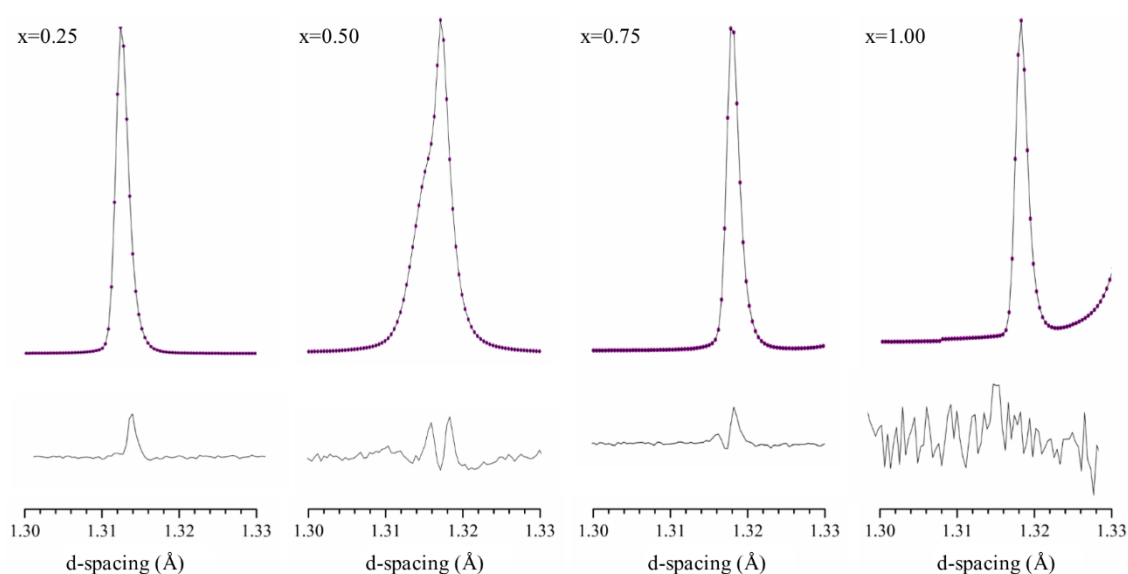


Figure 6.15: A single reflection observed between 1.30 - 1.33\AA refined as indicative of the rutile phase for all compositions in the system $U_xCr_xTi_{3-2x}O_6$ with $x=0.25$, 0.50 , 0.75 and 1.00 . All reflections have been normalised with respect to each other.

The secondary phase identified during analysis of target compositions $U_{0.75}Cr_{0.75}Ti_{1.50}O_6$ and $UCrTiO_6$ has been refined to the structure expected of hexagonal uranium dichromate, with space group $P-31m$, with refined parameters summarised in Table 6.8. The refinement for the hexagonal uranium dichromate structure was successfully completed using composition $Cr_{0.98(4)}Ti_{1.09(3)}U_{0.95(4)}O_6$ for both materials. This was completed with the titanium cations on the A-site of the general formula A_2BO_6 , with the chromium, and the uranium solely on the B-site.

Both the rutile and hexagonal uranium dichromate phases refined during the Rietveld analysis, within target compositions $U_{0.75}Cr_{0.75}Ti_{1.50}O_6$ and $UCrTiO_6$, have comparable lattice

parameters. The comparable compositions and lattice parameters enabled direct comparison of the proportion of each phase. The proportions of each phase were quantified through the scaling feature of the GSAS software, which refined the ratio of the structures to one another, the phase split has been represented as a percentage in Table 6.8. For target composition $U_{0.75}Cr_{0.75}Ti_{1.50}O_6$ refinement indicated ~57.3(4)% rutile and ~42.7(4)% hexagonal uranium dichromate. For target composition $UCrTiO_6$, refinement showed a dominance of the hexagonal uranium dichromate, at ~95.3(3)%, with minor contributions from rutile, ~4.7(3)%. This was as indicated by the BSE electron images.

Bond lengths refined from Rietveld analysis for all the materials of both rutile and uranium dichromate materials, where appropriate, are summarised in Table 6.9. The bond lengths have been used for the R_i values (Equation 6.1) in order to complete BVS calculations (Table 6.11 and 6.12).

Table 6.9: Key bond lengths refined from neutron diffraction data using the GSAS software for compositions of series $U_xCr_xTi_{3-2x}O_6$ where $x=0.25, 0.50, 0.75$ and 1.00

Space group	Bond	Multiplicity	Bond Length (Å)				
			x = 0.25	x = 0.50		x = 0.75	x = 1.00
P42/mnm	A-O ₁	2	1.995(2)	2.003(4)	2.007(1)	2.030(3)	2.030(1)
	A-O ₂	4	1.963(2)	1.976(3)	1.969(1)	1.957(3)	1.957(4)
P-31m	U-O ₁	6	N/A	N/A		2.166(6)	2.166(2)
	B-O ₁	4				1.968(1)	1.968(7)
	B-O ₂	2				1.967(3)	1.967(3)

High resolution neutron diffraction analysis is a powerful technique and often identifies impurities within materials not seen via XRD analysis. Within both $U_{0.25}Cr_{0.25}Ti_{2.50}O_6$ and $U_{0.75}Cr_{0.75}Ti_{1.50}O_6$ materials an unindexed impurity was removed from the data for analysis. This was not visible by other analysis methods so is assumed to be a contaminant from the sample preparation.

6.4.4 X-ray absorption near edge spectroscopy (XANES)

XANES data was collected on the X23A2 beamline at the National Synchrotron Light Source (NSLS), Brookhaven National Laboratory (BNL), USA, operating in transmission mode. Specimens were finely ground and dispersed in polyethylene glycol to achieve a thickness of one absorption length, full experimental set up can be found in section 3.6.1.1. Analysis of the average uranium oxidation within a material was completed at energies characteristic of the U

L₃-edge. Uranium standards CaU⁶⁺O₄, U_{0.5}⁵⁺Y_{0.5}Ti₂O₆ and U⁴⁺Ti₂O₆ with known oxidation states of uranium; U⁶⁺, U⁵⁺ and U⁴⁺, respectively, were used to draw conclusions on uranium oxidation state of the materials with target compositions U_{0.50}Cr_{0.50}Ti_{2.00}O₆ and UCrTiO₆ [14]. Information was taken from the absorption edges of XANES data for each target composition U_{0.50}Cr_{0.50}Ti_{2.00}O₆ and UCrTiO₆. The absorption edge is defined as the point where a sharp rise within the $\mu(E)$ value is noted, symbolic of a sharp rise in the X-ray energies, this is due to their interaction with an electronic shell of the probed atom. The electronic shell is analysed in order to quantify the valence electrons of the uranium cation within the materials and infer the oxidation state of the absorbent element. The absorption threshold, E_0 , is used to quantify this, where E_0 is defined as the half height of the normalised ($\mu(E)=1$) data. Reference materials are simultaneously collected during data acquisition in order to verify the alignment of the instrument. Back ground removal and normalisation of the data to $\mu(E)=1$ was performed using the Athena Programme [36]. The linear fitting of the standards are utilised to calculate the average uranium oxidation state in the measured materials.

The shape of the XANES data can be used as a fingerprint to quantify the uranium oxidation state. However, the full shape of the peak is influence by the oxidation state and the coordination number of the absorbent element. A direct comparison of the shape of the measures peak of the material analysed to standards requires the use of standards with the same local coordination environment. The coordination of the uranium in standards U⁴⁺Ti₂O₆ and U⁵⁺_{0.5}Y_{0.5}Ti₂O₆, have a 6-fold coordinated local environment. Standard CaU⁶⁺O₄ has uranium with an 8-fold coordination environment. As a result, the linear deconvolution feature of the Athena software, which enables the proportions of U⁴⁺, U⁵⁺ and U⁶⁺ within the materials to be calculated from the shape of the leading edge of the standards, could not be completed. Alternatively the E_0 value of the materials have been used and compared to E_0 values of the standards in order to determine the average uranium oxidation state. This was completed through the construction of a calibration line of the E_0 values for each of the standards, Table 6.10. The inferred average uranium oxidation state of the compositions is then taken from a linear line of best fit. Fit analysis is included within Appendix C.

Instrument access limited the number of materials which could be analysed, therefore XANES analysis has been completed on samples of materials with target compositions U_{0.50}Cr_{0.50}Ti_{2.00}O₆ and UCrTiO₆, see Figure 6.16, with the measured E_0 threshold energies, and the inferred average uranium oxidation state summarised in Table 6.10.

XANES analysis showed that the multiphase rutile material, target composition U_{0.50}Cr_{0.50}Ti_{2.00}O₆, was predominantly U⁶⁺, with a measured average uranium oxidation state

of 5.96(2). Within Table 6.7 the uranium oxidation state was calculated using the measured cation stoichiometry from EDS analysis, for material with target composition $U_{0.50}Cr_{0.50}Ti_{2.00}O_6$ an oxidation state of 5.58 was calculated, in good agreement with the XANES measured value, with a variance of $\sim 6.4(1)\%$.

Table 6.10: Measured absorption threshold, E_0 for target composition $U_{0.5}Cr_{0.5}Ti_2O_6$ and $UCrTiO_6$ with inclusion of standards utilised for the analysis and fitting.

Target composition	E_0 energy (eV)	U average oxidation state
$U_{0.5}Cr_{0.5}Ti_2O_6$	17158.1(2)	5.96(2)
$UCrTiO_6$	17156.9(2)	5.34(1)
U^{4+}	17154.3(2)	-
U^{5+}	17156.2(2)	-
U^{6+}	17158.2(2)	-

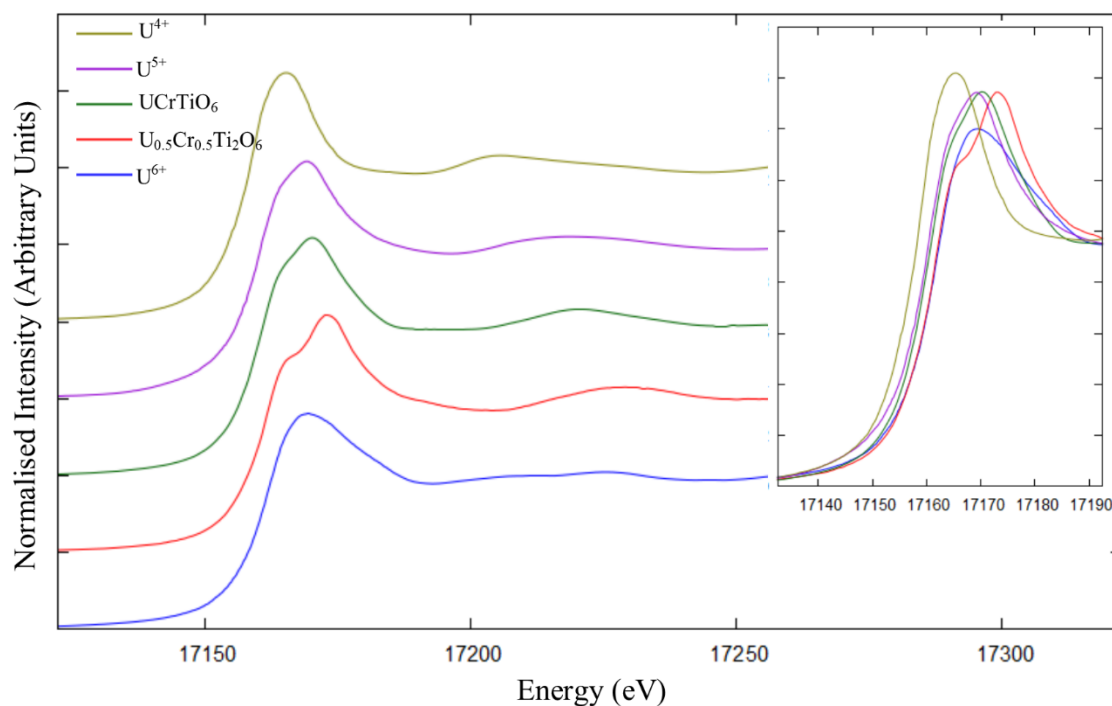


Figure 6.16: X-ray Absorption Near Edge Structure (XANES) data of the uranium within materials of target composition $U_{0.50}Cr_{0.50}Ti_{2.00}O_6$ and $UCrTiO_6$ with $CaU^{6+}O_4$, $U_{0.5}^{5+}Y_{0.5}Ti_2O_6$ and $U^{4+}Ti_2O_6$ as reference materials for U^{6+} , U^{5+} and U^{4+} , respectively.

Similarly, the average oxidation state of uranium within target composition $UCrTiO_6$ was measured at 5.34. Refinement of the phase split of high resolution neutron diffraction data indicated a 4.7(3)% rutile and 95.3(3)% hexagonal uranium dichromate material fraction.

Using the calculated average uranium oxidation states for each of the stoichiometries of target composition UCrTiO_6 (Table 6.7), the average oxidation state of the material was calculated at 5.03(8), ~6.16(9)% smaller than the measured average oxidation state, indicating the calculated uranium oxidation states within Table 6.7 are in close agreement to the measured values.

6.4.4 Bond Valence Summations (BVS)

Bond valence sum calculations, using Equation 6.1, were calculated using the bond lengths refined from neutron diffraction analysis (Table 6.9) and R_0 values as defined by Brese and O’Keeffe [33]. In the absence of a reference bond length for U^{5+} the R_0 value of 2.20Å, as defined in Section 6.3.5, was used.

Analysis of the BVS aids identification of the stability of the structure with the cation substitutions. The stability of the bond of an atom is described by the valence (in valence units, v.u.), the number of electrons gained or lost in order to stabilise the bond of the atom. This is compared to valence electrons on the cation within the bond, which is equivalent to the charge of the cation.

The average uranium oxidation state has been calculated in Table 6.7, assuming a stoichiometry of 6 oxygen anions and 3 cations. BVS calculations will identify the stability of U^{4+} , U^{5+} and U^{6+} within the structure. Titanium (Ti^{4+}) and chromium (Cr^{3+}) cation oxidation states have been assumed. This has been completed for the rutile structure of compositions $\text{U}_{0.25}\text{Cr}_{0.25}\text{Ti}_{2.5}\text{O}_6$ and $\text{U}_{0.5}\text{Cr}_{0.5}\text{Ti}_2\text{O}_6$, Table 6.11. Both the rutile and uranium dichromate structures for the multiphase materials have been analysed for measured component phases of target compositions, $\text{U}_{0.75}\text{Cr}_{0.75}\text{Ti}_{1.5}\text{O}_6$ and UCrTiO_6 , Table 6.12.

BVS calculation indicated that both the titanium and chromium cations in rutile materials of target composition $\text{U}_{0.25}\text{Cr}_{0.25}\text{Ti}_{2.5}\text{O}_6$ and $\text{U}_{0.5}\text{Cr}_{0.5}\text{Ti}_2\text{O}_6$ are within 5% of the theoretical values of 4+ and 3+, respectively. However, irrespective of the uranium oxidation state, the BVS for the uranium cation indicates the cation is unstable within the structure. XANES analysis of the materials indicate an average uranium oxidation state of the uranium in target material $\text{U}_{0.5}\text{Cr}_{0.5}\text{Ti}_2\text{O}_6$ was predominantly U^{6+} (Table 6.10). The large discrepancy between the calculated values and the target valence is characteristic of a heavy strain within the structure which the material is able to tolerate due to the small uranium inclusion. This strain is realised by the presence of two rutile materials within the target composition $\text{U}_{0.5}\text{Cr}_{0.5}\text{Ti}_{2.0}\text{O}_6$.

The chromium and titanium cations within the rutile phase, composition $\text{U}_{0.29(2)}\text{Cr}_{0.46(2)}\text{Ti}_{2.27(5)}\text{O}_{6.0}$, as determined for multiphase materials with target compositions

$U_{0.75}Cr_{0.75}Ti_{1.5}O_6$ and $UCrTiO_6$, are within 10% of the expected valence of 3 and 4, respectively. However, the uranium within the structure, irrespective of the oxidation state, is unstable as previous, indicating the instability of the uranium within the rutile structure.

Table 6.11: Bond valence summation (BVS) calculations as the result of the substitution of uranium and chromium into the composition $U_xCr_xTi_{3-2x}O_6$ for the rutile phase formed in target composition $U_{0.25}Cr_{0.25}Ti_{2.5}O_6$ and $U_{0.50}Cr_{0.50}Ti_{2.0}O_6$. The calculations are completed for both U^{4+} , U^{5+} and U^{6+} with reference bond valence lengths, R_0 taken from Breese and O'Keefe [33].

Target Composition	Space Group	Bond	Multiplier	R_0	R_{ij}	v_i	Cation Valence
$U_{0.25}Cr_{0.25}Ti_{2.5}$	P42/mnm	$U^{4+}-O_1$	2	2.11	2.00	1.35	8.69
		$U^{4+}-O_2$	4		1.96	1.50	
		$U^{5+}-O_1$	2	2.20	2.00	1.74	11.09
		$U^{5+}-O_2$	4		1.96	1.91	
		$U^{6+}-O_1$	2	2.08	2.00	1.24	8.02
		$U^{6+}-O_2$	4		1.96	1.35	
		$Cr-O_1$	2	1.72	2.00	0.48	3.06
		$Cr-O_2$	4		1.96	0.52	
		$Ti-O_1$	2	1.82	2.00	0.62	3.91
		$Ti-O_2$	4		1.96	0.67	
$U_{0.5}Cr_{0.5}Ti_2$	1-P42/mnm	$U^{4+}-O_1$	2	2.11	2.00	1.34	8.47
		$U^{4+}-O_2$	4		1.98	1.45	
		$U^{5+}-O_1$	2	2.20	2.00	1.72	10.68
		$U^{5+}-O_2$	4		1.98	1.91	
		$U^{6+}-O_1$	2	2.08	2.00	1.22	7.66
		$U^{6+}-O_2$	4		1.98	1.31	
		$Cr-O_1$	2	1.72	2.00	0.47	2.97
		$Cr-O_2$	4		1.98	0.51	
		$Ti-O_1$	2	1.82	2.00	0.60	3.80
		$Ti-O_2$	4		1.98	0.65	
$U_{0.5}Cr_{0.5}Ti_2$	2-P42/mnm	$U^{4+}-O_1$	2	2.11	2.01	1.34	8.46
		$U^{4+}-O_2$	4		1.97	1.45	
		$U^{5+}-O_1$	2	2.20	2.01	1.67	10.79
		$U^{5+}-O_2$	4		1.97	1.86	
		$U^{6+}-O_1$	2	2.08	2.01	1.22	7.80
		$U^{6+}-O_2$	4		1.97	1.31	
		$Cr-O_1$	2	1.72	2.01	0.47	2.99
		$Cr-O_2$	4		1.97	0.51	
		$Ti-O_1$	2	1.82	2.01	0.60	3.83
		$Ti-O_2$	4		1.97	0.65	

Table 6.12: Bond valence summation (BVS) calculation from the substitution of uranium and chromium into the ideal composition $U_{0.75}Cr_{0.75}Ti_{1.5}O_6$ and $UCrTiO_6$ with phases $U_{0.30}Cr_{0.50}Ti_{2.5}O_{6+\delta}$ (rutile) and $Cr_{1.10}Ti_{1.20}U_{1.00}O_6$ (Hexagonal Uranium Chromate). The calculations are completed for both U^{4+} and U^{6+} , should the uranium oxides from the original U^{4+} .

Average Composition	Space Group	Bond	Multiplier	R_0	R_{ij}	v_i	Cation Valence
$U_{0.29(2)}$ $Cr_{0.46(2)}$ $Ti_{2.27(5)}$	P42/mnm	$U^{4+}-O_1$	2	2.11	2.03	1.24	8.48
		$U^{4+}-O_2$	4		1.96	1.50	
		$U^{5+}-O_1$	2	2.20	2.03	1.58	10.82
		$U^{5+}-O_2$	4		1.96	1.91	
		$U^{6+}-O_1$	2	2.08	2.03	1.15	7.82
		$U^{6+}-O_2$	4		1.96	1.38	
		$Cr-O_1$	2	1.72	2.03	0.44	2.99
		$Cr-O_2$	4		1.96	0.53	
		$Ti-O_1$	2	1.82	2.03	0.56	3.82
		$Ti-O_2$	4		1.96	0.68	
$Cr_{0.98(4)}$ $Ti_{1.09(3)}$ $U_{0.95(4)}$	P-31m	$U^{4+}-O_1$	6	2.11	2.17	0.85	5.10
		$U^{5+}-O_1$	6	2.20		1.08	6.51
		$U^{6+}-O_1$	6	2.08		0.78	4.70
		$Cr-O_1$	4	1.72	1.97	0.51	3.05
		$Cr-O_2$	2		1.97	0.51	
		$Ti-O_1$	4	1.82	1.97	0.67	4.00
		$Ti-O_2$	2		1.97	0.67	

BVS calculations of the hexagonal uranium dichromate material, of composition $Cr_{0.98(4)}Ti_{1.09(3)}U_{0.95(4)}O_6$, show the titanium and chromium cations are stable with calculated values with <10% discrepancy to the theoretical value, of 4 and 3 respectively. The additional charge, due to the substitution of Ti^{4+} for Cr^{3+} , will destabilise the structure and require accommodating within the material. The desirable mechanism for this would be the reduction in the uranium oxidation state in order to stabilise the structure. Ideal uranium brannerite (UTi_2O_6) has a defined uranium oxidation state of U^{4+} [35]. The BVS calculations indicate the U^{6+} would be under bonded within the structure, with a discrepancy of ~21.67%. The inclusion of U^{5+} would be unstable within the material due to over bonding, by ~23.20%, and U^{4+} over bonded by ~21.57%.

6.4.5 Transmission electron microscopy of $U_{0.25}Cr_{0.25}Ti_{2.5}O_6$ material

TEM investigations was completed on single grains of material with target composition $U_{0.25}Cr_{0.25}Ti_{2.5}O_6$, as ground from the bulk material and mounted on a holey carbon-copper grid for analysis.

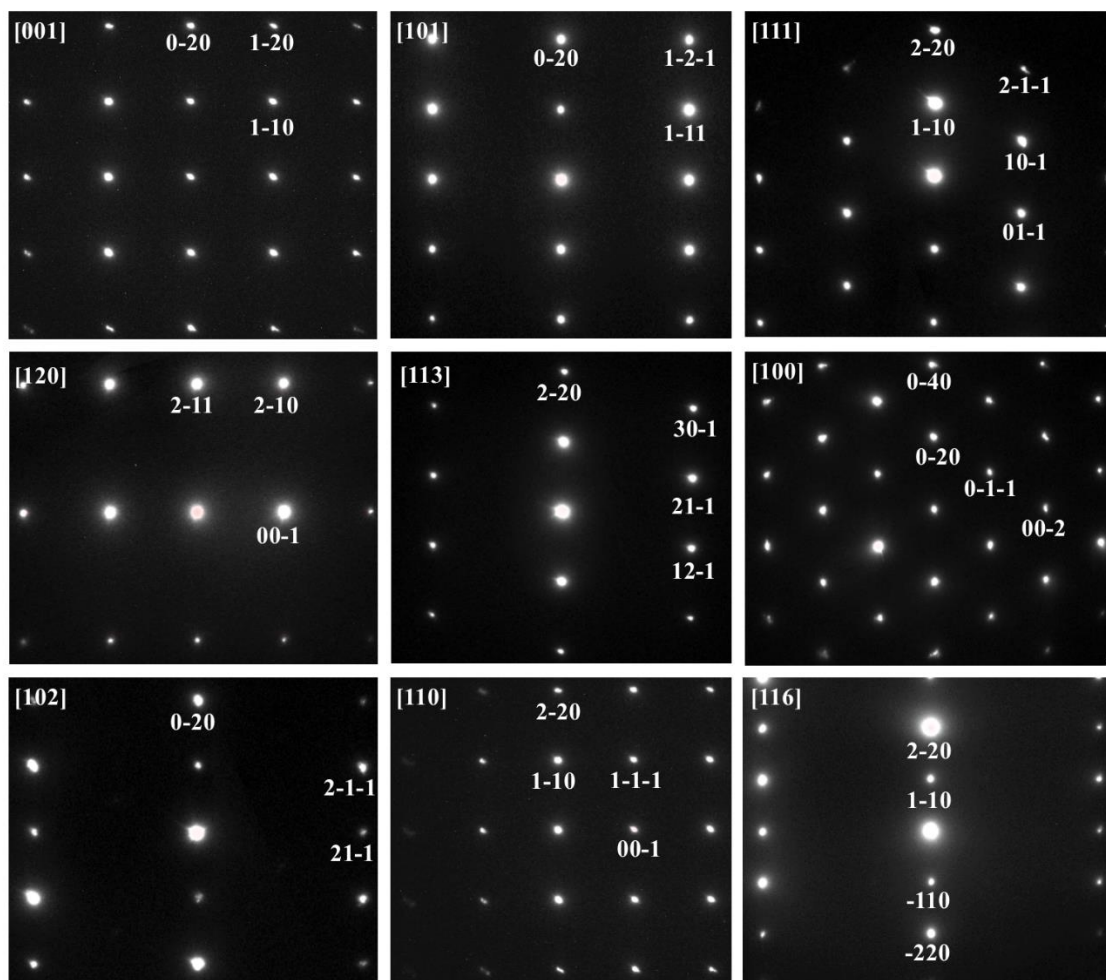


Figure 6.17: Electron diffraction images, indexed to the rutile structure, of material with target composition $U_{0.25}Cr_{0.25}Ti_{2.5}O_6$.

Electron diffraction images have been collected on a transmission electron microscope, more specifically the Technai G²F20 XT TEM instrument at The Institute of Transuranium Elements (ITU), Karlsruhe, Germany, full experimental set up can be found in Section 3.4.1. Analysis has been completed on multiple axis in order to gain information on the single phase rutile structure of target composition $U_{0.25}Cr_{0.25}Ti_{2.5}O_6$. This was completed in order to confirm there is no ordering of the substituted cations on the rutile site creating an underlying superstructure. TEM enables analysis of crystallographic stresses / strains through the presence of diffuse

scattering of the reflections. The definition of the reflections from TEM analysis indicate a crystalline structure absent of stresses / strains. A lack of additional electron diffraction intensities in Figure 6.18 to the indexed rutile structure incates a single phase rutile structure, with no underlying supercell from the ordering of the substituted cations. This signifys that the uranium and chromium cations have randomly arranged on the titanium site of the rutile structure, TiO_2 .

6.4.7 Chromium Substituted Material Conclusions

Synthesis of material with target composition $\text{U}_{0.25}\text{Cr}_{0.25}\text{Ti}_{2.5}\text{O}_6$ resulted in the formation of a material with a crystalline structure indicative of a rutile, space group P42/mnm . Confirmation of the single phase assemblage was provided through SEM / EDS analysis (Figure 6.11 and Table 6.7), with a measured composition of $\text{U}_{0.19(1)}\text{Cr}_{0.27(2)}\text{Ti}_{2.54(5)}\text{O}_{6.00(8)}$ defined. Structural refinement completed using high resolution neutron diffraction data collected on the HRPD instrument, ISIS (Figure 6.12). BVS calculations indicated the potential instability within the structure due to the inclusion of the uranium cation, irrespective of the uranium oxidation state (Table 6.11). However, TEM analysis of the material did not show any diffuse scattering, therefore no stresses / strains were identified within the crystal lattice.

The half width full maximum of the reflections, from both XRD and neutron diffraction analysis, of target composition $\text{U}_{0.5}\text{Cr}_{0.5}\text{Ti}_2\text{O}_6$ indicated the presence of two or more rutile structures of similar cation stoichiometries. However, BSE images (Figure 6.11) did not indicted a multiple phase assemblage, due to a lack of contrast being evident. Point to point EDS analysis did not identify compositions of significant difference to indicate multiple phases, an average material composition of $\text{U}_{0.45(2)}\text{Cr}_{0.43(2)}\text{Ti}_{2.08(4)}\text{O}_{6.00(8)}$ was measured. Rietveld refinement to obtain structural parameters (Table 6.8), and the lack of variance in the SEM / EDS analysis, are characteristic of a phase assemblage existing of similar chemical composition and structural arrangement. No unindexed reflections were identified in the fitting of the $\text{U}_{0.5}\text{Cr}_{0.5}\text{Ti}_2\text{O}_6$ material, Figure 6.13, indicating the materials precursor oxides had fully reacted. A further heat treatment did not alter the profile shape of the reflections, indicating the material formation was at equilibrium. Calculated uranium oxidation state is in good agreement with XANES analysis of the average uranium oxidation state (Table 6.7 and Table 6.10), with a measured uranium average oxidation state of $5.96(2)$.

Synthesis of materials with target compositions $\text{U}_{0.75}\text{Cr}_{0.75}\text{Ti}_{1.5}\text{O}_6$ and UCrTiO_6 , resulted in the formation of a material with a multiphase assemblage. XRD and neutron diffraction

analysis identified the formation of two phases, EDS analysis provided cation stoichiometries of the materials. The phases were defined as a rutile of composition $U_{0.29(2)}Cr_{0.46(2)}Ti_{2.27(5)}O_{6.0(7)}$, and a hexagon uranium dichromate of composition $Cr_{0.98(4)}Ti_{1.09(3)}U_{0.95(4)}O_{6.0(9)}$. No unreacted precursor materials were identified in the multiphase assemblage. Rietveld refinement of the neutron diffraction data, using the GSAS software, indicated both materials contained compositions with comparable lattice parameters, and the fraction of each phase for both target compositions was refined from relative intensities of the phases within the Rietveld refinement. Target composition $U_{0.75}Cr_{0.75}Ti_{1.5}O_6$ was refined with a 42.7% hexagonal uranium dichromate structure and 57.3% with a rutile structure. The material with target composition $UCrTiO_6$ was refined with predominantly hexagonal uranium dichromate, at 95.3%, and a minor contribution of rutile, at 4.7%. XANES analysis was completed on the material with target composition $UCrTiO_6$, and an average uranium oxidation state 5.34(1) was analysed, in good agreement with the calculated uranium oxidation state in Table 6.7. BVS calculations for both compositions indicated stability of the bond of the titanium and chromium cations, however the uranium was unstable in both composition. The uranium within the rutile phase was heavily over bonded within the material. Uranium within the hexagon uranium dichromate was over bonded should the material contain U^{4+} or U^{5+} . However, as identified as the predominant oxidation within the material by XANES analysis, uranium with an average oxidation state of U^{6+} would be under bonded when compared to BVS calculations.

6.5 Future Work

Further work for this chapter should be undertaken in the following areas:

- Quantification of the uranium average oxidation state of single phase rutile material with target composition $U_{0.25}Cr_{0.25}Ti_{2.5}O_6$.
- Attempt to isolate the uranium hexagon dichromate material with titanium substitution with target composition $Cr_{0.95}U_{0.95}Ti_{1.1}O_6$, determined from the measured composition $Cr_{0.98(4)}Ti_{1.09(3)}U_{0.95(4)}O_6$. This will enable an understanding of the uranium oxidation state by XANES analysis with the substitution of Ti^{4+} cation for the Cr^{3+} cation.

6.6 References

- [1] Carter ML, Li H, Zhang Y *et al.* Titanate ceramics for immobilisation of uranium-rich radioactive wastes arising from Mo-99 production. *Journal of Nuclear Materials* 2009; 384:322-326.
- [2] Hart KP, Lumpkin GR, Giere R *et al.* Naturally-occurring zirconolites analogues for the long-term encapsulation of actinides in Synroc. *Radiochimica Acta* 1996; 74:309-312.
- [3] Ringwood AE, Kesson SE, Ware NG *et al.* Immobilization of high-level nuclear-reactor wastes in Synroc. *Nature* 1979; 278:219-223.
- [4] Vance ER. Development of titanate ceramic wastefoms and crystal chemistry of incorporated uranium and plutonium. In: *Environmental Issues and Waste Management Technologies in the Ceramic and Nuclear Industries VIII*. Edited by: Sundaram SK, Spearing DR, Vienna JD. 2003. pp. 301-311.
- [5] Vance ER, Stewart MWA, Moricca SA. Progress at ANSTO on SYNROC. *Journal of the Australian Ceramic Society* 2014; 50:38-48.
- [6] Helean KB, Navrotsky A, Lumpkin GR *et al.* Enthalpies of formation of U-, Th-, Ce-brannerite: implications for plutonium immobilization. *Journal of Nuclear Materials* 2003; 320:231-244.
- [7] Helean KB, Ushakov SV, Brown CE *et al.* Formation enthalpies of rare earth titanate pyrochlores. *Journal of Solid State Chemistry* 2004; 177:1858-1866.
- [8] Atuchin VV, Zhang ZM. Chemical bonding between uranium and oxygen in U6+-containing compounds. *Journal of Nuclear Materials* 2012; 420:222-225.
- [9] Balek V, Zelenak V, Benes M, Subrt J. Thermal behaviour of brannerite ceramics and its natural analogue mineral brannerite. *Ceramics-Silikaty* 2009; 53:9-14.
- [10] Charalambous FA, Ram R, McMaster S *et al.* An investigation on the dissolution of synthetic brannerite (UTi₂O₆). *Hydrometallurgy* 2013; 139:1-8.
- [11] Colella M, Lumpkin GR, Zhang Z *et al.* Determination of the uranium valence state in the brannerite structure using EELS, XPS, and EDX. *Physics and Chemistry of Minerals* 2005; 32:52-64.
- [12] Helean KB, Navrotsky A, Lian J, Ewing RC. Thermochemical investigations of zirconolite, pyrochlore and brannerite: Candidate materials for the immobilization of plutonium. In: *27th Symposium on Scientific Basis for Nuclear Waste Management*. Kalmar, SWEDEN: Materials Research Society; 2003. pp. 297-302.
- [13] James M, Watson JN. The synthesis and crystal structure of doped uranium brannerite phases U_{1-x}M_xTi₂O₆ (M=Ca²⁺, La³⁺ and Gd³⁺). *Journal of Solid State Chemistry* 2002; 165:261-265.
- [14] James M, Carter ML, Watson JN. The synthesis, crystal chemistry and structures of Y-doped brannerite (U_{1-x}Y_xTi₂O₆) and thorutite (Th_{1-x}Y_xTi₂O_{6-delta}) phases. *Journal of Solid State Chemistry* 2003; 174:329-333.
- [15] Vance ER, Watson JN, Carter ML *et al.* Crystal chemistry and stabilization in air of brannerite, UTi₂O₆ Crystal chemistry and stabilization in air of brannerite, UTi₂O₆. *Journal of the American Ceramic Society* 2001; 84:141-144.
- [16] Vance ER, Carter ML, Stewart MWA *et al.* Ionic size limits for a ions in brannerite (ATi₂O₆) and pyrochlore (CaATi₂O₇) titanate structures - (A = tetravalent rare earths and actinides). In: *25th Symposium on Scientific Basis for Nuclear Waste Management*. Boston, Ma: 2001. pp. 319-326.

- [17] Zhang Y, Gregg DJ, Lumpkin GR *et al.* The incorporation of neptunium and plutonium in thorite ThTi_2O_6 . *Journal of Alloys and Compounds* 2013; 581:665-670.
- [18] Hess FL, Wells RC. Brannerite, a new uranium mineral. *Journal of the Franklin Institute* 1920; 189:225-237.
- [19] Stupp HD, Saager R. New observations on the mineral brannerite - uranium containing rutile and leukoxen. *Fortschritte Der Mineralogie* 1983; 61:253-255.
- [20] Zhang Y, Lumpkin GR, Li H *et al.* Recrystallisation of amorphous natural brannerite through annealing: The effect of radiation damage on the chemical durability of brannerite. *Journal of Nuclear Materials* 2006; 350:293-300.
- [21] Lumpkin GR, Smith KL, Blackford MG. Electron-microscope study of SYNROC before and after exposure to aqueous- solutions. *Journal of Materials Research* 1991; 6:2218-2233.
- [22] Smith KL, Hart KP, Lumpkin GR *et al.* A description of the kinetics and mechanisms which control the release of HLW elements from SYNROC. 1991.
- [23] Smith KL, Lumpkin GR, Blackford MG *et al.* The durability of SYNROC. *Journal of Nuclear Materials* 1992; 190:287-294.
- [24] Implementing Geological Disposal. In: Edited by: Change DoEC. Crown; 2014.
- [25] Szymanski JT, Scott JD. A crystal-structure refinement of synthetic brannerite, UTi_2O_6 , and its bearing on rate of alkaline-carbonate leaching of brannerite in ore. *Canadian Mineralogist* 1982; 20:271-280.
- [26] James M, Carter ML, Zhang Z *et al.* Crystal Chemistry and Structures of (Ca,U) Titanate Pyrochlores. *Journal of the American Ceramic Society* 2010; 93:3464-3473.
- [27] Sugiyama K, Takeuchi Y. The crystal-structure of rutile as a function of temperature up to 1600C. *Zeitschrift Fur Kristallographie* 1991; 194:305-313.
- [28] Baur WH, Khan AA. Rutile-Type Compounds IV. SiO_2 , GeO_2 and a Comparison with other Rutile-Type Structures. *Acta Crystallographica Section B-Structural Crystallography and Crystal Chemistry* 1971; B 27:2133-&.
- [29] Bots P, Behrends T. Uranium mobility in subsurface aqueous systems: the influence of redox conditions. *Mineralogical Magazine* 2008; 72:381-384.
- [30] Vance ER, Watson JN, Carter ML *et al.* Crystal chemistry and stabilization in air of brannerite, UTi_2O_6 . *Journal of the American Ceramic Society* 2001; 84:141-144.
- [31] Larson AC, Von Dreele RB. General Structure Analysis System (GSAS). In: Los Alamos National Laboratory Report LAUR. 1994. pp. 86-748.
- [32] Toby BH. EXPGUI, a graphical user interface for GSAS. *J. Appl. Cryst.* 2001; 34:210-213.
- [33] Brese NE, Okeeffe M. Bond-Valence Parameters for Solids. *Acta Crystallographica Section B-Structural Science* 1991; 47:192-197.
- [34] Collomb A, Capponi JJ, Gondrand M, Joubert JC. Synthesis of some $\text{A}^{6+}\text{B}_2^{3+}\text{O}_6$ in hydrothermal medium under very high-pressure. *Journal of Solid State Chemistry* 1978; 23:315-319.
- [35] Collomb A, Gondrand M, Lehmann MS *et al.* X-ray and neutron diffractions used to study UCr_2O_6 single-crystal obtained by hydrothermal synthesis under very high pressure. *Journal of Solid State Chemistry* 1976; 16:41-48.

[36] Ravel B, Newville M. ATHENA, ARTENIS, HEPHAESTUS: data analysis for X-ray absorption spectroscopy using IFEFFIT. In: Journal of Synchrotron Radiation; 2005.

Chapter 7 Conclusions

The aim of this thesis was to assess the chemical and structural flexibility of synthetic ceramic materials, which adopt either a brannerite and pyrochlore structure, to provide information on the materials ability to tolerate varied waste streams. Ceramic materials are an option for the long term disposal of uranium and plutonium oxides within a geological disposal facility (GDF). Through analysis of the chemical and structural flexibility information is provided on how variations in fission products, associated with uranium and plutonium oxides, will be accommodated within the ceramic structure.

The intension of Chapter 4 is to address the first aim in Section 2.4. Materials with a pyrochlore structure of general formula $A^{2+}A^{3+}B_{1.5}^{5+}B_{0.5}^{3+}O_7$ was explored to understand the structural response of the phase with varied compositions. Materials with target compositions $CaLnM_{0.5}Nb_{1.5}O_7$ where $Ln = La, Nd, Gd, Sm, Ho$ or Yb and $M = Al, Cr, Fe, Sc$ or Y were synthesised. Materials where $Ln = La, Nd, Gd, Sm, Ho$ or Yb and $M = Al, Fe, Sc$ or Y were largely single phase, with the exception of materials with compositions; $CaLaAl_{0.5}Nb_{1.5}O_7$, $CaHoY_{0.5}Nb_{1.5}O_7$ and $CaYbY_{0.5}Nb_{1.5}O_7$, here a multiphase assemblage was identified. Rietveld refinement of high resolution neutron diffraction data (HRPD, ISIS) enabled quantification of lattice parameters and the 48f oxygen x-coordinate position. A linear relationship was identified between the chemical composition, represented by the ionic radius ratio (r_A/r_B), and the shift in the 48f oxygen x-parameter. Analysis of the a-parameter, which describes the unit cell of the cubic structure, as a function of r_A/r_B , indicated a linear relationship the unit cell size and the r_A/r_B value with substituted B-site cation. The relationship between the valence shell of the B-site cation ($M = Al, Fe, Sc$ or Y) and the a-parameter is hypothesised due to the similarities between the Fe and Sc materials, however, the reason for this was not identified.

Also in Chapter 4 the second aim of Section 2.4 has been met through in-situ irradiation of materials with target compositions $CaLnFe_{0.5}Nb_{1.5}O_7$, where $Ln = La, Nd, Gd, Sm, Ho$ or Yb , was completed at the IVEM-TANDEM facility (ANL). This enabled definition of the critical temperature (T_C) of the materials, the temperature at which the recovery rate of the radiation induced damage is equal to the damage rate. T_C was established for materials with target compositions $CaLnFe_{0.5}Nb_{1.5}O_7$, where $Ln = La, Sm, Ho$ or Yb . A linear relationship was identified between the critical temperature and the a-

parameter, however the refined 48f oxygen x-parameters were approximately constant, and indicated no relationship with the calculated T_C values.

In Chapter 5 uranium was substituted into lanthanum zirconate pyrochlore (target composition $\text{La}_2\text{Zr}_{2-x}\text{U}_x\text{O}_{7+\delta}$ $0.1 \leq x \leq 0.9$) and synthesised in variable atmospheres. This allowed for the effect on the structural stability of the pyrochlore phase, and the correlation with the uranium oxidation state, in the materials to be analysed meeting the objective in Section 2.4. Synthesised materials up to, and including, $\text{La}_{2.06(2)}\text{Zr}_{1.51(1)}\text{U}_{0.48(1)}\text{O}_{7.45(3)}$ and $\text{La}_{1.94(2)}\text{Zr}_{1.20(1)}\text{U}_{0.81(1)}\text{O}_{7.4(1)}$, were successfully formed in air and hydrogen / nitrogen atmospheres, respectively. XANES analysis enabled quantification of the average uranium oxidation state in the materials formed in air and hydrogen / nitrogen atmosphere of 5.57(13) and 5.13(4), respectively. XANES analysis showed that material formed in a hydrogen / nitrogen reduced the average uranium oxidation state more than the air formed material. As a result a greater fraction of uranium was successfully substituted for zirconium in hydrogen / nitrogen formed material. However, oxygen stoichiometries calculated were comparable for both materials, indicating the limit of substitution is driven by the accumulation of oxygen within the pyrochlore structure anion vacancy.

Chapter 6 meets the fourth aim set in Section 2.4 where brannerite materials were formed via a solid state synthesis with substitutions of Fe, Yb, Pr or Y ($\text{U}_{1-x}\text{M}_x\text{Ti}_2\text{O}_6$). The substitution of Fe did not result in the formation of a material with a single phase assemblage. Despite multiple heat treatments, precursor oxides were identified via XRD analysis. Materials with target compositions $\text{U}_{1-x}\text{REE}_x\text{Ti}_2\text{O}_6$, where REE = Yb, Pr or Yb, all formed a single phase assemblage with a structure indicative of a brannerite. Compositions were confirmed via EDS analysis, with measured compositions normalised to 2 formula units (f.u.) of titanium, at $\text{U}_{0.56(4)}\text{Pr}_{0.43(2)}\text{Ti}_{2.00(8)}\text{O}_6$, $\text{U}_{0.54(2)}\text{Y}_{0.41(1)}\text{Ti}_{2.00(7)}\text{O}_6$ and $\text{U}_{0.53(4)}\text{Yb}_{0.46(3)}\text{Ti}_{2.00(3)}\text{O}_6$. A linear relationship was identified between both the size of the REE cation and the uranium stoichiometry, as a function of the volume of the unit cell. With an average uranium oxidation state of 5 assumed for material with composition $\text{U}_{0.54(2)}\text{Y}_{0.41(1)}\text{Ti}_{2.00(7)}\text{O}_6$ (unpublished), bond valence sums (BVS) for U^{5+} within brannerite were calculated. In absence of XANES analysis of the uranium oxidation state the stability of the cations within the structure was explored through the BVS. This indicated stability of the titanium within all materials, however the substitution of the REE has resulted in instability on the A site in the general formula ATi_2O_6 . For Y and Yb materials the BVS suggest that only the U is unstable, whereas the Pr substituted material suggests both the Pr and U are unstable. Further analysis, including XANES analysis of

energies for the uranium and praseodymium cations to identify the average oxidation state of the cations and TEM analysis, would provide information of the structural stability of the material.

Chapter 6 also presented results for the substitution of chromium in $U_{1-x}Cr_xTi_2O_6$ ($x = 0.50$), this resulted in the formation of a uranium and chromium substituted rutile of general formula $U_xCr_xTi_{3-2x}O_6$. In order to explore this substitutions of $x = 0.25, 0.50, 0.75$ and 1.00 in the general composition $U_xCr_xTi_{3-2x}O_6$ were synthesised. Material of target composition $U_{0.25}Cr_{0.25}Ti_{2.50}O_6$ was analysed by neutron diffraction, and data refined to a model of a single phase rutile. This was confirmed via TEM analysis on the $U_{0.25}Cr_{0.25}Ti_{2.50}O_6$ material, which indicated no supercell arrangement (no additional reflections) of the uranium, chromium and titanium cations. Neutron diffraction data of material with target composition $U_{0.50}Cr_{0.50}Ti_{2.00}O_6$ highlighted the presence of at least two rutile materials, despite being unable to identify a multiphase assemblage in SEM / EDS analysis. Rietveld refinement confirmed the presence of two rutile phases, indicating the limit of substitution of uranium and chromium in titanium rutile had been exceeded. Materials with target compositions $U_{0.75}Cr_{0.75}Ti_{1.50}O_6$ and $UCrTiO_6$ formed a multiphase assemblage, identified as a rutile (EDS measured composition $U_{0.29(2)}Cr_{0.46(2)}Ti_{2.27(5)}O_6$) and a hexagonal uranium dichromate material (EDS measured composition $Cr_{0.98(4)}Ti_{1.09(3)}U_{0.95(4)}O_6$). The ratios between the two phases varied, dependant on the target compositions $U_{0.75}Cr_{0.75}Ti_{1.50}O_6$ and $UCrTiO_6$. With the rutile phase slightly dominating the $U_{0.75}Cr_{0.75}Ti_{1.50}O_6$ material (57.3% rutile to 42.7% hexagonal uranium dichromate) and the material with target composition $UCrTiO_6$ dominated by the hexagonal uranium dichromate (4.7% rutile to 95.3% hexagonal uranium dichromate). This indicated that in an excess of titanium the rutile phase will preferentially form.

The data chapters meet the objective to explore the chemical and structural flexibilities of the ceramic materials which adopt the pyrochlore or brannerite phase. Areas of interest for future research include further studies on the irradiation induced damage of the materials and investigation of the chemical durability of the materials (leaching and compatibility with the geological environment). In addition to this further analysis of the rutile and hexagonal uranium dichromate materials, including investigating whether material with composition $Cr_{0.98(4)}Ti_{1.09(3)}U_{0.95(4)}O_6$ can be synthesised.

Appendix A

A.1 Introduction

Within this appendix is additional data collated for ‘Chapter 4- Systematic substitutions in the calcium niobate pyrochlore system $\text{CaLnM}_{0.5}\text{Nb}_{1.5}\text{O}_7$ (where Ln = La, Nd, Sm, Gd, Ho or Yb and M = Al, Fe, Sc or Y). This includes material where the desired phase was unable to form, compositions of $\text{CaLnCr}_{0.5}\text{Nb}_{1.5}\text{O}_7$, with Ln= La, Nd, Sm, Gd, Ho or Yb. These materials were part of the work completed within Chapter 4 of this thesis, however despite much attempt the desired crystalline phase was unable to be formed.

A.2 Iron Materials

A.2.1 Iron Materials Neutron Diffraction

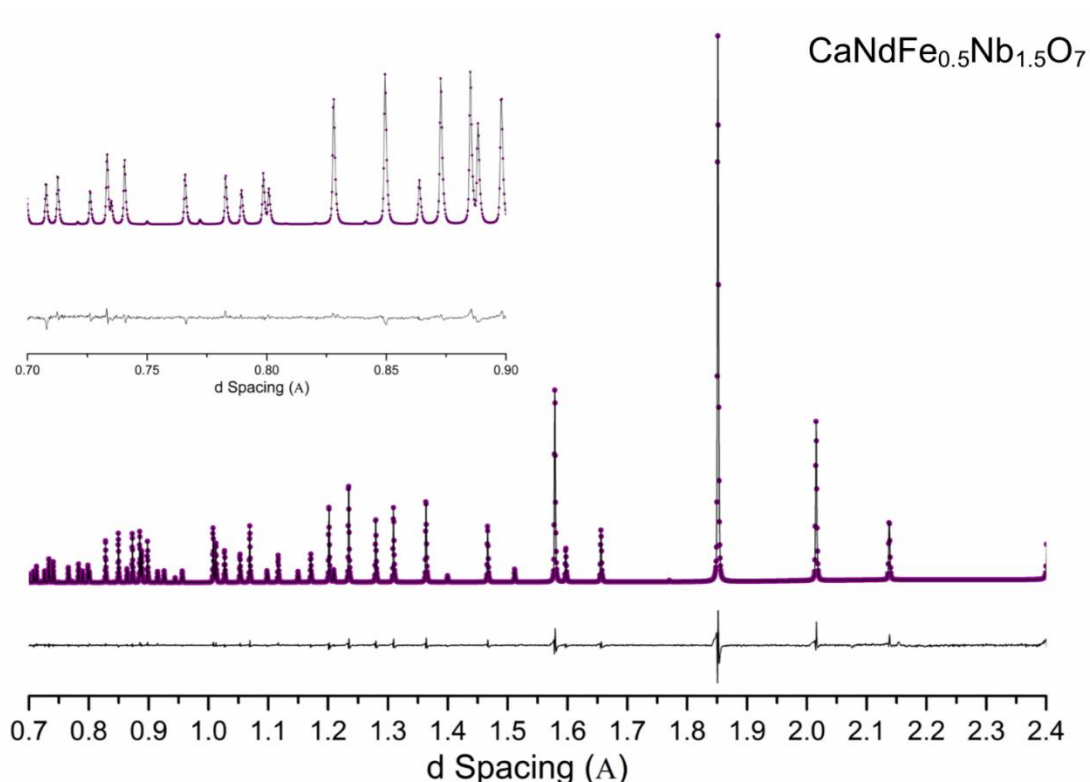


Figure A.1: Rietveld refinement fitting of neutron diffraction data collected on material with composition $\text{CaNdFe}_{0.5}\text{Nb}_{1.5}\text{O}_7$ on the High Resolution Powder Diffractometer (HRPD) instrument. Image shows fitted neutron diffraction trace and the error within the fitting (actual-calculated). Insert: Magnification of low d spacing and fitting quality.

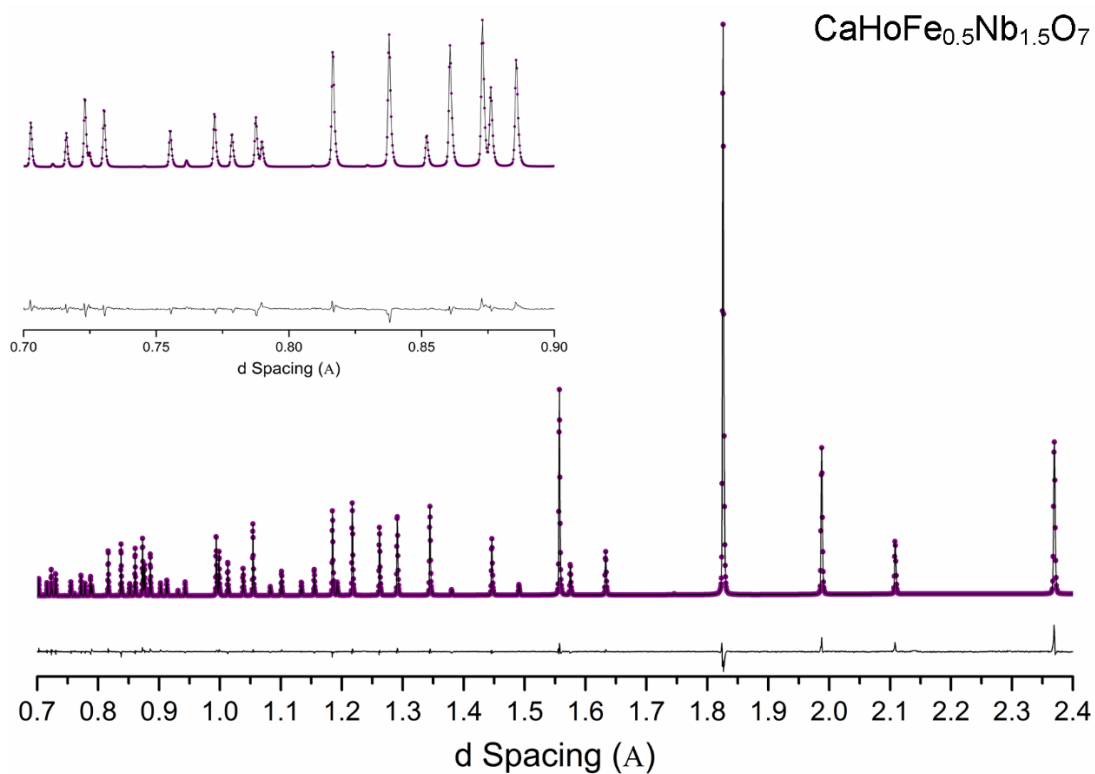


Figure A. 2: Rietveld refinement fitting of neutron diffraction data collected on material with composition CaHoFe_{0.5}Nb_{0.5}O₇ on the High Resolution Powder Diffractometer (HRPD) instrument. Image shows fitted neutron diffraction trace and the error within the fitting (actual-calculated). Insert: Magnification of low d spacing and fitting quality.

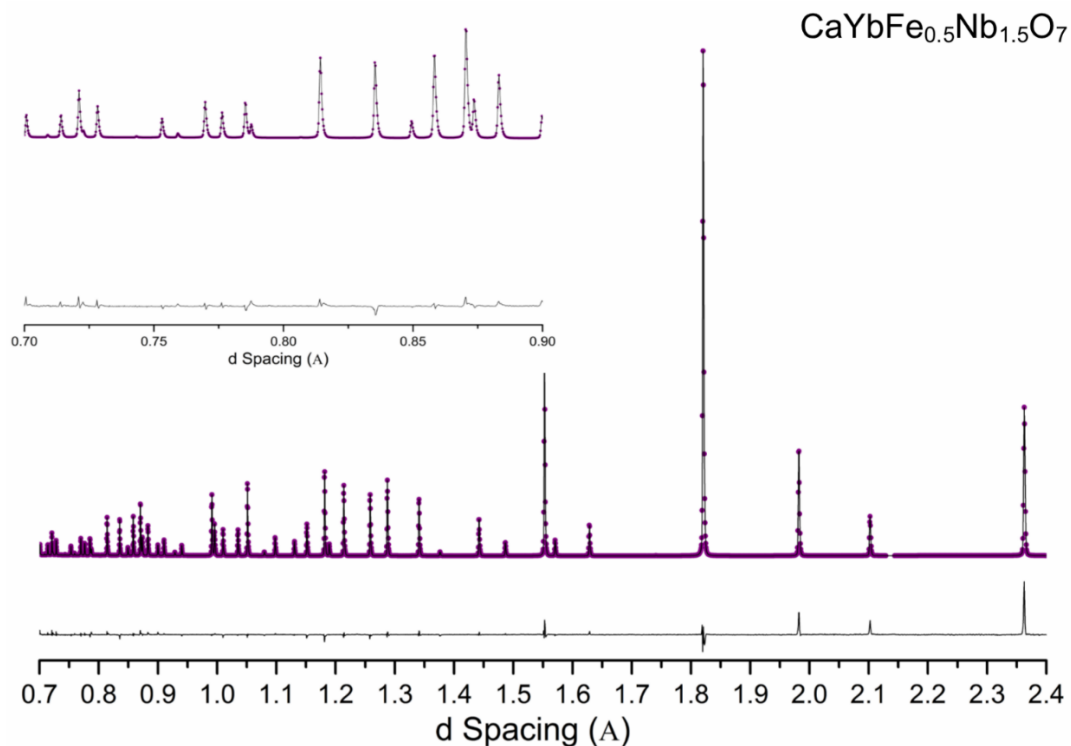


Figure A.3: Rietveld refinement fitting of neutron diffraction data collected on material with composition CaYbFe_{0.5}Nb_{0.5}O₇ on the High Resolution Powder Diffractometer (HRPD) instrument. Image shows fitted neutron diffraction trace and the error within the fitting (actual-calculated). Insert: Magnification of low d spacing and fitting quality.

A.3 Scandium Materials Experimental Data and Discussion

A.3.1 Scandium Materials XRD

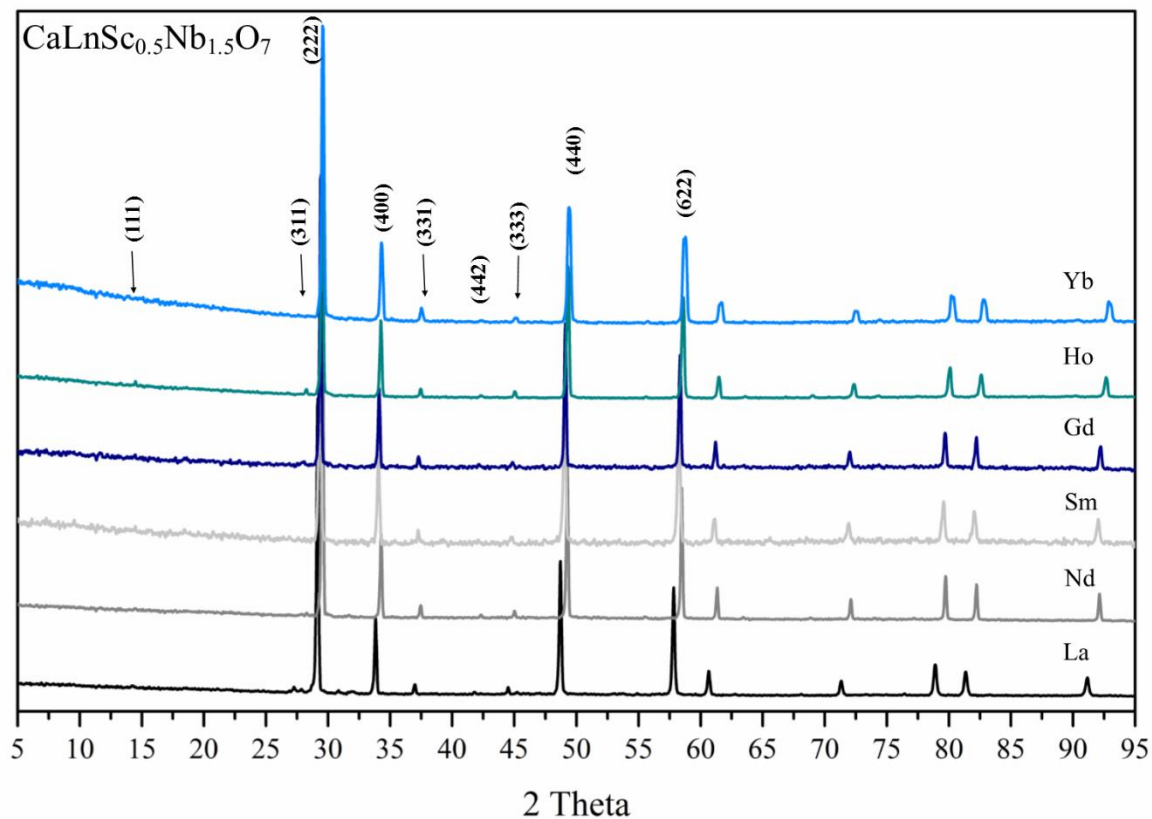


Figure A.4: X-ray diffraction data of the series of materials with ideal compositions $\text{CaLnSc}_{0.5}\text{Nb}_{1.5}\text{O}_7$, where Ln= La, Nd, Sm, Gd, Ho or Yb, as collected on the Stoe-IP instrument. Reflections indicative of the pyrochlore superstructure are highlighted with the arrow in the figure.

A.3.2 Scandium SEM

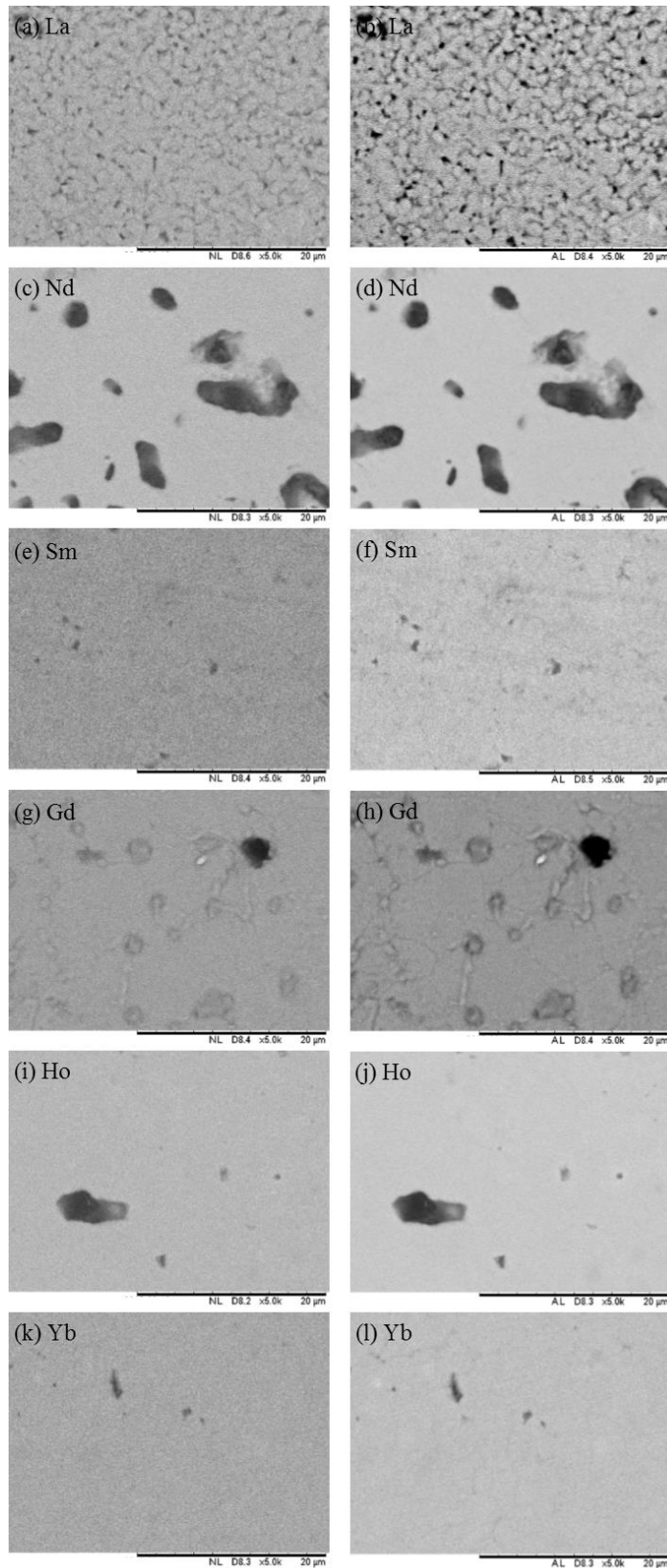


Figure A.5: SEM images of samples with target composition $\text{CaLnSc}_{0.5}\text{Nb}_{1.5}\text{O}_7$ where Ln = La for images (a) and (b), Ln = Nd for (c) and (d), Ln = Sm for (e) and (f), Ln = Gd for (g) and (h), Ln = Ho for (i) and (j) and Ln = Yb for images (k) and (l). Images on the left are the secondary electron images and the right hand side showing the back-scattered electron micrographs of compositions.

A.3.3 Scandium Neutron Diffraction

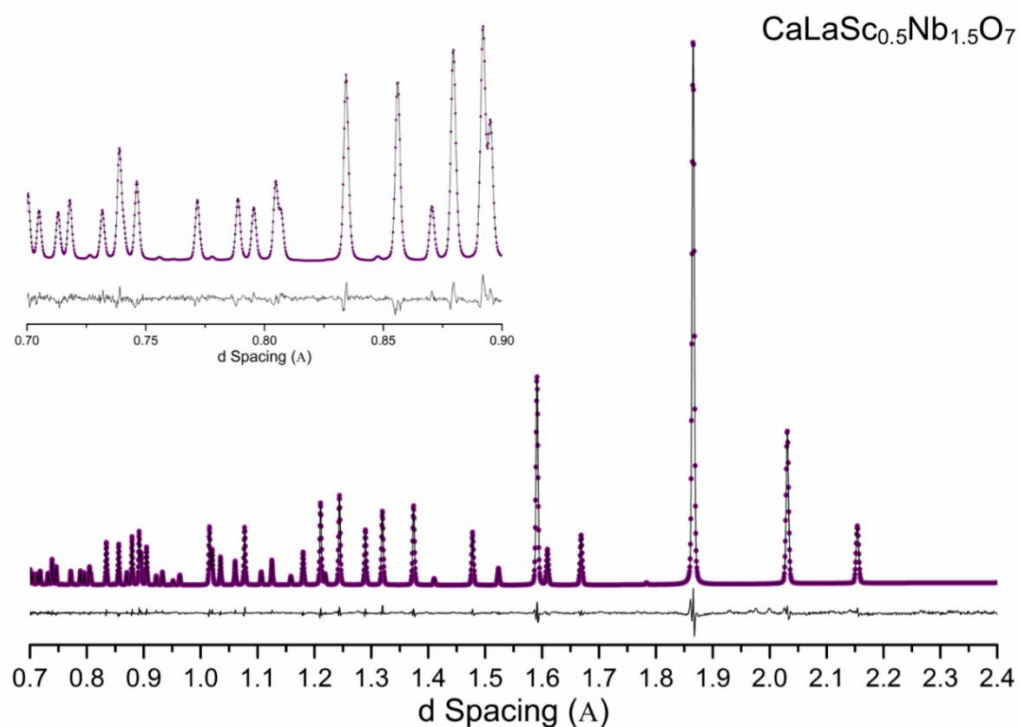


Figure A.6: Rietveld refinement fitting of neutron diffraction data collected on material with composition $\text{CaLaSc}_{0.5}\text{Nb}_{0.5}\text{O}_7$ on the High Resolution Powder Diffractometer (HRPD) instrument. Image shows fitted neutron diffraction trace and the error within the fitting (actual-calculated). Insert: Magnification of low d spacing and fitting quality.

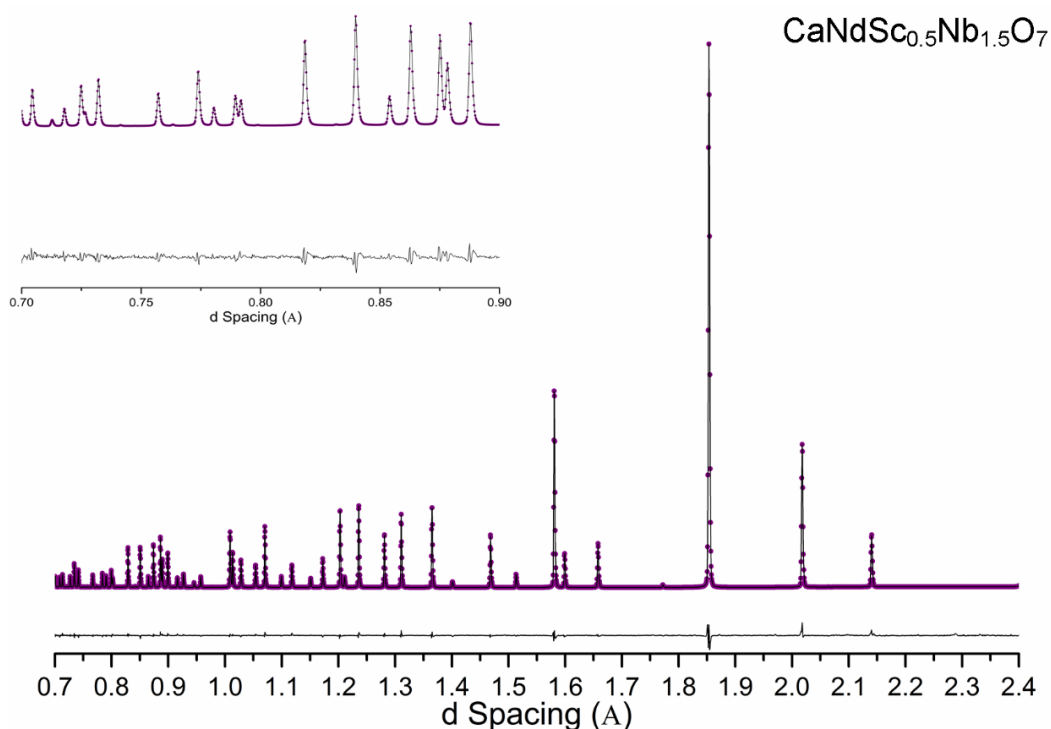


Figure A.7: Rietveld refinement fitting of neutron diffraction data collected on material with composition $\text{CaNdSc}_{0.5}\text{Nb}_{0.5}\text{O}_7$ on the High Resolution Powder Diffractometer (HRPD) instrument. Image shows fitted neutron diffraction trace and the error within the fitting (actual-calculated). Insert: Magnification of low d spacing and fitting quality.

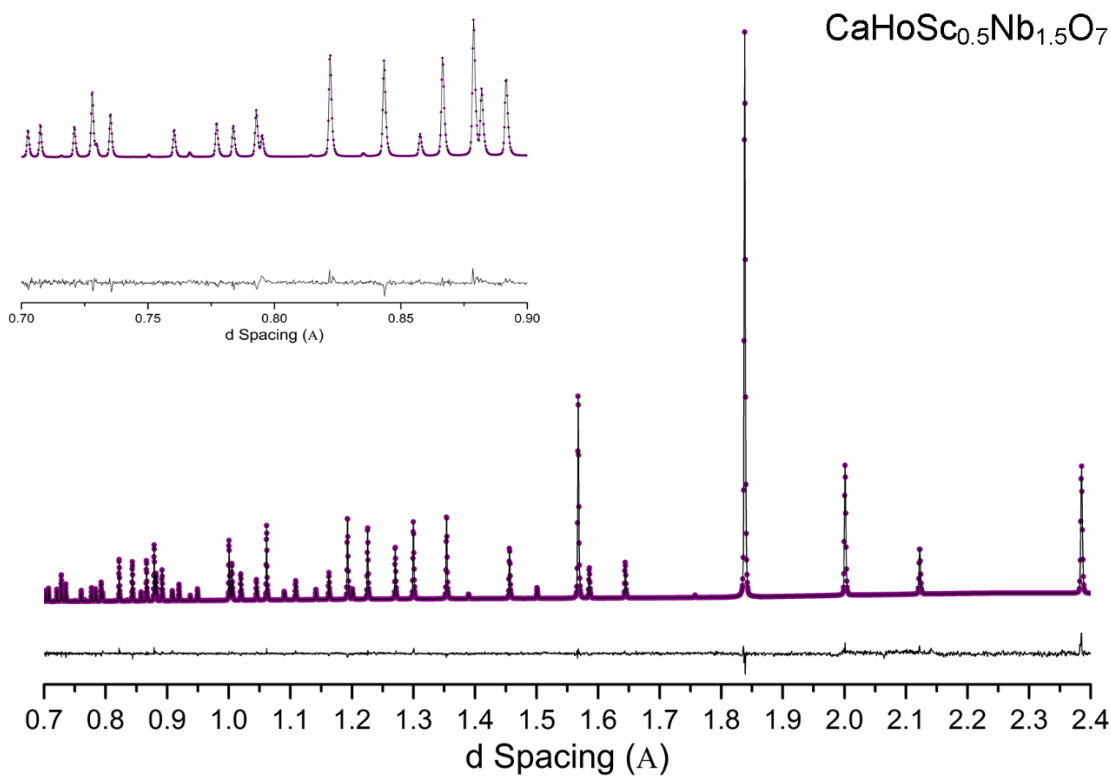


Figure A.8: Rietveld refinement fitting of neutron diffraction data collected on material with composition CaHoSc_{0.5}Nb_{0.5}O₇ on the High Resolution Powder Diffractometer (HRPD) instrument. Image shows fitted neutron diffraction trace and the error within the fitting (actual-calculated). Insert: Magnification of low d spacing and fitting quality.

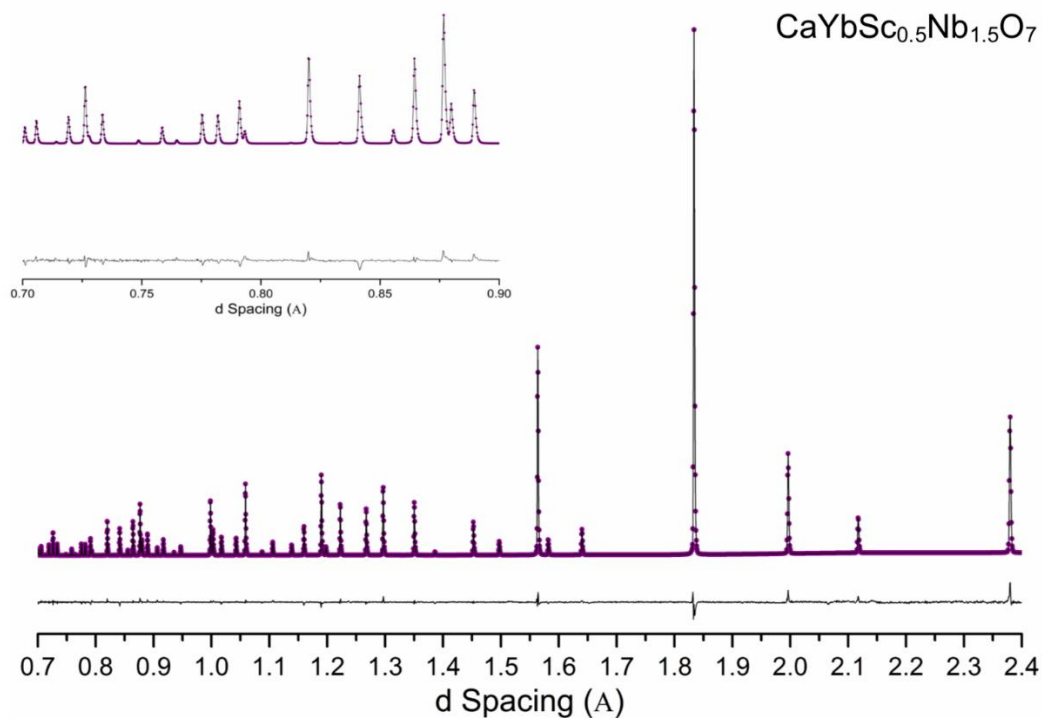


Figure A.9: Rietveld refinement fitting of neutron diffraction data collected on material with composition CaYbSc_{0.5}Nb_{0.5}O₇ on the High Resolution Powder Diffractometer (HRPD) instrument. Image shows fitted neutron diffraction trace and the error within the fitting (actual-calculated). Insert: Magnification of low d spacing and fitting quality.

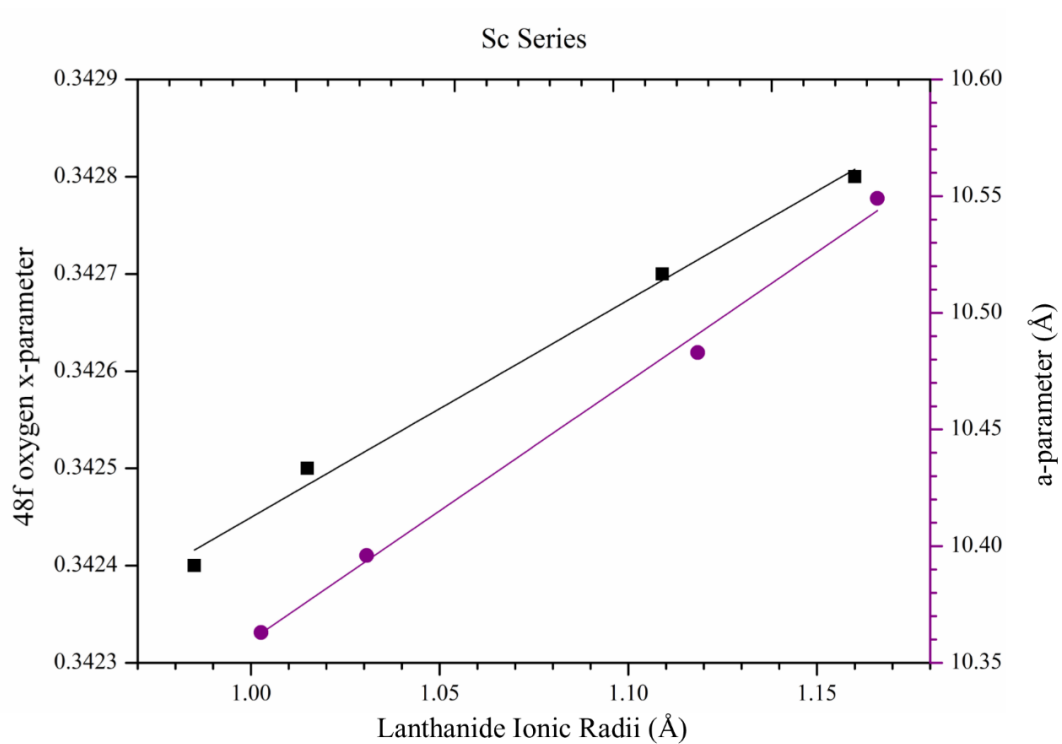


Figure A.10: Linear fitting of refined 48f oxygen x-parameter and a-parameter for compositions $\text{CaLnSc}_{0.5}\text{Nb}_{1.5}\text{O}_7$ with $\text{Ln}=\text{La}, \text{Nd}, \text{Ho}, \text{Yb}$.

A.4 Yttrium Materials

A.4.1 Yttrium Material XRD

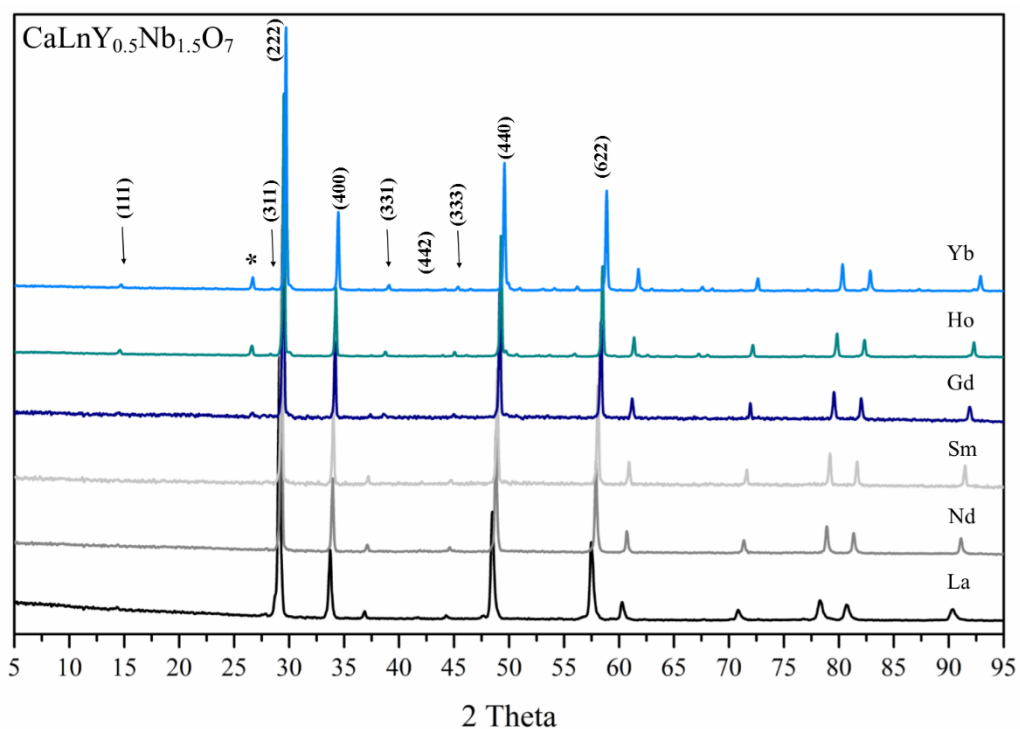


Figure A.11: X-ray diffraction data of the series of materials with ideal compositions $\text{CaLnY}_{0.5}\text{Nb}_{1.5}\text{O}_7$, where $\text{Ln}=\text{La}, \text{Nd}, \text{Sm}, \text{Gd}, \text{Ho}$ or Yb , as collected on the Stoe-IP instrument. Reflections indicative of the pyrochlore superstructure are highlighted with the arrow in the figure.

A.4.2 Yttrium Material SEM

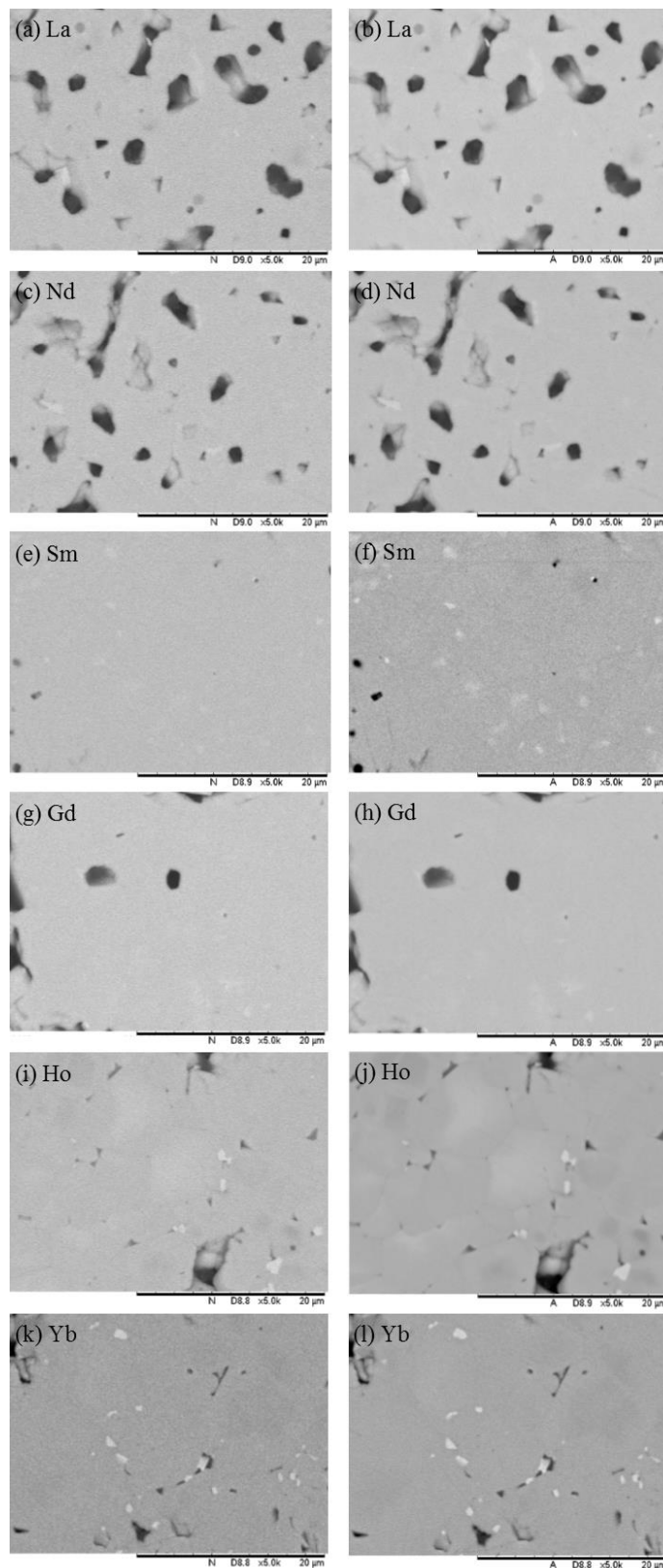


Figure A.12: SEM images of samples with target composition $\text{CaLnY}_{0.5}\text{Nb}_{1.5}\text{O}_7$ where $\text{Ln} = \text{La}$ for images (a) and (b), $\text{Ln} = \text{Nd}$ for (c) and (d), $\text{Ln} = \text{Sm}$ for (e) and (f), $\text{Ln} = \text{Gd}$ for (g) and (h), $\text{Ln} = \text{Ho}$ for (i) and (j) and $\text{Ln} = \text{Yb}$ for images (k) and (l). Images on the left are the secondary electron images and the right hand side showing the back-scattered electron micrographs of compositions.

A.4.3 Yttrium Material Neutron Diffraction

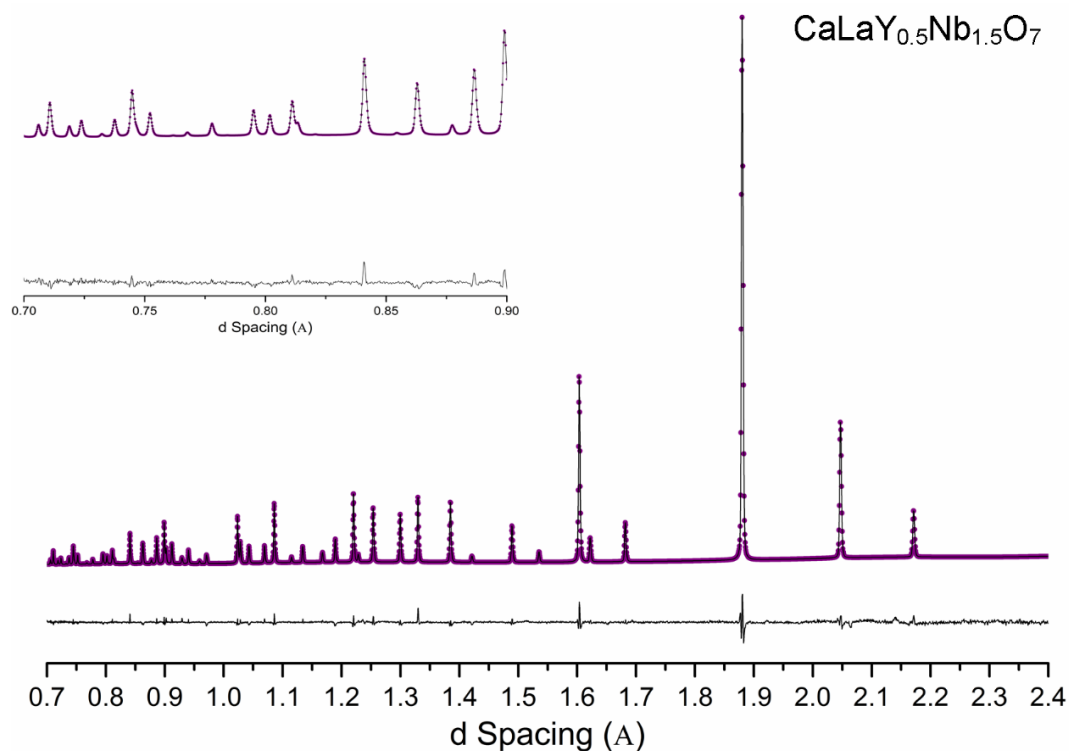


Figure A.13: Rietveld refinement fitting of neutron diffraction data collected on material with composition $\text{CaLaY}_{0.5}\text{Nb}_{1.5}\text{O}_7$ on the High Resolution Powder Diffractometer (HRPD) instrument. Image shows fitted neutron diffraction trace and the error within the fitting (actual-calculated). Insert: Magnification of low d spacing and fitting quality.

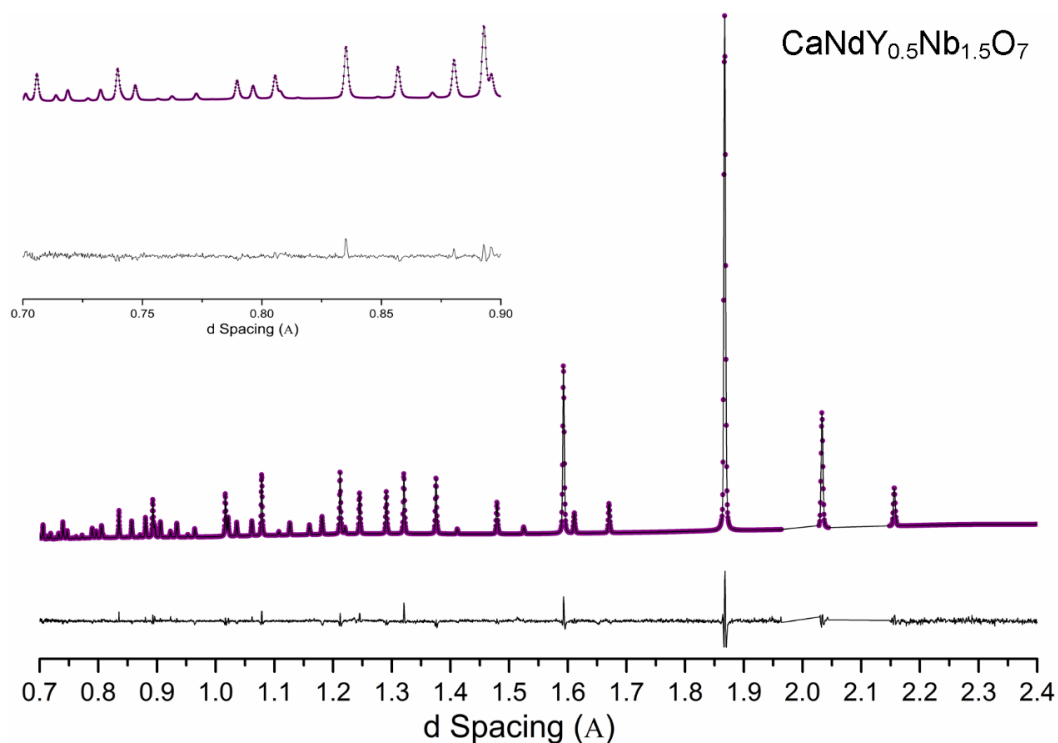


Figure A. 14: Rietveld refinement fitting of neutron diffraction data collected on material with composition $\text{CaNdY}_{0.5}\text{Nb}_{1.5}\text{O}_7$ on the High Resolution Powder Diffractometer

(HRPD) instrument. Image shows fitted neutron diffraction trace and the error within the fitting (actual-calculated). Insert: Magnification of low d spacing and fitting quality.

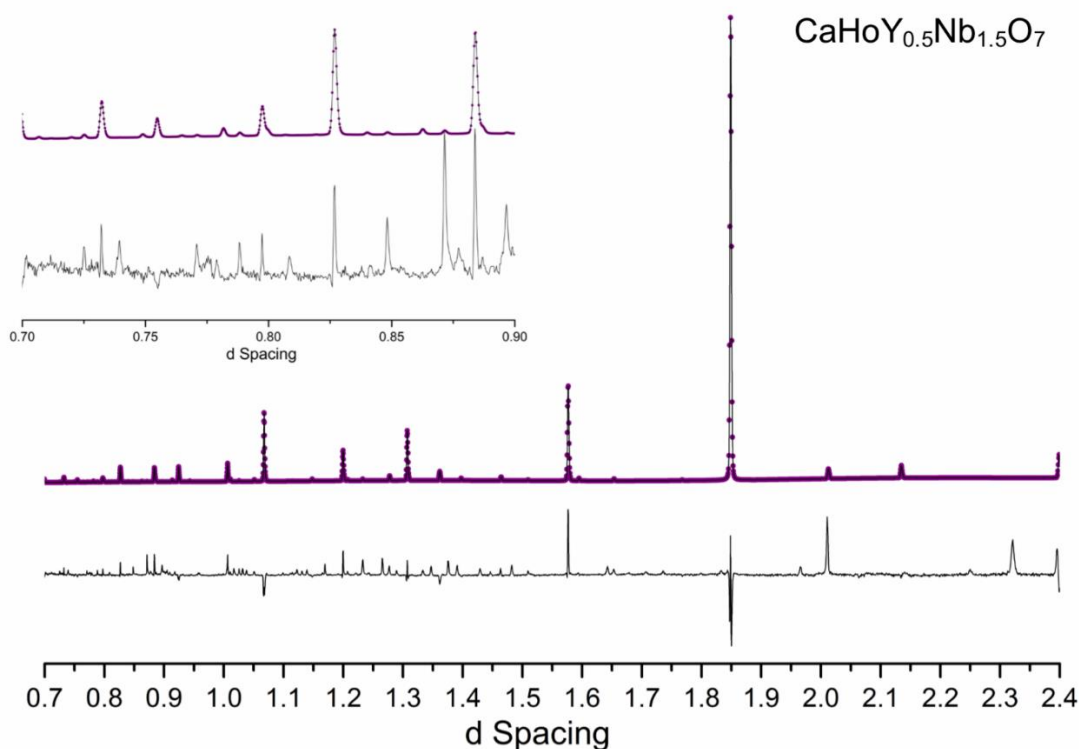


Figure A.15: Rietveld refinement fitting of neutron diffraction data collected on material with composition $\text{CaHoY}_{0.5}\text{Nb}_{0.5}\text{O}_7$ on the High Resolution Powder Diffractometer (HRPD) instrument. Image shows fitted neutron diffraction trace and the error within the fitting (actual-calculated). Insert: Magnification of low d spacing and fitting quality.

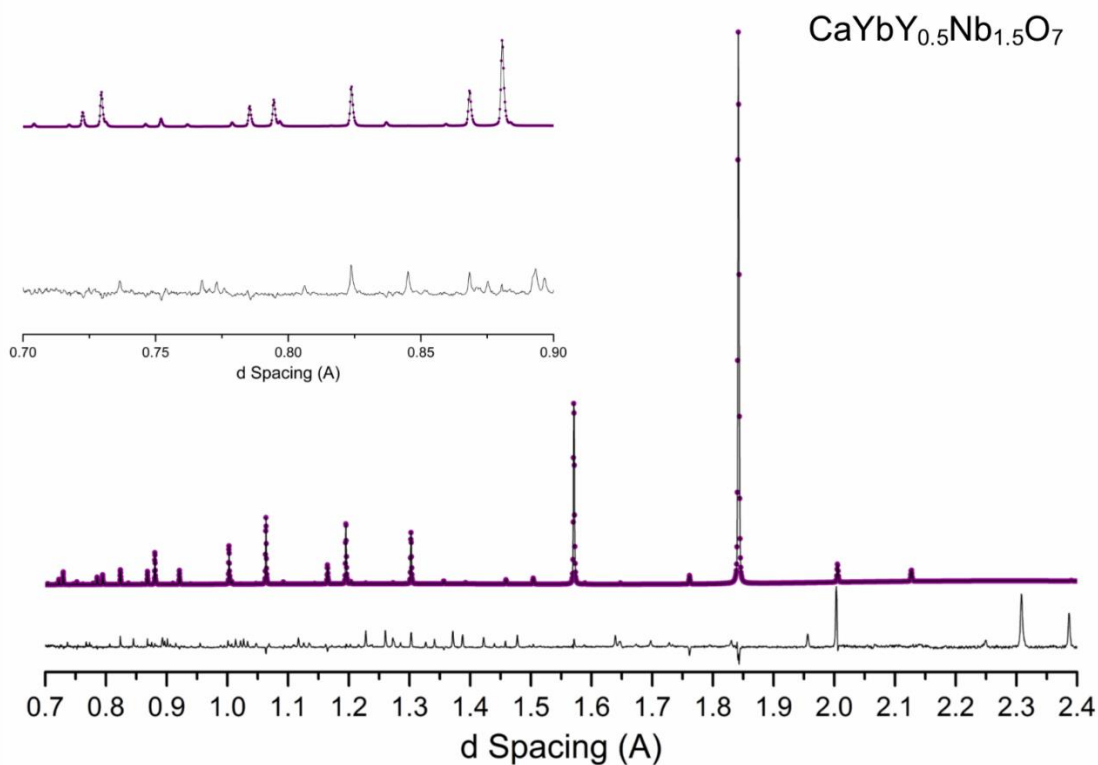


Figure A.16: Rietveld refinement fitting of neutron diffraction data collected on material with composition $\text{CaYbY}_{0.5}\text{Nb}_{0.5}\text{O}_7$ on the High Resolution Powder Diffractometer

(HRPD) instrument. Image shows fitted neutron diffraction trace and the error within the fitting (actual-calculated). Insert: Magnification of low d spacing and fitting quality.

BSE images of compositions $\text{CaHoY}_{0.5}\text{Nb}_{1.5}\text{O}_7$ and $\text{CaYbY}_{0.5}\text{Nb}_{1.5}\text{O}_7$ indicated the presence of a secondary phase, Figure A.6. XRD analysis showed the presence of un-indexed reflections within these materials XRD patterns, indicated with the ‘*’ in Figure A.11. However, the number and intensity of the reflections of the secondary phase are low so could not be utilised to identify the crystal structure present. This is seen by the splitting of the reflections at high angles and the broader than would be expected of XRD analysis on an instrument with a monochromator.

The fitting achieved within GSAS of the neutron diffraction data for the holmium and ytterbium yttrium materials, $\text{CaHoY}_{0.5}\text{Nb}_{1.5}\text{O}_7$ and $\text{CaYbY}_{0.5}\text{Nb}_{1.5}\text{O}_7$, respectively, show a non-single phase material, highlighted by the fitting of the model to the data, Figures A.22 and A.23. This is reflected in the high χ^2 and wRp in Table A.1. The GSAS refined parameters for the fitting of a pyrochlore structure to the data for the materials are included in Table A.1, but have not been used for analysis within Chapter 4 due to the un-identified additional phases.

Table A.1: Unit cell parameter ‘a’ and 48f oxygen x-position determined from neutron diffraction data collected on the HRPD instrument, ISIS, Oxford, refined using Rietveld refinement on GSAS software. The errors within the parameters are as determined using standard deviation estimations in the results calculated by the GSAS software.

Ln	‘a’ Parameter	48f-x	χ^2	wRp	U _{iso}			
					Ca & Ln (σ)	Y & Nb (σ)	O1 (σ)	O2 (σ)
Ho	10.455(8)	0.362(5)	26.01	0.1999	1.070 (162)	2.144 (181)	4.092 (133)	3.465 (168)
Yb	10.417(6)	0.390(10)	20.16	0.1788	2.991 (145)	0.496 (86)	8.927 (184)	3.748 (142)

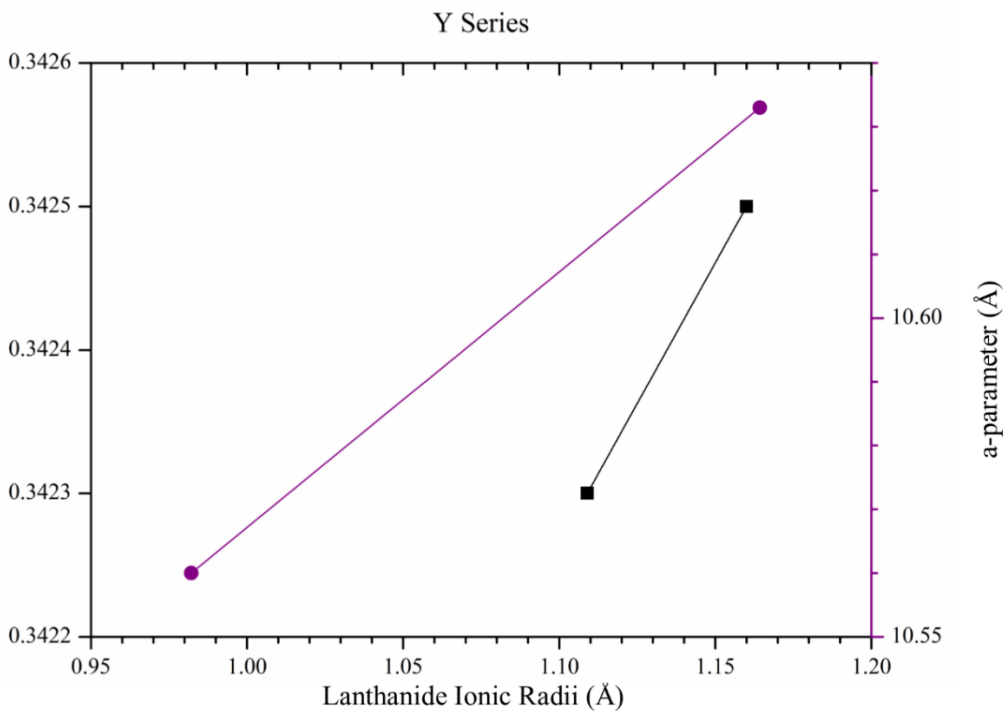


Figure A.17: Linear fitting of refined 48f oxygen x-parameter and a-parameter for compositions $\text{CaLnY}_{0.5}\text{Nb}_{1.5}\text{O}_7$ with $\text{Ln}=\text{La}$ and Nd .

A.5 Aluminium Materials

A.5.1 Aluminium Material XRD

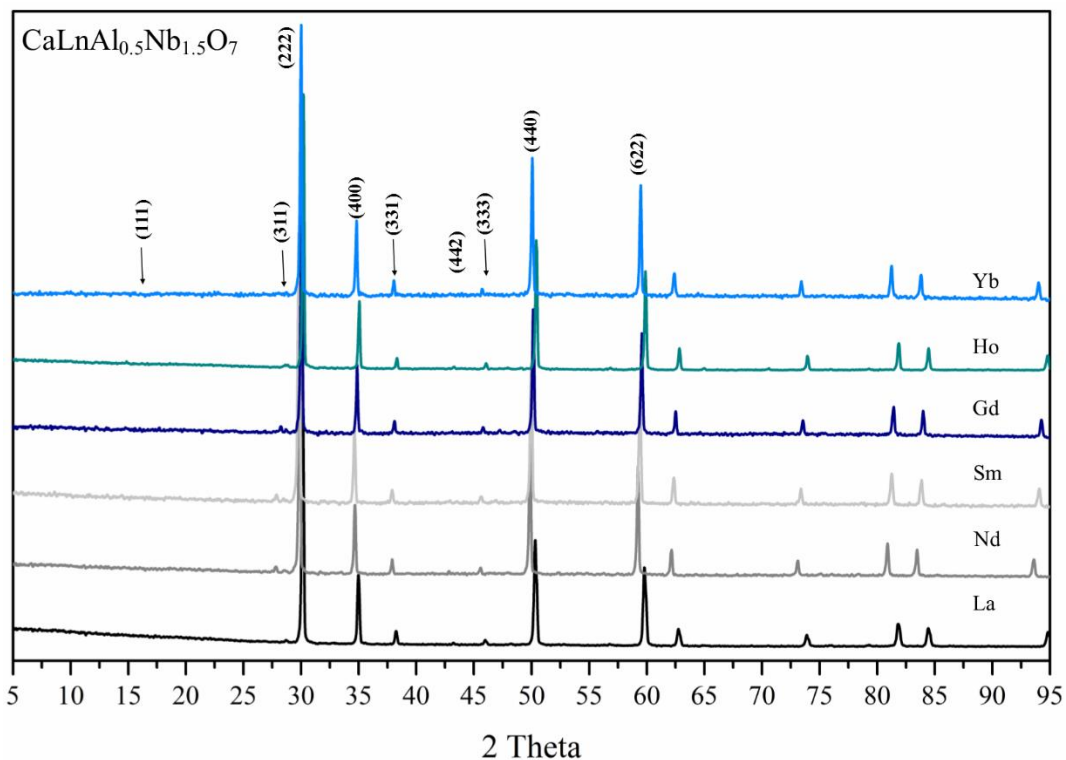


Figure A.18: X-ray diffraction data of the series of materials with ideal compositions $\text{CaLnAl}_{0.5}\text{Nb}_{1.5}\text{O}_7$, where $\text{Ln}=\text{La}$, Nd , Sm , Gd , Ho or Yb , as collected on the Stoe-IP instrument. Reflections indicative of the pyrochlore superstructure are highlighted with the arrow in the figure.

A.5.2 Aluminium Material SEM

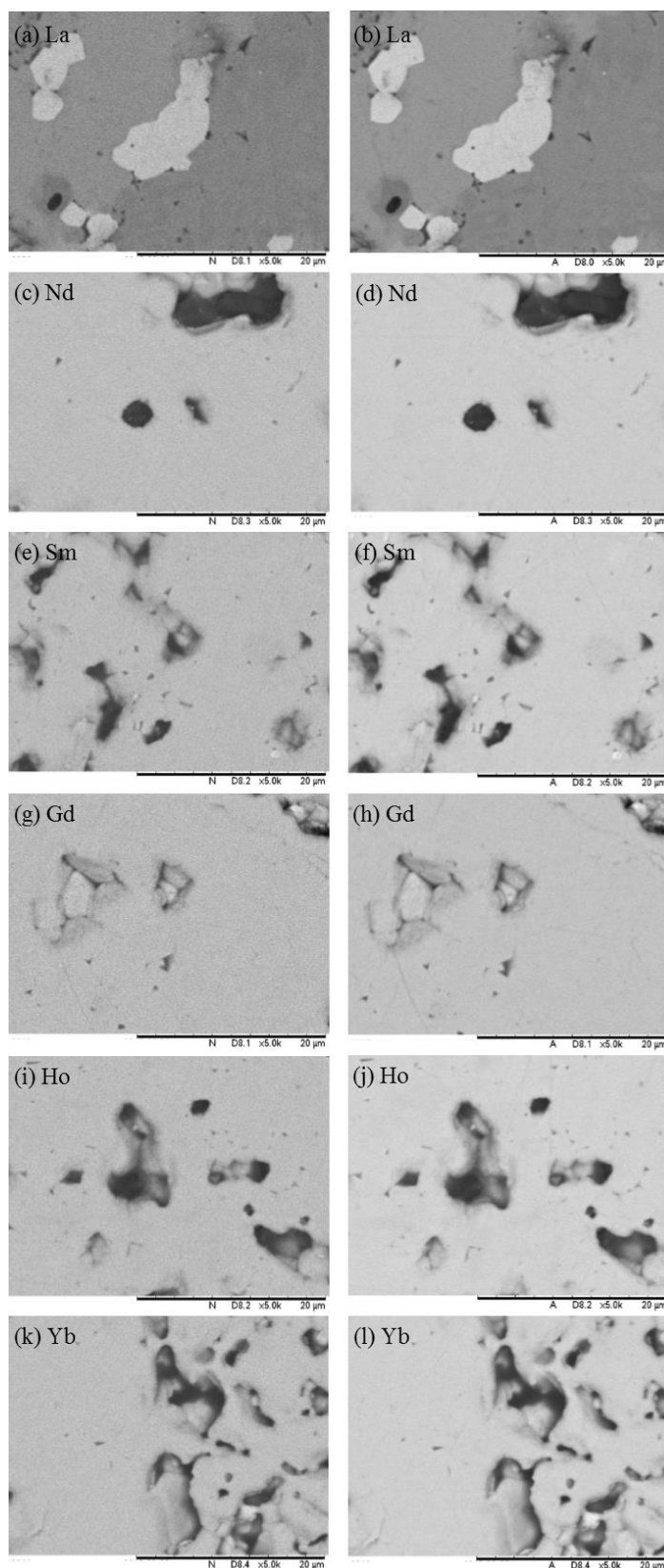


Figure A.19: SEM images of samples with target composition $\text{CaLnAl}_{0.5}\text{Nb}_{1.5}\text{O}_7$ where Ln = La for images (a) and (b), Ln = Nd for (c) and (d), Ln = Sm for (e) and (f), Ln = Gd for (g) and (h), Ln = Ho for (i) and (j) and Ln = Yb for images (k) and (l). Images on the left are the secondary electron images and the right hand side showing the back-scattered electron micrographs of compositions.

A.5.3 Aluminium Material Neutron Diffraction

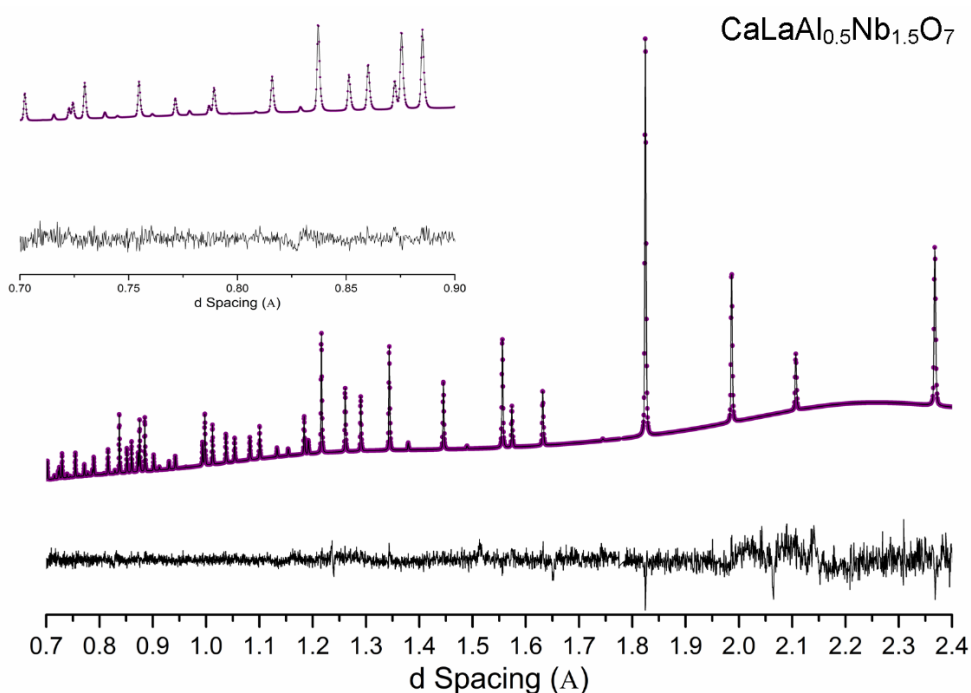


Figure A.20: Rietveld refinement fitting of neutron diffraction data collected on material with composition $\text{CaLaAl}_{0.5}\text{Nb}_{0.5}\text{O}_7$ on the High Resolution Powder Diffractometer (HRPD) instrument. Image shows fitted neutron diffraction trace and the error within the fitting (actual-calculated). Inset: Magnification of low d spacing and fitting quality.

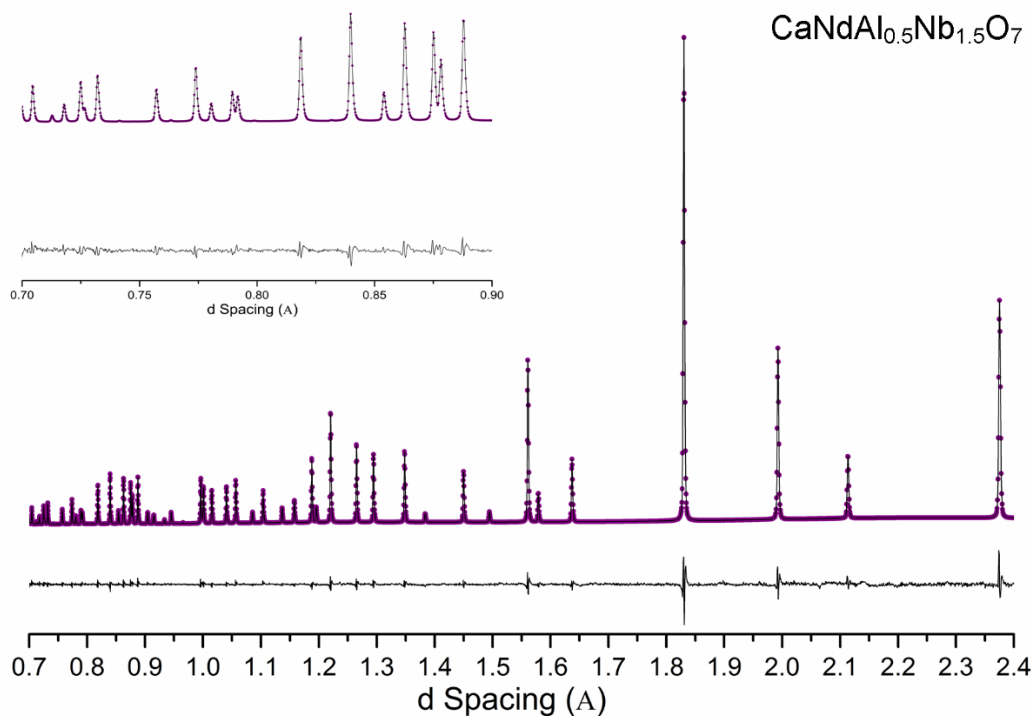


Figure A.21: Rietveld refinement fitting of neutron diffraction data collected on material with composition $\text{CaNdAl}_{0.5}\text{Nb}_{0.5}\text{O}_7$ on the High Resolution Powder Diffractometer

(HRPD) instrument. Image shows fitted neutron diffraction trace and the error within the fitting (actual-calculated). Insert: Magnification of low d spacing and fitting quality.

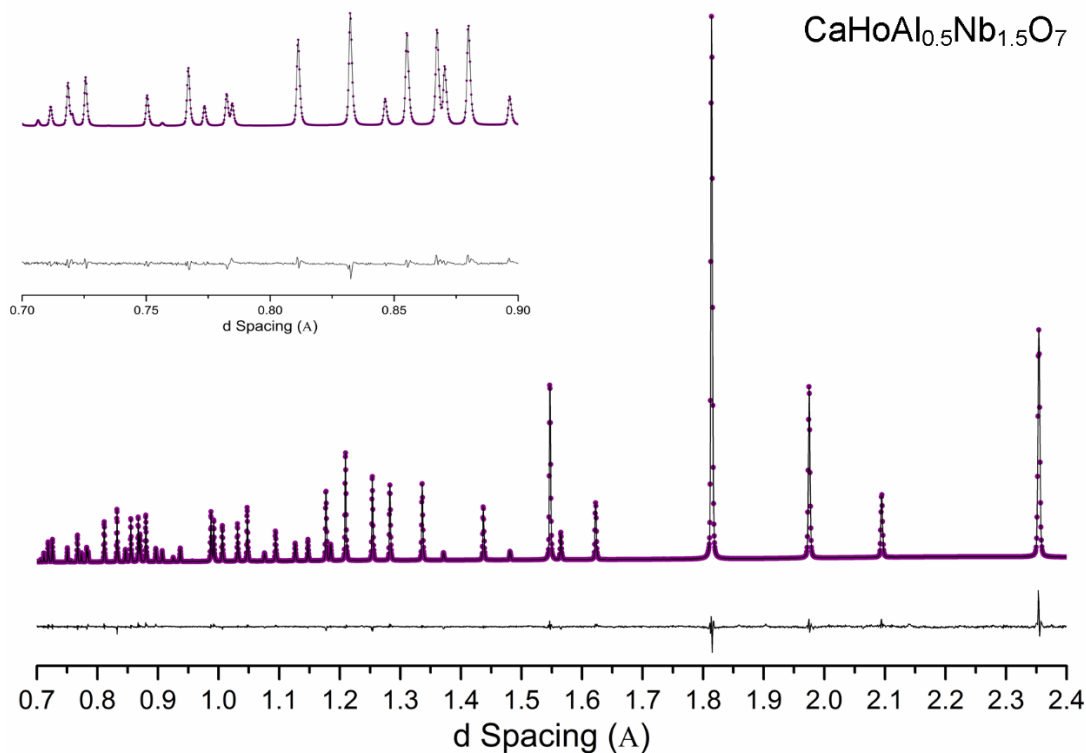


Figure A.22: Rietveld refinement fitting of neutron diffraction data collected on material with composition CaHoAl_{0.5}Nb_{0.5}O₇ on the High Resolution Powder Diffractometer (HRPD) instrument. Image shows fitted neutron diffraction trace and the error within the fitting (actual-calculated). Insert: Magnification of low d spacing and fitting quality.

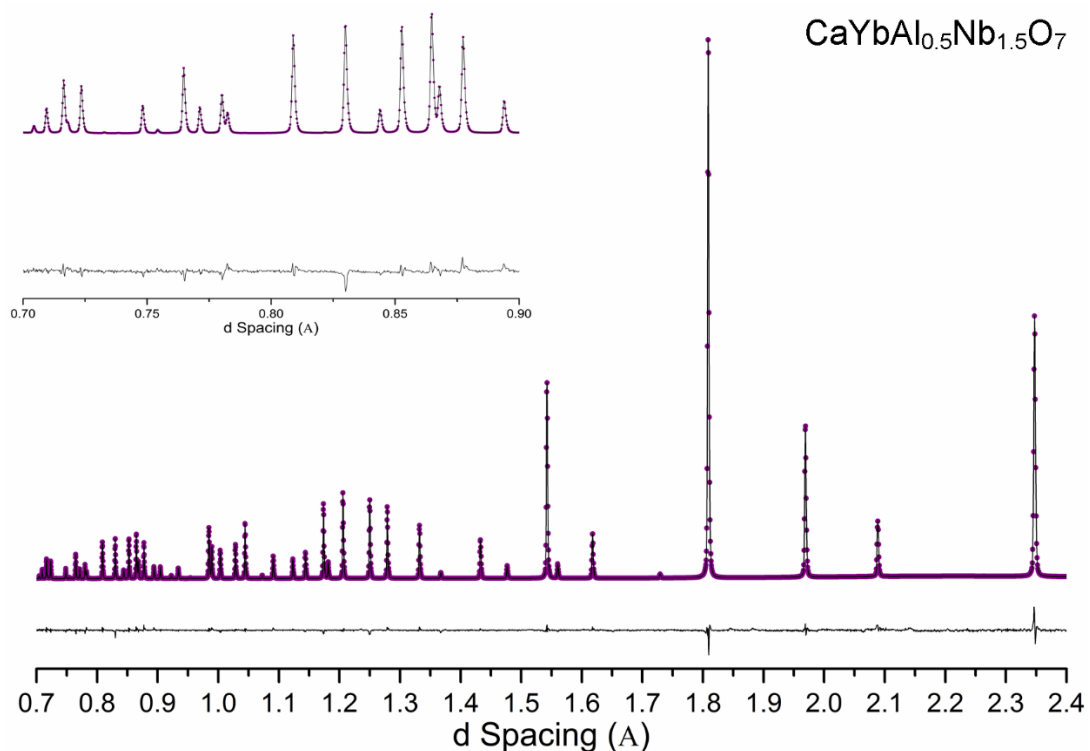


Figure A.23: Rietveld refinement fitting of neutron diffraction data collected on material with composition CaYbAl_{0.5}Nb_{0.5}O₇ on the High Resolution Powder Diffractometer

(HRPD) instrument. Image shows fitted neutron diffraction trace and the error within the fitting (actual-calculated). Insert: Magnification of low d spacing and fitting quality. All compositions show a single phase pyrochlore material with the exception of the composition $\text{CaLaAl}_{0.5}\text{Nb}_{1.5}\text{O}_7$, the SEM analysis of which highlights a large secondary phase which, Figure A4 (a) (g). This is absent from the x-ray diffraction analysis, however analysis of the background function of the neutron diffraction data fitting indicated the potential presence of an amorphous material. Rietveld refinement to neutron diffraction data indicated a single pyrochlore assemblage for target composition $\text{CaLaAl}_{0.5}\text{Nb}_{1.5}\text{O}_7$ (Figure A.20). XRD analysis did not indicate the presence of an amorphous material or secondary phase, therefore it was assumed to be a contaminant in the material after the X-ray diffraction analysis, but prior to the SEM and high resolution powder neutron diffraction.

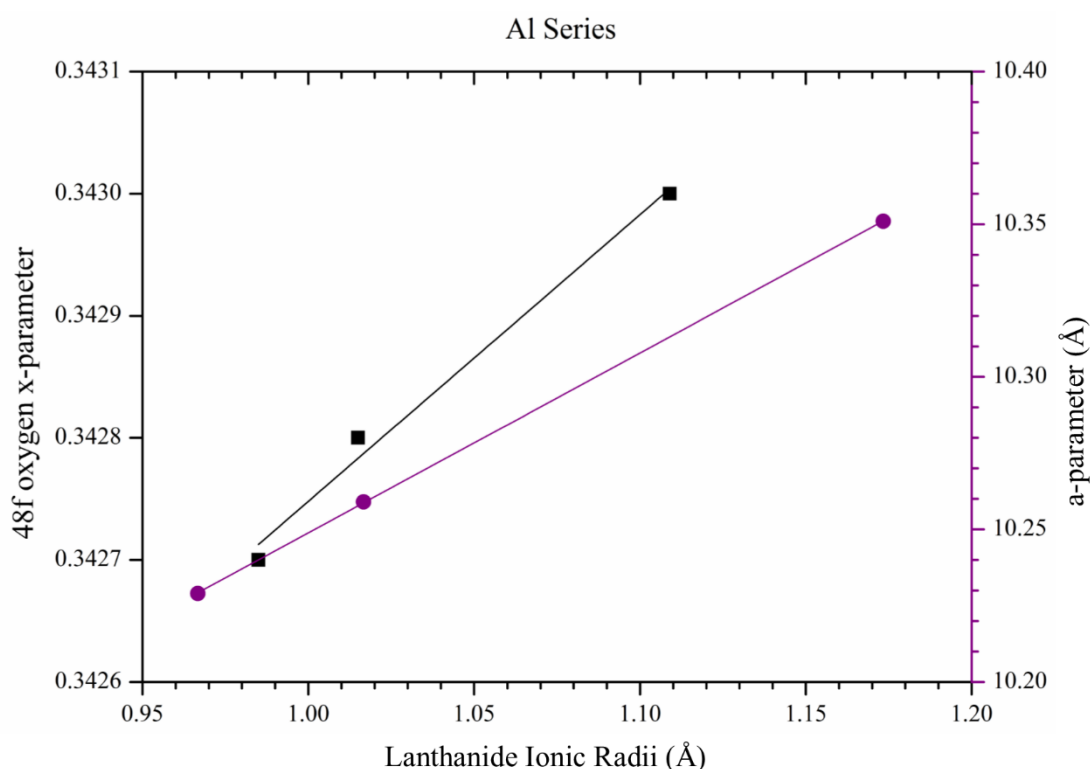


Figure A.24: Linear fitting of refined 48f oxygen x-parameter and a-parameter for compositions $\text{CaLnAl}_{0.5}\text{Nb}_{1.5}\text{O}_7$ with Ln=La, Nd, Ho, Yb.

A.6 Chromium Materials

Materials have been synthesised as described in chapter 4, section 4.2.1, the proportions of CaCO_3 , Ln_2O_3 , Cr_2O_3 and Nb_2O_5 with $\text{Ln} = \text{La, Nd, Sm, Gd, Ho}$ and Yb to form target composition $\text{CaLnCr}_{0.5}\text{Nb}_{1.5}\text{O}_7$.

A.6.1 Chromium Material XRD

Multiple heating regimes have been utilised in order to attempt to produce a material which has a crystal structure indicative of the pyrochlore structure. With temperatures ranging from 1100-1550°C and for dwell times of up to 168hours (7 days), with intermediate regrinding. A vast range of materials have been produced, all of which show minor secondary phases present, and potentially a secondary pyrochlore / fluorite related structure. X-ray diffraction data, Figure A.25, highlights the pyrochlore phase, with un-indexed reflections being of additional phases which are minor in quantity.

Analysis has been completed on the materials using scanning electron microscopy (SEM) and energy dispersive spectroscopy (EDS) on the Hitachi TM3030 microscope in order to ascertain the chemical composition of the secondary phases.

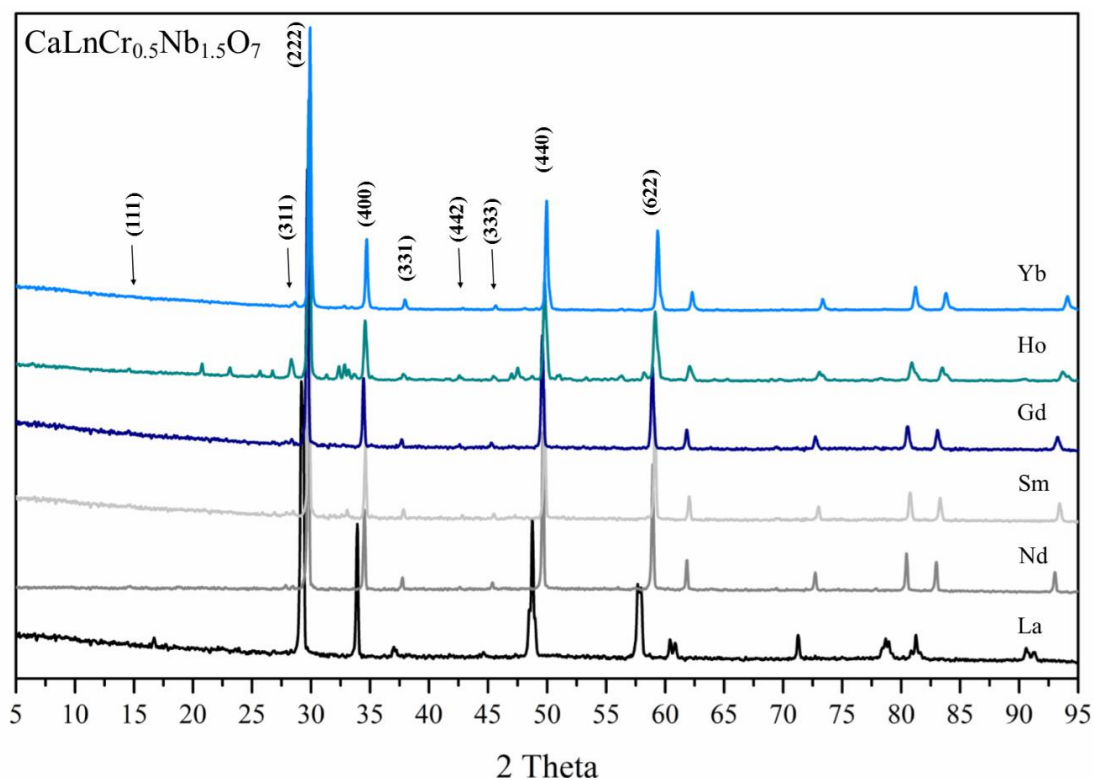


Figure A. 25: X-ray diffraction data of the series of materials with ideal compositions $\text{CaLnCr}_{0.5}\text{Nb}_{1.5}\text{O}_7$, where $\text{Ln} = \text{La, Nd, Sm, Gd, Ho}$ or Yb , as collected on the Stoe-IP instrument. Reflections indicative of the pyrochlore superstructure are highlighted with the arrow in the figure.

A.6.2 Chromium Material SEM

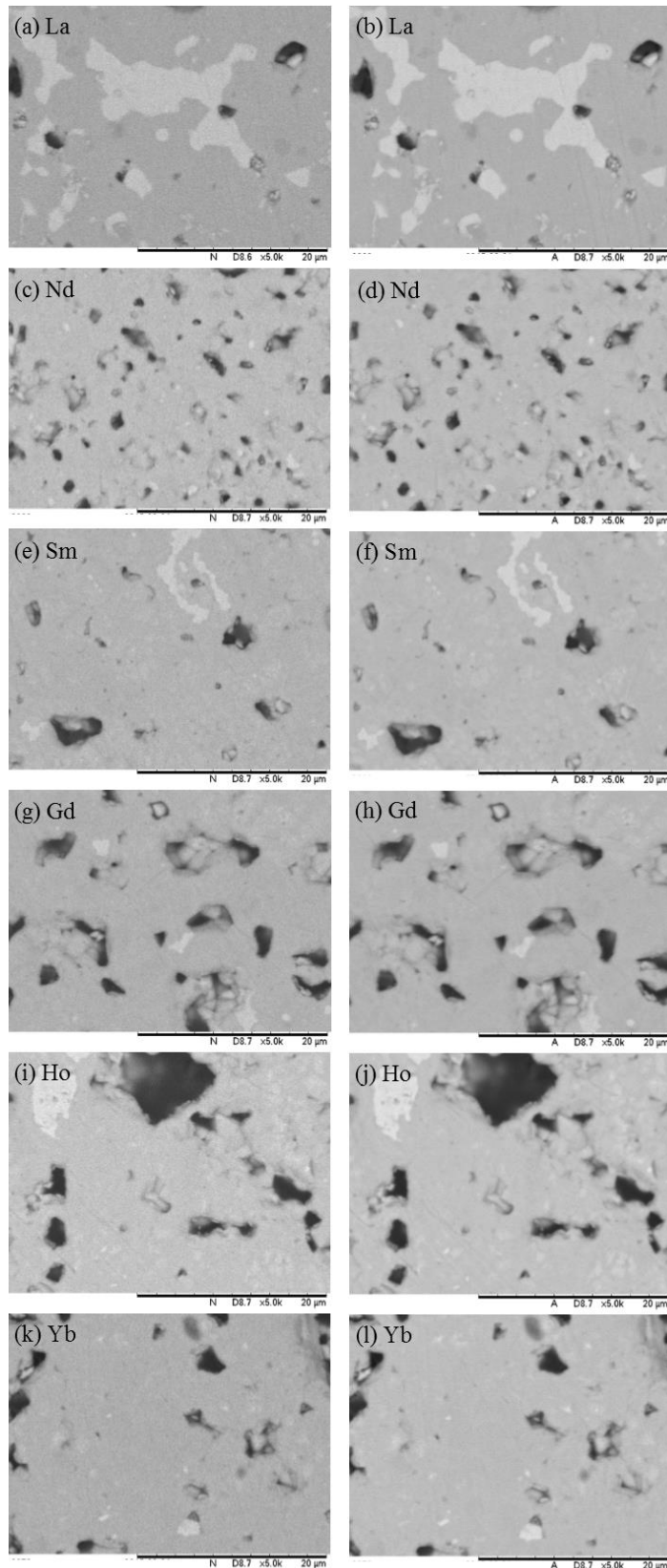


Figure A.26: SEM images of samples with target composition $\text{CaLnCr}_{0.5}\text{Nb}_{1.5}\text{O}_7$ where $\text{Ln} = \text{La}$ for images (a) and (b), $\text{Ln} = \text{Nd}$ for (c) and (d), $\text{Ln} = \text{Sm}$ for (e) and (f), $\text{Ln} = \text{Gd}$ for (g) and (h), $\text{Ln} = \text{Ho}$ for (i) and (j) and $\text{Ln} = \text{Yb}$ for images (k) and (l). Images on the left are the secondary electron images and the right hand side showing the back-scattered electron micrographs of compositions.

The bulk material has been defined as phase 1. It is assumed that the bulk material will adopt the pyrochlore structure, due to the dominance of the pyrochlore phase within the XRD data. The bulk materials are identified as calcium rich, in comparison to the target compositions. Phase 2, the minor secondary phase identified within the materials, are deficient in calcium and chromium cations. Also included within Table A.2 oxygen stoichiometries have been determined assuming Ca^{2+} , Ln^{3+} , Cr^{3+} and Nb^{5+} . Neutron diffraction analysis was not completed on the multiphase materials.

Table A.2: Semi-quantitative EDS results from the average of 5 spot analysis on the 2 distinguishable phases. The bulk material is identified as phase 1, which phase 2 being the secondary phase within the material.

Ln	Phase 1 (Bulk Phase)	Phase 2 (Secondary Phase)
La	$\text{Ca}_{1.13(3)}\text{La}_{0.99(9)}\text{Cr}_{0.45(2)}\text{Nb}_{1.57(12)}\text{O}_{7.2(3)}$	$\text{La}_{1.46(12)}\text{Nb}_{1.56(11)}\text{O}_{6.1(2)}$
Nd	$\text{Ca}_{1.07(3)}\text{Nd}_{0.84(8)}\text{Cr}_{0.48(2)}\text{Nb}_{1.34(11)}\text{O}_{6.4(2)}$	$\text{Ca}_{0.50(2)}\text{Nd}_{1.18(10)}\text{Cr}_{0.24(1)}\text{Nb}_{1.50(11)}\text{O}_{6.4(2)}$
Sm	$\text{Ca}_{1.30(3)}\text{Sm}_{1.02(9)}\text{Cr}_{0.56(2)}\text{Nb}_{1.72(11)}\text{O}_{8.0(3)}$	$\text{Ca}_{0.17(1)}\text{Sm}_{1.85(13)}\text{Nb}_{2.09(11)}\text{O}_{8.2(3)}$
Gd	$\text{Ca}_{1.19(3)}\text{Gd}_{0.89(8)}\text{Cr}_{0.47(2)}\text{Nb}_{1.54(11)}\text{O}_{7.1(2)}$	$\text{Ca}_{0.24(1)}\text{Gd}_{1.65(13)}\text{Cr}_{0.10(1)}\text{Nb}_{1.95(11)}\text{O}_{7.7(3)}$
Ho	$\text{Ca}_{1.33(3)}\text{Ho}_{0.95(9)}\text{Cr}_{0.52(2)}\text{Nb}_{1.65(11)}\text{O}_{7.7(3)}$	$\text{Ho}_{1.60(13)}\text{Nb}_{1.70(10)}\text{O}_{6.7(2)}$
Yb	$\text{Ca}_{1.26(3)}\text{Yb}_{0.82(9)}\text{Cr}_{0.48(2)}\text{Nb}_{1.52(10)}\text{O}_{7.0(2)}$	$\text{Ca}_{0.36(1)}\text{Yb}_{1.64(14)}\text{Cr}_{0.13(1)}\text{Nb}_{1.99(10)}\text{O}_{8.0(3)}$

Appendix B

B.1 Introduction

Within this appendix is additional data collated for ‘Chapter 5- Uranium Substituted Lanthanum Zirconate Pyrochlores’. This includes data from the refinement of the pyrochlore model to X-ray diffraction data, and XANES analysis not explicitly included in but discussed within the chapter.

B.2 Additional Experimental Data and Discussion

B.2.1 Additional X-ray Diffraction Refinement Data

B.2.1.1 Air Formed Materials

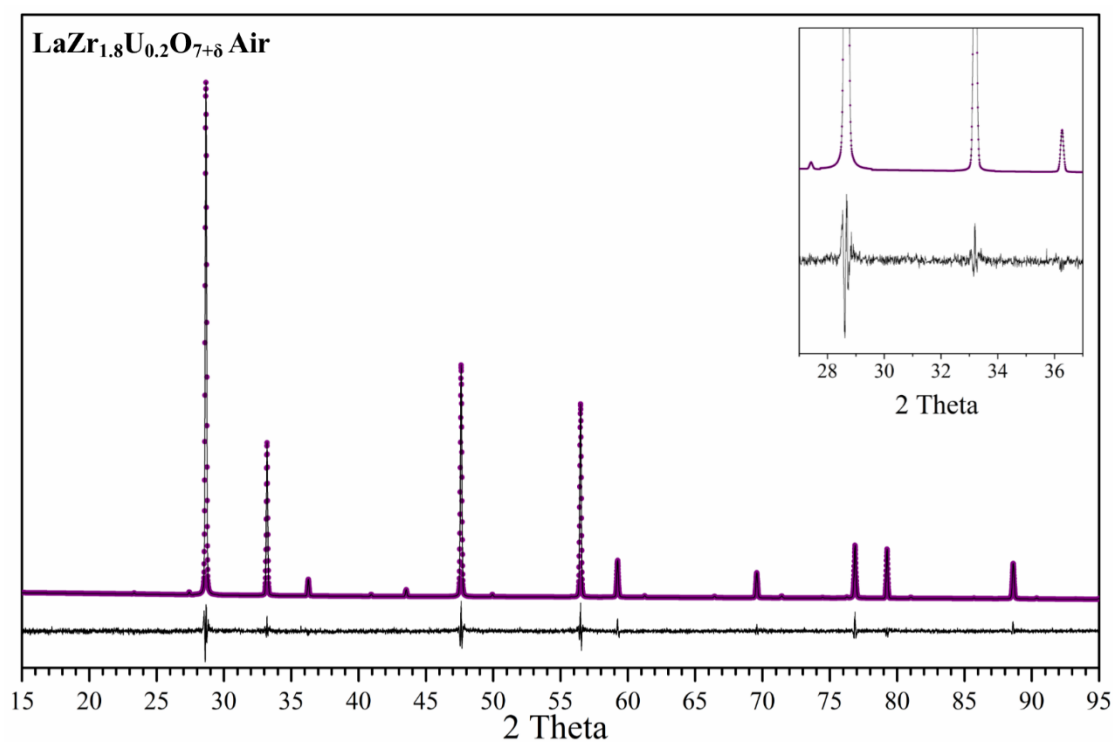


Figure B. 1: Material of target composition $\text{La}_2\text{Zr}_{1.8}\text{U}_{0.2}\text{O}_{7+\delta}$ formed in an air atmosphere, fitted using the GSAS software. Data shown is the calculated fit (black) and the observed – calculated difference trace highlighting the quality of the fit.

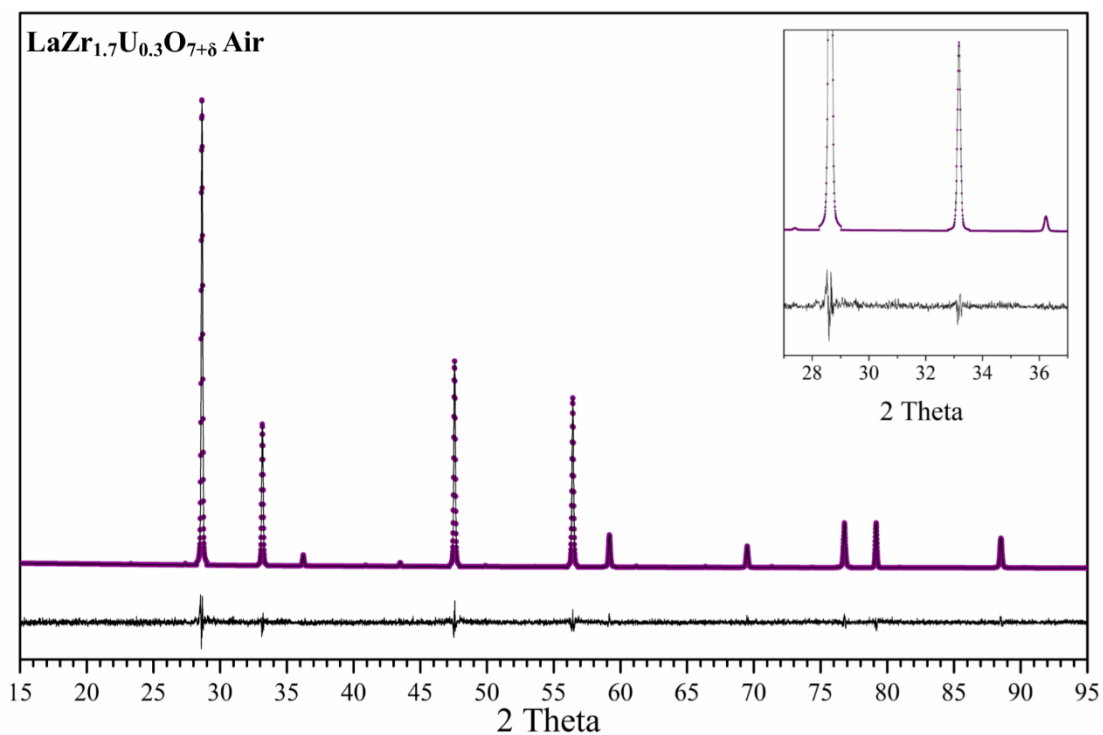


Figure B.2: Material of target composition $\text{La}_2\text{Zr}_{1.7}\text{U}_{0.3}\text{O}_{7+\delta}$ formed in an air atmosphere, fitted using the GSAS software. Data shown is the calculated fit (black) and the observed – calculated difference trace highlighting the quality of the fit.

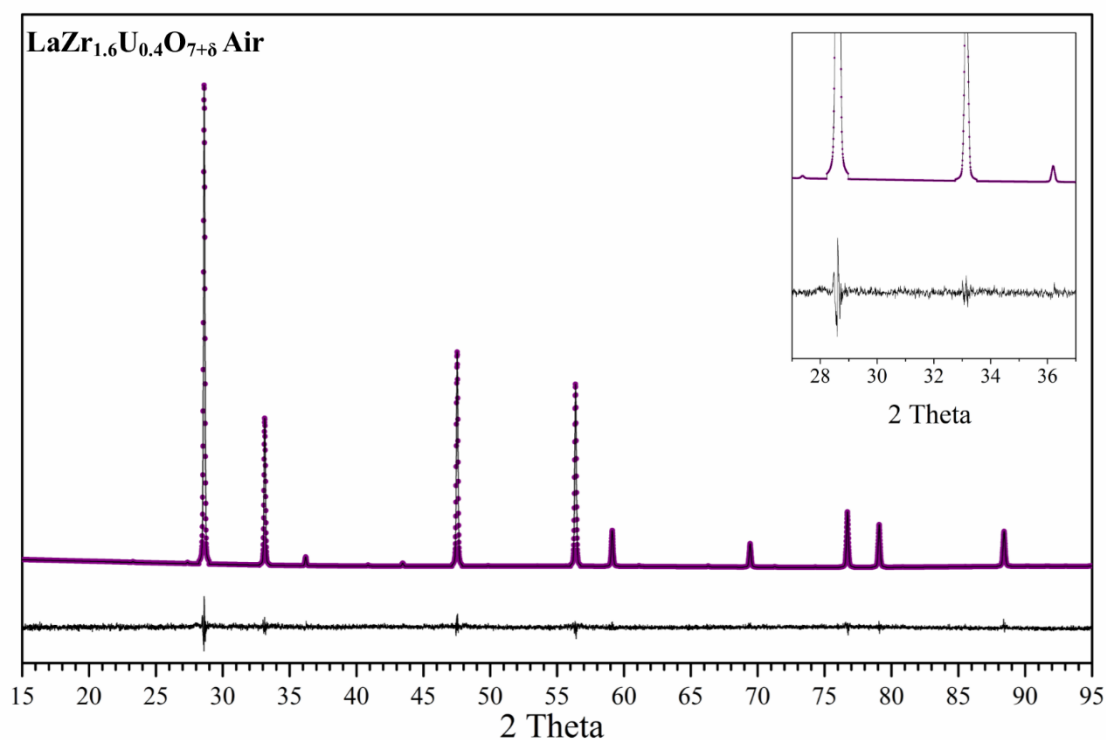


Figure B.3: Material of target composition $\text{La}_2\text{Zr}_{1.6}\text{U}_{0.4}\text{O}_{7+\delta}$ formed in an air atmosphere, fitted using the GSAS software. Data shown is the calculated fit (black) and the observed – calculated difference trace highlighting the quality of the fit.

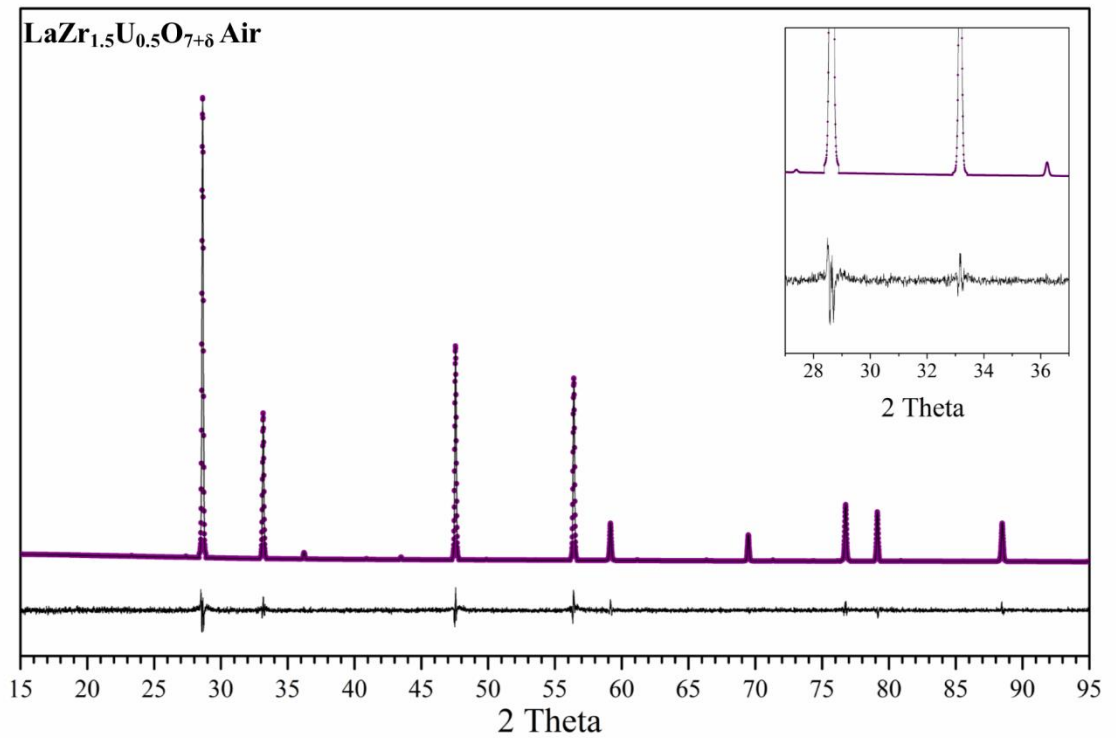


Figure B.4: Material of target composition $\text{La}_2\text{Zr}_{1.5}\text{U}_{0.5}\text{O}_{7+\delta}$ formed in an air atmosphere, fitted using the GSAS software. Data shown is the calculated fit (black) and the observed – calculated difference trace highlighting the quality of the fit.

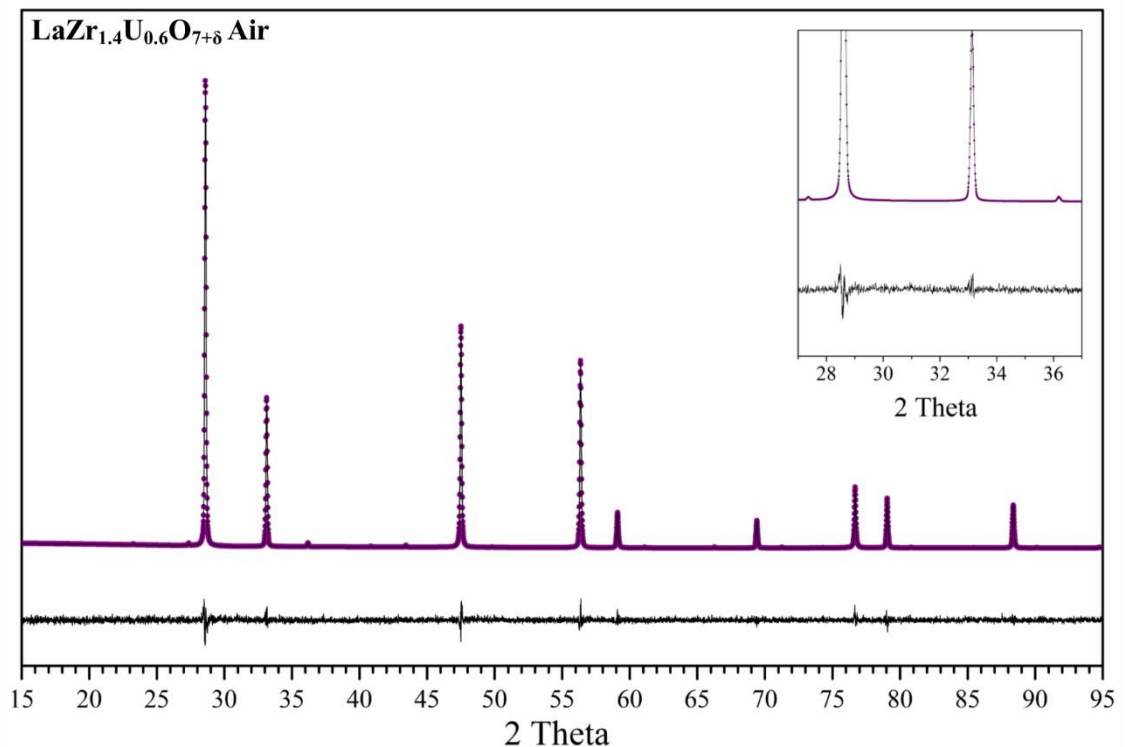


Figure B.5: Material of target composition $\text{La}_2\text{Zr}_{1.4}\text{U}_{0.6}\text{O}_{7+\delta}$ formed in an air atmosphere, fitted using the GSAS software. Data shown is the calculated fit (black) and the observed – calculated difference trace highlighting the quality of the fit. This fit is achieved through the use of 2 pyrochlore structures, whose refinement parameters are included within Table 5.4 and Table 5.5.

B.2.1.2 Hydrogen / Nitrogen formed materials

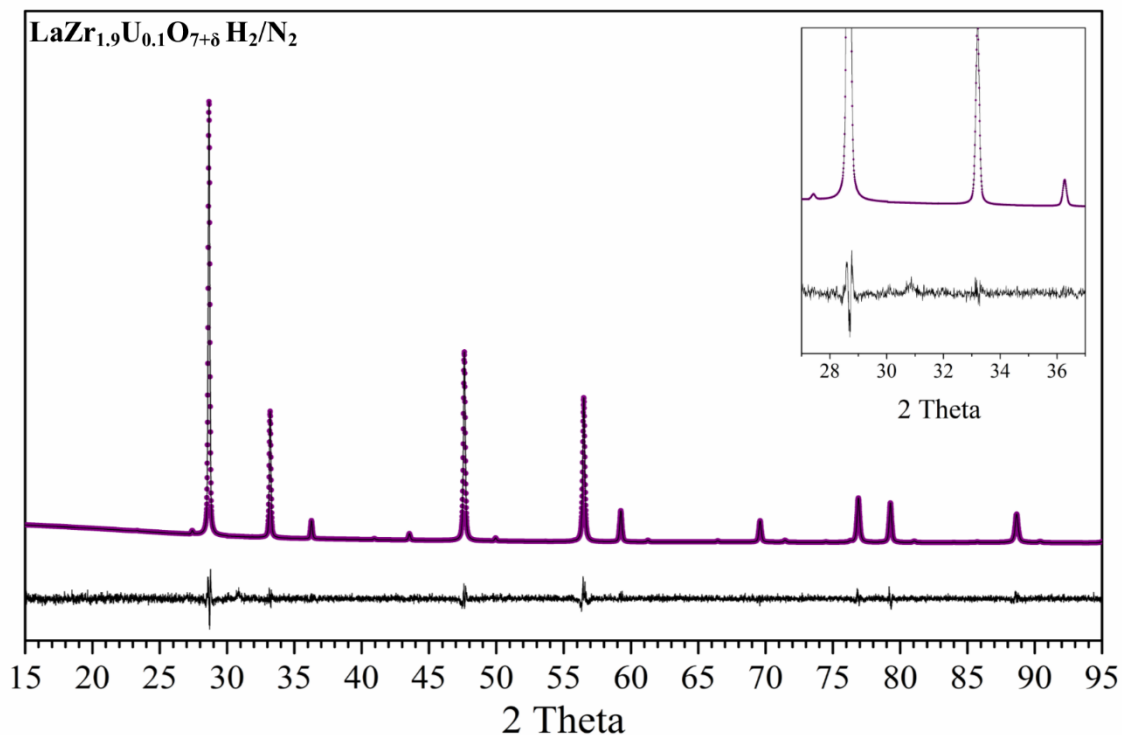


Figure B.6: Material of target composition $\text{La}_2\text{Zr}_{1.9}\text{U}_{0.1}\text{O}_{7+\delta}$ formed in a reducing hydrogen / nitrogen atmosphere, fitted using the GSAS software. Data shown is the calculated fit (black) and the observed – calculated difference trace highlighting the quality of the fit.

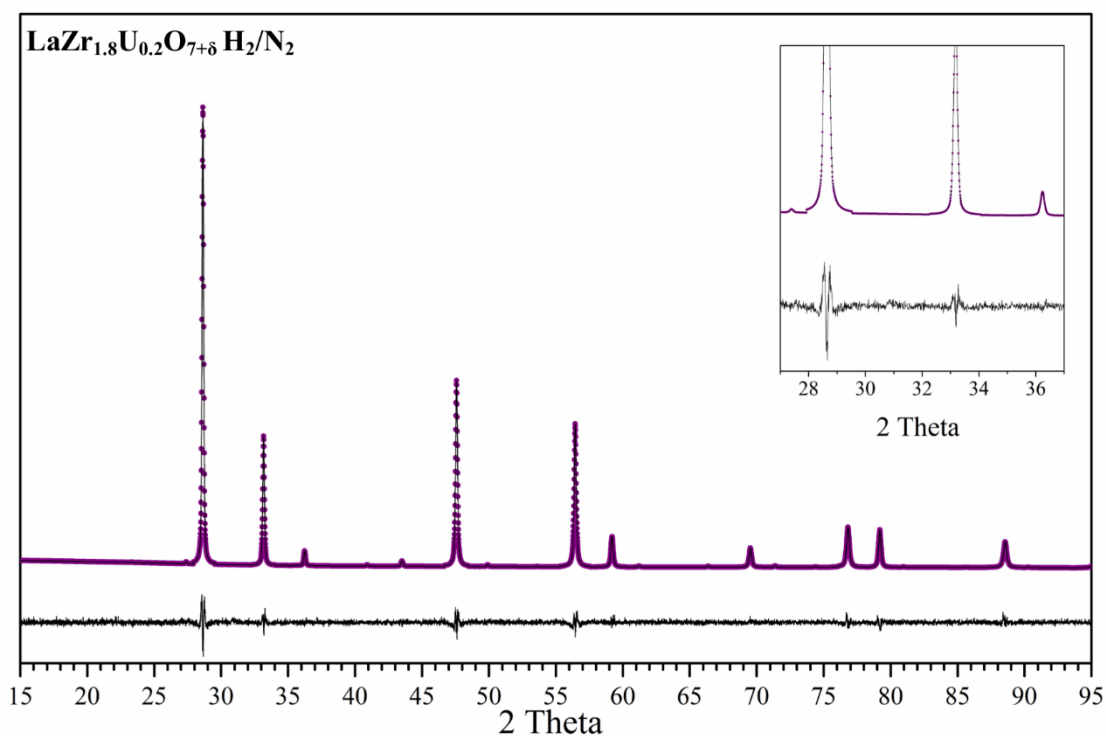


Figure B.7: Material of target composition $\text{La}_2\text{Zr}_{1.8}\text{U}_{0.2}\text{O}_{7+\delta}$ formed in a reducing hydrogen / nitrogen atmosphere, fitted using the GSAS software. Data shown is the calculated fit (black) and the observed – calculated difference trace highlighting the quality of the fit.

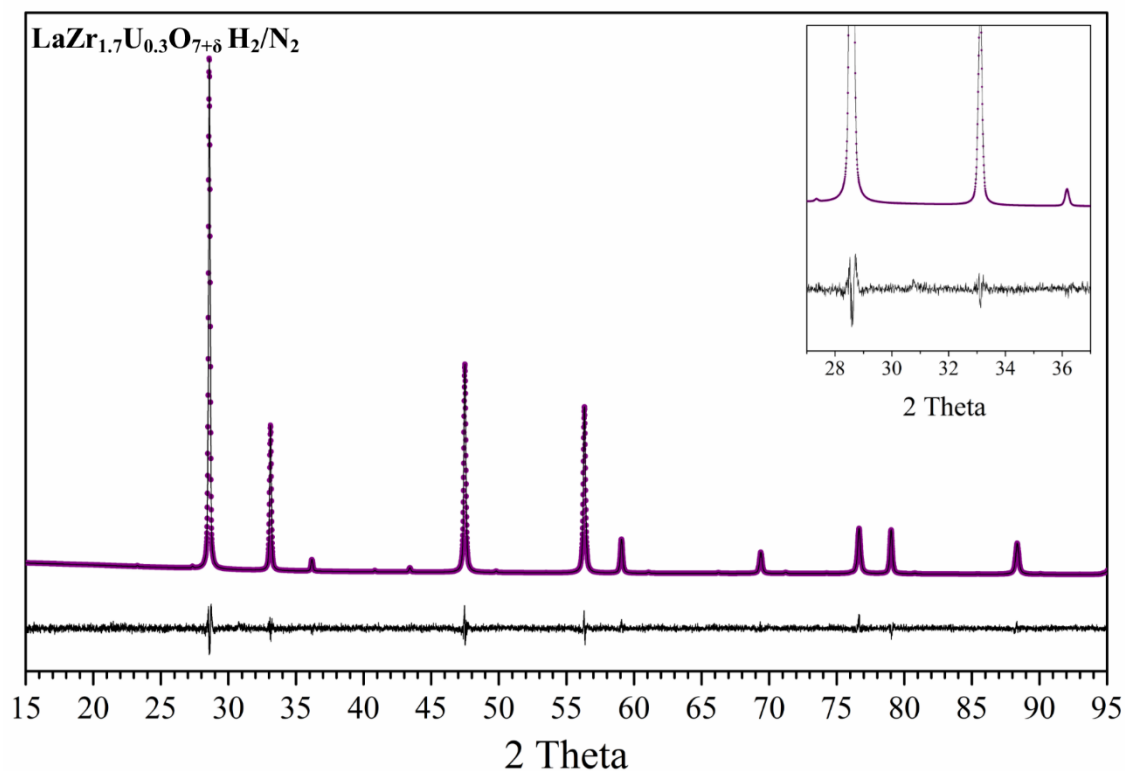


Figure B.8: Material of target composition La₂Zr_{1.7}U_{0.3}O_{7+δ} formed in a reducing hydrogen / nitrogen atmosphere, fitted using the GSAS software. Data shown is the calculated fit (black) and the observed – calculated difference trace highlighting the quality of the fit.

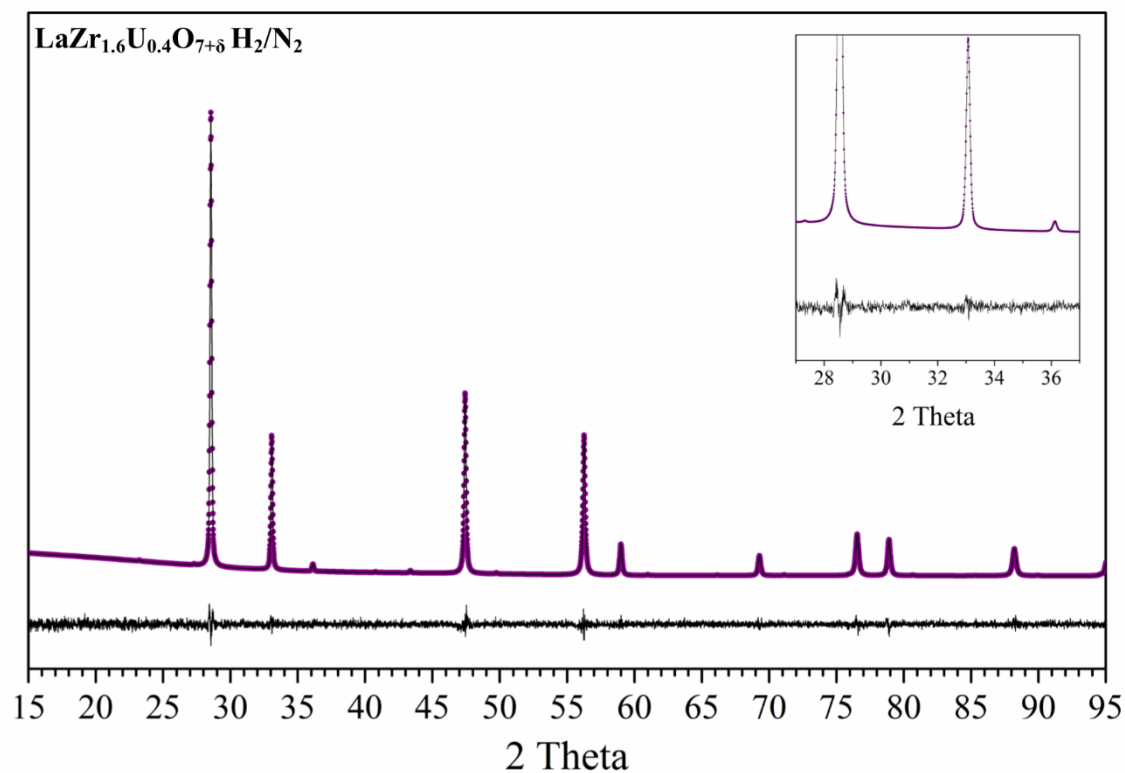


Figure B.9: Material of target composition La₂Zr_{1.6}U_{0.4}O_{7+δ} formed in a reducing hydrogen / nitrogen atmosphere, fitted using the GSAS software. Data shown is the calculated fit (black) and the observed – calculated difference trace highlighting the quality of the fit.

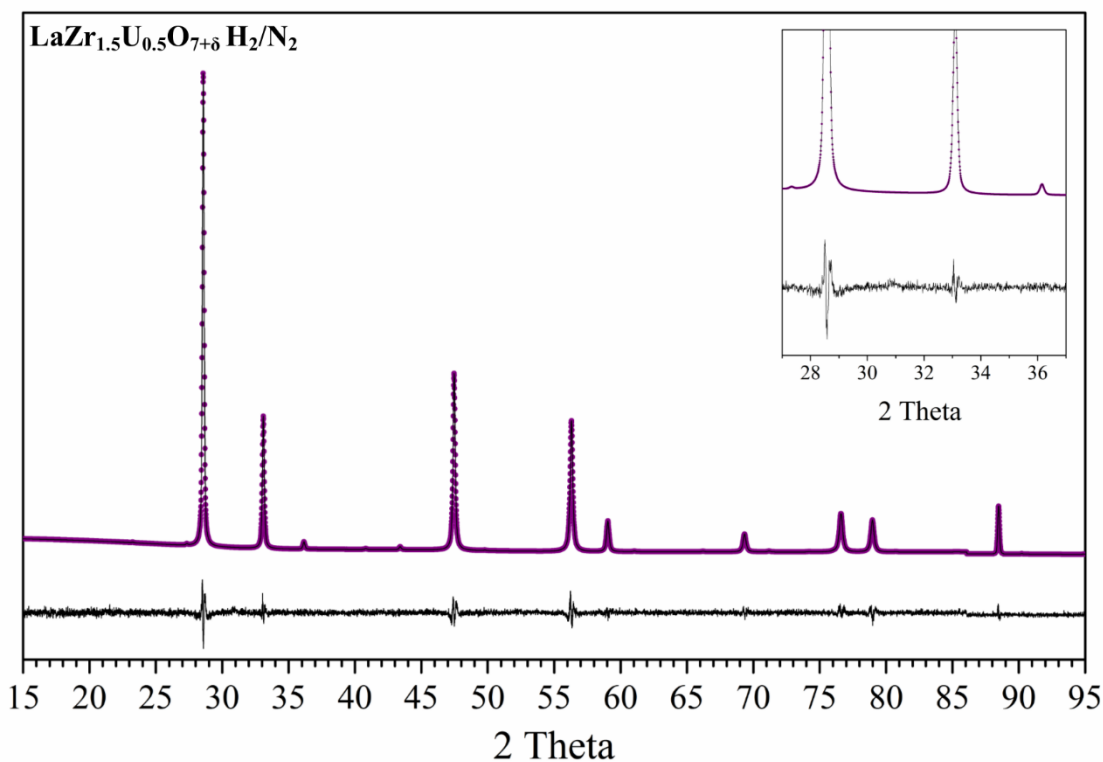


Figure B.10: Material of target composition $\text{La}_2\text{Zr}_{1.5}\text{U}_{0.5}\text{O}_{7+\delta}$ formed in a reducing hydrogen / nitrogen atmosphere, fitted using the GSAS software. Data shown is the calculated fit (black) and the observed – calculated difference trace highlighting the quality of the fit.

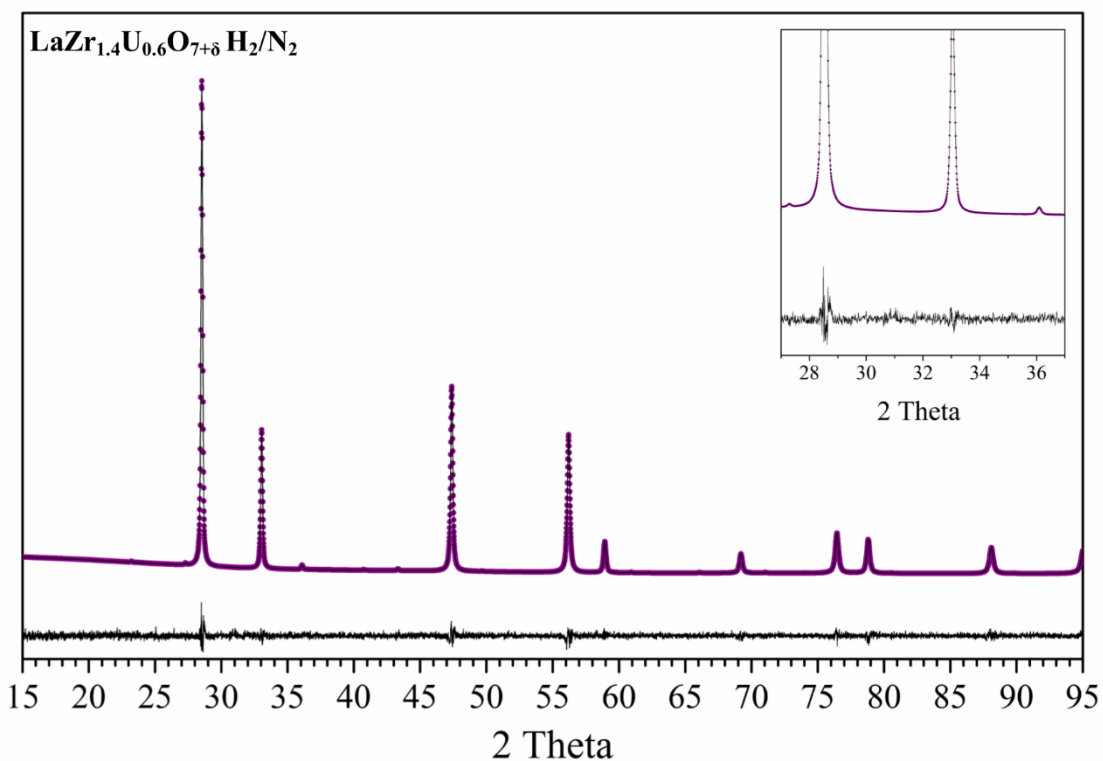


Figure B.11: Material of target composition $\text{La}_2\text{Zr}_{1.4}\text{U}_{0.6}\text{O}_{7+\delta}$ formed in a reducing hydrogen / nitrogen atmosphere, fitted using the GSAS software. Data shown is the calculated fit (black) and the observed – calculated difference trace highlighting the quality of the fit.

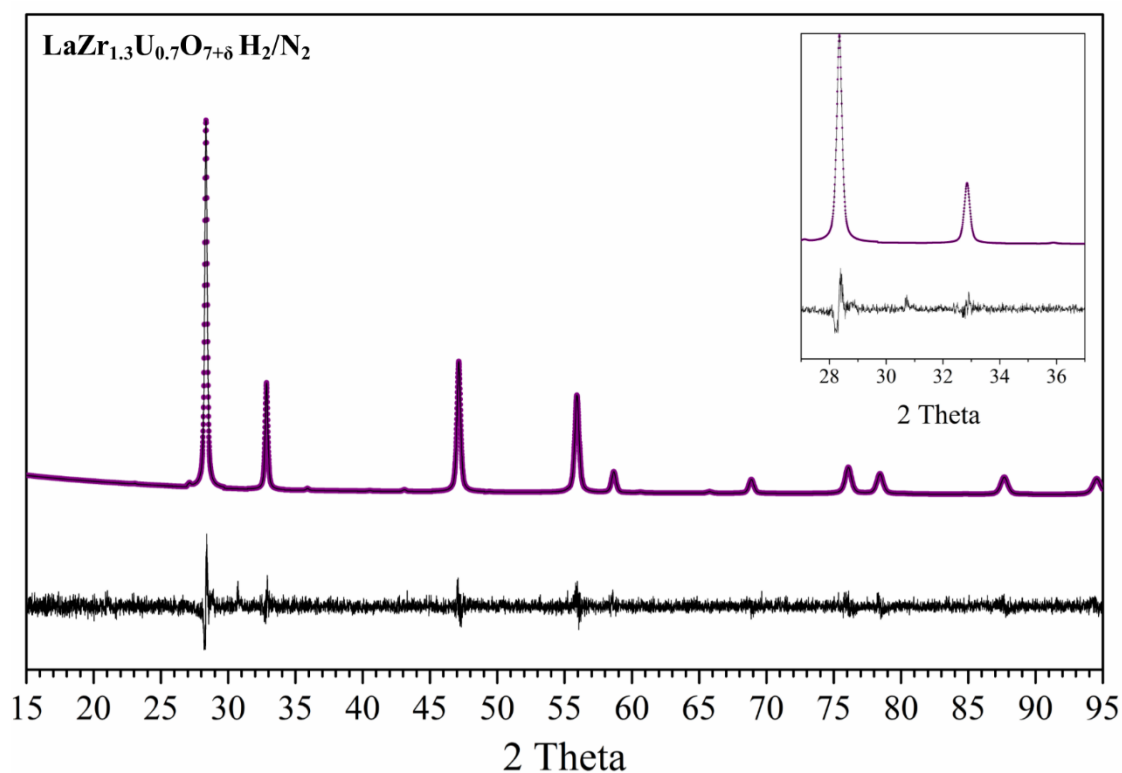


Figure B.12: Material of target composition $\text{La}_2\text{Zr}_{1.3}\text{U}_{0.7}\text{O}_{7+\delta}$ formed in a reducing hydrogen / nitrogen atmosphere, fitted using the GSAS software. Data shown is the calculated fit (black) and the observed – calculated difference trace highlighting the quality of the fit.

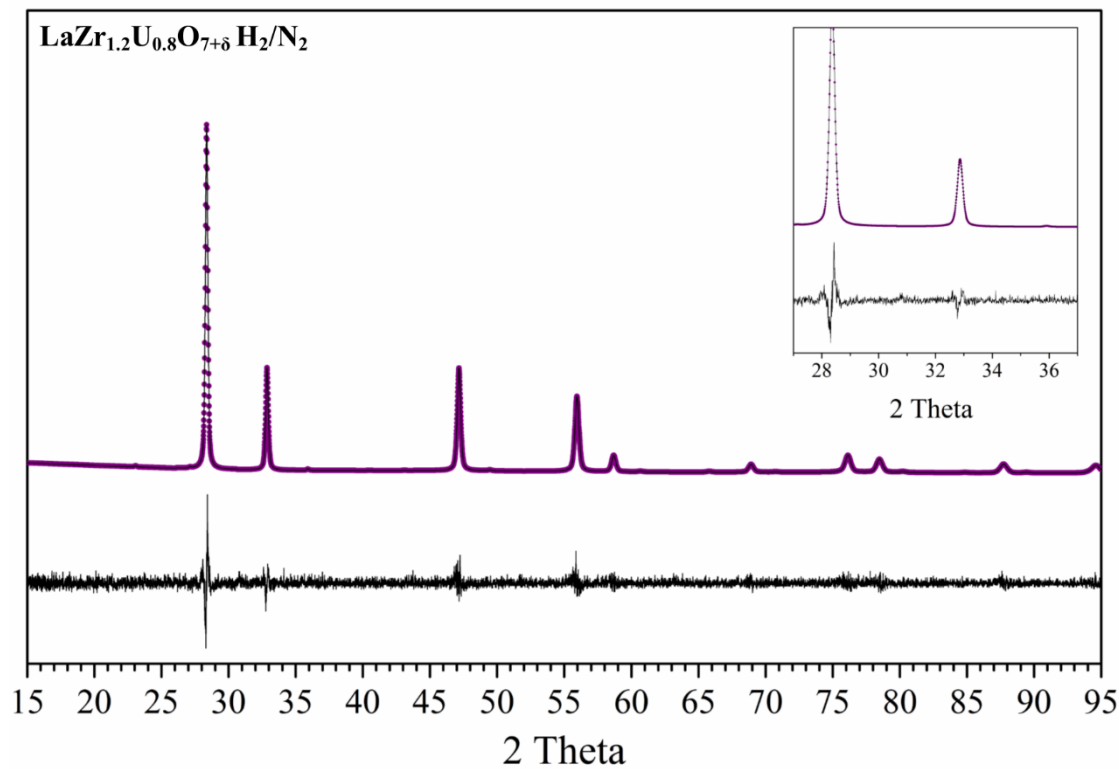


Figure B.13: Material of target composition $\text{La}_2\text{Zr}_{1.2}\text{U}_{0.8}\text{O}_{7+\delta}$ formed in a reducing hydrogen / nitrogen atmosphere, fitted using the GSAS software. Data shown is the calculated fit (black) and the observed – calculated difference trace highlighting the quality of the fit.

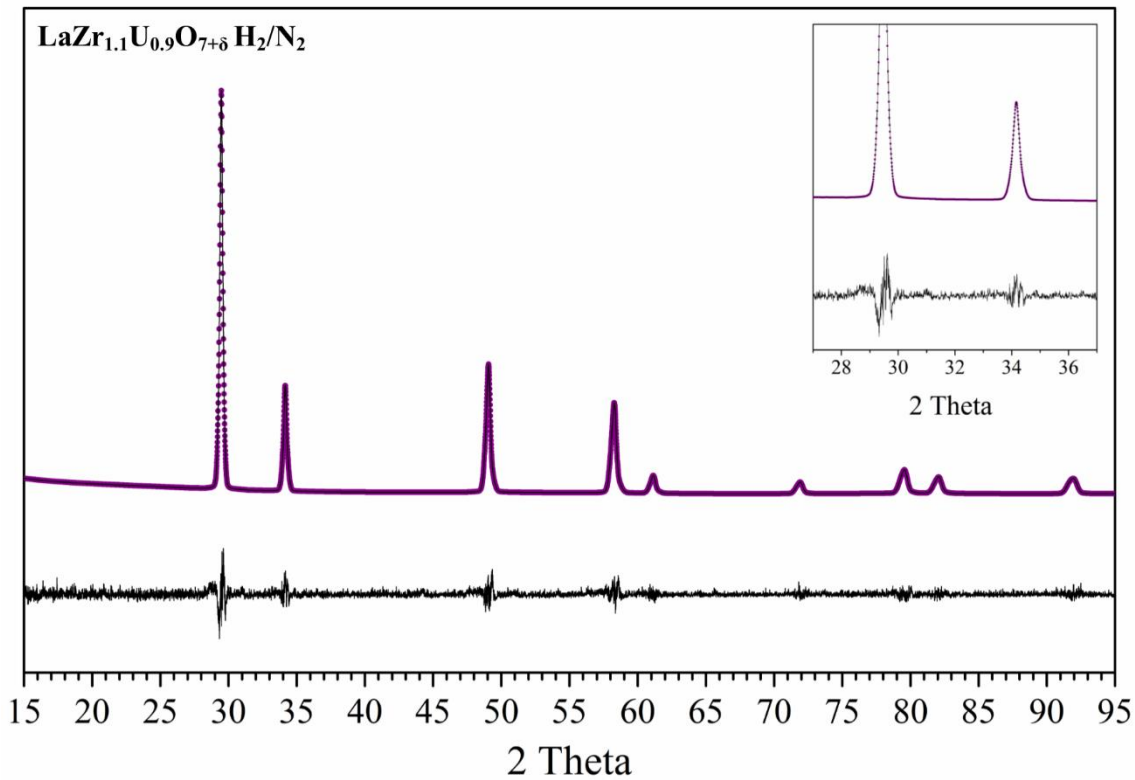


Figure B.14: Material of target composition $\text{La}_2\text{Zr}_{1.1}\text{U}_{0.9}\text{O}_{7+\delta}$ formed in a reducing hydrogen / nitrogen atmosphere, fitted using the GSAS software. Data shown is the calculated fit (black) and the observed – calculated difference trace highlighting the quality of the fit. This fitting has been achieved through the refinement of 3 fluorite structures, whose refinement can be found in Table 5.6.

B.3 Appendix B Reference

[1] Shannon R. Revised effective ionic radii and systematic studies of interatomic distances in halides and chalcogenides. *Acta Crystallographica Section A* 1976; 32:751-767.

Appendix C

C.1 Introduction

Within this appendix is additional data collated for 'Chapter 6- Formation of Uranium Titanate Materials'. This includes further data from refinement of high resolution neutron diffraction data.

C.2 Additional Experimental Data and Discussion

C.2.1 Additional High Resolution Neutron Diffraction Refinement Data

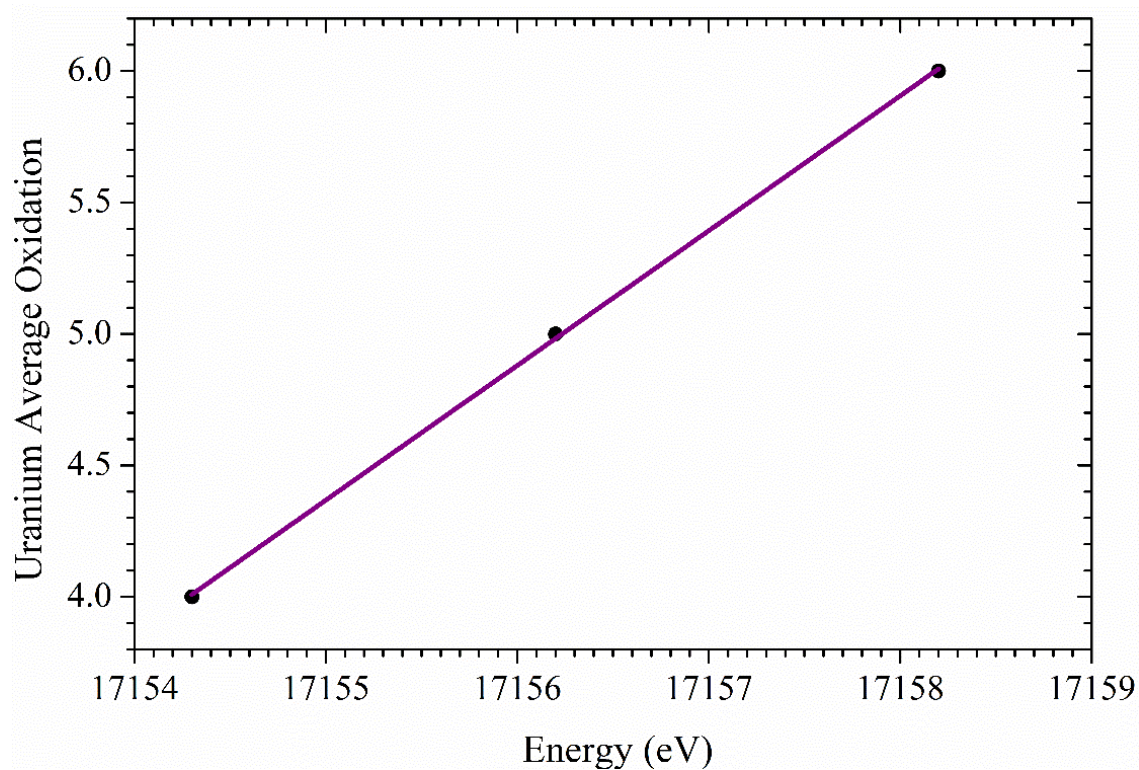


Figure C.1: Linear fitting of X-ray near Edge Absorption Spectroscopy (XANES) data collected on standard materials $\text{CaU}^{6+}\text{O}_4$, $\text{U}_{0.5}^{5+}\text{Y}_{0.5}\text{Ti}_2\text{O}_6$ and $\text{U}^{4+}\text{Ti}_2\text{O}_6$ with known uranium oxidations of U^{4+} , U^{5+} and U^{6+} .

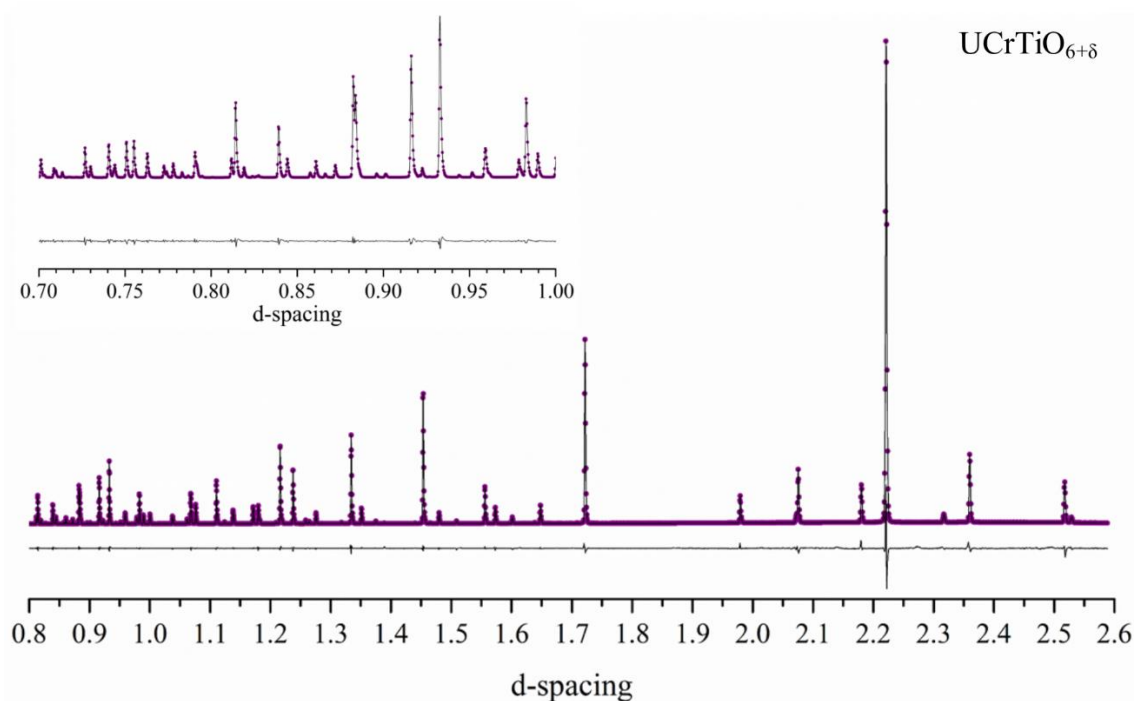


Figure C.2: Neutron diffraction refinement on sample with composition UCrTiO₆ completed using GSAS and neutron diffraction data collected on the HRPD instrument, ISIS, Oxford. Sample has a multiple rutile crystalline structure, this fitting has been achieved through the use of two rutile structures fitted to show the range of rutile structures formed, see Chapter 6, Table 6.7.

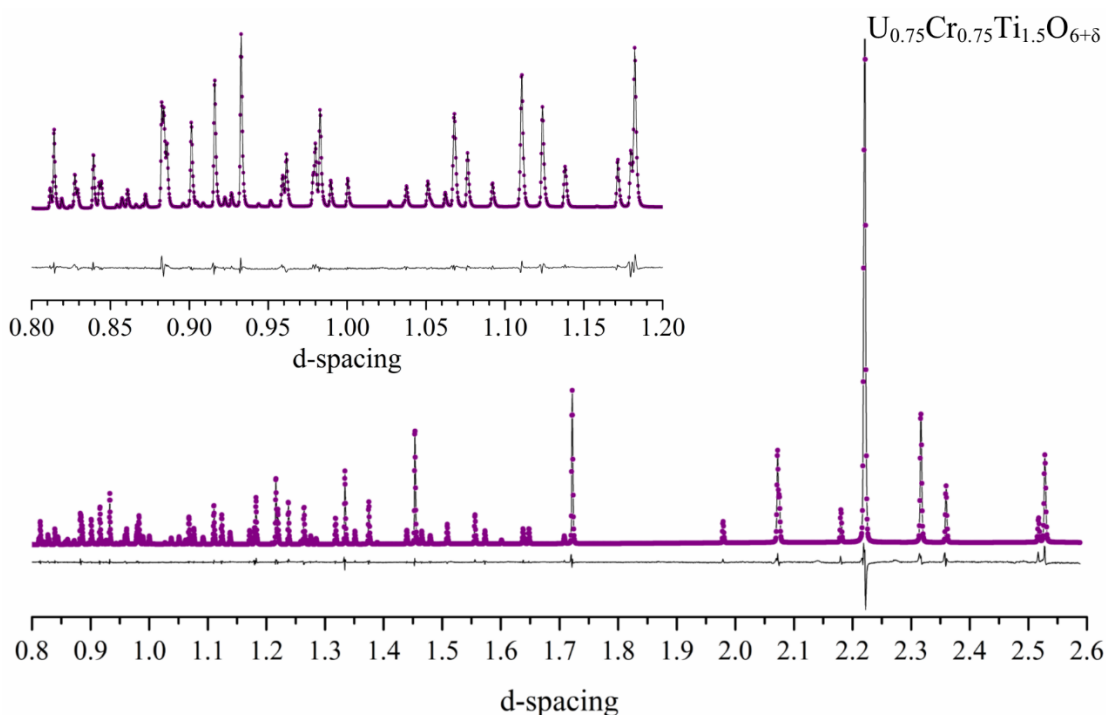


Figure C.3: Neutron diffraction refinement on sample with composition U_{0.75}Cr_{0.75}Ti_{1.5}O₆ completed using GSAS and neutron diffraction data collected on the HRPD instrument, ISIS, Oxford. Sample has a multiple rutile crystalline structure, this fitting has been achieved through the use of two rutile structures fitted to show the range of rutile structures formed, see Chapter 6, Table 6.7